New Trends in Enhanced, Hybrid and Integrated Geothermal Systems

Edited by

Alireza Dehghani-Sanij and Jatin Nathwani

Printed Edition of the Special Issue Published in *Applied Sciences*

MDPI

New Trends in Enhanced, Hybrid and Integrated Geothermal Systems

New Trends in Enhanced, Hybrid and Integrated Geothermal Systems

Editors

Alireza Dehghani-Sanij
Jatin Nathwani

MDPI

Editors

Alireza Dehghani-Sanij
University of Waterloo
Canada

Jatin Nathwani
University of Waterloo
Canada

This is a reprint of articles from the Special Issue published online in the open access journal *Applied Sciences* (ISSN 2076-3417) (available at: https://www.mdpi.com/journal/applsci/special_issues/Enhanced_Hybrid).

For citation purposes, cite each article independently as indicated on the article page online and as indicated below:

LastName, A.A.; LastName, B.B.; LastName, C.C. Article Title. *Journal Name* **Year**, *Volume Number*, Page Range.

Contents

About the Editors

Alireza Dehghani-Sanij, a Senior Research Fellow, is currently working at the University of Waterloo, Waterloo, ON, Canada. He holds a Ph.D. in Mechanical Engineering from Memorial University of Newfoundland, NL, Canada. His research interests include renewable energy, energy sources and production, energy conversion and storage, geothermal energy, hybrid energy systems, and sustainable development. With more than a decade of experience in academia and industry, he has published around 40 papers in peer-reviewed journals and presented more than 30 papers at conferences. He has also collaborated with other researchers to publish three scientific books in English with Elsevier, Springer and River Publishers, and six scientific books in Farsi with K.N. Toosi University of Technology and Yazda Publications. Among his scientific and professional memberships are ones in the American Society of Mechanical Engineers (ASME) and the Canadian Society for Mechanical Engineering (CSME).

Jatin Nathwani, Ph.D., P.Eng, Prof. of the Department of Management Sciences/Civil & Environmental Engineering, is the founding Executive Director, Waterloo Institute for Sustainable Energy (WISE). He held the prestigious Ontario Research Chair in Public Policy for Sustainable Energy (2007−2020). As the inaugural Ontario Research Chair in Public Policy for Sustainable Energy (2007−2020), he led research initiatives on accelerating energy transitions for a zero-carbon economy through systems assessments of technology, financing strategies, risk management and public policy. He is also a Fellow and currently leads the Research Cluster 'STEM for Global Resilience' at the Balsillie School for International Affairs (BSIA). Prof. Nathwani, co-Directs with Prof. Joachim Knebel (Karlsruhe Institute of Technology, Germany) is the Global Change Initiative-Affordable Energy for Humanity (AE4H). The consortium comprises 150+ leading STEM and social science researchers, energy access thought leaders and practitioners from 50 institutions in 30 countries committed to eradicating energy poverty by 2030.

Preface to "New Trends in Enhanced, Hybrid and Integrated Geothermal Systems"

The most important challenge for the global energy sector is to rapidly transform the entire system to one less dependent on fossil fuels and so reduce the harmful effects to climate. In sharp contrast, the global energy demand, mainly being met by fossil fuel resources, is continuing to grow, primarily in response to population and economic growth. Hence, finding, developing, and employing effective, economical, and practical solutions to the ongoing and emerging challenges is essential. Meeting global energy demand and simultaneously minimizing the negative consequences of climate change and the threat of global warming requires a transition to energy systems largely based on non-carbon renewable energy sources (e.g., solar, wind, geothermal, and hydro).

Geothermal energy installations—shallow, deep, or a combination of both—provide sustainable and environmentally friendly energy. Exploiting this source consists of extracting and/or storing the Earth's thermal energy for use in meeting electricity and heating/cooling needs for a variety of applications, including to heat and cool dwellings and greenhouses, provide warm and/or cold water for agricultural products in greenhouses, and even to de-ice roadways and parking areas.

The main goal of this Special Issue has been to address the existing knowledge gaps and help advance the deployment of geothermal energy projects worldwide. Of the twelve articles submitted, eight were accepted for publication after the peer-review process, an acceptance rate of 67 percent. The published articles cover a range of topics and applications central to geothermal energy. Although submission to this Special Issue is now closed, the need for further in-depth research and development related to geothermal technologies and systems (stand-alone or hybrid) remains. Due to the nature/specifications of geothermal energy, such as a local, robust, climate-independent, potentially constant, generally available, resilient, almost greenhouse gas-free, and long-lived energy source, it is anticipated that this renewable and sustainable source of energy will play a more prominent role in the future global energy supply mix.

In the end, we would like to take this opportunity to express our most profound appreciation to the MDPI Book staff, the editorial team of Applied Sciences journal, especially Ms. Lexie Gang, the assistant editor of this Special Issue, talented authors, and hardworking and professional reviewers.

Alireza Dehghani-Sanij, Jatin Nathwani
Editors

Editorial

Special Issue: New Trends in Enhanced, Hybrid and Integrated Geothermal Systems

Alireza Dehghani-Sanij [1,*] **and Jatin Nathwani** [1,2]

[1] Waterloo Institute for Sustainable Energy (WISE), University of Waterloo, Waterloo, ON N2L 3G1, Canada; nathwani@uwaterloo.ca

[2] Department of Management Science/Civil and Environmental Engineering, University of Waterloo, Waterloo, ON N2L 3G1, Canada

[*] Correspondence: a7dehgha@uwaterloo.ca; Tel.: +1-(416)-522-8809

1. Introduction

The most important challenge for the global energy sector is to rapidly transform the entire system to one less dependent on fossil fuels and so reduce the harmful effects on the climate. In sharp contrast, the global energy demand, mainly being met by fossil fuel resources, is continuing to grow, primarily in response to population and economic growth [1]. Therefore, finding, developing, and utilizing effective, economical, and practical solutions to the ongoing and emerging challenges is essential. Meeting the global energy demand and simultaneously minimizing the negative consequences of climate change and the threat of global warming requires a transition to energy systems largely based on non-carbon renewable energy sources (e.g., solar, wind, geothermal, and hydro) [2]. Geothermal energy installations—shallow, deep, or a combination of both—provide sustainable and environmentally friendly energy. Exploiting this source consists of extracting and/or storing the Earth's thermal energy for use in meeting electricity and heating/cooling needs for a variety of applications, including to heat and cool dwellings and greenhouses, provide warm and/or cold water for agricultural products in greenhouses, and even to de-ice roadways and parking areas [3].

The main goal of this Special Issue has been to address the existing knowledge gaps and help advance the deployment of geothermal energy projects worldwide. Of the twelve articles submitted, eight were accepted for publication after the peer-review process, an acceptance rate of ~67 percent. The published articles, briefly described in the following section, cover a range of topics and applications central to geothermal energy.

2. Summary of Published Articles

In the first article, Akbari Kordlar et al. [4] proposed a novel and adjustable tri-generation system—driven by geothermal heat sources—to meet the heating and cooling demands of a particular district network in Germany based on ambient air temperature. Their tri-generation system integrates a modified absorption refrigeration cycle and a Kalina cycle, utilizing a mixture of ammonia–water as the working fluid for the entire system. To examine the impact of various operational parameters on the system's performance before optimization, they conducted a sensitive analysis in off-design conditions, taking into account mass, energy, and exergy balances, and also off-design model equations for each component as a control volume. Their simulation results reveal that the proposed tri-generation system can meet the required heating and cooling demands. The authors also optimized the proposed system based on two criteria: the maximum exergy efficiency (the first scenario) and minimum total exergy destruction rate (the second scenario). The optimization results indicate that (1) a maximum mean exergy efficiency in the first scenario is obtained as 44.67 percent at the expense of a 14.52 percent increase in the total exergy destruction rate compared to the second scenario; (2) a minimum mean total exergy

destruction rate in the second scenario is calculated as 2980 kW at the expense of an 8.32 percent reduction in the exergy efficiency in the first scenario; and (3) taking into account both the exergy efficiency and total exergy destruction rate in off-design conditions, the best enhancement via the optimization process is achieved on a typical cloudy workday in winter, with 53.21 percent exergy efficiency and a 2570 kW total exergy destruction rate. Comparing the optimization results for both scenarios shows that the system's performance is more improved in the second scenario.

Kim et al. [5] experimentally analyzed a smart geothermal heating and cooling heat pump system consisting of an open loop—meaning the use of underground water from an aquifer—by means of a standing column well (SCW) and cross-mixing balancing well heat exchangers. To do so, they modified the present operational technique of two adjacent SCW geothermal heat exchangers, each with a single well. The authors employed this technology in order to improve the coefficient of performance (COP) of the geothermal system, basically through preventing underground water discharge and sustaining a constant temperature in the underground heat exchanger. The two balancing wells were utilized in the cross-mixing methods to restrain the bleed water discharge. According to the authors' findings, the mean amounts of COP measured from the balanced well cross-heat exchange system were, respectively, 3.76 and 3.27 throughout the cooling and heating operations. In other words, they achieved COP enhancements of 23 and 12 percent, respectively, during the cooling and heating operations compared to the present SCW method of the heat exchange system. Moreover, while utilizing a balancing well cross-mixed heat exchange system, the initial underground temperature was kept constant, with only a small standard deviation of 0.08–0.12 °C over 3–5 days of continuous operation, meaning that a relatively stable heat source supply is possible.

Maleki Zanjani et al. [6] numerically investigated the effect of utilizing fins on both the interior and exterior U-tube surfaces of a ground heat exchanger (GHE) under cooling mode, plus axial speed and temperature contours due to the tube curvature for an internally finned U-tube at different speeds. They then compared the results with results obtained from a finless U-tube GHE under the same physical conditions. The authors also simulated both dynamic and static behaviour of simple and finned (both internally and externally) U-tube GHEs to determine the impacts of longitudinal fins on the thermal performance of borehole heat exchangers (BHEs) and the heat transfer rate between circulating fluid and soil around the tubes. The dynamic simulations contained short timescale and frequency response tests. In fact, the authors' goal in performing the dynamic and static simulations was to find the best thermal efficiency. The simulation results illustrate that interior fins enhance the rate of heat transfer more effectively, so that the maximum fluid temperature variation was ~2.9 percent in the tube with exterior fins, and ~11.3 percent in the tube with interior fins, instead of the simple tube. Additionally, increasing the inlet fluid speed can make the differences more substantial in temperature profiles and changes, so changing the inlet fluid speed in the range of 0.02–0.06 m/s enhances the fluid temperature variation in the internally finned U-tube by 5–11.3 percent, in comparison with the finless U-tube. In contrast, the fluid temperature variation is only increased by 0.5–2.9 percent when the external fins are utilized. As for the dynamic behaviour, the priority of the interior fins is also apparent. Generally, the research performed by Maleki Zanjani et al. [6] confirms that the use of fins positively influences fluid temperature variations within the tube as well as the rate of heat transfer between the fluid and the borehole wall. The use of fins, especially interior fins, also enhances the thermal efficiency of a ground source heat pump system and reduces the length of the tube required and the initial expenses of the system.

Huang et al. [7] evaluated and reported on a location for a planned geothermal project, called the Alberta No. 1 project, which would produce power and heat (for direct use) at a commercial scale. The project is situated within the Municipal District of Greenview, south of the city of Grande Prairie, Alberta, Canada, and the evaluations demonstrate that there is a high likelihood of fluids up to 120 °C at depths of approximately 4000 m. According to the assessments conducted by the Alberta No. 1 project team, the target formations for

this planned geothermal project consist of dolomitized carbonate units of the Devonian age from the Beaverhill Lake Group to the top of the Precambrian Basement. Additionally, Permeable Devonian-aged sandstone units such as the Granite Wash Formation are also targets. The authors' findings suggest that elevations at the top of the Beaverhill Lake Group range from 3104 m to 4094 m, and temperatures at the top of the formation range from 87 °C to 123 °C in the project area.

Several potential challenges regarding the performance of sedimentary geothermal well-doublet systems, including heat conductivity, geochemical, and geomechanical conditions and issues, have been comprehensively examined and discussed by Mahbaz et al. [8]. These challenges may occur in the processes inside the reservoir itself, such as channelling, mineral precipitation and flow, and in the access and energy systems such as wells, heat exchangers, pumps, and surface tubing insulation. Some of their findings include that: (1) Chemical reactions can result in changes of flow-path, plus alterations of the rate of heat exchange between rock and water, and, consequently, changes in the reservoir's porosity-permeability and heat capacity; (2) Corrosion and scaling damage in the well-doublet systems diminish their performance and also influence their life-span; (3) Factors such as energy discharge rate and strategy, rate of injection, temperature and heat management, and well spacing contribute substantially to the heat recovery and life-span of a geothermal well-doublet system; (4) The injection of geothermal fluid such as water, carbon dioxide, and air into a well-doublet system can induce stress variations at a scale that will increase the likelihood of fault/fracture reactivation and induced seismicity. Therefore, realizing the magnitude of these events and their recurrence in time is important; (5) Factors including channeling, short-circuiting, leaking, heterogeneity, and permeability impairment can influence project viability, so they must be carefully evaluated during site assessment. Recognizing and understanding these challenges and issues will assist designers/engineers in better designing, implementing, and operating sedimentary geothermal well-doublet systems, leading to improved performance and increased efficiency of these types of systems, in addition to lessening their associated expenses and risks.

Gao et al. [9], by means of a hydro-thermal coupling model, numerically examined the impact of fluid flow direction on the heat transfer performance and specifications in a granite single fracture and validated the accuracy of the numerical modeling results experimentally. Their findings indicate a consistently robust relationship between the distribution of the local heat transfer coefficient and the fracture profile, independent of the axis. An alteration in the direction of the fluid flow is likely to change the amount of the heat transfer coefficient, but does not influence the distribution specifications along the flow pathway. An increase in the rate of injection fluid flow has an enhanced influence. Although the heat transfer capacity in the fractured rises with the rate of fluid flow, a sharp reduction in the rate of heat extraction and the total heat transfer coefficient is also seen. In addition, the model with the smooth fracture surface in the flow direction reveals a greater heat transfer capacity in comparison with that of the fracture model with differing roughness. This finding is attributed to the existence of fluid deflection and dominant channels.

The study conducted by Gizzi et al. [10] deals with the reuse of abandoned or disused deep hydrocarbon wells in Italian oilfields to extract the associated geothermal resources. The authors utilized existing information on Italian oil and gas wells and on-field temperatures to employ a simplified closed-loop coaxial wellbore heat exchanger (WBHE) model at three hydrocarbon wells positioned in different Italian oilfields, namely, the Villafortuna–Trecate, Val d'Agri-Tempa Rossa, and Gela fields. The goal was, in fact, to appropriately examine the heat transfer mechanisms of the three, focusing on the fact that the potential to extract thermal energy can alter based on the geological and sedimentary context. The results demonstrate considerable difference between the potential quantities of thermal energy to be extracted from the three wells studied. Taking into account the maximum extracted working fluid temperature of 100 °C and hypothesizing a cascading exploitation mode of the heat accumulated, it was only possible for the Villafortuna 1

WBHE to consider a multi-purpose and comprehensive use of the resource, based on the use of existing infrastructure, available technologies, and current knowledge.

In the last article, Ćuković Ignjatović et al. [11] evaluated an approach for the cascade utilization of geothermal energy potential for space heating and cooling and balneological treatments in the most south-eastern region of the Pannonian basin, in Central Europe. For this purpose, they selected two specific sites with various geothermal resources (meaning different temperatures and chemical compositions) and located within different urban contexts—one in a natural environment called Ljuba and the other inside a small settlement called Banatsko Veliko Selo—situated in the province of Vojvodina, northern Serbia. At the Ljuba site, a geothermal spring with a temperature of 20.5 °C was characterized to employ a geothermal heat pump (GHP) for the production of heat, whereas at the Banatsko Veliko Selo site, a geothermal well with a temperature of 54 °C was appropriate for direct use. The authors calculated the available thermal power from the geothermal resource according to geothermal conditions for both sites, ranging from 300 kW (GHP) to 950 kW (direct use), along with the cascade method of utilization. At the same time, they proposed a development concept with an architectural design, matched with energy availability based on the modularity concept, to enable sustainable energy-efficient development of wellness and spa/medical facilities that can be supported by local authorities. The resulting energy heating demands for different scenarios were 16–105 kW, which can fully be supplied by geothermal energy.

3. Future Research Need

Although submission to this Special Issue is now closed, the need for further in-depth research and development related to geothermal technologies and systems (stand-alone or hybrid) remains. Due to the specifications of geothermal energy, such as a local, potentially constant, robust, generally available, resilient, almost greenhouse gas-free, and long-lived energy source, it is anticipated that this renewable and sustainable source of energy will play a more prominent role in the future global energy supply mix.

Conflicts of Interest: The authors declare no conflict of interest.

Abbreviations

BHEs	Borehole Heat Exchangers
COP	Coefficient of Performance
GHP	Geothermal Heat Pump
GHE	Ground Heat Exchanger
SCW	Standing Column Well
WBHE	Wellbore Heat Exchanger

References

1. Dehghani-Sanij, A.R.; Bahadori, M.N. *Ice-Houses: Energy, Architecture, and Sustainability*; Elsevier, Imprint by Academic Press: Amsterdam, The Netherlands, 2021.
2. Kazemi, A.R.; Mahbaz, S.B.; Dehghani-Sanij, A.R.; Dusseault, M.B.; Fraser, R. Performance evaluation of an enhanced geothermal system (EGS) in the Western Canada Sedimentary Basin. *Renew. Sustain. Energy Rev.* **2019**, *113*, 109278. [CrossRef]
3. Kinney, C.; Dehghani-Sanij, A.R.; Mahbaz, S.B.; Dusseault, M.B.; Nathwani, J.S.; Fraser, R.A. Geothermal energy for sustainable food production in Canada's remote northern communities. *Energies* **2019**, *12*, 4058. [CrossRef]
4. Akbari Kordlar, M.; Heberle, F.; Brüggemann, D. Evaluation and Optimization of the Annual Performance of a Novel Tri-Generation System Driven by Geothermal Brine in Off-Design Conditions. *Appl. Sci.* **2020**, *10*, 6532. [CrossRef]

5. Kim, D.; Lim, M.; Yu, B.; Lee, C. Smart Heating and Cooling Heat Pump System by Standing Column Well and Cross-Mixing Balancing Well Heat Exchangers. *Appl. Sci.* **2020**, *10*, 7643. [CrossRef]
6. Maleki Zanjani, A.; Gharali, K.; Al-Haq, A.; Nathwani, J. Dynamic and Static Investigation of Ground Heat Exchangers Equipped with Internal and External Fins. *Appl. Sci.* **2020**, *10*, 8689. [CrossRef]
7. Huang, K.K.; Hickson, C.J.; Cotterill, D.; Champollion, Y. Geothermal Assessment of Target Formations Using Recorded Temperature Measurements for the Alberta No. 1 Geothermal Project. *Appl. Sci.* **2021**, *11*, 608. [CrossRef]
8. Mahbaz, S.B.; Yaghoubi, A.; Dehghani-Sanij, A.; Sarvaramini, E.; Leonenko, Y.; Dusseault, M.B. Well-Doublets: A First-Order Assessment of Geothermal SedHeat Systems. *Appl. Sci.* **2021**, *11*, 697. [CrossRef]
9. Gao, X.; Zhang, Y.; Hu, Z.; Huang, Y. Numerical Investigation on the Influence of Surface Flow Direction on the Heat Transfer Characteristics in a Granite Single Fracture. *Appl. Sci.* **2021**, *11*, 751. [CrossRef]
10. Gizzi, M.; Taddia, G.; Lo Russo, S. Reuse of Decommissioned Hydrocarbon Wells in Italian Oilfields by Means of a Closed-Loop Geothermal System. *Appl. Sci.* **2021**, *11*, 2411. [CrossRef]
11. Ćuković Ignjatović, N.; Vranješ, A.; Ignjatović, D.; Milenić, D.; Krunić, O. Sustainable Modularity Approach to Facilities Development Based on Geothermal Energy Potential. *Appl. Sci.* **2021**, *11*, 2691. [CrossRef]

Article

Sustainable Modularity Approach to Facilities Development Based on Geothermal Energy Potential

Nataša Ćuković Ignjatović [1,*], Ana Vranješ [2,*], Dušan Ignjatović [1], Dejan Milenić [2] and Olivera Krunić [2]

[1] University of Belgrade - Faculty of Architecture, 11000 Belgrade, Serbia; ignjatovic.dusan@arh.bg.ac.rs
[2] University of Belgrade - Faculty of Mining and Geology, 11000 Belgrade, Serbia; dejan.milenic@rgf.bg.ac.rs (D.M.); olivera.krunic@rgf.bg.ac.rs (O.K.)
[*] Correspondence: natasa@arh.bg.ac.rs (N.Ć.I.); ana.vranjes@rgf.bg.ac.rs (A.V.)

Abstract: The study presented in this paper assessed the multidisciplinary approach of geothermal potential in the area of the most southeastern part of the Pannonian basin, focused on resources utilization. This study aims to present a method for the cascade use of geothermal energy as a source of thermal energy for space heating and cooling and as a resource for balneological purposes. Two particular sites were selected—one in a natural environment; the other within a small settlement. Geothermal resources come from different types of reservoirs having different temperatures and chemical compositions. At the first site, a geothermal spring with a temperature of 20.5 °C is considered for heat pump utilization, while at the second site, a geothermal well with a temperature of 54 °C is suitable for direct use. The calculated thermal power, which can be obtained from geothermal energy is in the range of 300 to 950 kW. The development concept was proposed with an architectural design to enable sustainable energy efficient development of wellness and spa/medical facilities that can be supported by local authorities. The resulting energy heating needs for different scenarios were 16–105 kW, which can be met in full by the use of geothermal energy.

Keywords: geothermal energy; Pannonian basin; geothermal cascade use; energy efficiency; wellness and spa facilities; balneology; bioclimatic architecture; passive design strategies; modular building

1. Introduction

Geothermal energy is recognized as a valuable resource having a variety of uses: from electricity generation (through geothermal power plants or through cogeneration systems) [1] and space heating and cooling (using the heat pumps) to direct use in a wide range of applications in areas such as balneotherapy [2,3], agriculture, industry, swimming pool heating, and in individual and district heating systems [4,5]. While harnessing geothermal energy for electricity production is mainly related to specific tectonic regions, its direct use is more common. Coupling the energy potential with the healing properties of water's temperature and chemical composition, is recognized as a versatile and efficient way of exploiting this geothermal resources [6–9].

Hot water springs have been used for healing and medical recovery since ancient times. Today, however, balneology is undergoing a transition both concerning its place in formal medical science and as an asset for the development of tourism, local and state economies and general popular well-being. Contemporary definitions of medical tourism encompass medical travel, recreational travel and traveling for other purposes [10]. All of the stated aspects are highly relevant for balneotherapy, which, by its nature, can successfully meet a variety of their needs if provided with adequate infrastructure. Serbia is particularly rich in mineral, thermal and thermo-mineral waters with sites that have been in use ever since the Roman Empire [11]. The same hydrogeological resources show great potential as a convenient source of hydrogeothermal energy [12] that could be used to achieve high levels of energy efficiency in wellness and spa facilities. The Serbian province of Vojvodina, despite its abundance of various resources, is undergoing constant depopulation and even

7

impoverishment in certain agricultural areas. Although current national and regional planning documents barely consider geothermal energy to be a strategic resource [13,14], its great potential should be used as a tool for sustainable development, especially in areas where the abundance of this resource may help address the economic challenges and a decades-long trend of depopulation.

In recent times, comprehensive research has been carried out in northern Serbia—Vojvodina province—with the aim of considering and estimating the geothermal potential. The defined potential of geothermal resources represents a strategic foundation for planning sustainable economic development, since geothermal energy is an abundant source of renewable energy that requires low-carbon and non-intermediary technology [15,16]. A multidisciplinary research concept was applied, which tended to display, in a single place, the potential for geothermal resources to provide sustainable models for development supported by local municipalities. The areas for the application of geothermal energy were analyzed through an integrated approach of economic-commercial factors based on the main assumption of cascade use [17]. In that respect, among other things, an analysis of increasing the share of geothermal energy within the field of balneology was performed. Geothermal resources were observed both as a healing factor due to temperature and chemical composition and also as an energy source for heating and cooling facilities where geothermal waters are already used for medical and wellness purposes.

The studied terrain represents a typical basin structure genetically correlated to southeastern parts of the Pannonian basin, which extends over the territory that includes present-day Hungary, Croatia, Slovenia, Romania and Serbia, where it occupies terrain to the north of the Sava and Danube rivers (Figure 1) [18]. Generally speaking, the Pannonian basin represents an area that has an expressed geothermal anomaly and extraordinary geothermal potential [19,20]. The basin's highest heat flow values, above 100 mW/m^2, have been registered in the northeastern part and in the central part with distribution towards the southern peripheral parts, that is, towards the Serbian basins and the Vardar zone [21,22]. The values of geothermal gradients in the area of Vojvodina province range from 4.0 to 7.5 °C/100 m [23,24]. The dominant way of geothermal exploitation is via wells. The average geothermal outlet temperature ranges from 25 to 75 °C. In Vojvodina province, 50 new balneological facilities were proposed for development [25–27]. When defining prospective locations for them, wellness and spa, sports and recreation, and medical programs were all taken into account as was the urban-development potential for these facilities. These were also analyzed from the point of view of energy efficiency, different building material, energy independence, energy self-sustainability, and carbon footprint minimization.

The architectural programs, derived from the multidisciplinary research and conceived as illustrative proposals for potential developments on the site, range from modest drinking fountains to complex resorts with variety of facilities (Figure 2). Since 20 out of 50 proposals refer to wellness and spa facilities, they have remained in the spotlight of further investigations. Throughout the process, a series of model units was developed and tailored to match medical and therapeutical requirements bearing in mind the imperatives of environmental consciousness, sustainability and architectural resilience suited to the local municipalities' needs and resources. The two sites, Ljuba and Banatsko Veliko Selo, were chosen to further explore the proposed model in two different settings regarding the built-up environment and geothermal capacities. The study presented in the paper aims to point out the general design guidelines for development of wellness and spa/medical facilities that can be supported by local municipalities. The resulting proposals should help them gradually develop facilities for public or commercial use by relying primarily on their own resources rather than waiting for developers to exploit the balneological potential.
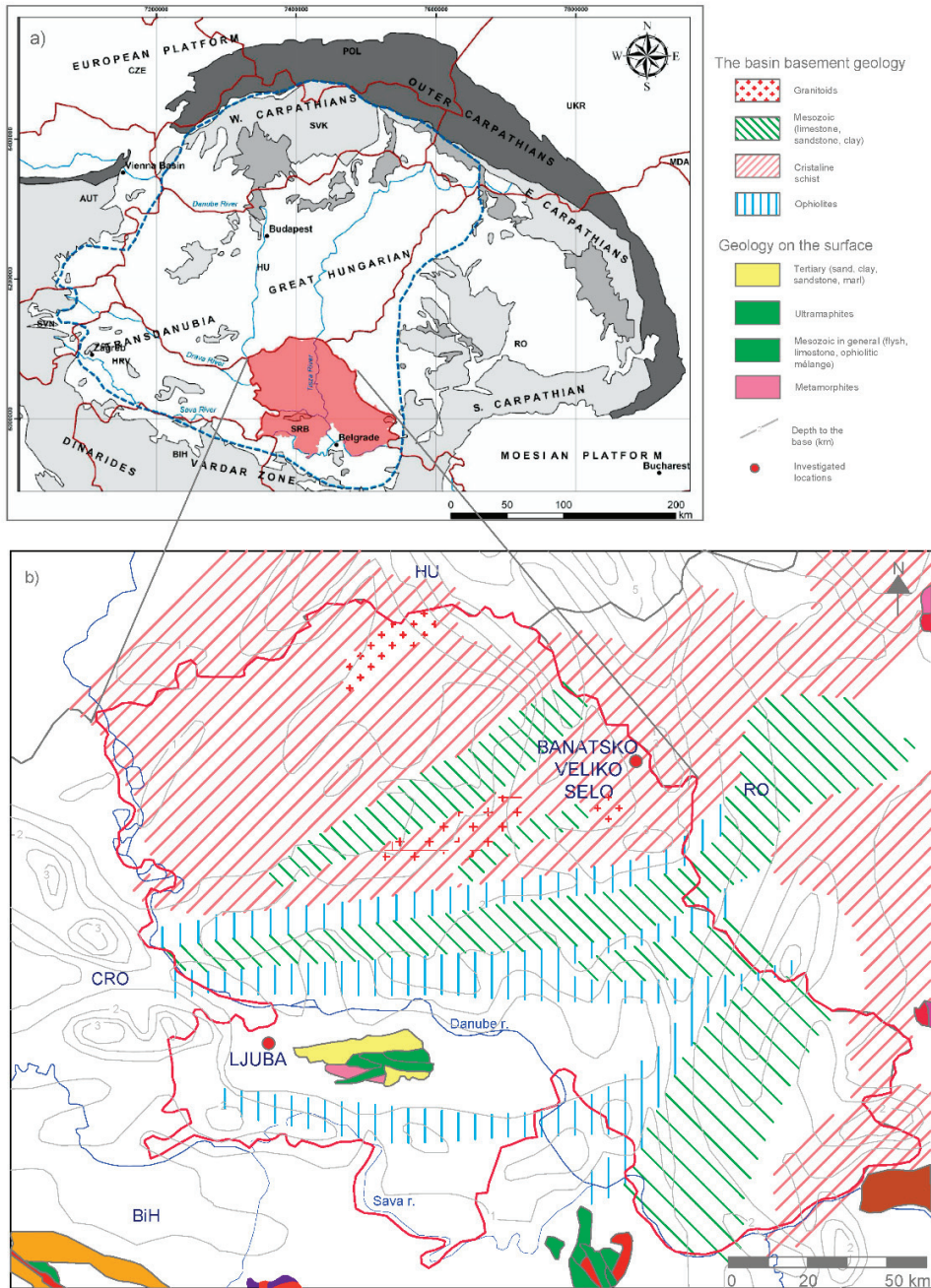
Figure 1. (**a**) Main tectonic units of the Alpine Fold Belt and Alpine–Carpathian–Dinaric Mountains (modified after [28]); (**b**) Geological map of the Vojvodina part of the Pannonian basin basement (modified after [29]).
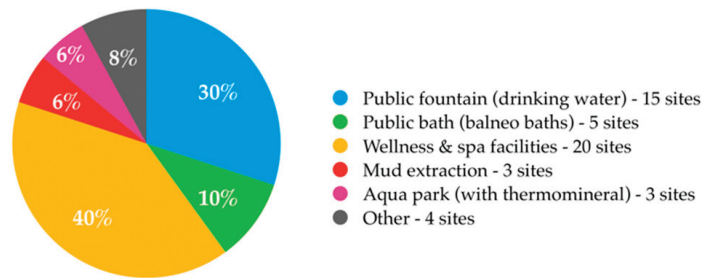
Figure 2. Proposed programs for new balneological sites in Vojvodina.

Since the design proposals referred to on-site use of the balneological resource, the character of the sites also varied greatly, from facilities placed within urban or rural settlements to sometimes rather remote places with poor or no infrastructure.

2. Materials and Methods

This paper shows two sites where geothermal resources were formed within different types of reservoirs, as well as with different temperatures and diverse chemical compositions. According to the features of these resources and spatial-urban conditions of the terrain, the manner of exploiting the resources and an architectural concept was suggested. The first site, Ljuba, is characterized by low-temperature geothermal water (<30 °C), which requires a geothermal heat pump (GHP) for heat production. The geothermal source is in the form of a spring, which is very rare for the basins. The reservoir is formed within Triassic limestone, and the water belongs to the HCO_3–Ca type as expected with this kind of reservoir. The uniqueness of this geothermal water may be seen from the chemical-specific composition of its microelements. From a water sample, a high concentration of arsenic was detected. The second location presented typical geothermal resources formed in basin sediments. The reservoir was formed within the sandy layers of the Pliocene epoch, with temperatures that ensure direct use (54 °C). The geothermal waters, produced by the geothermal well, belong to the HCO_3–Na type, and the main balneological factor is temperature. The available thermal power from the geothermal resource was calculated for both sites, along with setting the cascade system concept. Simultaneously, the architectural concept was developed, matching energy availability according to the concept of modularity.

2.1. Architectural Model—Design Premises

Design premises were in line with UN sustainability goals [30], where sustainable and resilient architecture for healthcare and spa facilities was conceived as the driver for a circular economy and improved well-being of the local population. The design approach was tailored with regard to the urban environment, the facility's current development status, need for (and availability of) accommodation, and seasonal sensitivity. The study of such a size was also seen as an opportunity to explore options for "branding" the wellness and spa/medical facilities of Vojvodina through recognizable design features.

The urban context was classified as "town" for sites within small urban settlements, "village" for those within rural settlements, and "remote" for those the farthest away from existing settlements (Figure 3). The fact that remote sites have no infrastructure and the ones in the villages are often poorly equipped stressed the necessity of providing a high level of infrastructure independence.

Figure 3. Number of proposed wellness and spa/medical facilities regarding urban/rural context.

The majority of proposed facilities (13 out of 20, Figure 4) were supposed to be completely new developments, while 7 cases were supposed to offer additional content mainly to partly developed outdoor facilities (usually pools, baths or ponds). In almost all cases, small scale structures were more suitable than conventional buildings that had all utilities in a single volume (Figure 5).

Figure 4. Number of proposed new developments and complementary contents that are adjacent to already existing wellness and spa or leisure facilities.

Figure 5. (**a**) Ljuba—currently an undeveloped site although used in Roman era; (**b**), Banatsko Veliko Selo—paths to outdoor pools (**c**,**d**) Banatsko Veliko Selo—outdoor swimming pool (existing facility).

The need to provide accommodation directly associated with the exploitation of balneological resource varied (Figure 6a). In 7 cases there was already accommodation in the vicinity (usually within walking distance); in 7 cases accommodation was not necessary due to the location and the nature of the balneological resource; and in 6 cases some accommodation had to be provided within the new development. This led the team to

explore flexible design concepts where accommodation would be an optional feature rather than placing all functions within a single volume. While allowing gradual development in pace with the local municipality's strategies and investment capability, this approach also provided more options for public use, which is of great importance to the community, giving the locals easier access to the wellness and spa/medical facilities.
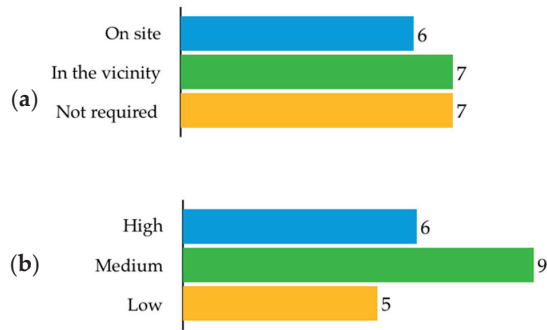
Figure 6. Number of proposed wellness and spa/medical facilities regarding (**a**) the need for and availability of accommodation, and (**b**) seasonal sensitivity.

The nature of the resource along with the site and the expected modes of use reflect the facility's "seasonal sensitivity" (Figure 6b). Most developments show medium seasonal sensitivity, which means that they can operate year-round in but with greater variation in capacity, while the ones with low seasonal sensitivity show less oscillation in seasonal use. In both cases, more demand on weekends than on weekdays can be expected. The modular approach presented in this paper addresses the issues of flexibility in the use of certain features and mitigation of operating costs for periods of lower demand. High seasonal sensitivity implies that the facility may operate only during the summer, so providing thermal comfort and natural ventilation on warmer days while staying in direct contact with the environment was dominant.

Climate in Vojvodina is classified as warm temperate, predominantly Cfa with areas of Cfb according to the Köppen–Geiger system. Month-to-month weather data for Vojvodina (Table 1) indicates that for 6 to 7 months some additional heating is needed while cooling might be needed for certain periods during the summer.

Table 1. Weather data for Vojvodina [31].

	January	February	March	April	May	June	July	August	September	October	November	December
Avg. Temperature (°C)	0.8	2.5	7.4	13.2	18	21.9	23.9	23.9	18.6	13.2	7.9	2.2
Min. Temperature (°C)	−2.3	−1.4	2.5	7.9	12.6	16.5	18.5	18.5	14	9	4.6	−0.6
Max. Temperature (°C)	4.3	6.7	12.4	18.2	23	26.7	28.7	28.9	23.4	17.9	11.8	5.4
Precipitation/Rainfall (mm)	43	43	46	60	67	75	64	56	55	49	50	53
Humidity (%)	80	76	69	63	63	61	58	57	64	71	77	81
Rainy days (d)	6	6	6	8	8	9	7	6	6	6	6	7

The issues of sustainability and resilience were addressed on several levels:

- program—defined to be sensitive to local needs and capacities, conceived for gradual development (reflected on various design aspects);
- adaptive capacities—aimed at enabling year-round functioning bearing in mind seasonal changes as well as prospective changes (anticipated and unexpected) throughout the facility's lifespan;
- infrastructure independence—aimed at off-grid functionality, especially for the remote sites;
- carbon footprint—aimed at carbon-neutral developments;

- local production—supported by the choice of proposed building technology and materials.

While resource efficiency in material use with reference to the 3R (reduce, reuse, recycle) concept remained as a general design goal, specific design strategies were proposed for energy efficiency, stressing the impact of architectural design on minimizing demand, thereby enabling coverage from on-site (renewable) energy sources. Program-specific energy efficiency design strategies focused on a wide range of passive design measures that integrated the technology related to necessary active systems from the conceptual design phase.

Water management in these facilities is very dependent on water composition, flow and temperature yet needs to be treated with extreme delicacy case be case to preserve the unique hydrogeological characteristics. All proposals were designed with extreme care to maximize porous surfaces, minimize potential contamination of surface water, and to make recommendations for rainwater collection and use where appropriate.

Design goals were addressed through a variety of design strategies, which were applied to 20 sites with wellness and spa facilities that ranged in size from small mobile units for balneotherapy to complex multifunctional developments. The main design strategies, developed mainly based on bioclimatic architecture, [32] included

- modularity,
- sizing and positioning of open-air and indoor features,
- passive design, and
- use of on-site renewable energy sources.

The general concept was developed with south-facing wellness and spa/medical units and corresponding utility spaces in the centre with optional additions of hospitality and medical facilities (Figure 7). However, adjacent medical and hospitality facilities might be planned with program-specific design strategies, so they were not further discussed in detail at this stage of the research.
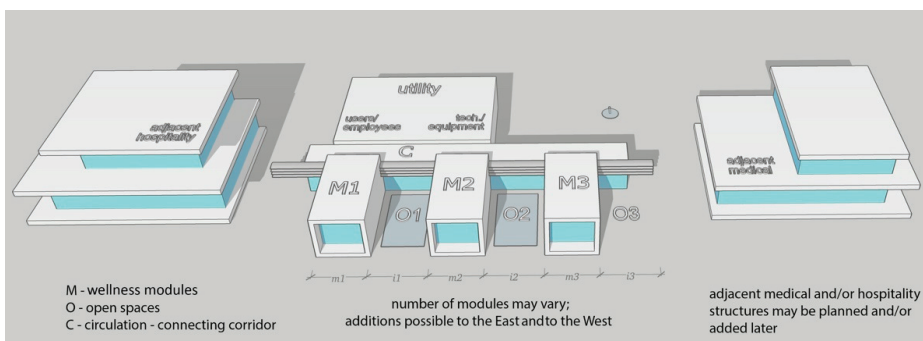
Figure 7. Model for modular wellness facilities with optional hospitality and medical facilities.

2.2. Architectural Model—Boundary Conditions and Calculation Methodology

Following the principles of modular design, modules of the same footprint (5.5 × 10 m) were used for both wellness and spa/medical facilities and utility spaces (heated and unheated). To enhance functionality and energy efficiency of the study model, balneotherapy units were grouped in pairs with a small joint space to access interior and exterior facilities. Heated auxiliary spaces were designed as combinations of 2–4 modules, while unheated modules may be placed along the northern side of the connecting corridor in a manner that enables efficient service and easy access. Figure 8 presents three development stages.
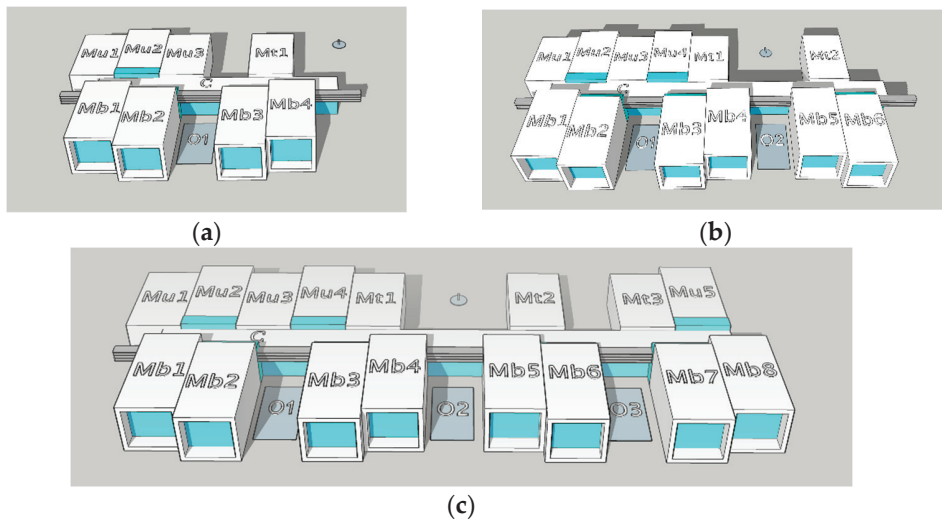
Figure 8. Three development stages for balneotherapy facility: (**a**) Stage 1 with 4 balneotherapy units, (**b**) Stage 2 with 6 balneotherapy units, and (**c**) Stage 3 with 8 balneotherapy units.

(1) an initial stage, with a small number of units and basic utility spaces (475 m², 2 × 2 units for balneotherapy);

(2) an intermediate stage, conceived as an extension of the initial stage (737 m², 3 × 2 units for balneotherapy), and

(3) high-capacity stage, (988 m², 4 × 2 units for balneotherapy).

Stage 1 (Figure 8a) comprises of 4 balneotherapy units *Mb1–Mb4* with 3 additional utility modules *Mu1–Mu3* for reception, changing rooms, office, examination room and café, and an unheated module *Mt1* as the mechanical room. Stage 2 (Figure 8b) is conceived as an expansion of Stage 1 with 2 added balneotherapy units *Mb5–Mb6*, an additional utility module *Mu4* and an additional technical module *Mt2*. The third stage (Figure 8c) presents a further extension with balneotherapy modules *Mb7–Mb8*, additional utility module *Mu5* and technical module *Mt3*. An overview of the basic data for all three stages is given in Table 2.

Table 2. Development stages—an overview of basic data.

Development Stage	Balneo Units (Heated)		Utility Units (Heated)		Utility Units (Unheated)		Intermediate (Heated)		Corridor (Heated)	Net Heated Area	Total Useful Area
	pcs.	(m²)	pcs.	(m²)	pcs.	(m²)	pcs.	(m²)	(m²)	(m²)	(m²)
1. Initial phase	4	220	3	165	1	55	2	17	18	420	475
2. Extended	6	330	4	220	2	110	4	34	43	627	737
3. High capacity	8	440	5	275	3	165	7	59	49	823	988

In terms of energy performance, two different approaches to building the thermal envelope were explored:

(a) base case, designed to comply with national regulations—EPC class C structure, with all envelope components meeting the mandatory *U*-values (thermal transmittance coefficient) thresholds; and

(b) enhanced performance case, with *U*-values of thermal envelope components designed in accordance with Passive House standards.

The thermal envelope components and their *U*-values are presented in Table 3.

Table 3. Thermal envelope components.

Component	U_{max} [W/(m² × K)] National [1]	EnerPHit [2]	Base Case	Enhanced Case
External wall	0.3	0.15	$U = 0.294$ W/(m² × K) gypsum board 1.25 cm; gypsum board 1.25 cm; wood particle board 1 cm; vapor barrier -; insulation/wood 50/10cm 15 cm; wood particle board 1 cm; rainscreen -; air 5 cm; wood cladding 1.8 cm	$U = 0.148$ W/(m² × K) gypsum board 1.25 cm; gypsum board 1.25 cm; wood particle board 1 cm; vapor barrier -; insulation/wood 50/10cm 32 cm; wood particle board 1 cm; rainscreen -; air 5 cm; wood cladding 1.8 cm
Flat roof above heated space	0.15	0.15	$U = 0.148$ W/(m² × K) hydroinsulation (membrane) 1.25 cm; wood particle board 2.5 cm; air layer / wood 10 cm; wood particle board 2.5 cm; wood particle board 2.5 cm; insulation / wood 50/10cm 30 cmn; vapor barrier -; air layer / wood 3 cm; gypsum board 1.25 cm; gypsum board 1.25 cm	
Windows, balcony doors to heated areas	1.5	0.85	$U = 1.5$ W/(m² × K) Aluminium frame with enhanced thermal break, Low-e double glazing with krypton gas filling $Fx = 1$ solar factor $g = 0.4$ frame factor $ff = 0.25$	$U = 0.85$ W/(m² × K) Aluminium frame with enhanced thermal break, Low-e triple glazing with krypton gas filling $Fx = 1$ solar factor $g = 0.35$ frame factor $ff = 0.25$
Glass roofs	1.5	1.1	$U = 1.50$ W/(m² × K) Aluminium frame with enhanced thermal break, Low-e double glazing with krypton gas filling $Fx = 1$ solar factor $g = 0.4$ frame factor $ff = 0.25$	$U = 1.1$ W/(m² × K) Aluminium frame with enhanced thermal break, Low-e triple glazing with krypton gas filling $Fx = 1$ solar factor $g = 0.35$ frame factor $ff = 0.25$
Wall to unheated space	0.4	0.35	$U = 0.278$ W/(m² × K) gypsum board 1.25 cm; gypsum board 1.25 cm; wood particle board 1 cm; vapor barrier -; insulation/wood 50/10cm 15 cm; wood particle board 1 cm; gypsum board 1.25 cm; gypsum board 1.25 cm	$U = 0.144$ W/(m² × K) gypsum board 1.25 cm; gypsum board 1.25 cm; wood particle board 1 cm; vapor barrier -; insulation/wood 50/10cm 32 cm; wood particle board 1 cm; gypsum board 1.25 cm; gypsum board 1.25 cm
Floor on the ground	0.35		$U = 0.280$ W/(m² × K) ceramic tiles 1 cm; adhesive 1 cm; membrane 0.2 cm; screed / floor heating 6 cm; insulation XPS 12 cm; hydroinsulation 1 cm; concrete 10 cm; gravel 10 cm	$U = 0.149$ W/(m² × K) ceramic tiles 1 cm; adhesive 1 cm; hydroinsulation 0.2 cm; screed / floor heating 6 cm; insulation XPS 24 cm; hydroinsulation 1 cm; concrete 10 cm; gravel 10 cm

[1] Values defined for new construction in national Rulebook on energy efficiency of buildings [33]. [2] Values defined for cool-temperate climate in Criteria for the Passive House, EnerPHit and PHI Low Energy Building Standard [34].

For all six scenarios, energy needs were calculated in accordance with national legislation [33,35], which is based on the methodology defined by EN-ISO13790. All calculations regarding the annual energy needed for heating were done using the software *KnaufTerm2s v.27.20* [36] using the following calculation parameters:

- Linear thermal bridges $\sum A \times 0.1$ W/(m²K)
- Air exchange rate—infiltration 0.5 n
- Indoor temperature—winter 22 °C
- Indoor temperature—summer 26 °C
- Occupancy—surface per person (all regimes) 30 m²/pers
- Metabolic heat emission per person 80 W/pers
- Metabolic heat emission per m2 2.7 W/m²
- Dissipated heat from appliances 30 W/m²
- Fresh air flow per surface area 1 (m³/h)/m²
- Fresh air flow per person 30 (m³/h)/pers
- Heat gain utilization factor for the heating period $\eta_{H,gn} = 0.9$ (value for lightweight construction)

Maximum values for annual energy needs for heating for relevant building categories are shown in Table 4.

Table 4. Maximum values for annual energy needs for heating for mandatory EPC class C [35].

Building Category	$Q_{H,an}$ [kWh/m²]
Healthcare and social welfare	100
Tourism and hospitality	90
Sport and recreation	80

Energy demands were compared to the resource capacity for two sites in Vojvodina: Ljuba, a remote location with no available infrastructure, and Banatsko Veliko Selo, a settlement with a population of 2525 [37]. Here, the proposed structure should be placed adjacent to an existing outdoor swimming pool.

Complementary structures for hospitality and healthcare services were not considered in the study since the focus was on investigating innovative design approaches for wellness and spa/medical facilities, such as wellness and spa and public baths. In regard to estimating overall potential use of geothermal energy for heating, an approximation was made using current national regulations (estimated energy needs according to the EPC mandatory class C).

2.3. Geothermal Potential—Geological and Geothermal Conditions

Generally speaking, in the lithological structure of the Pannonian basin, one can clearly observe two massive lithological complexes: (1) The basin's Palaeozoic–Mesozoic bedrock and (2) the Neogene–Quaternary complex and the related two main types of geothermal reservoirs: fractured and karstified basement reservoirs, and sand/sandy-clay basin-fill reservoirs. The bedrock of the basin in a wider study area is represented by all types of rock: metamorphic, igneous and sedimentary, whereas the Neogene-Quaternary complex is represented by conglomerates, sandstones, clay stones, marl, alevrolites, clay sediments, sands and pebbles (Figure 1). The rocks of the basin bedrock were discovered on the surface of the terrain in the zone of the Fruska Gora horst.

The site of Ljuba is located in the southwestern part of Vojvodina province on the southern slopes of the Fruska Gora horst. The horst structure, extending east–west on its southern and northern sides, is controlled by gravity faults, along which blocks were downthrown in the Neogene period [38]. On Fruska Gora three outcropping domains can be distinguished: (1) a metamorphic core from the Palaeozoic era, (2) a clastic–carbonate sequence with intercalated ophiolites, ophiolitic mélange, and volcanics of the Upper

Permian–Paleogene period, and (3) Miocene–Quaternary sediments [39]. Palaeozoic meta-morphites are in tectonic contact with low- and middle-Triassic rock [40].

In terms of its geothermal features, this part of the terrain is characterized by high geothermal gradients, particularly on the edges of Fruska Gora. These values range from 6 to 7.5 °C/100 m. Geothermal basement reservoir discharge is carried out in two ways: predominantly via deep geothermal wells or in a natural way over the springs. The natural discharge is connected only to the terrain of Fruska Gora, where it takes place along fault-line structures and at the contact point of water-permeable and water-resistant rocks. The outlet temperatures of geothermal waters formed within this type of reservoir in the vicinity of Fruska Gora vary from 15 to 60 °C. At the study site, geothermal resources were formed within the dolomite and partially silicified Triassic limestone.

The site of Banatsko Veliko Selo is located in the northeastern part of Vojvodina province and is known for largest depths to the basin bedrock, which has the largest thickness of Neogene sediments. The terrain belongs to the area of intensive sinking (Great Hungarian Depression) from the Neogene period. This area is characterized by block structure and gravitational faults. In this part of the terrain, there is a dominant exploitation of geothermal waters formed within the basin-fill reservoirs. The Geothermal reservoir is represented by sands and sandstones of the Pliocene and Upper Pontian age and this kind of reservoir can be followed continuously over the whole area.

In this part of the terrain, relatively low of geothermal gradients were registered. The reason is the presence of very thick Neogene sediment (up to 3.5 km), overlaying magmatite and metamorphic rock. The correlation between low geothermal gradients and geological settings of this area can also be found in the existence of marly and silty layers at depths greater than 1000 m. Geothermal gradients measured in Pliocene sediment displayed very low values from 2.5 °C/100 m to 3 °C/100 m. Basin-fill reservoir discharge is performed exclusively via geothermal wells, whereas outlet temperatures do not exceed 60 °C. Geothermal waters, from the Pliocene and Upper Pontian belong to the HCO_3–Na–Cl water type, respectively to HCO_3–Na type and are characterized by relatively low mineralization (up to $\approx$8 g/L). As for gases, the dominant one is methane with 84–88 mol%, followed by nitrogen and CO_2.

2.4. Geothermal Potential—Calculation Methodology

Available thermal power from the geothermal resource is calculated based on geother-mal conditions at the sites along with the cascade method of usage. The geothermal resource is considered as a source of energy for providing heat for facilities and balenologi-cal purposes. This principle led to the three limiting parameters for the system:

- temperature stability,
- available resource quantity,
- and chemical composition

The possibility of geothermal energy application depends on fluid temperature. The two selected locations covering the whole range of geothermal heating purposes. The Ljuba site comes with hydrogeothermal resources accumulated in the groundwater of a temperature scope to 30 °C which is conditioned by the application of geothermal heat pumps [41], while Veliko Banatsko Selo comes with hydrogeothermal resources accumulated in the groundwater of temperature above 30 °C, which means direct use is possible. Therefore, the heating operating system on the Ljuba site is considered to be an open loop GHP system contrary to the passive geothermal system with heat exchanger at the Banatsko Veliko Selo site.

The thermal power availability for the both geothermal sites can be calculated as in Equation (1)

$$E = H \times Q \times \Delta T \tag{1}$$

where E is the nominal available power quantity (kW); H the specific heat of water (constant, 4.2 kJ/kg/°C); Q the yield of the source (kg/s, for water the same as l/s); and ΔT denotes the temperature difference between the entering water and the leaving water.

Geothermal systems on the both sites perform heating operations and must be able to cover the maximum thermal load demands. The physical and chemical characteristics have been analyzed simultaneously to define the method for balneological use (drinking, swimming, inhalation). Furthermore, the concept of the geothermal heating system is conditioned by the method of balneological application. For example, drinking does not consider temperature, but swimming does, which means a projected geothermal system must satisfy these conditions.

In order to provide relevant data for calculations, a geological/hydrogeological reconnaissance was carried out, followed by groundwater parameters regime monitoring (temperature, chemical composition, flow capacity). For the purpose of geothermal water and reservoir characterization, the D'Amore method and diagram was applied [42]. The method is based on the determination of six main genetic parameters, mainly based on cation–anion ratios. Calculated genetic parameters are in line with geothermal reservoir geology and are applied for both sites, Ljuba and Banatsko Veliko Selo. Geothermal investigations and monitoring last for 12 months.

3. Results and Discussion

The concept of a multidisciplinary approach to geothermal energy utilization has been justified by building modular wellness facilities. The calculated thermal power that can be obtained from geothermal energy is in the range of 300 kW (GHP) to 950 kW (direct use). The size of wellness facilities can be predicted by matching developed scenarios based on different standards for envelope U values and outside temperature in modular facilities with available geothermal energy. The results of the investigation on geothermal waters showed that resources can be used as a balneological resource as well. Two factors determine multipurpose usage: chemical composition, in the case of the first site, and increased temperature, in the case of the second location. The direct benefit is increased efficiency of the geothermal cascade systems.

3.1. Available Thermal Power and Potential Balneological Utilization

3.1.1. The Site of Ljuba

The yield of geothermal waters at the discharge site is changeable, and its average value equals Q = 4.5 L/s. Geothermal resources at the site of Ljuba can be classified as subgeothermal [43] since the temperature is 20.5 °C. According to their chemical composition, groundwater belongs to the HCO_3–Ca water type with low mineralization.

Table 5 shows basic physical–chemical values of the analyzed geothermal phenomenon. Taking into account the complex geological composition of the terrain and its active tectonics, what was carried out is the classification of geothermal water using the method of D'Amore's genetic parameters. According to the calculations of genetic parameters, geothermal water on the Ljuba site belong to the carbonated type, and this confirmed that the primary geothermal reservoir was formed in the Triassic rocks of the basin bedrock (Figure 9).

Table 5. Physical-chemical features of geothermal waters on the site of Ljuba.

T	Conductivity	pH	Na	K	Ca	Mg	HCO$_3$	SO$_4$
(°C)	(µS/cm)		mg/L	mg/L	mg/l	mg/L	mg/L	mg/L
20.5	850	7.2	20.5	2.7	102.9	39.9	495.8	26.5
Cl	**Fe**	**Mn**	**F**	**Al**	**As**	**Cu**	**Zn**	**Cr**
mg/L	mg/L	mg/L	mg/L	mg/L	µg/L	mg/L	mg/L	mg/L
14.4	<0.1	<0.02	0.276	<0.05	47.6	<0.05	<0.03	<0.01
Cd	**Ni**	**Pb**	**Se**	**Si**	**Hg**	**Sr**	**Li**	**H$_2$SiO$_3$**
mg/L	mg/L	mg/L	mg/L	mg/L	µg/L	mg/L	mg/L	mg/L
<0.002	<0.02	<0.01	<0.002	5.6	<0.5	0.77	<0.04	15.6
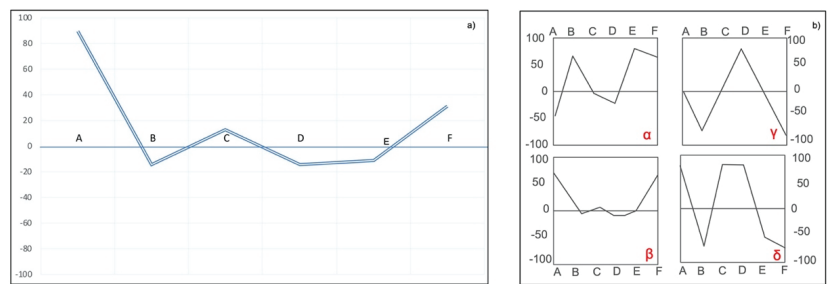
Legend for Figure 9a: A—indicates that geothermal waters had circulated through a calcareous terrains rather than an evaporative one; B—indicates that the geothermal water is enriched by sodium and may come from sedimentary terrains; C—is low, which excludes water deriving from a flysch, volcanite or schistose basement; D—indicates water circulation through dolomite; E—indicates that geothermal water had circulated in a carbonated reservoir rather than in a sulfated one; F—no indication in growth of potassium content, which excludes possible circulation in granitic field.

Figure 9. (**a**) D'Amore parameters diagram of chemical analyses; (**b**) α: evaporative terrains; β circulation in limestone; γ: circulation through a crystalline basement; δ: circulation in argillaceous rocks.

Available thermal power from the geothermal resource at the Ljuba site is calculated for the following scenario:

- open-loop geothermal heat pump system
- covering peak-load demands
- first cascade stage (temperature reduction for heating)
- second cascade stage (balneological purposes but not bathing)
- temperature reduction, ΔT = 16 °C. This temperature reduction, which we obtained from the resource temperature of 20.5 °C, was taken to calculate the total available thermal power on the site. In that case, the leaving water temperature was near 4 °C, reaching the highest liquid density.

In accordance with Equation (1) the available thermal power was:

$$E = 4.2 \, kJ/kg/°C \, 4.5 \, l/s \times 16°C$$

which generates around 300 kW of thermal power available for use.

Geothermal waters on the Ljuba site, apart from their energy significance, also possess a healing importance, so they can be used for balneological purposes as well. On the basis of their physical–chemical characteristics, these are characterized as natural, hypothermal, arsenic oligomineral waters, which can be used for health purposes under medical surveillance.

3.1.2. The Site of Banatsko Veliko Selo

At the site of Banatsko Veliko Selo, two geothermal wells were drilled: VS-1/H (925 m) and VS-2/H (895 m). The maximum measured outlet temperature was 43 °C at VS-1/H and 54 °C at VS-2/H. The yield of the VS-1/H well equaled 10 l/s, whereas the VS-2/H well had a somewhat higher yield of 12 L/s. According to the temperature values, geothermal resources at Banatsko Veliko Selo could be categorized as geothermal resources with low enthalpy, and according to their chemical composition belong to the HCO_3–Na water type. Table 6 shows the basic physical–chemical values of geothermal waters sampled from the borehole VS-2/H. Applying the method of D'Amore's genetic parameters, geothermal waters at Banatsko Veliko Selo belong to the clastic water type, and this confirmed that the primary geothermal reservoir was formed within the sands of Pliocene epoch (Figure 10).

Table 6. Physical-chemical features of geothermal waters VS-2/H.

T	TDS	pH	Na	K	Ca	Mg	HCO_3	SO_4	Cl
(°C)	(mg/L)		(mg/L)	(mg/L)	(mg/L)	(mg/L)	(mg/L)	(mg/L)	(mg/L)
54	219	7.6	478.5	4.0	12.0	11.0	1415.2	14.0	12.0
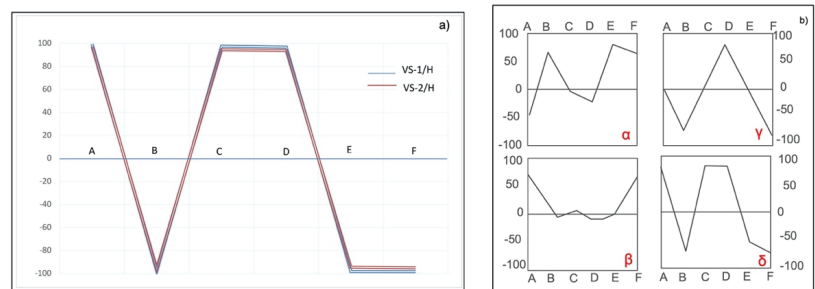
Legend for Figure 10a: A—indicates that geothermal waters had circulated through calcareous terrain rather than an evaporative one; B—indicates that this geothermal water, highly rich in sodium, may have come from sedimentary terrain; C—indicates that the geothermal water may have circulated through flysch sediments; D—excludes water circulations through dolomite; E—indicates the geothermal water had circulated in a sulfated reservoir rather than a carbonated reservoir; F—indicates no in growth of potassium content, which excludes possible circulation in a granitic field

Figure 10. (**a**) D'Amore parameters diagram of chemical analyses from Table 3; (**b**) α: evaporative terrains; β circulation in limestone; γ: circulation through a crystalline basement; δ: circulation in argillaceous rocks.

Available thermal power from the geothermal resource at B.V. Selo (VS-2/H) site is calculated for the following scenario:

- passive geothermal system with plate heat exchanger
- covering peak-load demands
- first cascade stage (temperature reduction for heating)
- second cascade stage (for balneological purposes, for bathing)
- temperature reduction, ΔT = 19 °C, which is adopted to meet temperature conditions for bathing (35 °C).

The calculation of disposable thermal energy from the geothermal borehole VS-2/H was performed according to the Equation (1).

$$E = 4.2 \text{ kJ/kg/°C} \times 12 \text{ l/s} \times 19°C$$

which brought around 950 kW of thermal power.

The first cascade level of exploitation provided energy for facilities heating, and the second level was provided a warm bath for balneological purposes. After geothermal waters pass through the heat exchanger, what remained disposable was water at 12 L/s at 35 °C, which is the most frequent temperature of healing waters used for curative purposes.

3.2. Architectural Design

Architectural design (general layout, massing, orientation, thermal zoning and materialization) was developed through a holistic approach and the consistent application of the design principles described in "Methodology". The result was a model for developing wellness and spa facilities, as well as public baths that were applicable at various sites and satisfied site conditions, sustainability goals and development scenarios.

3.2.1. Modularity

Structuring the program into modular units proved to be a very powerful and effective design tool for accomplishing the several design goals set for this study. While easily enabling programmatic diversification and flexibility, the modular approach also opened the door for local production of prefabricated elements by small and medium enterprises.

Carefully planned and positioned modules allowed for phase execution, which significantly reduced initial construction costs. This is even more important when the local community is funding or co-funding the facility since the median value of overall costs for 20 proposals included in the study (excluding the land, which is already publicly owned) is estimated to be approximately 1,500,000 euros. Only two of them were designed as single multifunctional buildings (total area 300 m^2 and 1000 m^2) due to the specific site and programmatic conditions.

Interconnected modules, which can be individually included or excluded from the facility's current operation, allow for very economical operation in reduced capacity as well, which is very important, having in mind that 15 out 20 facilities were characterized as being significantly seasonal, meaning that with this concept all of them may remain open to the public year round with optimized operational costs.

The modular approach, which visually and functionally brings together nearly isolated open-door and enclosed spaces (Figure 11), provides a layout with a high level of privacy, which minimizes contact among users of different treatments while allowing optimal hygiene and maintenance intervals during operating hours.

Figure 11. Visualization of proposed model for wellness and spa facilities.

The modular design also permits capacity expansion beyond the initial plans while retaining original design features or remaining at a reduced number of constructed modules for long periods in case of unfavourable economic, social or climate conditions. Expansions can be anticipated mainly along the east–west axes in two basic scenarios.

(1) Planning phases: Capacity is anticipated during the development period as the majority of auxiliary and technical spaces are planned according to the final capacity, and the modular units and adjacent programs (medical and hospitality) are executed in stages.

(2) Open development: The majority of auxiliary and technical spaces are planned according to initial capacity, and the main layout features are designed to support additional extensions until reaching a given site's full capacity.

Simple layout and structure of individual modules makes them very flexible, allowing for partial adaptations, changes in use, or even regaining functionality after an extreme catastrophic event and severe material damage.

3.2.2. Sizing and Positioning of Open-Air and Indoor Features

The general placement and interconnection of open-air features with built-up structures was proposed through a holistic design approach, taking into consideration functional demands, passive design principles [32,44], and the advantages of the modular approach as described in the previous section. The design strategies presented were developed bearing in mind the specific nature and demands of the wellness and spa features that incorporate balneotherapy as well as the geothermal potential of those sites.

Open-air and indoor features were purposely sized and organized in a way that allowed a shared use of auxiliary spaces like reception, changing rooms, lockers, and service rooms (Figure 7). The therapy functions are distributed throughout the open-air and enclosed spaces in a way that facilitates compatibility and provides a continuity of various treatments in different weather scenarios. This enables extended operation time, mitigating the sensitivity to seasonal or annual variations in climate while optimizing running costs.

Most open-air features are rather small, following the general concept of modularity and phase execution and operation. The width i of intermediate open-air spaces O may vary in regard to the height of the neighbouring modules M (Figure 7) for functional and privacy requirements. Additional screens may be added for enhanced privacy and additional sun protection of intermediate open spaces.

The modest capacities of both enclosed and open-air spaces allow the local production of most common types and enable less demanding maintenance, which may be one of the preconditions for sustainability of such features in small communities.

3.2.3. Passive Design Strategies

Striving for high level of energy efficiency and climate-responsive design, a series of passive design strategies were proposed to support the overall design goals.

Placement and orientation: Placement of all open-air features and enclosed spaces was done in a way that provided optimal daylight, solar exposure and shading. North-facing sections were used for technical rooms like storage and sanitary spaces. Circulation corridors connecting the modules were also placed on the northern side, leaving the south-facing open-air spaces between the modules to be sheltered and functionally supported by the side volumes. Longitudinal circulation space can be open or enclosed with glazed south-facing walls to serve as a buffer space for modules.

Massing, solar gains and shading: Modules are compact to provide a good shape factor for each unit. The same principles were applied to all public and utility spaces except for the longitudinal circulation corridor. Modular units and the corridor were mainly opaque on the north façade for improved thermal performance and almost fully glazed on the South façade to maximize solar gain. Adequate shading was provided by various design features tailored to provide unobstructed views under various weather

conditions (Figure 12) and additionally supported by an adequate choice of glazing and flexible interior shading.
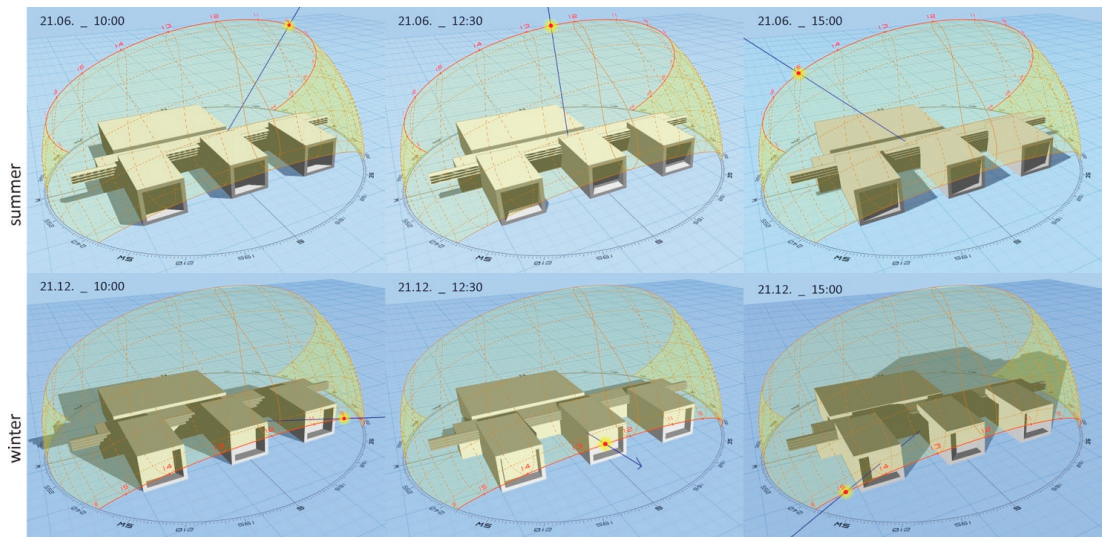

Figure 12. Solar exposure and shading: all glazed surfaces of wellness modules and circulation volume are fully shaded during the summer to prevent overheating (**upper row**) while remaining almost completely exposed during winter (**lower row**), enabling direct passive solar gain.

Natural ventilation and cooling: Glazed surfaces are designed to maximize the share of operable elements with cross-ventilation that are provided for all spaces. The basic layout, as previously described in this chapter, provides very good preconditions for natural ventilation and effective application of night cooling, which are further enhanced by the green areas and water features. Under favourable weather conditions, the glazed façade of the long corridor can be open along the intermediate semi-atrium spaces.

Thermal mass and materials: The modules are designed as lightweight structures where a low thermal mass optimizes comfort and energy efficiency in intermittently used spaces. Enhanced thermal insulation and a high-performance glazed element could significantly contribute to further mitigation of energy demands for cooling and heating. The façade and roof finishing also affect the energy efficiency, but they should be considered case by case. In exposed sites, with peak occupancy in summer season, reflective surfaces or green roofs should be prioritized. In more secluded sites, where structures are surrounded by deciduous trees (naturally shaded in summer and exposed in winter), reflectivity is not so much of an advantage.

3.3. Energy Demands

Energy demands were calculated for 6 cases—3 development stages with different operational capacities and two approaches to thermal envelope materialization. The basic climate data, as defined by the Rulebook on Energy Efficiency [33] for both sites are given in Table 7. The data for Banatsko Veliko Selo are somewhat less favourable (lower temperatures and higher HDD values) and were used as input to calculate the energy needed for heating.

Table 7. Basic climate data for Ljuba and Banatsko Veliko Selo.

	Average Temperature [1]	Design Temperature [2]	Heating Days	HDD
Ljuba	5.4 °C	−15 °C	184	2686
Banatsko Veliko Selo	4.9 °C	−15.3 °C	183	2763

[1] Average temperature during the hating season. [2] Design temperature for sizing the heating system, HDD—Heating degree-days.

The calculated annual energy needs for heating are presented in Table 8. The potential reduction of energy demand resulting from an improved thermal envelope are 40.35%, 35.74% and 35.98% for stages 1–3, respectively. While the enhanced model shows notably better energy performance, the results still remain within the EPC class C (50–100 kWh/m^{2}a).

Table 8. Annual energy needed for heating.

	Stage 1		Stage 2		Stage 3	
	Base Case	**Enhanced**	**Base Case**	**Enhanced**	**Base Case**	**Enhanced**
Heat losses (kWh)						
Transmission	51,597.94	35,625.64	75,290.03	52,198.15	100,799.42	69,786.58
Ventilation	15,675.93	15,675.93	23,436.22	23,436.22	30,824.67	30,824.67
Total losses (kWh)	67,273.87	51,301.57	98,726.25	75,634.37	131,624.09	100,611.25
Heat gains (kWh)						
Solar	21,189.90	18,541.00	31,567.60	27,621.50	42,303.60	37,015.80
People	3316.48	3316.48	4956.10	4956.10	6503.62	6503.62
Appliances	6309.89	6309.89	9429.41	9429.41	12,373.71	12,373.71
Total gains (kWh)	30,816.27	28,167.37	45,953.11	42,007.01	61,180.93	55,893.13
$Q_{H,nd}$ **(kWh/a)**	36,457.60	23,134.20	52,773.14	33,627.36	70,443.16	44,718.12
$Q_{H,nd}$ **(kWh/m^{2}a)**	83.46	53.37	80.86	51.96	82.25	52.66

The monthly heating energy demands for all six scenarios is shown in Figure 13. It can be observed that the values of "enhanced case" for one stage almost correspond to the values of "base case" for a smaller stage. Stage 3 enhanced case is lower than Stage 2 base case and Stage 2 enhanced case is just slightly above Stage 1 base case (lower in March). These findings indicate that the heating system and materialization should be chosen to correspond to seasonal sensitivity and the anticipated capacity of the final stage to achieve a balance between the initial costs and the effects throughout the facility's lifespan.
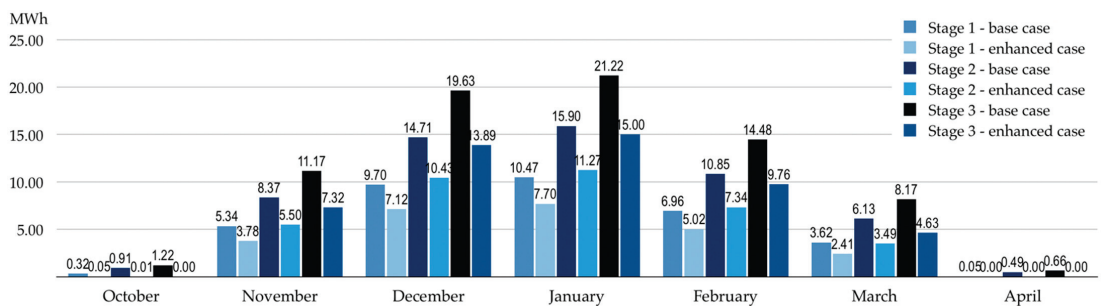

Figure 13. Energy needed for heating.

Cooling energy is not calculated since the model was designed to enable natural ventilation whenever necessary. In July and August, the average temperature is 23.9 °C and maximums are 28.7 and 28.9 °C, respectively (Table 1), which means that the cooling

systems (if any) should be designed primarily to meet the specific medical and therapy-related demands of a particular facility or specific modules within the facility.

The power demands P for heating were calculated for two different outside temperature settings:

- Pa—for average outside temperature (per the procedure for establishing EPC class), and
- Pd—for design temperature (per the procedure for sizing the overall capacity of a heating system).

The power demands Pd for the heating with regard to the outside design temperature were calculated based on Pa, using the following formula

$$Pd = \frac{Pa \times (t_i - t_d)}{(t_i - t_a)} \tag{2}$$

where t_i is the designed interior temperature, t_d is designed exterior temperature and t_a is the average exterior temperature.

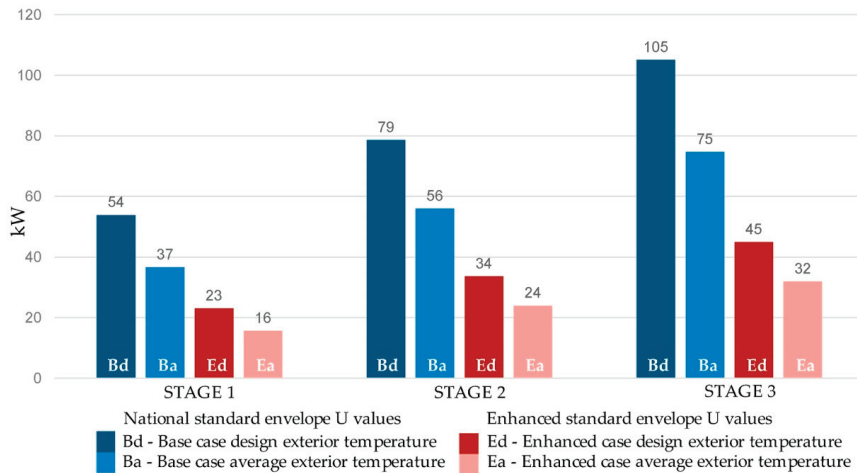The resulting power demands for the study cases are shown in Figure 14.

Figure 14. Power needed for heating.

During initial research, after developing the modularity-based approach, the modules were formed as single-purpose entities (one module for one type of balneological treatment—Figures 7, 11 and 12). This approach was rather successful in many cases, where it provided more options for interaction with the natural environment and versatility of outdoor balneological treatments on semi-private or private patios. However, extending such a concept to more units would be rather demanding because land occupancy, daily operation, supervision and other issues would have to be considered on case-by-case basis. The model used for the calculations is somewhat more compact with paired wellness modules (Figure 8). The initial module would obviously show higher energy demands for heating, but it is expected to be used in facilities that operate only during the summer. In both cases, special attention is dedicated to passive measures for thermal comfort during the summer, thereby minimizing mechanical ventilation and air conditioning while addressing the well-being of users, in addition to enhancing hygiene standards, new occupancy protocols and energy efficiency issues.

Exploring energy performance of three development stages in two types of materialization provided six scenarios where some additional observations can be made regarding thermal envelope components:

1. The share of the components' surface area in the overall thermal envelope area remained mostly constant throughout the development stages (Figure 15a). The ratio between the opaque and glazed elements was approximately 3:2 in all three stages, and the only component that showed a significant increase was the interior wall-to-unheated space as unheated technical modules are added.

2. The glazed surfaces accounted for more than half of heat transmission losses even in enhanced cases (Figure 15b). This component is key not only for energy efficiency but also for thermal comfort throughout the year, so the exact sun exposure and anticipated occupancy regime of particular facility should be specified on a case-by-case basis.

3. The materialization of opaque components reflects on the overall energy performance but further studies should be performed regarding the feasibility of using the enhanced option; the production of panels with more than 30 cm of thermal insulation (Table 3) requires technology and resources that might be more challenging for local companies. The composition of interior walls to unheated spaces may remain as proposed for the base case in all scenarios since their share in heat transmission losses is almost irrelevant (0.5–1.5%)

4. Since flat roofs cover a significant area, mounting PV units as additional renewable energy resources might cover the energy needs of electrical equipment.
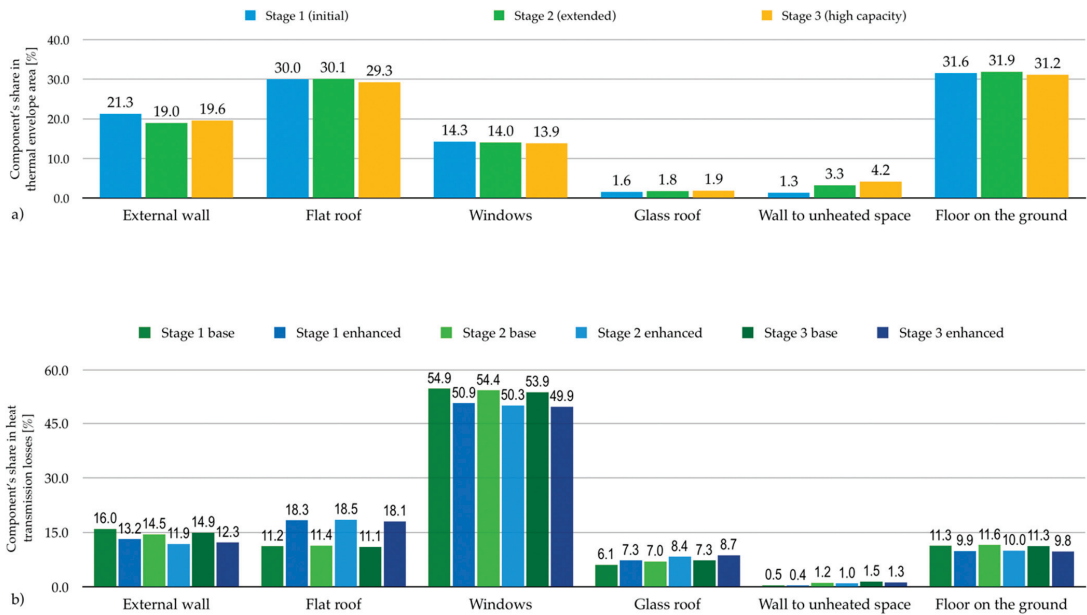
Figure 15. Distribution of thermal envelope components: (**a**) per surface area and (**b**) per contribution to heat transmission losses.

Regardless of the capacity of the location and the materialization variant, all development models consumed significantly less energy for heating than the geothermal potential provides. At Ljuba, the site with the lower capacity, development model 3 (maximum size) in the basic code-compliant state of materialization, and taking into account extreme external temperatures, yielded 35% of geothermal capacity; at Banatsko Veliko Selo 2, it was only 11%. In the improved variants, these needs are reduced to 13% and 4.7%, respectively.

Developed modules reached a significant level of energy efficiency, not only in heating demands but also in the sustainable use of groundwater. More than 50% of flow capacity was reduced in all three module stages between the base average exterior temperature and the enhanced average exterior temperature (Figure 16). The efficiency calculation was done for the Banatsko Veliko Selo site, where a cascade system with a constant ΔT value (19 °C) was adopted. The lower flow capacity may lead to less power consumption by circulation pumps and a low operational cost. In addition, these beneficial effects reflect resource preservation and sustainable exploitation.
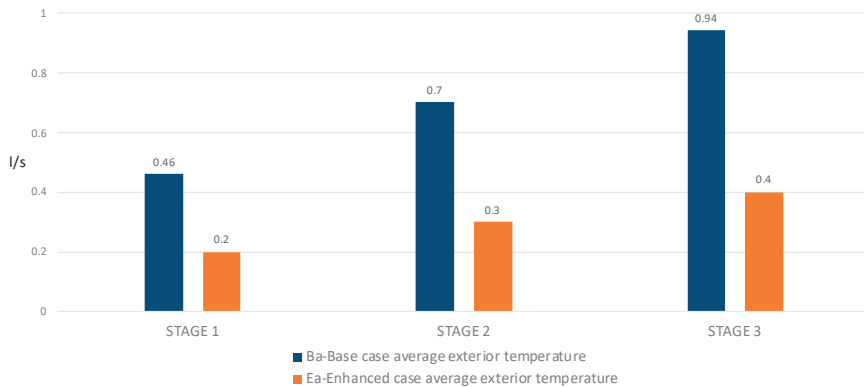

Figure 16. Modeled flow capacities—heating demand.

Additionally, the results indicated the possibility of the further use of the investigated geothermal potentials, primarily to provide energy for other facilities (healthcare, hospitality) or to heat complementary facilities, even larger pools or other aquatic venues.

4. Conclusions

Balneological usage presents one of the driving forces for the activation of geothermal resources in modern medical and rehabilitation practices. This paper addressed two sites chosen from previous interdisciplinary research conducted in the Vojvodina region that have different geothermal resources and placed within different urban contexts. Coupling the identified and analyzed geothermal potential with a purposely formulated architectural model for balneological application based on sustainable and green design strategies, the paper illustrated a possible development concept that could serve as an implementation tool for activation at various locations.

The developed architectural model showed good potential both for phase development and for effective and efficient use with adaptable capacities during the low season. The modular approach in placing indoor and outdoor balneotherapy as well as ancillary spaces enables a high level of flexibility with minimized operational costs. The base model was designed as a structure of approximately 500 m² of gross area, encompassing all basic wellness and spa activities with proper support spaces (e.g., reception, examination room, changing rooms and technical room). It was a modest start, but rather feasible for the local municipality that met all contemporary standards for this type of program. The largest structure was some 1000 m² as the result of preliminary design research, which indicated that for larger sites a different design approach should be explored to overcome certain functional shortcomings.

As far as materialization of thermal envelope was concerned, practically all variations remained within the boundaries of EPC class C, but enhanced envelope proposals were very close to EPC class B (for the smallest, initial case it was just below the threshold). Having in mind the abundance of geothermal energy at both sites, the pursuit of enhanced

energy efficiency might be questionable unless the NZEB (nearly zero-energy buildings) standard is targeted. However, Serbia has not yet established any formal NZEB definition.

The abundance of geothermal resources broadens the scope of the wellness and balneotherapies that can be offered within the facility. In this context, further feasibility studies should be conducted to explore more development options for health tourism in the province of Vojvodina.

On the other hand, the focus of further research regarding the architecture of wellness and spa/medical facilities in the Vojvodina region should be on enhanced comfort (while optimizing the construction and operation costs), building technologies that are based on local production, and flexibility of development and operation. The proposed model also includes a set of structured open spaces that were not developed in detail in this study. Some future research should address options for the multifunctional use of such spaces and the potential for their enclosure to provide extended use throughout the year.

Depending on the business model, we can consider this starting model to be not economically demanding and able to serve as a demonstration model to attracting further investment and multiplication in other locations.

References

1. Morrone, P.; Algieri, A. Integrated Geothermal Energy Systems for Small-Scale Combined Heat and Power Production: Energy and Economic Investigation. *Appl. Sci.* **2020**, *10*, 6639. [CrossRef]
2. Ilzarbe, J.M.B.; Malpartida, J.G.; Chandro, E.R. Recent Patents on Geothermal Power Extraction Devices. *Recent Patents Eng.* **2013**, *7*, 2–24. [CrossRef]
3. IRENA (International Renewable Energy Agency). Available online: https://www.irena.org/geothermal (accessed on 28 May 2020).
4. Stegnar, G.; Staničić, D.; Česen, M.; Čižman, J.; Pestotnik, S.; Prestor, J.; Urbančič, A.; Merše, S. A framework for assessing the technical and economic potential of shallow geothermal energy in individual and district heating systems: A case study of Slovenia. *Energy* **2019**, *180*, 405–420. [CrossRef]
5. Kljajić, M.V.; Anđelković, A.S.; Hasik, V.; Munćan, V.M.; Bilec, M. Shallow geothermal energy integration in district heating system: An example from Serbia. *Renew. Energy* **2020**, *147*, 2791–2800. [CrossRef]

6.   Soltani, M.; Kashkooli, F.M.; Dehghani-Sanij, A.; Kazemi, A.; Bordbar, N.; Farshchi, M.; Elmi, M.; Gharali, K.; Dusseault, M.B. A comprehensive study of geothermal heating and cooling systems. *Sustain. Cities Soc.* **2019**, *44*, 793–818. [CrossRef]

7.   Soltani, M.; Kashkooli, F.M.; Dehghani-Sanij, A.; Nokhosteen, A.; Ahmadi-Joughi, A.; Gharali, K.; Mahbaz, S.; Dusseault, M. A comprehensive review of geothermal energy evolution and development. *Int. J. Green Energy* **2019**, *16*, 971–1009. [CrossRef]

8.   Mahbaz, S.; Dehghani-Sanij, A.; Dusseault, M.; Nathwani, J. Enhanced and integrated geothermal systems for sustainable development of Canada's northern communities. *Sustain. Energy Technol. Assess.* **2020**, *37*, 100565. [CrossRef]

9.   Kinney, C.; Dehghani-Sanij, A.; Mahbaz, S.; Dusseault, M.B.; Nathwani, J.S.; Fraser, R.A.; Sanij, D. Geothermal Energy for Sustainable Food Production in Canada's Remote Northern Communities. *Energies* **2019**, *12*, 4058. [CrossRef]

10.   Schmerler, K. *Medical Tourism in Germany: Determinants of International Patients' Destination Choice*; Springer: Cham, Switzerland, 2018.

11.   Proticć, D. *Mineral and Thermal Waters of Serbia*; Geoinstitut—Special editions; Geoinstitut: Belgrade, Serbia, 1995; Volume 17, p. 35. (In Serbian)

12.   Dokmanović, P.B.; Krunić, O.Ž.; Martinović, M.K.; Magazinović, S.M. Hydrogeothermal Resources in Spa Areas of Serbia: Main Properties and Possible Improvement of Use. *Therm. Sci.* **2012**, *16*, 21–30. [CrossRef]

13.   Republic Agency for Spatial Planning of the Republic of Serbia. *Spatial Plan of the Republic of Serbia 2010–2020*; Official Gazette of the Republic of Serbia no. 88/10; Republic Agency for Spatial Planning of the Republic of Serbia: Belgrade, Serbia, 2010. (In Serbian)

14.   Institute for Urbanism of Vojvodina. *Regional Spatial Plan of the Autonomous Province of Vojvodina*; Official Gazette of APV no. 22/11; Institute for Urbanism of Vojvodina: Novi Sad, Serbia, 2011. (In Serbian)

15.   Zwaan, V.D.B.; Longa, D.L. Integrated assessment projections for global geothermal energy use. *Geothermics* **2019**, *82*, 203–211. [CrossRef]

16.   DiPippo, R.; Renner, J.L. Geothermal Energy. In *Future Energy, Improved, Sustainable and Clean Options for Our Planet*, 2nd ed.; Elsevier: Amsterdam, The Netherlands, 2014; pp. 471–492.

17.   Kaczmarczyk, M.; Tomaszewska, B.; Operacz, A. Sustainable Utilization of Low Enthalpy Geothermal Resources to Electricity Generation through a Cascade System. *Energies* **2020**, *13*, 2495. [CrossRef]

18.   Marović, M.; Djoković, I.; Peić, L.; Radovanović, S.; Toljić, M.; Gerzina, N. Neotectonics and Seismicity of the Southern Margin of the Pannonian Basin in Serbia. In *Neotectonics and Surface Processes: The Pannonian Basin and Alpine/Carpathian System*; EGU Stephan Mueller Special Publication Series; Cloetingh, S.A.P.L., Horvath, F., Bada, G., Lankreijer, A.C., Eds.; European Geosciences Union: Munich, Germany, 2002; Volume 3, pp. 277–295.

19.   Rman, N.; Lenuța, B.L.; Bobovečki, I.; Gál, N.; Jolović, B.; Lapanje, A.; Marković, T.; Milenić, D.; Skopljak, F.; Rotár, S.A.; et al. Geothermal sources and utilization practice in six countries along the southern part of the Pannonian basin. *Environ. Earth Sci.* **2020**, *79*, 1–12. [CrossRef]

20.   Nádor, A. (Ed.) *Cascades and Calories: Geothermal Energy in the Pannonian Basin for the 21st Century and Beyond*; Faculty of Mining and Geology, Belgrade University: Belgrade, Serbia, 2019; 130p.

21.   Nádor, A.; Sebess, Z.L.; Rotár, S.Á.; Gulyás, Á.; Markovic, T. New methods of geothermal potential assessment in the Pannonian basin. *Neth. J. Geosci.* **2020**, *98*, e10. [CrossRef]

22.   Lenkey, L.; Dövényi, P.; Horváth, F.; Cloetingh, S.A.P.L. Geothermics of the Pannonian basin and its bearing on the neotectonics. *EGU Stephan Mueller Spec. Publ. Ser.* **2002**, *3*, 1–12. [CrossRef]

23.   Horváth, F.; Musitz, B.; Balázs, A.; Végh, A.; Uhrin, A.; Nádor, A.; Koroknai, B.; Pap, N.; Tóth, T.; Wórum, G. Evolution of the Pannonian basin and its geothermal resources. *Geothermics* **2015**, *53*, 328–352. [CrossRef]

24.   Kostić, A. *Thermal Evolution of Organic Matter and Petroleum Generation Modelling in the Pannonian Basin (Serbia)*; Faculty of Mining and Geology, Belgrade University: Belgrade, Serbia, 2010; ISBN 978-86-7352-221-0.

25.   Milenić, D.; Vranješ, A. Evaluation of Geothermal Potential of the AP Vojvodina. In Proceedings of the XV Serbian Symposium of Hydrogeologist with International Participation, Kopaonik, Serbia, 14–17 September 2016; pp. 283–289.

26.   Milenić, D.; Vranješ, A.; Krunić, O. *Balneology Potential of the Territory of AP Vojvodina—Resources Research, Multiparameter Valorisation and Development Projections, Scientific Study*; Faculty of Mining and Geology, Belgrade University: Belgrade, Serbia, 2017; unpublished.

27.   Milenić, D.; Vranješ, A.; Krunić, O. Preliminary Assessment of the Balneological Potential of the Territory of AP Vojvodina. In Proceedings of the 17th Serbian Geological Congress (National Congress with International Participation), Vrnjačka Banja, Serbia, 17–20 May 2018; Volume 2, pp. 439–444.

28.   Royden, L.H.; Horvaáth, F. (Eds.) The Carpathian-Pannonian Region with Names and Locations in the Basins. In *The Pannonian Basin, A Study in Basin Evolution*; American Association of Petroleum Geologists Memoiry 45; AAPG: Tulsa, OK, USA, 1988.

29.   The Serbian Ministry of Natural Resources and Environmental Protection. *Geological Atlas of Serbia 1:2.000.000 No. 1 Geological Map*, 2nd ed.; The Serbian Ministry of Natural Resources and Environmental Protection: Belgrade, Serbia, 2002.

30.   United Nations. *Transforming Our World: The 2030 Agenda for Sustainable Development*; Resolution adopted by the General Assembly on 25 September 2015. A/RES/70/1; United Nations: New York, NY, USA, 2015.

31.   Climate Data. Available online: https://en.climate-data.org/europe/serbia/vojvodina-483/r/july-7/ (accessed on 11 February 2021).

32.   Szokolay, S. *Introduction to Architectural Science: The Basis of Sustainable Design*; Architectural Press: Oxford, UK, 2004.

33.   *Rulebook on Energy Efficiency of Buildings*; Official Gazette of RS, No. 61/2011; Official Gazette of RS: Belgrade, Serbia, 2011. (In Serbian)

34. Passive House Institute. *Criteria for the Passive House, EnerPHit and PHI Low Energy Building Standard*; Passive House Institute: Darmstadt, Germany, 2016.

35. *Rulebook on Conditions of Content and Manner of Issuing Certificates on Energy Properties of Buildings*; Official Gazette of RS, no. 69/2012 and 44/2018; Official Gazette of RS: Belgrade, Serbia, 2018. (In Serbian)

36. Knaufinsulation Serbia. Available online: https://www.knaufinsulation.rs/knaufterm-2-pro-srbija (accessed on 5 June 2020).

37. Statistical Office of the Republic of Serbia. *2011 Census of Population, Households and Dwellings in the Republic of Serbia*; Bulletin #540; Statistical Office of the Republic of Serbia: Belgrade, Serbia, 2011.

38. Marović, M.; Toljić, M.; Rundić, L.; Milivojević, J. *Neoalpine Tectonics of Serbia*; Serbian Geological Society: Belgrade, Serbia, 2007; ISBN 86-86053-03-3.

39. Toljić, M.; Matenco, L.; Ducea, M.N.; Stojadinović, U.; Milivojević, J.; Đerić, N. The evolution of a key segment in the Europe–Adria collision: The Fruška Gora of northern Serbia. *Glob. Planet. Chang.* **2013**, *103*, 39–62. [CrossRef]

40. Lesić, V.; Maárton, E.; Cvetkov, V. Paleomagnetic detection of Tertiary rotations in the Southern Pannonian Basin (Fruška Gora). *Geol. Carp.* **2007**, *58*, 185–193.

41. Allen, A.; Milenic, D. Low enthalpy geothermal heat resources from ground water in fluvioglacial gravels of buried valleys. *J. Appl. Energy* **2003**, *74*, 9–19. [CrossRef]

42. D'Amore, F.; Scandiffio, G.; Panichi, C. Some observations on the chemical classification of ground waters. *Geothermics* **1983**, *12*, 141–148. [CrossRef]

43. Milenić, D.; Vasiljević, P.; Vranješ, A. Criteria for use of groundwater as renewable energy source in geothermal heat pump systems for building heating/cooling purposes. *Energy Build.* **2010**, *42*, 649–657. [CrossRef]

44. Konstantinou, T.; Prieto, A. Environmental Design Principles for the Building Envelope and More Passive and Active Measures. In *Energy Resources and Building Performance*; Konstantinou, T., Ćuković Ignjatović, N., Zbasnik-Senegacnik, M., Eds.; TU Delft Open: Delft, The Netherlands, 2018; pp. 147–180.

Article

Reuse of Decommissioned Hydrocarbon Wells in Italian Oilfields by Means of a Closed-Loop Geothermal System

Martina Gizzi, Glenda Taddia * and Stefano Lo Russo

Department of Environment, Land and Infrastructure Engineering, Politecnico di Torino, C.so Duca degli Abruzzi 24, 10129 Torino, Italy; martina.gizzi@polito.it (M.G.); stefano.lorusso@polito.it (S.L.R.)
* Correspondence: glenda.taddia@polito.it

Abstract: Geological and geophysical exploration campaigns have ascertained the coexistence of low to medium-temperature geothermal energy resources in the deepest regions of Italian sedimentary basins. As such, energy production based on the exploitation of available geothermal resources associated with disused deep oil and gas wells in Italian oilfields could represent a considerable source of renewable energy. This study used information available on Italian hydrocarbon wells and on-field temperatures to apply a simplified closed-loop coaxial Wellbore Heat Exchanger (WBHE) model to three different hydrocarbon wells located in different Italian oilfields (Villafortuna-Trecate, Val d'Agri field, Gela fields). From this study, the authors have highlighted the differences in the quantity of potentially extracted thermal energy from different analysed wells. Considering the maximum extracted working fluid temperature of 100 °C and imagining a cascading exploitation mode of the heat accumulated, for Villafortuna 1 WBHE was it possible to hypothesise a multi-variant and comprehensive use of the resource. This could be done using existing infrastructure, available technologies, and current knowledge.

Keywords: renewable energy; geothermal energy; mature oilfield; abandoned hydrocarbon well; wellbore heat exchanger

1. Introduction

The policy visions of the 2030 UN Agenda for Sustainable Development and the Paris Agreement on Climate Change were both approved by the member states of the UN in 2015 and represent two fundamental contributions that guide the transition towards an economic model that aims not only for profitability but also for social progress and environmental protection. To achieve increased energy efficiency, all nations must change the ways in which they produce and manage natural energy resources in order to create more sustainable and environmentally resilient communities.

The current Italian urban energy paradigm relies heavily on fossil fuels; given the air pollution and resource depletion caused by fossil-fuel use, this is unsustainable. Public and private investments in energy must be increased, especially for innovative technological models that transform the energy system, integrating renewable energy into end-use applications in buildings, transportation and industry.

Geoscience offers solutions to this issue through the development of various options that could encourage decarbonisation and the transition to renewable energy sources at local and regional scales: electricity production from renewable sources, domestic heating/cooling using low-enthalpy geothermal energy resources and larger-scale technologies that target harmful emissions, such as bioenergy production and carbon capture and storage [1].

Geothermal energy is a weather-independent, environmentally friendly and currently available renewable resource; it represents an effective solution for power generation, heating and cooling, and direct-use applications. Specifically, energy production from available low- to medium-temperature geothermal resources associated with disused deep

31

oil and gas wells in Italian oilfields has considerable potential. As a renewable energy source, it could solve problems associated with suspended wells near municipalities and allow for longer-term use of hydrocarbon wells, even at the end of their production cycle, which would benefit industry, civil and agriculture districts. According to [2], the variety of possible direct applications of geothermal resources in production districts, together with the corresponding temperature demand, is wide. It includes space heating, industrial uses, swimming pools, horticulture (especially greenhouses) and aquaculture.

Studies have shown that hydrocarbon reservoirs and geothermal energy resources can coexist in sedimentary basin contexts because both have similar reservoir conditions [3–5]. Hydrocarbon resources are generated under specific temperature and pressure conditions in the source rocks, and groundwater is always involved in both the primary migration of oil from the source rock and the secondary migration of oil and gas to the reservoir. Consequently, oil and gas reservoirs in hydrocarbon basins act as geothermal reservoirs.

Sedimentary basins have been explored for both oil and gas extraction purposes, so deep hydrocarbon wells are located in this geological context. Well logs, temperature distribution profiles and reservoir properties, such as depth to basement and geological formation thickness, are generally well known.

Since 1985, 7246 wells have been drilled for hydrocarbon extraction in Italy, 898 of which are located onshore with varying operational statuses [6]. A variety of oil and gas reservoirs have been identified; geological and geophysical exploration campaigns into the deepest regions of such geological contexts have ascertained the coexistence of hydrocarbons and the low- to medium-temperature geothermal energy resources [7,8].

Recent investigations have attempted to assess geothermal potentials, exploring deep geothermal resources in different regions and reconstructing heat flow maps at different depths [9,10].

Additionally, in order to determine heat conductivity values at the regional and local scales, the thermal conductivity of 200 rock samples collected from four different regions of southern Italy (Calabria, Campania, Apulia and Sicily) was investigated by [11], measuring its value in both dry and wet conditions. Morover, in reference [12] it was utilised the framework of the MIUR−2008 project "Geothermal resources of the Mesozoic basement of the Po Basin: groundwater flow and heat transport" to accurately estimate the thermophysical properties of a wide variety of sedimentary and intrasedimentary volcanic rocks from the Po Basin through laboratory measurements of density and porosity.

Since it is stored in subsurface geological formations and associated with hydrocarbons, geothermal energy must be extracted before it can be used. Decommissioned or disused oil and gas wells, especially those in mature oilfields, are good candidates for geothermal heat exploitation and may provide access to subsurface energy resources.

Considering the large number of existing oil wells dismissed every year in Italian fields, various studies have proposed new engineering tools to evaluate the possible use of such thermal resources. In reference [13], it was developed an effective method for doing so through the use of a closed-loop system with associated Wellbore Heat Exchanger (WBHE) technology. Unlike in conventional open-loop geothermal systems, heat carrier fluids in closed-loop systems circulate inside WBHEs, with no ground fluids extracted from surrounding rocks.

Despite the recent success of theoretical oilfield geothermal closed-loop system experiments, certain challenges remain for understanding the possibility of large-scale access to geothermal resources in oilfields using closed-loop technologies. Additionally, due to the continuous spatial variability of geological formations associated with deep oil and gas wells in oilfields, the thermophysical parameters of geological strata surrounding the well, as well as the depth and thickness of the strata, must be considered to achieve accurate and realistic estimates of heat exchanger performance.

Given the above considerations, this study aims to contribute to the discussion, encouraging a reflection on the potential benefits and limitations of using low- to medium-

temperature geothermal energy resources associated with dismissed Italian hydrocarbon wells as a renewable source of energy.

Using the information on Italian hydrocarbon wells and on-field temperatures available from both the National Mining Office of the Italian Ministry for Economic Development (MISE) and the Italian National Geothermal Database, the simplified heat exchange model (coaxial WBHE) described in [13] was applied to three hydrocarbon wells. The main purpose was to properly analyse heat exchange mechanisms in three different Italian oil and gas fields, emphasising that the quantity of the potentially extracted thermal energy can change based on geological and depositional context. Wells from the Villafortuna–Trecate field, the Val d'Agri field and the Gela field were selected.

The assumption that the thermophysical parameters (thermal conductivity, volumetric heat capacity and rock density) are constant values, as described in [13], has been overcome by applying the elaborated model to the detailed stratigraphic data of each case study.

The final use of the potentially extracted heat would be in possible direct applications by means of a cascade plant system, which provides specific thermal energy amounts to production cycles in manufacturing, agricultural and recreational districts near the oilfields. Considering specifically the examples of disused hydrocarbon wells analysed, located in the Italian territory, it is possible to state that they are located far from inhabited areas or buildings: it is therefore not generally possible to hypothesize the use of the extracted thermal energy for heating purposes.

2. Materials and Methods

2.1. Oilfields in Italian Sedimentary Basins

To introduce the analysis of the selected case studies, this paper provides an overview of the main sedimentary systems and associated hydrocarbon fields.

The Italian landscape is dominated by the Southern Alps and the Apennines mountain chains. The two chains are bordered in their outer margins by well-developed sedimentary foreland basins, especially along the Adriatic sectors, and by relatively wide foreland areas (e.g., the Po Plain, Adriatic Sea and Hyblean Basin). Due to Italy's complex geological and sedimentary history, a variety of petroleum systems have been identified. Authors provided overviews of the Italian peninsula's geological evolution and described how Italian hydrocarbon occurrences can be classified by their association with three main tectono-stratigraphic systems (Figure 1) [14–16]: (1) carbonate Mesozoic substratum of the foredeep/foreland area and of the external thrust belts; (2) thrusted terrigenous Oligo-Miocene foredeep wedges (Southern Alps, Northern Apennines, Calabria and Sicily); and (3) terrigenous Pliocene-Pleistocene successions of the late foredeep basins of the Apennines, in both the central and northern Adriatic Sea and the Po Plain.

According to [17], at least five important source rocks have been recognised, with ages ranging from the Mesozoic through the Pleistocene. Three of the source rocks were deposited during Mesozoic crustal extension and are mainly oil-prone. Hydrocarbon occurrences associated with these sources are usually found in complex carbonate structures along the Apennines thrust-and-fold belt and in the foreland; the Villafortuna–Trecate (Po Plain), Val d'Agri-Tempa Rossa (southern Apennines) and Gela (Sicily) fields represent the largest oil accumulations pertaining to these systems.

The two other source rocks were deposited in the foredeep terrigenous units of the foreland basins, which formed during the Cenozoic orogenesis. The older of the two sources is thermogenic gas-prone and is found in the highly tectonised Oligo-Miocene foredeep wedges; gas occurrences associated with this source are mainly concentrated along the northern Apennines margin (e.g., the Cortemaggiore field), in Calabria (e.g., the Luna field) and in Sicily (e.g., the Gagliano field). The younger source is biogenic gas-prone and is situated in the outer Plio-Pleistocene foredeeps.

Reference [17] clearly showed the geographic limitation of the oil-prone Villafortuna–Trecate Middle Triassic and Val d'Agri-Tempa Rossa Cretaceous systems, as opposed to the

wide distribution of the Late Triassic–Early Jurassic system and of the biogenic gas-prone Plio-Pleistocene systems (Figure 1).
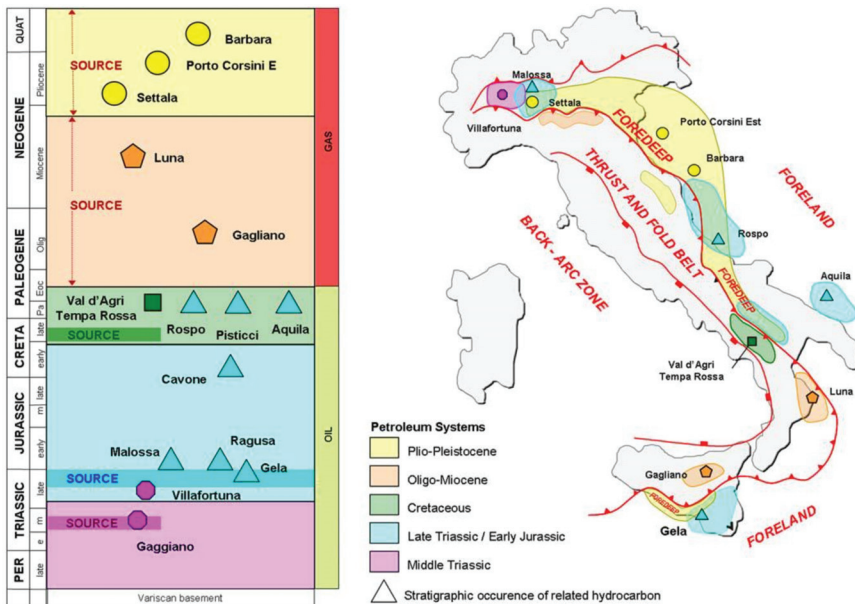
Figure 1. Stratigraphic and geographic location of the Italian petroleum systems [17].

This study focuses on the analysis of geothermal energy potential associated with disued hydrocarbon wells of the different petroleum systems of the Mesozoic carbonate succession. Three deep hydrocarbon wells located inside of the Villafortuna–Trecate oilfield, the Tempa Rossa Field and the Gela Field are discussed in detail.

Detailed information related to the litho-stratigraphic units and temperature data visualisation can be found on The Italian National Geothermal Database (BDNG), the largest collection of Italian geothermal data. BDNG was established in the 1980s and implemented by the Institute of Geosciences and Earth Resources (IGG) of the National Research Council (CNR) of Italy [9].

Information regarding productive and dismissed oil and gas wells in Italy was also provided by the National Mining Office of the Italian Ministry for Economic Development (MISE) and by the website of the VIGOR, promoted by the MISE-DGRME (Direzione Generale Risorse Minerarie ed Energetiche), the Italian Geological Society and the Assomineraria Association.

2.1.1. The Villafortuna–Trecate Field

First, data were analysed for the geothermal potential associated with the disused Villafortuna 1 hydrocarbon well, located within the Villafortuna–Trecate oilfield (Figure 1). The Villafortuna–Trecate system represents one of the largest oil accumulations of the Italian Middle Triassic carbonate petroleum system. The petroleum system is wholly developed inside the Triassic succession and consists of two main reservoirs, composed of dolomitised carbonate platform rocks and a set of source rocks deposited in the adjacent anoxic intra-platform basins.

Generally, the depth of the main reservoir associated with the Villafortuna–Trecate field is between 5800 m and 6100 m deep, with temperatures of approximately 160–170 °C [18]. Because of its depth, the main reservoir can be pursued only in the

outer sector of the foredeeps and in foreland regions (the Piedmont area); areas along the thrust belt (the Po Plain) are generally too deep.

As demonstrated by information related to the litho-stratigraphic units and temperature data visualisation reported in Table 1 and Figure 2, the stratigraphic succession is mainly composed of clastic sedimentary and carbonate rocks. The analysed well has a maximum depth of 6202 m and temperatures reaching 165 °C.

Table 1. Villafortuna 1 hydrocarbon well-lithostratigraphic profile (Villafortuna Trecate Oilfield, Western Po Plain).

Depth m	Litho-Stratigraphic Formation	Age	λ_s W/mK	ρc_s kJ/m^{3}K	ρ kg/m^3
609	Terrigenous sedimentary deposits Fine Sand (dry)	Holocene/Upper Pleistocene	0.30	800	1700
1258	Sand (dry)	Pleistocene	0.30	800	1700
1405	Clay Sand	Low Pliocene	1.61	1696	1890
5493	Clastic sedimentary rocks (Sandstone, Conglomerates and Silty Marl)	Aquitanian - Albian	3.16	1937	2359
6202	Carbonate rocks— Calcarenite/Dolostone	Low Cretaceous - Middle Triassic	3.50	2010	2480
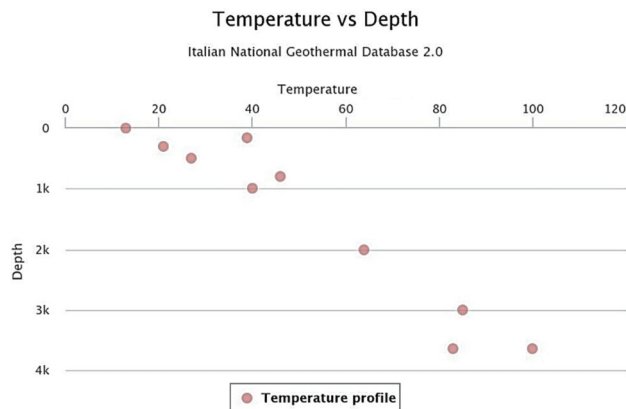
Figure 2. Temperature data visualisation for the Villafortuna 1 hydrocarbon well: Depth (m); Temperature (°C).

2.1.2. The Val d'Agri-Tempa Rossa Field

The second case study, the Tempa Rossa 1D hydrocarbon well, is located within the Tempa Rossa oilfield (Figure 1). The Tempa Rossa system lies in the Mesozoic carbonate substratum of the foredeep and foreland areas and in the external thrust belt of the southern Apennines. The system bears the largest oil and gas accumulations in Italy, including the Val d'Agri and Tempa Rossa oil fields.

The reservoirs are composed of fractured limestones from the buried Apulia Platform, which extends from the Cretaceous to the Miocene. The majority of the oil column exceeds 1000 m and sometimes exceeds 2000 m. The seal is composed of Lower Pliocene shales. The source rocks, identified in a few deep wells of the area, are mainly Albian–Cenomanian and are marine anoxic carbonates facies containing sulphur [19].

Unlike the Villafortuna 1 hydrocarbon well, the Tempa Rossa 1D well features litho-stratigraphic units mainly composed of sandstone and associated shales (Table 2). The maximum depth of the analysed well is 5042 m; temperatures reach 107 °C (Figure 3).

Table 2. Tempa Rossa 1D hydrocarbon well-lithostratigraphic profile (Tempa Rossa Field, Western Po Plain).

Depth m	Litho-Stratigraphic Formation	λ_s W/mK	ρc_s kJ/m^{3}K	ρ kg/m^3
23	Superficial sedimentary deposits Fine Sand (dry)	0.30	800	1700
2912	Sandstones interspersed with shale and clays	3.00	1884	2330
5042	Clays, argillites and calcarenites	2.34	1590	1917
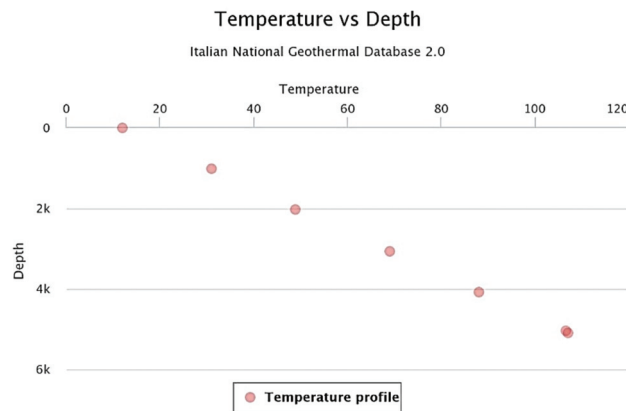
Figure 3. Temperature data visualisation for the Tempa Rossa 1D hydrocarbon well: Depth (m); Temperature (°C).

2.1.3. The Gela Field

The third case study is the Gela 38 hydrocarbon well, located in the Gela oilfield in Sicily. The Gela field is part of the Late Triassic–Early Jurassic petroleum system and is linked to the main phase of the Tethyan rifting. It is the most explored of the three systems, both in the foreland and in the thrust belt, and from Lombardy to Sicily. The source rocks are terrigenous or mixed carbonate-terrigenous and were deposited during the anoxic stage that preceded the extension of the Jurassic basins.

The Ragusa-Gela fields were discovered in the 1950s and have been the largest source of Italian oil for some of the past decades. The reservoir is composed of fractured, massive dolomites of the Upper Triassic Gela Formation. The traps are large-scale, probably polyphase anticlines bounded by high-angle normal faults.

Based on the available lithological and temperature data reported in Table 3 and Figure 4, the area's stratigraphic succession is composed of marl, calcareous marl and clays. The well has a maximum depth of 3446 m and temperatures that reach 85 °C.

Table 3. Gela 38 hydrocarbon well-lithostratigraphic profile (Gela Field, Sicily).

Depth m	Litho-Stratigraphic Formation	λ_s W/mK	ρc_s kJ/m^{3}K	ρ kg/m^3
1772 2117	Marls, clays and gypsum Marl, calcareous marl and clays	3.16	1937	2359
2556 2582	Limestone and marl Limestone	2.17	1495	1801
2860	Limestone, dolomitic limestone and marl	3.12	2010	2480
3156 3446	Limestone, marl and dolomite Marls, clays and gypsum	2.17	1495	1801
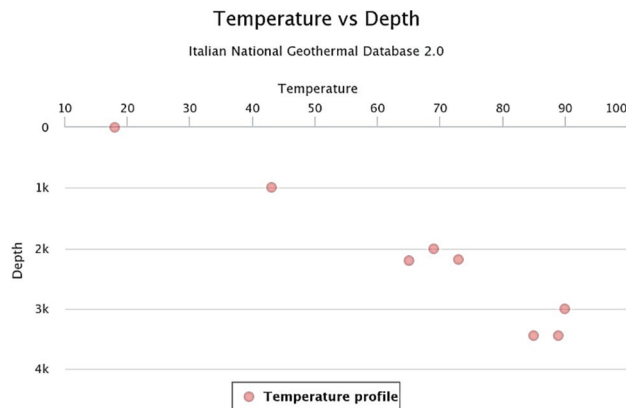
Figure 4. Temperature data visualisation for the Gela 38 hydrocarbon well: Depth (m); Temperature (°C).

2.2. Closed-Loop Geothermal Energy Systems: WBHEs

Exploiting the geothermal energy resources associated with decommissioned hydrocarbon wells requires that the borehole to be retrofitted with a heat exchanger. In current practice, two main types of closed-loop systems are used to harness geothermal energy resources by taking advantage of disused boreholes in oilfields: U-tube and coaxial double-pipe WBHE technologies [20,21]. Both kinds of systems allow for the extraction of heat from the ground without extracting or re-injecting any geothermal fluids.

In U-tube heat exchangers, fluid is pumped through one tube string and comes out the other, while coaxial heat exchangers are composed of two concentric pipes, as shown in Figure 5 and Table 4. In coaxial WBHEs circulating working fluid is injected into the outer pipe (the injection pipe), flows down to the lower part of the exchanger and is gradually warmed by heat from the rocks. After the fluid reaches the bottom hole of the well, it flows upwards through a thinner pipe, which acts as the inner pipe (the extraction pipe). The gap between internal pipes is filled with an insulating material, and the bottom hole is sealed. Heat exchange occurs between the geological formation and the fluid in the injection pipe and between the fluid in the injection pipe and the fluid in the extraction pipe.
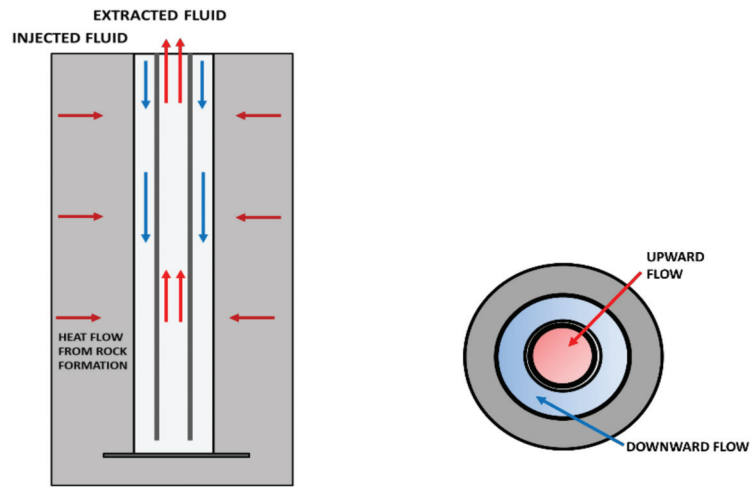
Figure 5. Schematic representation of a coaxial Wellbore Heat Exchanger (WBHE).

Table 4. Coaxial WBHE—geometric parameters.

Coaxial Wellbore Heat Exchanger—Geometric Parameters	Symbol	Unit of Measure
Outer pipe area	A_0	[m^2]
Inner pipe area	A_i	[m^2]
Radius of outside wellbore	r_w	[mm]
External radius of the external casing	r_c	[mm]
Internal radius of the external casing	r_i	[mm]
Radius of the internal casing	r_0	[mm]
Thicknesses of the pipe exchanger	d	[mm]
Depth	z	[m]

Corrosion must be considered when selecting this type of system; it may be ideal for heat exchange, but it may also reduce the system's operational life. Due to its low cost and its heat transfer and storage capacity, water is still one of the most commonly used fluids. The operating parameters of subsurface closed-loop systems, such as fluid flow rate and pipe diameter, should be selected to guarantee transient turbulent flow conditions, since these conditions facilitate heat transfer, and low hydraulic head losses, since this indicates lower energy expenditure on circulation pumping.

Compared to U-tube heat exchangers, coaxial heat exchangers have a higher surface area and a higher volume of the working fluid through which heat exchange occurs. As a result, under the same injection rate conditions (q), the fluid flow velocity in the coaxial pipe system and the hydraulic pressure required for fluid circulation can be lower, resulting in decreased energy consumption from pumping [21]. The coaxial geometry of a double-pipe heat exchanger also has the advantage of reducing thermal resistance between the circulating fluid and the wellbore.

In this paper, in order to evaluate and analyse the temperature profiles of the selected fluid (water) associated with a coaxial double-pipe WBHE technology, the simplified models proposed below were implemented in MATLAB and applied to the selected case studies: the Villafortuna 1, Tempa Rossa 1D and Gela 38 hydrocarbon wells.

For the elaborated model, two main assumptions were considered: the propagation of heat in the reservoir occurs by means of conduction (convection phenomena are neglected),

and the propagation of heat inside the wellbore tubes takes place through both conduction and convection.

2.3. Heat Transfer in Coaxial WBHEs

In coaxial WBHEs, the steel downward tube is cemented to the rock wall and so is in contact with the hole in the well. The energy balance of the fluid in the injection pipe can be expressed with the following equation:

$$\frac{\partial \left((\rho c)_f A_0 T_{fo} \right)}{\partial \tau} + \frac{\partial \left((\rho c)_f A_0 v_f T_{fo} \right)}{\partial z} = -\frac{dQ}{dz} + \frac{dQ_{i0}}{dz} \tag{1}$$

where A_0 and v_f are the outer pipe area and fluid velocity, respectively; T_{fo} is the fluid temperature in the outer pipe; and dQ/dz is the heat extraction from the formation at unit well depth (W/m).

Although insulation is used to prevent heat loss from the inner-pipe fluid, heat is partly transferred between the two pipes, so dQ_{i0}/dz represents the heat flux from the inner pipe to the outer pipe. Therefore, the energy equation for the inner pipe can be given as:

$$\frac{\partial \left((\rho c)_f A_i T_{fi} \right)}{\partial \tau} + \frac{\partial \left((\rho c)_f A_i v_f T_{fi} \right)}{\partial z} = -\frac{dQ_{i0}}{dz} \tag{2}$$

By assuming steady heat transfer and constant heat flux in wellbore components (e.g., insulation, casing and cement), heat extraction from the formation dQ/dz can be assumed to be equal to the heat flux through the outside surface of the wellbore (interface of the wellbore and rock formation) to the injected fluid [22]:

$$\frac{dQ}{dz} = 2\pi r_w k_w \left(T_{f0} - T_w \right) = \left(T_{f0} - T_w \right)/R_w \tag{3}$$

where T_w is the temperature at the interface of the wellbore and the formation, k_w is the heat transfer coefficient between the outer-pipe fluid and wellbore exterior and R_w is the resistance between the outer pipe and surrounding rocks.

At the well bottom, the heated fluid is forced to enter and flow through the internal pipe of the coaxial WBHE. Going up to the wellhead, heat transfer occurs only through the wall of the internal pipe. Thus, dQ_{i0}/dz is determined by considering the temperature difference between the outer-pipe and inner-pipe fluids, as well as the estimated thermal resistance of the insulation:

$$\frac{dQ_{i0}}{dz} = 2\pi r_0 k_{i0} \left(T_{fi} - T_{f0} \right) = \left(T_{fi} - T_{f0} \right)/R_{i0} \tag{4}$$

where T_{fi} is the fluid temperature in the inner pipe, k_{i0} is the heat transfer coefficient between the outer pipe and inner pipe and R_{i0} is the thermal resistance between the outer pipe and inner pipe.

2.3.1. Coaxial WBHE: Coefficient of Heat Exchange between Outer-Pipe Fluid and the Wellbore Exterior

In an analysis of the energy balance equation for the fluid in the outer pipe (injection pipe) of a coaxial WBHE, a careful estimate of the parameter k_w is fundamental for proper evaluation of the heat exchange between the outer-pipe fluid and the drilled geological formations.

For a coaxial WBHE, the heat exchange coefficient for the injection pipe can be expressed as the sum of heat transfer components, expressed in terms of thermal resistance values (R_w) [22]:

$$R_w = R_s + R_a + R_c \tag{5}$$

where R_s is a function of time that represents the thermal resistance due to conductive heat transfer in the rock, R_a is the thermal resistance due to convective heat transfer into the pipe and R_c is the thermal resistance due to conductive heat transfer through the casings of the well.

In the evaluation of total thermal resistance, the conductive term prevails; consequently, the thermal exchange is directly proportional to the convective transfer coefficient.

Conductive thermal resistance (R_s) can be expressed as follows:

$$R_s = \frac{1}{2\lambda_s} In \frac{2\sqrt{\alpha_s t}}{r_w} \tag{6}$$

where λ_s (W/mK) is the thermal conductivity of the rock and α_s (m/s) is the thermal diffusivity of the rock. In Equation (6), the relationship in the numerator of the second term represents the time-dependent radius of the thermal influence of the well (r_s).

Convective thermal resistance (R_a) can be determined by the following equation:

$$R_a = \frac{1}{2r_c h_f} \tag{7}$$

where r_c is the external radius of the external casing and h_f is the convective heat transfer coefficient, which was calculated by using the Nusselt number (Nu) and a form of the Dittus-Boelter equation that assumes turbulent flow inside the tubes (Reynolds number $\geq$ 104) [23]:

$$h_f = \frac{Nu\lambda_f}{2r_c} \tag{8}$$

$$Nu = 0.023 Re^{0.8} Pr^{0.4} \tag{9}$$

with $Pr = \frac{\rho c_f \mu}{\lambda_f}$ and $Re = \frac{\rho v_f 2r_c}{\mu}$.

Finally, the thermal resistance to heat conduction through the casings of the well can be determined as follows:

$$R_c = \sum_{i=1}^{n} R_{\lambda i} = \frac{1}{2} \sum_{i=1}^{n} \frac{1}{\lambda_i} In \frac{r_{c,i+1}}{r_{c,i}} \tag{10}$$

where λ_i is the thermal conductivity of the rock in correspondence with the different casings of the well. Generally, due to the high thermal conductivity of the steel piping, the total thermal resistance of the casing is negligible compared to the rock thermal resistance [13].

As a result, the heat exchange coefficient k_w can be correctly determined as follows:

$$\frac{1}{k_w} = \frac{2r_c}{2\lambda_s} In \frac{4\sqrt{\alpha_s t}}{2r_w} + \frac{1}{h_f} \tag{11}$$

where $rc = rw$ as the thickness of the external tube is negligible.

2.3.2. Coaxial WBHE: Coefficient of the Heat Exchange between the Outer-Pipe Fluid and the Inner Pipe

Unlike in the injection pipe, the total heat flux in the upward pipe (extraction pipe) is determined by a conductive component of the composite pipe and by two convective components, one on the internal wall and one on the external wall of the WBHE.

Consequently, the total heat exchange coefficient k_{i0} for the extraction pipe can be calculated as follows:

$$\frac{1}{k_{i0}} = \frac{r_0}{r_{0+d}} \frac{1}{h_i} + r_0 \sum_{i=1}^{n} \frac{1}{\lambda_i} In \left(\frac{r_{i+1}}{r_i} \right) + \frac{1}{h_0} \tag{12}$$

where r_0 is the radius of the inner pipe, d is the thicknesses of the pipe exchanger, h_0 and h_i are the coefficients of convective heat transfer to the inner and outer wall, respectively, and λ_i is the thermal conductivity of the pipe material.

2.4. WBHE Model Assumptions

MATLAB is a software for numerical and statistical calculations that is written in the C programming language. MATLAB R2018b version was used to perform the analysis of WBHEs by implementing the proposed model, with consideration of the following assumptions and approximations.

The reservoir model was built by assuming a single well-positioned at the centre of a circular reservoir. The temperature profile in the radial direction was assumed to be constant. Therefore, there was no temperature gradient in the annulus or in the inner tube. Due to turbulent flow, enhanced mixing phenomena occurred, decreasing the radial gradient. The temperature changed only in the annulus and in the vertical direction of the inner tube, so the temperature profile was vertically unidirectional.

The properties of the heat-carrier fluid were assumed to be constant. As the fluid used in this study was water (100 °C, 2 bar), no variations occurred due to pressure or/and temperature gradients.

The model was built under steady-state conditions; there were no temperature variations over time, with each point in the tubes (annulus and inner tube) maintaining the same temperature for the lifecycle of the system. For the elaborations, r_c (external radius of the external casing) was considered equal to r_w (radius of outside wellbore).

In addition, the model considered the resistance associated with tube thickness to be negligible. The tube material had very high conductivity, so its resistance could be considered small compared to the other resistances in the system. For estimation of the resistance associated with the rock (see Equation (6)), the time value used was 3 years after the starting of the system. This assumption made the method a conservative estimate: the system in the years before (1–2 years) turns out in fact to work better. As consequence, the heat exchange phenomena are bigger with the possibility of causing overestimations.

The proposed model followed the path of the fluid using a step-by-step approach. It considered intervals of length dz in which the inlet and outlet temperatures were calculated by solving the energy balance equation for each volume dv. For estimating the energy exchange in the radial direction, the mean value of the temperature in each volume dv was used.

3. Results and Discussion

The temperature profiles associated with the analysed coaxial WBHE system configurations were obtained by making use of the specific ground properties of the selected case studies (the Villafortuna 1, Gela 38 and Tempa Rossa 1D hydrocarbon wells). Values relating to the thermal properties of the different rock formations have been attributed in accordance with references [11,12] (Tables 1–3).

For all cases analysed, the flow rate of the fluid and the inlet temperature were first considered as 3 kg/s and 50 °C, respectively. This temperature is a typical value for direct applications like production cycles in manufacturing and agricultural districts [2]. Subsequently, an analysis was conducted on the thermovector fluid temperature at the outlet as the inlet flow rate varied.

The sizing of the inner and outer tubes, as well as the final casing size, were fixed according to the values proposed in Figure 6 and Table 5. The thermal conductivity value of the insulating material was set to 0.025 W/mK.
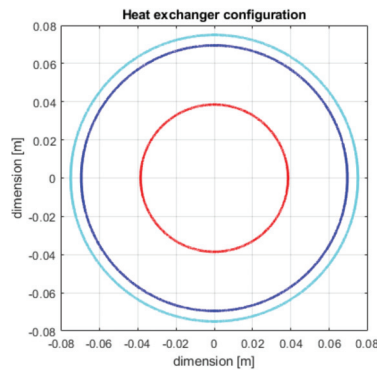
Figure 6. Coaxial WBHE geometry: considered configuration.

Table 5. WBHE tube sizing—ID: internal diameter, OD: external diameter.

Tube Sizing m	ID (mm)	OD (mm)
3 inches	77.9	88.9
5 inches	121.4	139.7
Casing 7 inches	150.4	177.8

In the first section of an external pipe of a coaxial WBHE system, the downward fluid is in thermal contact with both the ground on one side and the upward tube on the other.

Because of its thermal properties, the ground in contact with the external piping provides a negative heat contribution, while the inner tube of a coaxial WBHE provides a positive one. As the negative contribution is usually larger, the water temperature (working fluid temperature) decreases slightly. This behaviour can be observed by analysing the obtained temperature profiles associated with the Gela 38 and Tempa Rossa 1D hydrocarbon wells, in which the thermovector fluid was cooled at depths of up to 1800 m and 1200 m, respectively. Unlike in the Gela 38 and Tempa Rossa 1D hydrocarbon wells, the thermovector fluid maintained a constant temperature (50 °C) for the first portion of the borehole (1400 m) in the Villafortuna 1 hydrocarbon well (Figures 7a, 8a and 9a). The presence of a thick stratigraphic horizon made up of terrigenous sedimentary deposits (Table 1), which are characterised by very low conductivity and specific heat values, negatively influenced the heat exchange and so limited heat dispersion.

Figure 7. (**a**) Temperature profile associated with the coaxial WBHE configuration considering the site-specific stratigraphy of Villafortuna 1 well. (**b**) Wellhead temperature behaviour as the flow rate changes.
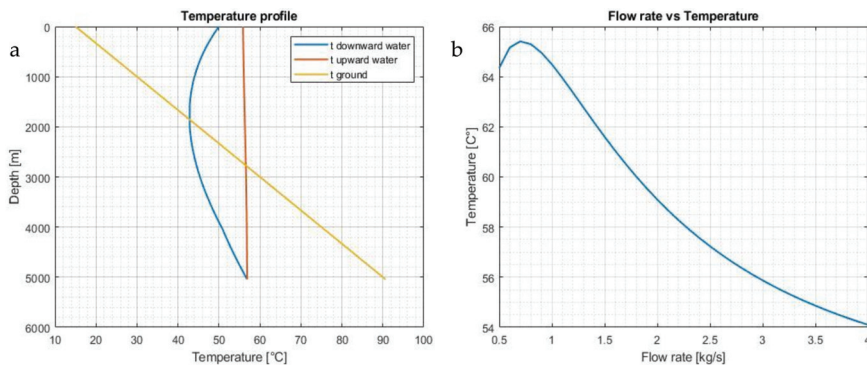
Figure 8. (**a**). Temperature profile associated with the coaxial WBHE configuration considering the site-specific stratigraphy of Tempa Rossa 1D well. (**b**) Wellhead temperature behaviour as the flow rate changes.

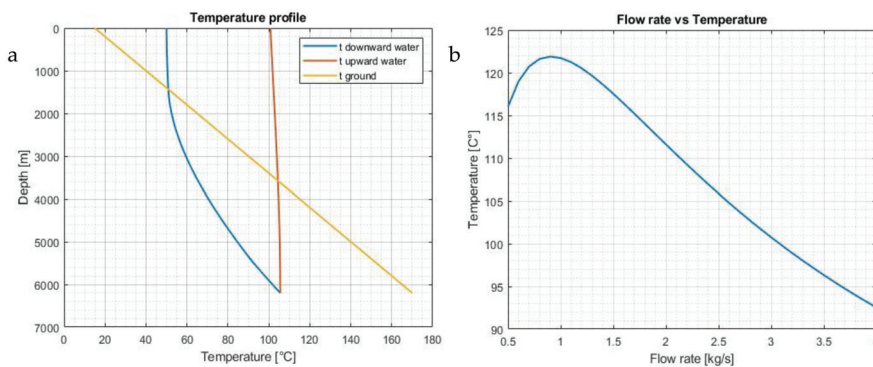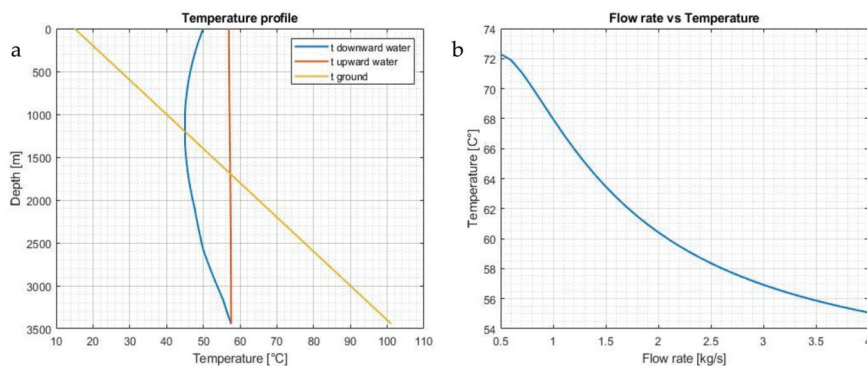**Figure 9.** (**a**) Temperature profile associated with the coaxial WBHE configuration considering the Scheme 38 well. (**b**) Wellhead temperature behaviour as the flow rate changes.

However, when the water and ground temperatures approached similar values in all three hydrocarbon wells, the negative contribution decreased, and water temperature increased. As the downward water profile line crossed the ground temperature line, the ground's heating process began, and the ground contribution became positive. Due to the presence of the insulating material, the heat exchange coefficient between the annulus and the inner tube was quite low, and the increase in the working fluid temperature could be mainly associated with the contribution of the ground.

Using the fixed inlet working fluid temperature (50 °C) and the estimated fluid temperature at the outlet for the three case studies (Figures 7a, 8a and 9a), thermal power values were evaluated for 627.9 KW (100 °C, Villafortuna 1), 75.3 KW (56 °C, Tempa Rossa 1D) and 100.5 KW (58 °C, Gela 38).

Considering a cascading exploitation mode of the heat accumulated by the working fluid water in Villafortuna 1 WBHE, it is correctly possible to hypothesize a multi-variant and comprehensive use of the resource. The outflow temperature of geothermal water at the wellhead is 100 °C, which allows it to progressively be used for greenhouse heating (100–80 °C), domestic hot water and food industry (80–70 °C), animal breeding (60 °C), biomass and agricultural culture (50 °C). On the contrary, the thermal load accumulated in correspondence with Tempa Rossa 1D and Gela 38 wells turns out to be sufficient neither to justify the costs of plant retrofitting nor to plan a cascading exploitation of the geothermal fluid produced.

As can be seen in Figures 7b, 8b and 9b, the inlet flow rate strongly influenced the temperature of the wellhead thermal fluid. In each case, it is possible to identify an inlet flow rate value (kg/s) in order to obtain a higher fluid temperature at the outlet and optimize the quantity of extracted thermal power. When considering inlet flow rate values between 0.5 and 0.8 kg/s, the output fluid temperature increased up to about 122 °C (0.8 kg/s, Villafortuna 1), 65.5 °C (0.7 kg/s, Gela 38) and 72 °C (0.5 kg/s Tempa Rossa 1D). For higher values, the trend was inverted in all three cases.

However, for coaxial WBHE systems like the one analysed, such low inlet flow rates may not be technically appropriate. The heat-exchange modalities are in fact not the only aspect that must be considered to carry out the correct analysis of the heat transfer mechanisms associated with coaxial WBHE. Pressure loss phenomena need to be analysed as they affect pumping costs and are not negligible in the management of a closed-loop geothermal system. In coaxial WBHE, the inlet flow rate strongly influences the temperature of the wellhead thermal fluid. As pressure losses are proportional to the velocity, an increase in the inlet flow rate values will cause an increase in the required pumping power.

4. Conclusions

Over time, the petroleum systems in Italian sedimentary basins have been explored for oil and gas extraction. Since 1985, 7246 wells have been drilled for hydrocarbon extraction. Of these, 898 wells are located onshore with various operational statuses. Geological and geophysical exploration campaigns have ascertained the coexistence of low- to medium-temperature geothermal energy resources in the deepest regions of such geological contexts. As such, energy production based on the exploitation of available low- to medium-temperature geothermal resources associated with disused deep oil and gas wells in Italian oilfields could represent a considerable source of renewable energy.

This study used information on Italian hydrocarbon wells and on-field temperatures to apply a simplified coaxial WBHE model to three hydrocarbon wells. The main purpose was to analyse heat exchange mechanisms in three different Italian oil and gas fields (the Villafortuna-Trecate, Val d'Agri and Gela fields), emphasizing differences in the quantity of extracted thermal energy and considering different geological and depositional contexts.

All calculations considered the detailed stratigraphic data and related thermophysical parameters (e.g., thermal conductivity, volumetric heat capacity and rock density) of each case study. The results indicate a substantial difference in the potential amount of extracted thermal energy between analysed sites, located in different Italian sedimentary contexts. With a fixed inlet working fluid flow rate of 3 kg/s and a fixed temperature of 50 °C, thermal power values were evaluated at 627.9 KW for Villafortuna 1, 75.3 KW for the Tempa Rossa 1D well and 100.5 KW for the Gela 38 hydrocarbon well. The Villafortuna 1 WBHE recorded a maximum extracted fluid temperature of 100 °C, which allows us to hypothesize a cascading exploitation mode of the heat accumulated. Unlike Villafortuna 1, Tempa Rossa and Gela fields had thermal load values that would be of no practical use. As such, the implementation of a coaxial borehole heat exchanger in a such hydrocarbon well may not be energetically or economically worthwhile.

Improving the accuracy of the proposed models by means of future analysis is required: the basic assumption related to the constancy of the properties of the water as working fluid must be overcome by properly analysing the possibility of having phase change (evaporation) in the well, which would change the proposed models. The role in heat transfer and performance of extracting heat from abandoned wells of intraformational flows also needs to be properly considered.

Despite the above considerations, the analysis approach with the associated simplified model proposed in this paper could represent a useful simplified methodological tool to allow the preliminary definition of the possibility of a selected Italian hydrocarbon well to be converted into a geothermal one by means of a coaxial-WBHE technology.

After a preliminary analysis about the presence of industries and agricultural districts, it will be useful to produce a detailed evaluation of the industrial plants available in the

area near the Villafortuna 1 well: a technical feasibility and cost–benefit analysis of the selected configuration in this proposed case study could represent the subject of future research work.

Abbreviations

Parameter	Symbol	Unit of Measure
Volumetric heat capacity of the fluid	ρc_f	[J m^{-3} K^{-1}]
Volumetric heat capacity of the rock	ρc_s	[J m^{-3} K^{-1}]
Density	ρ	[Kgm^{-3}]
Thermal conductivity of the fluid	λ_f	[W m^{-1} K^{-1}]
Thermal conductivity of the rock	λ_s	[W m^{-1} K^{-1}]
Heat conductivity of the porous media	λ_m	[W m^{-1} K^{-1}]
Heat conductivity of the pipe material	λ_i	[W m^{-1} K^{-1}]
Viscosity	μ	[kgm^{-1}s^{-1}]
Thermal diffusivity of the rock	α_s	[ms^{-1}]
Radius of thermal influence	r_s	[m]
Temperature of the rock	T	[°C]
Temperature at the interface of wellbore/formation	T_w	[°C]
Fluid temperature in the outer pipe	T_{fo}	[°C]
Fluid temperature in the inner pipe	T_{fi}	[°C]
Temperature of the environment at the inlet	T_{ei}	[°C]
Temperature of the environment at the surface	T_{es}	[°C]
Time	t	[h]
Flow rate	q	[m^{3}h^{-1}]
Fluid velocity	v_f	[ms^{-1}]
Heat transfer coefficient—outer pipe fluid and wellbore outside	k_w	[Wm^{-2}K^{-1}]
Heat transfer coefficient—the outer pipe and inner pipe	k_{i0}	[Wm^{-2}K^{-1}]
Convective heat transfer coefficient	h_f	[m^{-2} K^{-1}]
Coefficient of convective heat transfer to the inner wall	h_0	[Wm^{-2}K^{-1}]

References

1. Stephenson, M.H.; Ringrose, P.; Geiger, S.; Bridden, M.; Schofield, D. Geoscience and decarbonization: Current status and future directions. *Pet. Geosci.* **2019**, *25*, 501–508. [CrossRef]
2. Kaczmarczyk, M.; Tomaszewska, B.; Operacz, A. Sustainable Utilization of Low Enthalpy Geothermal Resources to Electricity Generation through a Cascade System. *Energies* **2020**, *13*, 2495. [CrossRef]
3. Busby, J. Geothermal energy in sedimentary basins in the UK. *Hydrogeol. J.* **2014**, *22*, 129–141. [CrossRef]
4. Gascuel, V.; Bédard, K.; Comeau, F.A.; Raymond, J.; Malo, M. Geothermal resource assessment of remote sedimentary basins with sparse data: Lessons learned from Anticosti Island, Canada. *Geotherm. Energy* **2020**, *8*, 1–32. [CrossRef]
5. Nasr, M.; Raymond, J.; Malo, M.; Gloaguen, E. Geothermal potential of the St. Lawrence Lowlands sedimentary basin from well log analysis. *Geothermics* **2018**, *75*, 68–80. [CrossRef]
6. Soldo, E.; Alimonti, C.; Scrocca, D. Geothermal Repurposing of Depleted Oil and Gas Wells in Italy. *Proceedings* **2020**, *58*, 9. [CrossRef]
7. Cataldi, R.; Mongelli, F.; Squarci, P.; Taffi, L.; Zito, G.; Calore, C. Geothermal ranking of Italian territory. *Geothermics* **1995**, *24*, 115–129. [CrossRef]

8. Montanari, D.; Minissale, A.; Doveri, M.; Gola, G.; Trumpy, E.; Santilano, A.; Manzella, A. Geothermal resources within carbonate reservoirs in western Sicily (Italy): A review. *Earth Sci. Rev.* **2017**, *169*, 180–201. [CrossRef]

9. Trumpy, E.; Manzella, A. Geothopica and the interactive analysis and visualization of the updated Italian National Geothermal Database. *Int. J. Appl. Earth Obs. Geoinf.* **2017**, *54*, 28–37. [CrossRef]

10. Trumpy, E.; Botteghi, S.; Caiozzi, F.; Donato, A.; Gola, G.; Montanari, D.; Pluymaekers, M.P.D.; Santilano, A.; Van Wees, J.D.; Manzella, A. Geothermal potential assessment for a low carbon strategy: A new systematic approach applied in southern Italy. *Energy* **2016**, *103*, 167–181. [CrossRef]

11. Di Sipio, E.; Galgaro, A.; Destro, E.; Giaretta, A.; Chiesa, S.; Manzella, A. Thermal Conductivity of Rocks and Regional Mapping. In Proceedings of the European Geothermal Congress 2013, Pisa, Italy, 3–7 June 2013.

12. Pasquale, V.; Gola, G.; Chiozzi, P.; Verdoya, M. Thermophysical properties of the Po Basin rocks. *Geophys. J. Int.* **2011**, *186*, 69–81. [CrossRef]

13. Alimonti, C.; Soldo, E. Study of geothermal power generation from a very deep oil well with a wellbore heat exchanger. *Renew. Energy* **2016**, *86*, 292–301. [CrossRef]

14. Bertello, F.; Fantoni, R.; Franciosi, R. Overview of the Italy's Petroleum Systems and Related Oil and Gas Occurrences. In Proceedings of the 70th EAGE Conference and Exhibition Incorporating SPE EUROPEC 2008, Rome, Italy, 9 June 2008; European Association of Geoscientists & Engineers: Houten, The Netherlands, 2008; Volume 1, pp. 74–78. [CrossRef]

15. Cazzola, A.; Fantoni, R.; Franciosi, R.; Gatti, V.; Ghielmi, M. From thrust and fold belt to foreland basins: Hydrocarbon exploration in Italy, AAPG. *Int. Conf.* **2011**, *10374*, 2–5.

16. Fantoni, R.; Galimberti, R.; Ronchi, P.; Scotti, P. Po Plain Petroleum Systems: Insights from Southern Alps Outcrops (Northern Italy). *Search Discov. Artic.* **2011**, *20120*, 7.

17. Bertello, F.; Fantoni, R.; Franciosi, R.; Gatti, V.; Ghielmi, M.; Puglise, A. From thrust-and-fold belt to foreland: Hydrocarbon occurrences in Italy. *Pet. Geol. Conf. Proc.* **2010**, *7*, 113–126. [CrossRef]

18. Bello, M.; Fantoni, R. Deep oil plays in Po Valley: Deformation and Hydrocarbon Generation in a Deformed Foreland. In Proceedings of the AAPG Hedberg Conference "Deformation History, Fluid Flow Reconstruction and Reservoir Appraisal in Foreland Fold and Thrust Belts", Sicily, Italy, 14–18 May 2002; Palermo e Mondello: Sicily, Italy, 2002; Volume 14, p. 18.

19. Cazzini, F.F. The history of the upstream oil and gas industry in Italy. *Geol. Soc. Lond. Spec. Publ.* **2018**, *465*, 243–274. [CrossRef]

20. Lo Russo, S.; Gizzi, M.; Taddia, G. Abandoned oil and gas wells exploitation by means of closed-loop geothermal systems: A review. *Geoing. Ambient. E Min.* **2020**, *160*, 3–11. [CrossRef]

21. Wang, K.; Yuan, B.; Ji, G.; Wu, X. A comprehensive review of geothermal energy extraction and utilization in oilfields. *J. Pet. Sci. Eng.* **2018**, *168*, 465–477. [CrossRef]

22. Nian, Y.-L.; Cheng, W.-L. Evaluation of geothermal heating from abandoned oil wells. *Energy* **2018**, *142*, 592–607. [CrossRef]

23. Davis, A.P.; Michaelides, E.E. Geothermal power production from abandoned oil wells. *Energy* **2009**, *34*, 866–872. [CrossRef]

Article

Numerical Investigation on the Influence of Surface Flow Direction on the Heat Transfer Characteristics in a Granite Single Fracture

Xuefeng Gao [1], Yanjun Zhang [1,2], Zhongjun Hu [1,*] and Yibin Huang [1]

[1]   College of Construction Engineering, Jilin University, Changchun 130012, China;
      gaoxf18@mails.jlu.edu.cn (X.G.); Zhangyanj@jlu.edu.cn (Y.Z.); Huangyb16@mails.jlu.edu.cn (Y.H.)
[2]   Key Lab of Groundwater Resource and Environment, Ministry of Education, Jilin University,
      Changchun 130026, China
*   Correspondence: huzj@jlu.edu.cn

Abstract: As fluid passes through the fracture of an enhanced geothermal system, the flow direction exhibits distinct angular relationships with the geometric profile of the rough fracture. This will inevitably affect the heat transfer characteristics in the fracture. Therefore, we established a hydro-thermal coupling model to study the influence of the fluid flow direction on the heat transfer characteristics of granite single fractures and the accuracy of the numerical model was verified by experiments. Results demonstrate a strong correlation between the distribution of the local heat transfer coefficient and the fracture morphology. A change in the flow direction is likely to alter the transfer coefficient value and does not affect the distribution characteristics along the flow path. Increasing injection flow rate has an enhanced effect. Although the heat transfer capacity in the fractured increases with the flow rate, a sharp decline in the heat extraction rate and the total heat transfer coefficient is also observed. Furthermore, the model with the smooth fracture surface in the flow direction exhibits a higher heat transfer capacity compared to that of the fracture model with varying roughness. This is attributed to the presence of fluid deflection and dominant channels.

Keywords: heat transfer; granite fracture; flow direction; enhanced geothermal system

1. Introduction

Geothermal energy is a clean and environmentally friendly renewable energy source with a wide distribution range, large reserves, and long duration [1–3]. The high temperature rock mass buried 3–10 km underground is characterized by low permeability and low porosity [4]. In order to extract thermal energy from such high temperature rock mass, several countries (led by the United States) proposed the use of artificial hydraulic fracturing, which led to the development of reservoir-transforming hydro-shearing techniques to establish fracture network channels and improve the heat transfer capacity [5]. This geothermal project is often referred to as an enhanced geothermal system (EGS). The fracture surface formed by hydraulic fracturing is typically rough, which directly affects the heat transfer performance of the working medium (water or CO_2) [6].

The key to extracting geothermal resources by EGS is the flow and heat exchange process of working fluid in fractures of high temperature rock mass [7]. However, when the fluid begins to flow from the injection well into the fracture, the initial direction of flow often has an angle equal to the direction of the rough fracture surface, which inevitably affects the heat exchange effect. The accurate determination of the convection heat transfer coefficient between the fluid and fracture is crucial to the optimization of the reservoir transformation and productivity predictions [8]. In addition, a clear heat transfer law within the fractures is of great significance to the establishment of EGS heat recovery models [9].

47

Numerous studies have attempted to quantify the roughness of fracture surfaces. For example, Patton [10] proposed the concept of the wave angle and established the relationship between wave angle and fracture morphology. Mandelbrot [11] proposed the concept of fractal geometry and developed a fractal dimension framework to describe the geometrical characteristics of fracture rough surfaces. Barton [12] used the joint roughness coefficient (*JRC*) to characterize the section geometry of fracture surfaces to determine 10 fracture types with an approximate length of 10 cm. Xie [13] demonstrated the fractal dimension to be the measured values of the joint roughness coefficients.

Experimental and numerical simulations have demonstrated the fluid flow and heat transfer processes in fractures to be affected by many factors, including the aperture, roughness, type of fluid, injection flow rate, initial temperature of rock, and rock thermophysical parameters [14]. Early scholars used the plate model to describe the heat transfer characteristics in fracture. However, Tsang and Brown [15,16] pointed out that the parallel plate theory may cause flow estimation errors of 1–2 orders of magnitude. In an experimental study on the seepage heat transfer in a single fracture of granite, Zhao and Tso [17] revealed the single fracture with a certain roughness to have a better heat transfer performance than the smooth-plate fracture. Similarly, the two-dimensional coupled heat transfer model of a single fracture established by He [18] also demonstrated a strong correlation between the local convection heat transfer coefficient and the fracture profile. Neuville [19] established a self-affine rough fracture coupling model that assumes a reduced heat transfer efficiency in a rough fracture with constant temperature due to the channel effect. Research carried out by Huang [20] also showed that a larger relative roughness increases the flow friction and significantly reduces the heat exchange. Luo [21] investigated the influence of initial rock temperature on the heat transfer efficiency of fractures, demonstrating a positive relationship between the heat transfer rate and rock temperature. The two-dimensional single-fracture heat transfer model established by He [22] shows that the effect of fracture surface roughness on heat transfer intensity decreases with an increasing injection flow rate. Confining pressure has a significant impact on the fracture aperture. Shu [23] employed a novel experimental device to simulate the evolution of the hydraulic and heat transfer characteristics of fractures under a confining pressure. Results show that both the heat transfer rate and total heat transfer coefficient decrease with an increasing confining pressure. Zhang [24] established a three-dimensional numerical model based on three-dimensional laser scanning to evaluate the effects of rock temperature, water flow velocity, roughness, and fracture aperture on the heat transfer coefficient. Simulation tests reveal the dominant influence of the flow rate on the rock roughness, followed by the aperture size. Andrade et al. [25] simulated the flow and heat transfer between two-dimensional parallel rough surfaces, demonstrating the minimal effect of wall roughness on the heat transfer for the characteristic parameter $Pe = u(d/2)2/L < 200$. Zhang [26] performed convection heat transfer tests of carbon dioxide in a single fracture to establish a numerical model and proposed the rough fracture channel effect. Experimental and numerical simulations can increase our understanding of the geothermal field model. Fox et al. [27] established a discrete fracture network and investigated the relationship between hydraulic aperture and fluid runoff, concluding that variations in the fracture aperture can cause flow channeling and reduce the heat transfer area. Furthermore, several studies [28,29] have employed Monte-Carlo [30,31] stochastic simulations to build fracture network models with different geometric parameters, and in particular, the EGS site model to predict the heat recovery performance. Bruel [32] integrated experimental data into a single model used to generate an estimation model of the main hydraulic parameters. Chen [33] established a geothermal reservoir model with a rough fracture surface based on small-scale research results, revealing the constant heat transfer coefficient (HTC) recommended in previous studies to underestimate the final outlet fluid temperature in the case of rough fractures. These studies demonstrate that research on the influence of fracture morphology on the fluid flow and heat transfer process at the experimental scale can be applied to the actual site model [28,34].

In summary, previous studies have shown that the geometry of the fracture surface has a profound influence on the fluid flow and heat transfer process in the fracture [35,36]. According to the different influencing factors, many scholars [23,37,38] have designed experiments and carried out corresponding numerical simulations to determine how these influence factors affect the heat transfer process in fractures. The results of such studies are very important for the development of EGS stimulation technology.

The aforementioned research generally focuses on the influence of fracture morphology on fluid heat transfer, while studies on the effect of the angle between the direction of the fluid flow and the morphology of the fracture wall on the heat transfer performance are limited. In addition, because of the geological history, the fracture aperture of EGS reservoirs range from the micron to centimeter scale [39]. This makes it difficult to obtain the temperature distribution of rock fractures and thermal mediums under laboratory conditions. Hence, in the current study, we established a single fracture heat transfer model with a random geometry profile that was subsequently verified by experiments. Four cases with fracture profiles and varying angles between flow direction were set up to simulate and explore the heat transfer performance of distilled water through fractures. The influence of the fluid flow direction on the fracture heat transfer characteristics was then discussed.

2. Numerical Simulations

2.1. Mathematical and Physical Models

A three-dimensional single fracture model was established to study the influence of flow direction on the heat transfer characteristics in a granite single fracture. The geometry profile of the fracture was constructed using a random method (Figure 1a), while the rough fracture wall was built by stretching in the vertical direction (Figure 1b,c).
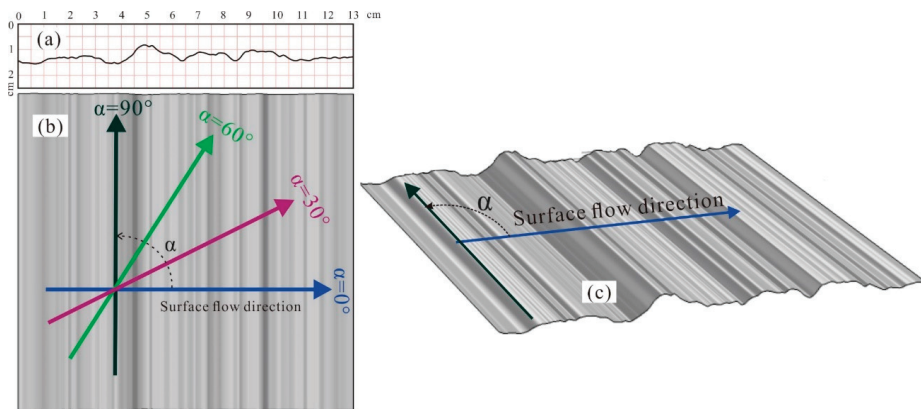
Figure 1. Fracture surface and surface flow direction distribution. (**a**) 2D random fracture profile; (**b**) pseudo-three-dimensional fractured rough surface stretched towards the page direction. (**c**) 3D view of pseudo-three-dimensional fracture rough surface.

The surface flow of the fracture surface was assumed to have four different directions, with the 0° direction taken as the *z*-axis direction (Figure 1b). The angle between the surface flow direction and the positive direction of the *z*-axis is denoted as α. The surface flow direction had a gradient of 30° and was rotated counterclockwise around the *z*-axis by 30°, 60°, and 90° to obtain the fracture wall. The rough single-fracture numerical model shown in Figure 2 was obtained by embedding these fracture walls into a cylindrical model with a size of 100 × 50 mm (length × diameter). The vertical displacement of the fracture in the model was determined as 0.3 mm by translation method. Table 1 lists the geometric parameters of the four fracture models. The surface area and inlet area

deviations of the four fractures were 1.87% and 0.33%, respectively. Therefore, at the scale of this study, the effects on the simulation results due to differences in surface area and inlet area are negligible.
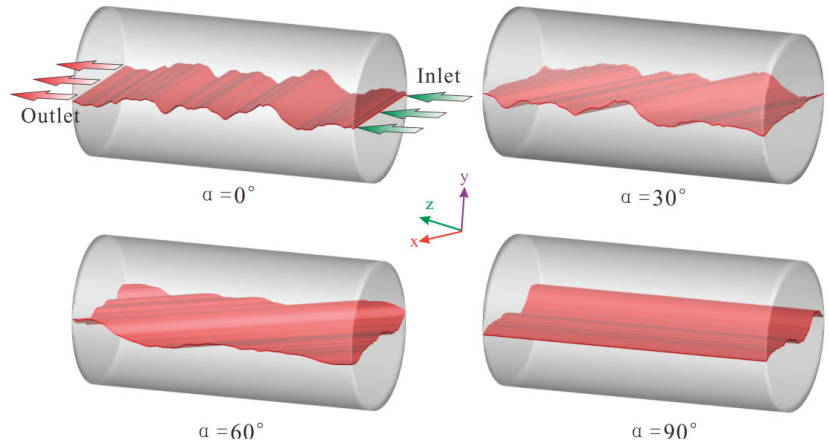
Figure 2. Fracture seepage heat transfer model.

Table 1. Geometric parameters of the fracture.

Model Case (α =)	0°	30°	60°	90°	Maximum Deviation
Surface area (mm²)	5588.95	5620.33	5658.53	5553.84	1.87%
Inlet area (mm²)	14.9883	14.9391	14.9405	14.9425	0.33%
Volume (mm³)	1496.28	1495.96	1494.91	1494.25	0.14%
Vertical offset (mm)	0.3	0.3	0.3	0.3	\

For natural fracture, the Reynolds number is much smaller than the critical Reynolds number (Re < 1800 [35]) due to its small aperture and low flow rate of underground fluid. Thus, the fluid flow in a granite fracture remains laminar. Convective heat transfer in three-dimensional rock fractures was modeled using FLUENT 6.3 [40] by employing a finite volume method (FVM) to solve the Navier–Stokes equations.

The governing equations for the conservation of momentum, mass, and energy in the fracture are described as follows:

Continuity equation:

$$\frac{\partial \rho_w}{\partial t} + \nabla \cdot (\rho_w \boldsymbol{V}) = 0 \tag{1}$$

Momentum equation:

$$\frac{\partial (\rho_w \boldsymbol{V})}{\partial t} + \nabla (\rho_w \boldsymbol{V}\boldsymbol{V}) = -\nabla P + \nabla \cdot \left(\mu \left[\left(\nabla \boldsymbol{V} + \nabla \boldsymbol{V}^T \right) - \frac{2}{3} \nabla \cdot \boldsymbol{V} I \right] \right) \tag{2}$$

Energy equation:

$$\frac{\partial}{\partial t} (\rho_w E) + \nabla \cdot (\boldsymbol{V}(\rho_w E + p)) = \nabla \cdot \left(\lambda_w \nabla T + \mu \left[\left(\nabla \boldsymbol{V} + \nabla \boldsymbol{V}^T \right) - \frac{2}{3} \nabla \cdot \boldsymbol{V} I \right] \cdot \boldsymbol{V} \right) \tag{3}$$

where ρ_w (kg/m^3) and ρ_r (kg/m^3) are the densities of water and rock, respectively; V (m/s) is the velocity vector; p (Pa) is the pressure; I is the unit tensor; E is the total energy; λ_w (W/(m·°C)) is the fluid thermal conductivity; μ (Pa s) is the fluid viscosity.

In EGS frameworks, water is typically used as a heat exchange medium. However, the physical properties of water are more susceptible to temperature than pressure. Hence, the relationship between the physical properties of water and temperature was described by the following empirical formula [41]:

Dynamic viscosity of water:

$$\mu_w = 1.3799 - 0.0212T + 1.3604 \times 10^{-4}T^2 - 4.6454 \times 10^{-7}T^3 + 8.9043 \times 10^{-10}T^4 - 9.0791 \times 10^{-13}T^5 \\ + 3.8457 \times 10^{-16}T^6 \tag{4}$$

Specific heat capacity of water:

$$C_{p,w} = 12010 - 80.4 \times T + 0.3 \times T^2 - 5.4 \times 10^{-4}T^3 + 3.6 \times 10^{-7}T^4 \tag{5}$$

Thermal conductivity of water:

$$\lambda_w = -0.8691 + 8.9 \times 10^{-3}T - 1.5837 \times 10^{-5}T^2 + 7.9754 \times 10^{-9}T^3 \tag{6}$$

Water density:

$$\rho_w = 838.4661 + 1.4005 \times T - 3 \times 10^{-3}T^2 + 3.7182 \times 10^{-7}T^3 \tag{7}$$

where T (°C) is the water temperature and which ranges from 10 to 100 °C.

The fracture inlet and outlet employ mass flow rate and outflow boundary conditions, respectively. The outer surface of the rock is considered to be an adiabatic boundary, while the inner wall of the fracture is considered as an impervious and no-slip boundary.

2.2. Model Meshing and Mesh Independence Verification

In order to focus on fluid flow and heat transfer in fractures, we employed structured hexahedral grids in fracture spaces (Figure 3a) and an increased grid density around fractures (Figure 3b,c), while an unstructured tetrahedral grid was used for the computational domain outside the fracture. Furthermore, we selected $\alpha = 0°$ as the verification sample to verify that the simulation results are not affected by the number of meshes. Table 2 lists the four grid numbers for $\alpha = 0°$ and Figure 3 presents the grid characteristics of the fourth grid number.

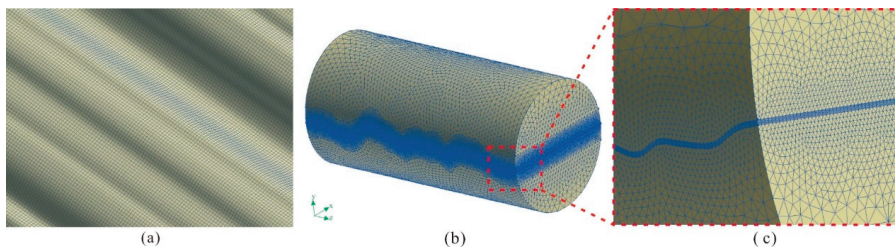| (a) | (b) | (c) |

Figure 3. Mesh features of mesh 4. (**a**) Fracture surface mesh characteristics; (**b**) overall mesh distribution; (**c**) mesh distribution characteristics around the fracture.

Table 2. Four grid numbers for $\alpha = 0°$.

Mesh Case	1	2	3	4
Mesh Number	691,257	1,366,554	2,628,825	3,120,142

Under the same simulation conditions, four models with different numbers of grids were constructed and the average temperature of the fluid at the outlet was monitored (Figure 4). Mesh case 1 is distorted due to the presence of grids with a high value and aspect ratio. When the number of meshes exceeds 1.3 million, the outlet temperature of different mesh cases is generally consistent with time. In order to accurately reflect the geometry of the fracture surface and save computer resources, we selected mesh case 3 for further numerical calculations. Table 3 details the grid numbers for the four models.
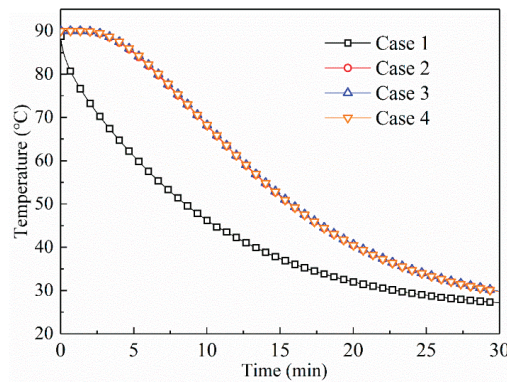
Figure 4. Variation of outlet temperature with time for the four mesh cases.

Table 3. Number of simulated sample grids for the four models.

Model Case (α =)	0°	30°	60°	90°
Mesh Number	2,628,825	2,586,743	2,645,426	2,653,564

2.3. Initial Conditions and Simulations

The initial temperature of the rock was set to 90 and 70 °C to prevent a water phase transformation. The initial flow rates were 10, 20, 30, and 40 mL/min, respectively, depending on the performance of the plunger pump. The injection temperature of water was 25 °C without considering the change of room temperature. Table 4 lists the simulation conditions.

Table 4. Numerical simulation conditions.

Model Case (α =)	Rock Temperature, T_0 (°C)	Flow Rate, V_0 (mL/min)
0° 30° 60° 90°	70 90	10 20 30 40

Calculations were performed following the unsteady double precision method and the second-order implicit mode to improve calculation accuracy. The SIMPLEC (semi-implicit method for pressure-linked equations consistent) algorithm, an improved SIMPLE algorithm, was adopted to amend the fluid pressure and flow rate, while the PRESTO (PREssure STaggering Option) scheme was used for the pressure discretization. The second order discretization scheme was used for the convection terms. The residual convergence criteria for the computational equations was set to 10^{-5} and the time step size for the transient simulations time was equal to 1 s. The total solution time was taken as 30 min.

3. Model Verification

Although the establishment of a realistic fracture model proves to be a complicated task, a single-fracture granite model with a flat and smooth surface can validate the

proposed model. Thus, experimental and numerical simulation results for smooth-plate fractures are compared.

A fracture heat transfer laboratory simulation system was independently developed by our research group for the experiments. Figure 5 depicts the experimental system, which can be divided into five key components including the seepage, confining pressure, heating, core holder, and data measurement systems. Six temperature sensor mounting holes were preset on the top of the holder to ensure direct contact between the sensor and the outer surface of the rock sample. The data measurement system monitored the rock and fluid temperatures on the outer surface of the core and at the core outlet in real time, respectively.
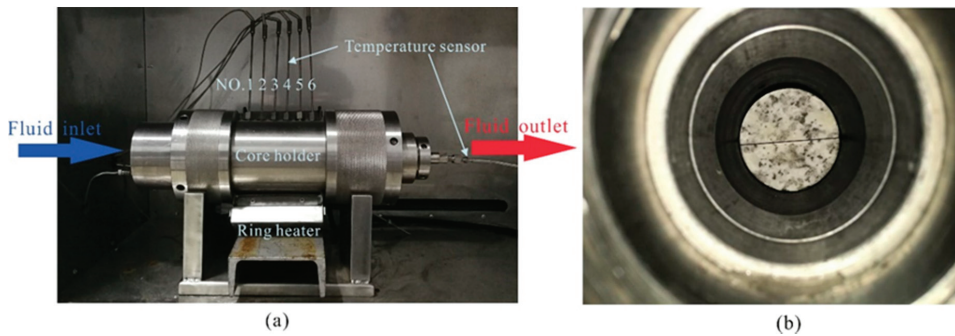
Figure 5. The fracture heat transfer laboratory simulation system. (**a**) Core holder system; (**b**) a granite sample with a smooth-plate single fracture in the holder.

The rock sample with smooth-plate fractures shown in Figure 6a,b was tested to verify the correctness of the numerical model, while a numerical model (Figure 6c) was established to simulate the test results. The rocks used in this study were obtained from important geothermal resource targets in the northern Songliao Basin of China. The granite was processed into a cylindrical specimen with a diameter and height of 50 and 100 mm, respectively. The thermophysical properties of the granite were obtained from tests. The specific heat capacity measuring device (BBR series, made in Xiangtan Xiangyi Instrument Co., Ltd., Xiangtan, China) based on cooling method and the thermal conductivity scanner (TCS, made in Lippmann and Rauen GbR, Schaufling, Germany) based on optical scanning principle are used to measure the specific heat capacity and thermal conductivity of rock, respectively. Figure 7 presents the variations in specific heat capacity and the thermal conductivity of rock with temperature.
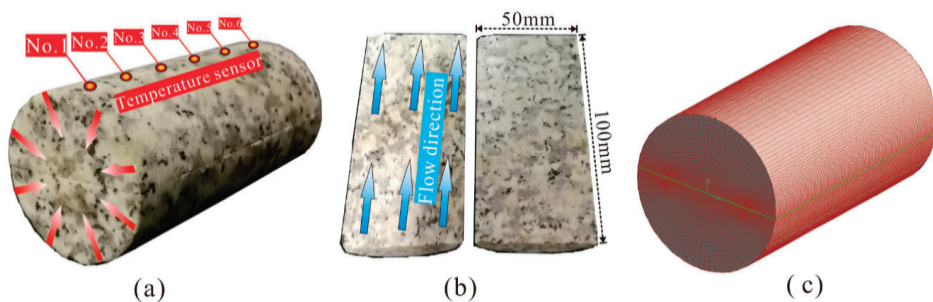
Figure 6. Smooth-plate fracture and mesh model. (**a**) Temperature sensor arrangement. (**b**) Flow direction. (**c**) Mesh generation characteristics of numerical model.
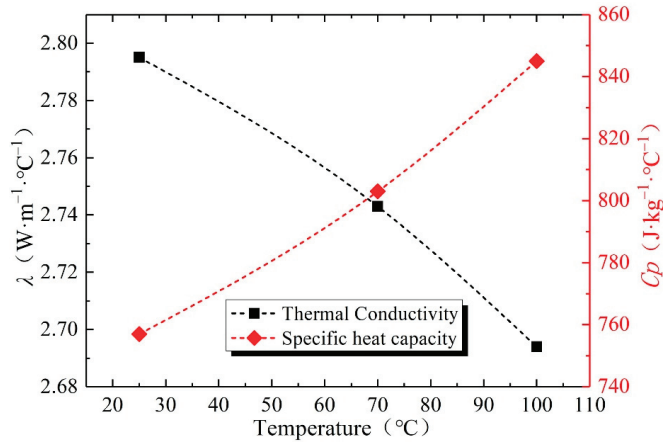
Figure 7. Variations in thermal conductivity and specific heat capacity of rock with temperature.

The experimental flow rates were set as 5, 10, 20, and 30 mL/min for temperatures of 60, 70, 80, and 90 °C, respectively. Both the boundary and initial conditions followed those detailed in Section 2.3. Numerical simulations were performed based on the experiments to ensure that the results were not affected by other factors. The unsteady numerical simulation of fluid temperature T_{outlet} at the fracture outlet for a given time was calculated as follows:

$$T_{outlet} = \frac{\int_{A_{out}} T_w(x,y,z)\mu_w(x,y,z)\rho_w(x,y,z)c_{p,w}(x,y,z)dA}{\int_{A_{out}} \mu_w(x,y,z)\rho_w(x,y,z)c_{p,w}(x,y,z)dA} \tag{8}$$

where A_{out} (m^2) is the area of the fracture outlet.

Figure 8 clearly describes the comparison between the numerical simulation and experimental results for a smooth single fracture. Although there are some errors in the outlet temperature and the rock surface temperature obtained from the experiments and numerical simulation, the maximum errors are only 0.8% and 1.3%, respectively. This indicates that the numerical model established using FLUENT 6.3 can accurately reflect the convection heat of single-fracture granite.
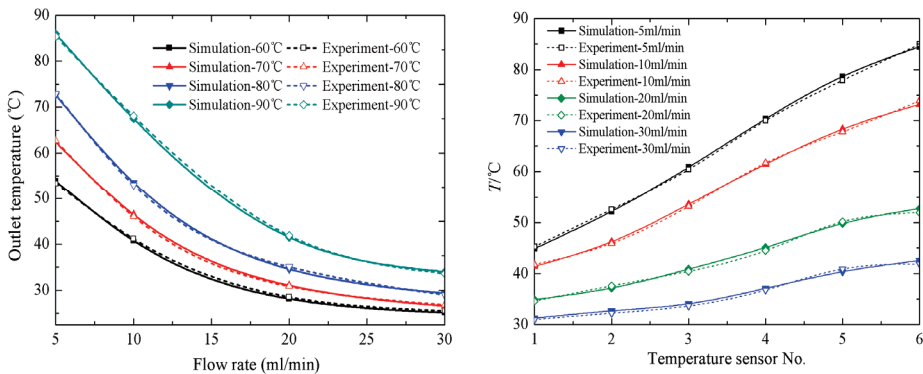
Figure 8. Comparison of experimental and numerical results (t = 10 min). (**Left**) Outlet temperature varies with injection flow rate at different initial rock temperatures. (**Right**) Surface temperature varies with sensor position at different injection velocities.

4. Data Processing

4.1. Heat Extraction Rate

The heat extraction rate can measure the heat absorbed by water flowing through a rock fracture per unit time and is calculated as follows [26]:

$$Q = (H_{outlet} - H_{inlet})M, \tag{9}$$

where M (kg/s) is the flow rate; H_{inlet} (kJ/kg) and H_{outlet} (kJ/kg) are the water enthalpy at the inlet and outlet, respectively. The enthalpy of water can be determined by numerical simulations of the inlet and outlet temperature and pressure.

4.2. Total Heat Transfer Coefficient

For fracture channels with complex surface morphology, the total heat transfer coefficient can describe the overall convective heat transfer performance within the fracture. The total heat transfer coefficient can be calculated from Newton's law of cooling [42]:

$$h_{total} = \frac{q_f}{T_f - T_w}, \tag{10}$$

where q_f (W/m^2) is the average heat flux on the inner wall of the fracture; T_f (°C) is the average temperature on the inner wall of the fracture; T_w (°C) is the average temperature of the water in the fracture. These parameters can be calculated from the numerical simulation results as follows:

$$q_f = \frac{\int_{A_f} q(x,y,z)\mathrm{d}A}{\int_{A_f} \mathrm{d}A}, \tag{11}$$

$$T_f = \frac{\int_{A_f} T(x,y,z)\mathrm{d}A}{\int_{A_f} \mathrm{d}A}, \tag{12}$$

$$T_w = \frac{\int_{V_f} T(x,y,z)\rho(x,y,z)C_p(x,y,z)u(x,y,z)\mathrm{d}V}{\int_{V_f} \rho(x,y,z)C_p(x,y,z)u(x,y,z)\mathrm{d}V}, \tag{13}$$

where A_f (m^2) is the surface area of the fracture; V_f (m^3) is the volume of the fracture.

4.3. Local Heat Transfer Coefficient

The local heat transfer coefficient can describe the local heat transfer characteristics in fractures and is an important parameter reflecting the heat transfer characteristics in the flow direction. Here, we calculated the discrete form of the local heat transfer coefficient via Equation (10) as follows:

$$h_x = \frac{q_{fx}}{T_{fx} - T_{wx}}, \tag{14}$$

where q_{fx} (W/m^2), T_{fx} (°C), and T_{wx} (°C) are the heat flux, temperature, and fluid temperature at position x of the fracture wall, respectively. Furthermore, the Reynolds number (*Re*) can be calculated using the following formula for seepage in single fracture of rock:

$$R_e = \frac{2M}{d\mu_w}, \tag{15}$$

where M (kg/s) is the mass flow rate and d (m) is the fracture aperture.

The overall Nusselt number (*Nu*) can be determined as follows:

$$N_u = \frac{h_{total}d_e}{\lambda_w}, \tag{16}$$

where d_e (m) is the equivalent hydraulic diameter of a channel with arbitrary shape.

5. Results and Discussion

5.1. Temperature Field Distribution

Table 5 lists the outlet water temperature determined from the 32 simulations. The outlet water temperature is maximized at $\alpha = 90°$, followed by models $\alpha = 0°$, $\alpha = 30°$, and $\alpha = 60°$.

Table 5. Results from 10-min numerical simulation.

T_0 (°C)	V_0 (mL/min)	T_{outlet} (°C)			
		$\alpha = 0°$	$\alpha = 30°$	$\alpha = 60°$	$\alpha = 90°$
	10	54.08	53.93	53.87	54.19
	20	36.47	36.36	36.23	36.51
70°C	30	30.92	30.87	30.80	30.99
	40	28.67	28.65	28.59	28.73
	10	68.45	68.38	68.23	68.58
	20	42.03	41.96	41.87	42.18
90°C	30	33.75	33.70	33.62	33.84
	40	30.44	30.34	30.27	30.53

Figure 9 depicts the distribution characteristics of the temperature fields on the fracture surfaces of four different model cases at several injection flow rates. With the injection of low temperature water, the temperature inside the fracture begins to decrease and the cold front pushes towards the outlet. This phenomenon is consistent with previous studies [37,43,44]. The temperature at the center of the fracture typically exceeds that on both sides of the fracture. This is attributed to the greater thermal replenishment at the center of the fracture by the cylinder model compared to the two sides. Increasing the flow rate enhances the rate of the temperature reduction in the fracture. The temperature on the fractured surface of model $\alpha = 0°$ is distributed symmetrically along the z-axis due to the symmetry of the model. At $\alpha = 30°$ and $\alpha = 60°$, the fracture surface temperature in the positive direction of the x-axis exceeds that in the negative direction. This indicates that the angle between the fracture morphology and flow direction has an important influence on the convection heat transfer process.

Figure 10 presents the local temperature distribution along the z-axis at $x = 0.02$ m and $x = -0.02$ m. At $\alpha = 30°$ and $\alpha = 60°$, the local wall temperature at $x = 0.02$ m is lower than that at $x = -0.02$ m. This is related to the migration of the channel formed by the fracture profile towards the x-axis, which makes the fracture geometry profile no longer perpendicular to the flow direction. The fluid preferentially flows through the fractures in an easily accessible path where the flow direction is deflected. In addition, Figure 10 shows that the temperature curve at low flow rates (10 mL/min) reaches its peak value, while the temperature curve at high flow rates (30 mL/min) does not. This indicates that the cryogenic fluid injected at high flow rates penetrates the fractures more quickly and results in a thermal breakthrough in a short time, which causes rapid wall temperature reduction and no timely thermal replenishment. Fluids with low flow rates are more likely to utilize matrix heat transfer to compensate for the decrease in wall temperature caused by convection heat transfer.

Figure 11 illustrates the streamline distribution characteristics of the models with $\alpha = 30°$ and $\alpha = 60°$. The flow direction is observed to slightly deflect in the fracture towards the x-axis, which results in the temperature difference shown in Figures 9 and 10. This deflection is attributed to the presence of a gently inclined microfractured surface in front of the flow field, preventing the flow from passing. Figure 12 simplifies fracture surface morphology to account for the deflection of the fluid flow direction. A fractured surface consists of a limited number of microfractured surfaces. When the direction of the fluid injection is not parallel to the microfracture dip, the fluid will slightly deflect towards a blunt angle between the flow direction and the microfracture surface strike.
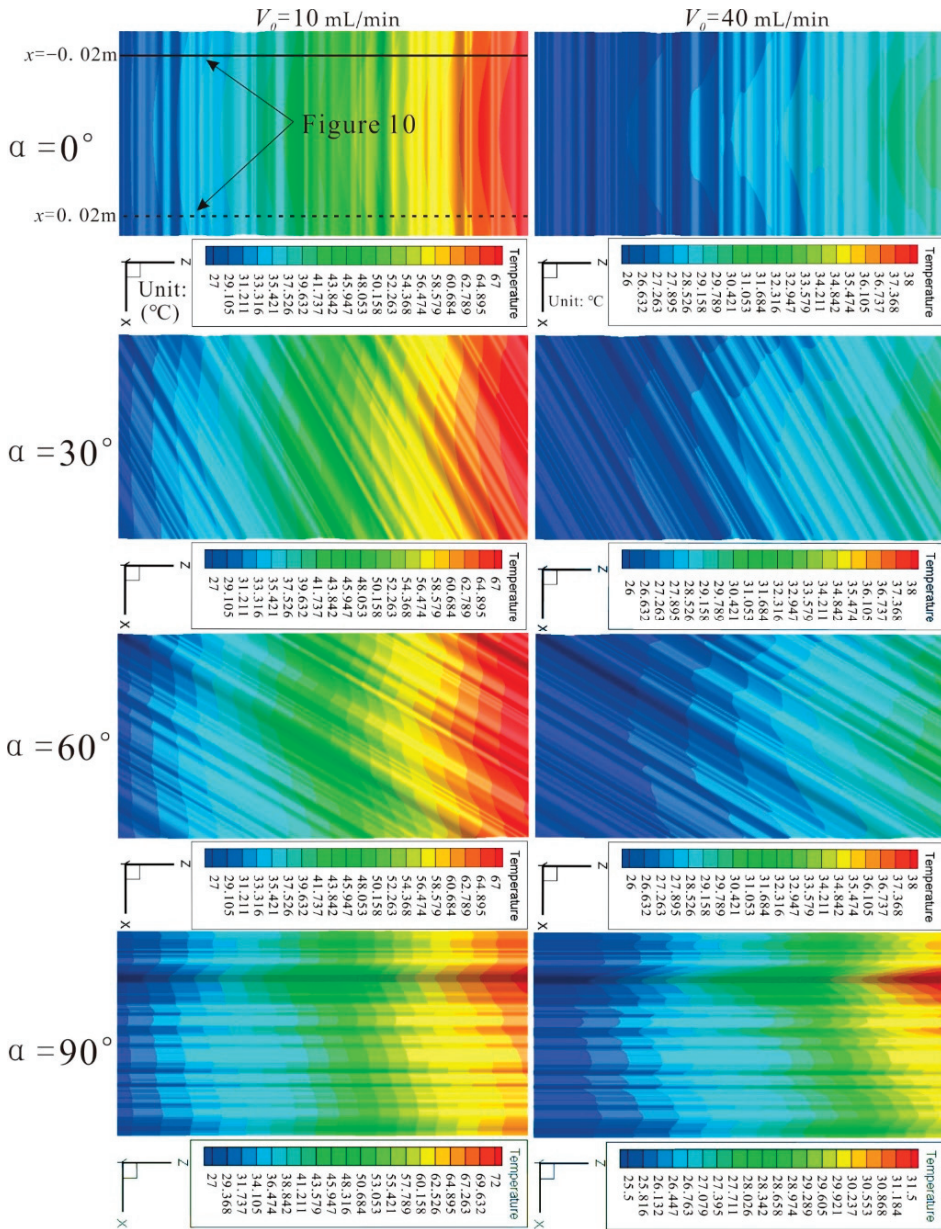
Figure 9. Temperature field distribution on the fracture surface (*t* = 10 min).
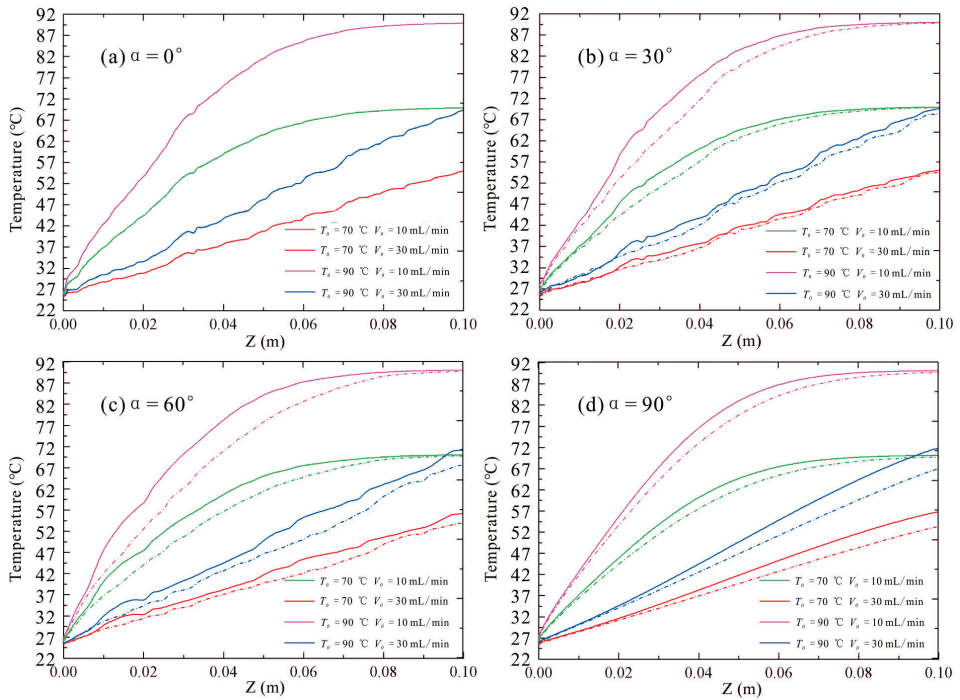
Figure 10. Local temperature distribution along the flow direction at different locations of the *x*-axis on the inner wall of fracture (solid line: *x* = −0.02 m, dashed line: *x* = 0.02 m, *t* = 2 min).
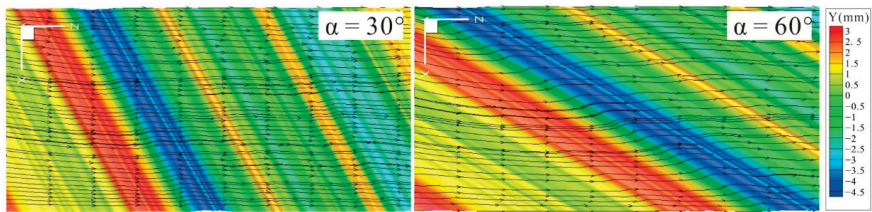
Figure 11. Streamline distribution characteristics of models with *α* = 30° and *α* = 60° (*V*₀ = 10 mL/min).
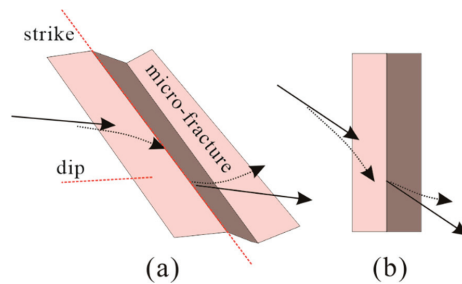
Figure 12. Schematic illustration of fluid flow direction deviation. (**a**) The up- and down-hill direction of the fluid migration. (**b**) Top view: solid and dotted lines are the ideal flow direction path and the flow deflection path, respectively.

5.2. Heat Extraction Rate

The average Reynolds and Nusselt numbers in the fracture are calculated based on Equations (15) and (16), respectively (Figure 13). Based on the simulation conditions, the Reynolds number calculated using Equation (16) ranges from 14.5 to 53.3, which is much lower than the critical Reynolds number leading to the change of laminar flow state [35]. The results of Reynolds number calculation also show that the assumption of using laminar flow model in Section 2.1 is reasonable. The difference of thermophysical properties of water results in a greater Reynolds number at initial temperature $T_0 = 90\ °C$ compared to that with initial temperature $T_0 = 70\ °C$. The maximum Nusselt number at $\alpha = 90°$ is 15.8 (Figure 13b).
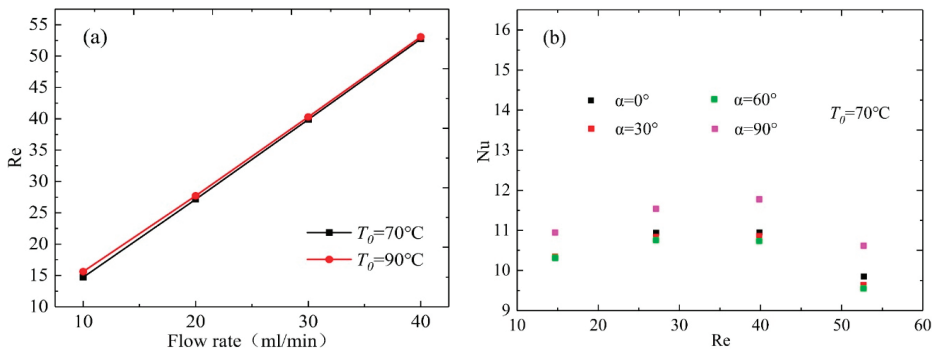
Figure 13. Reynolds number in relation to (**a**) the flow rate and (**b**) Nusselt number.

Considering the small scale of the model in this study, we used the cumulative heat extraction rate to represent the heat absorbed by water from the model. The cumulative heat extraction rate can be calculated as follows:

$$Q_{sum} = \sum(H_{outlet,t} - H_{inlet,t})M. \tag{17}$$

Figure 14 presents the cumulative heat extraction rate Q_{sum} (W) under different operating conditions. The cumulative heat extraction rate is maximized at $\alpha = 90°$, followed by $\alpha = 0°$, $\alpha = 30°$, and $\alpha = 60°$. Within the local range, increasing the roughness of the fracture does not necessarily enhance its heat transfer capacity. This is inconsistent with the results of other studies because other researchers use two-dimensional models [22,45]. Moreover, although the cumulative heat extraction increases with the injection flow rate under the same model [24,43], the increasing rate (ΔQ_{sum}, see Figure 14a) will gradually decrease. Thus, blindly increasing the injection flow rate during EGS operation may be detrimental to heat recovery. At the same flow rate level, an increase of the initial temperature from 70 to 90 °C will enhance the cumulative heat extraction rate by approximately 45%. Figure 15 demonstrates the variation of heat extraction rate with time, indicating that a larger initial flow rate at the initial stage of the heat transfer will improve the heat extraction capacity. The heat loss on the fracture wall caused by high convection heat exchange caused by high flow rate is much greater than that supplied by the matrix by heat conduction, which causes a sharp decrease in heat extraction rate. The higher the flow rate, the faster the descent rate.
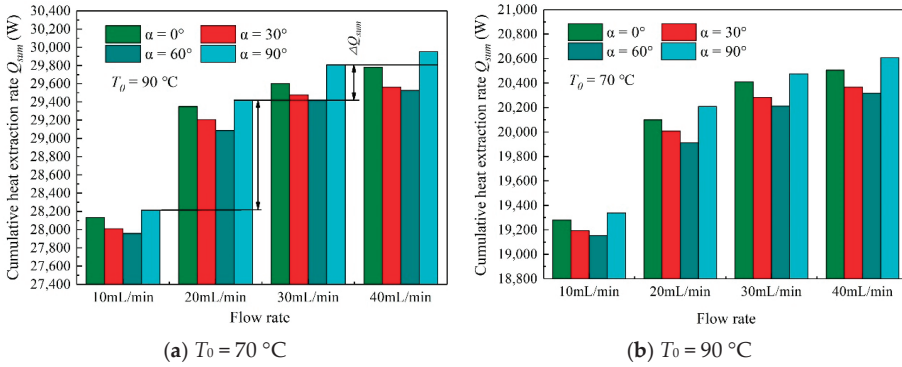
Figure 14. Histogram of cumulative heat extraction rate determined for 30 min.
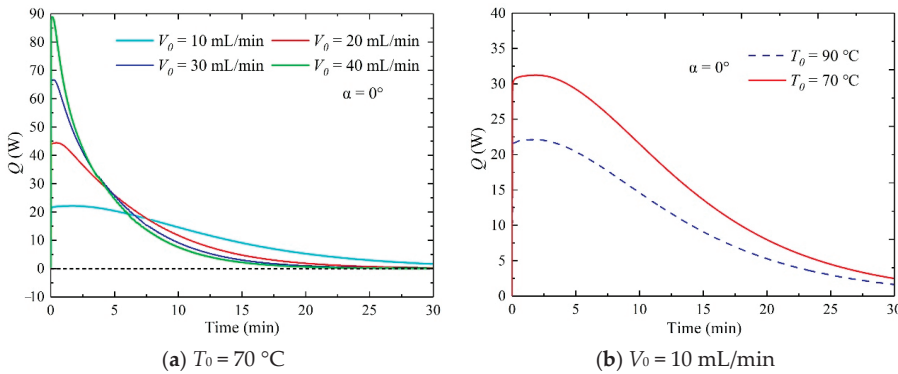
Figure 15. Variation of heat extraction rate with time at several initial flow rates and initial temperatures.

5.3. Total Heat Transfer Coefficient

Figure 16 shows the variation of the total convective heat transfer coefficient with time. The total heat transfer coefficient curve can be divided into increasing and decreasing stages. During the increasing stage, the low temperature water injection causes severe convection heat exchange on the fracture wall, which can prevent cold water from penetrating the whole fracture. Therefore, the total heat transfer coefficient increases rapidly with the injection of fluid until it reaches its peak value. At the decreasing stage, the low temperature water enters the fractures continuously and the heating effect of the rock matrix begins to weaken with the decrease of temperature. In addition, the fluid and fracture wall temperatures further decrease, and the low temperature water begins to penetrate the fractures. Although increasing the initial flow rate and temperature can amplify the total heat transfer coefficient, increasing the flow rate will shorten the time required by the total heat transfer coefficient to reach its peak value. This is obviously not conducive to the sustainability of heat recovery. Figure 16 shows that the total heat transfer coefficient in descending order is $\alpha = 90°$, $\alpha = 0°$, $\alpha = 30°$, and $\alpha = 60°$.
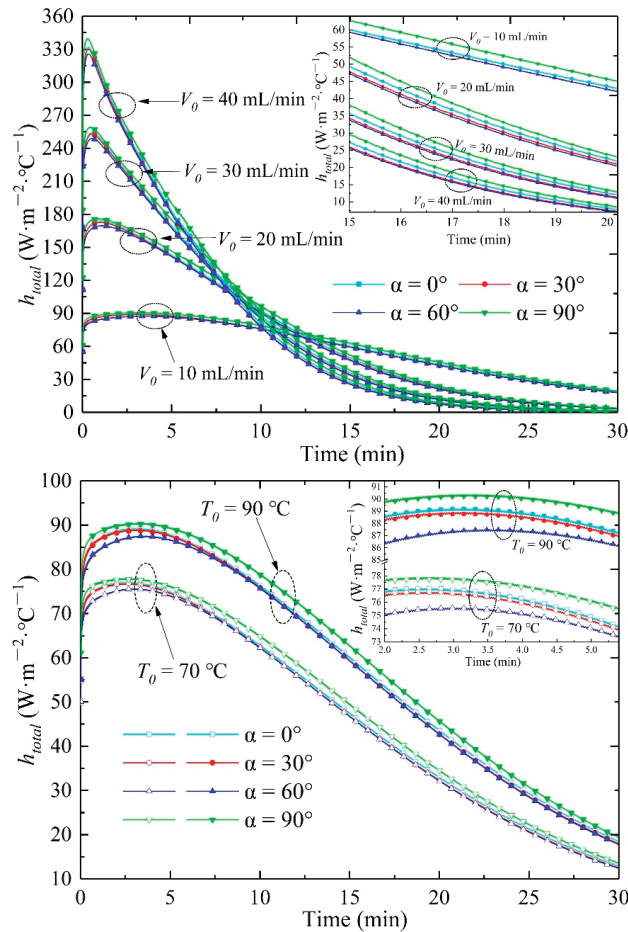
Figure 16. Variations in the total heat transfer coefficient with time for various initial conditions. Top: $T_0 = 90\ °C$. Below: $V_0 = 10\ mL/min$.

5.4. Local Heat Transfer Coefficient

Figure 17 depicts the local heat transfer coefficients of the rock fracture surfaces. The local convection heat transfer coefficient is observed to gradually decrease along the outlet direction, which is consistent with the previous study [22,42]. This is attributed to the gradual decrease in the temperature difference between the fluid and fracture wall along the outlet direction. The fracture model shows that the fracture roughness of $\alpha = 30°$ and $\alpha = 60°$ are different in the three axes, while that of $\alpha = 0°$ and $\alpha = 90°$ are different in the two axes. The flow direction on the fractured surface is slightly deflection, and consequently the local convection heat transfer coefficient in the negative direction of the x-axis exceeds that of the positive direction (Figures 11 and 12). In addition, the distribution of the local heat transfer coefficient is strongly correlated with the rough fracture profile [45]. Figure 18 shows the distribution of the local heat transfer coefficients on the fracture profile at $x = 0\ m$. Figure 18 shows that the model of fracture roughness from large to small at $x = 0\ m$ is $\alpha = 0°$, $\alpha = 30°$, $\alpha = 60°$, and $\alpha = 90°$. The fluctuation of local convection heat transfer coefficient increases with the increase of fracture roughness. At $\alpha = 90°$, the local heat transfer coefficients exhibit a logarithmic distribution in the smooth section along the z-axis. Similar to the fracture profile, the distribution curve of the local heat transfer

coefficient is characterized by peaks and troughs. The local heat transfer coefficient curves at $\alpha = 0°$, $\alpha = 30°$, and $\alpha = 60°$ reveal that the local heat transfer coefficient at the peaks of the fracture profile is consistently greater than that at the troughs. Moreover, increasing the injection flow rate not only improves the local heat transfer coefficient, but also has an enhancing effect that makes the difference between the peaks and troughs of the local heat transfer coefficient more evident. The enhanced effect can be observed via the increased slope of the local heat transfer coefficient curve. Figure 19 shows the enhancement effect of increasing the flow rate on the convective heat transfer intensity.
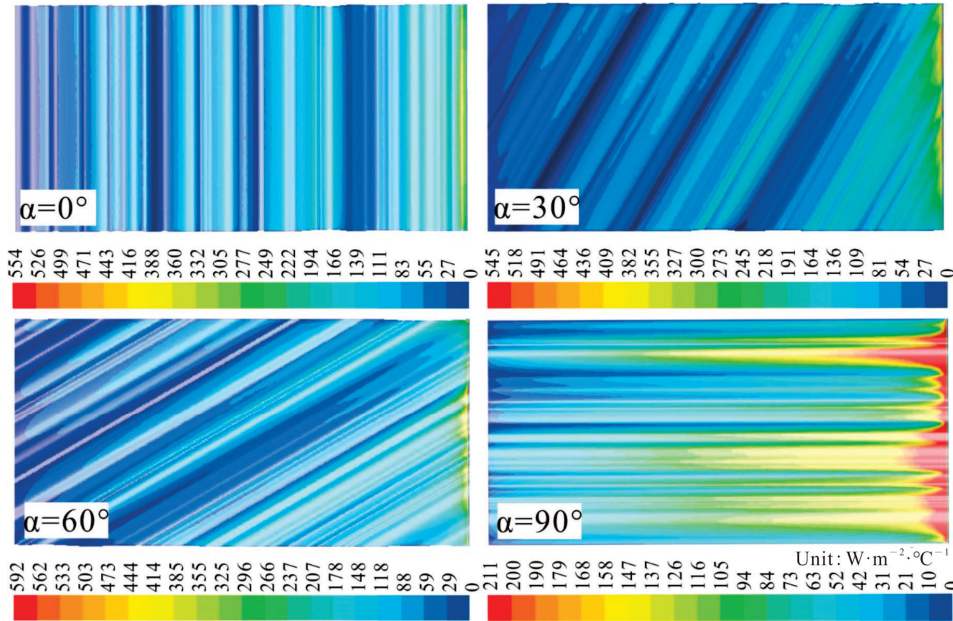
Figure 17. Distribution of local heat transfer coefficients on rock fractures as water flows through the fracture ($V_0 = 10$ mL/min. $T_0 = 90$ °C. $t = 10$ min).
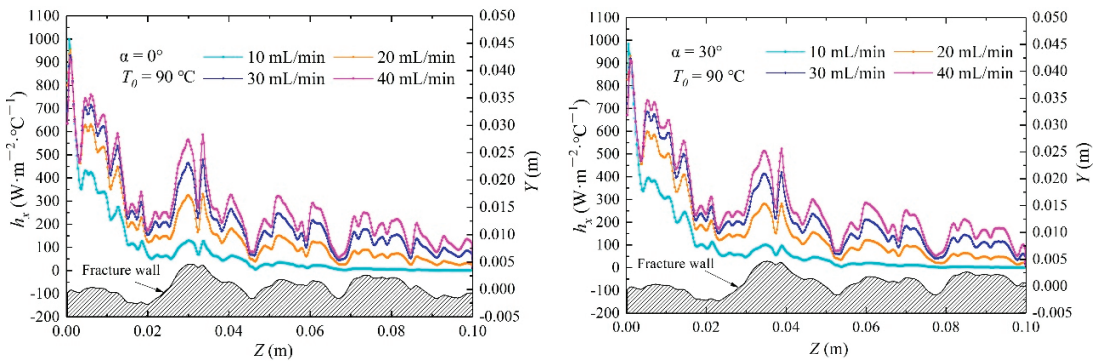
Figure 18. *Cont.*
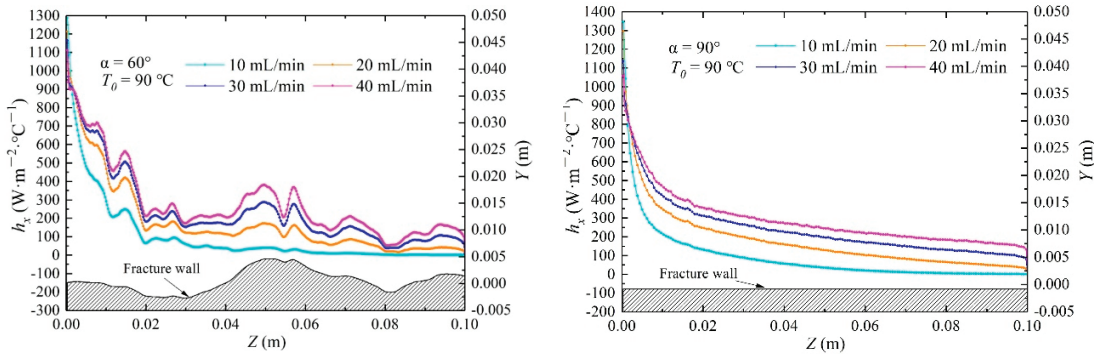
Figure 18. Distribution of local heat transfer coefficients along the outlet direction at different flow rates.
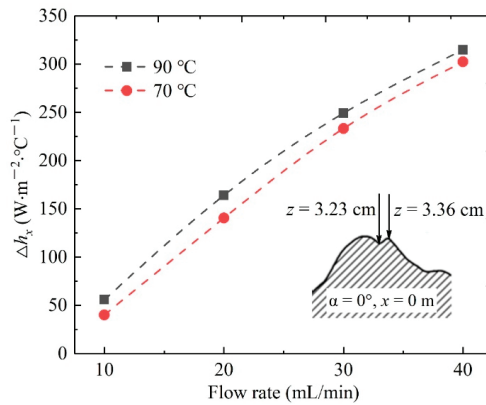
Figure 19. Variation of h_x with the flow rate at adjacent peak and troughs of the fracture profile.

Figure 20 presents the distribution of the local heat transfer coefficient, wall temperature, and average flow rate on the fracture profile at $z = 0.05$ m. The curves of the average flow rate and local heat exchange coefficient become increasingly complex as α increases from $0°$ to $90°$. Since the fracture model is constructed by translating along the y-axis, the distribution of fracture aperture in each direction of the model is not uniform. Therefore, a position with a higher absolute gradient results in a smaller fracture aperture, which results in a low flow rate as the water flows through the path of the small aperture. In contrast, fractures with larger aperture will form a dominant channel where the flow rate is greater. Compared with the temperature, the difference of flow rates at fractures with different apertures is the main factor causing uneven distribution of local heat transfer coefficient. In addition, a strong positive correlation is observed between the local heat exchange coefficient and the flow rate distribution, which indicates that the flow rate is the main factor affecting the heat transfer intensity.
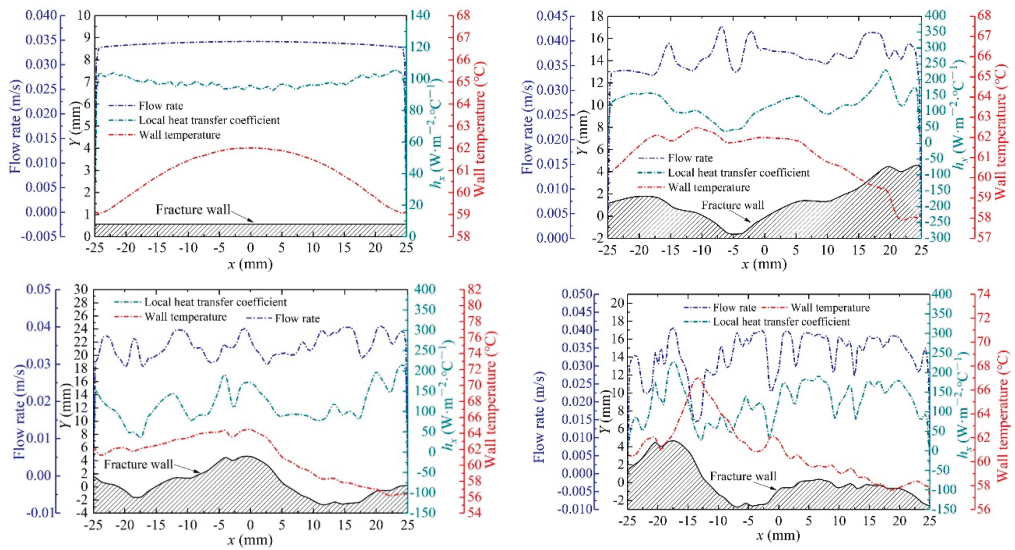
Figure 20. Local heat transfer coefficient, wall temperature, and average velocity distributed along the *x*-direction at $z = 0.05$ m ($V_0 = 20$ mL/min, $T_0 = 90$ °C).

5.5. Limitations of the Present Study

The rough fracture surface used in this study is actually a pseudo-3D fracture surface that ignores the anisotropy of roughness to a certain extent. Therefore, models for this study are not common in actual natural environments. Moreover, the scale of the fracture model may weaken the impact of the proposed flow direction deflection on the heat transfer effect. The heat transfer characteristics of inhomogeneous three-dimensional rough fractures need to be further studied. However, the focus of this work is to study how different angles between flow direction and fracture profile affect the heat transfer process in fractures. In fact, a certain size fracture surface is composed of a limited number of microfractures with occurrence, which have different angles with the flow direction of fluid. From this point of view, this work can actually provide basic knowledge for EGS research.

6. Conclusions

In this study, a hydro-thermal coupling model was developed to investigate the influence of fluid flow direction on the heat transfer characteristics of fractures. The accuracy of the proposed numerical model was verified by laminar convection heat transfer tests of smooth-plate fractured rock samples. A detailed analysis of the temperature field distribution, total heat transfer coefficient, and local heat transfer coefficient of the model were provided based on the numerical simulations. The main conclusions are as follows:

(1) At $\alpha = 30°$ and $\alpha = 60°$, the temperature of the fracture surface in the negative direction of the *x*-axis is higher than that in the positive direction. This is because the flow direction of the fluid is not parallel to the orientation of the microfracture surface that prevents the fluid from flowing forward, resulting in fluid deflection.

(2) When the initial temperature is raised from 70 to 90 °C, the cumulative heat extraction rate Q_{sum} increases the yield by 45%. Although the cumulative heat extraction increases with the injection flow rate, the rate of increase gradually decreases. An increase in the injection flow rate from 10 to 40 mL/min enhances the peak heat extraction rate. However, the increase in flow rate speeds up the rate of reduction of the heat extraction rate.

(3) Variations in the total heat transfer coefficient with time can be divided into increasing and decreasing stages. The total heat transfer coefficients decrease with α. This

indicates that the presence of rough fractured surfaces in the forward direction of the fluid does not necessarily increase the convection heat transfer intensity between the fluid and the fractured surfaces. Increasing the flow rate and temperature can enhance the total heat transfer coefficient. However, a higher flow rate will shorten the time required by the total heat transfer coefficient to reach its peak value, while also increasing the rate of reduction of the total heat transfer coefficient in the decreasing stage.

(4) The local heat transfer coefficient gradually decreases along the direction of the water flow, which is consistent with the conclusions drawn by Bai [46]. An increasing flow rate not only increases the local heat transfer coefficient, but also has an enhancing effect that highlights the influence of the fracture profile on the local heat transfer coefficient distribution.

(5) There is a consistently strong correlation between the local heat transfer coefficient and the fracture profile, independent of the axis. In particular, although a change in the angle between the flow direction and the fracture profile can affect the local heat transfer coefficient, it does not affect the distribution characteristics of the local heat transfer coefficient.

Author Contributions: Conceptualization, writing—original draft preparation, X.G.; supervision and review, Y.Z.; formal analysis, data curation, Z.H.; software, Y.H. All authors have read and agreed to the published version of the manuscript.

Institutional Review Board Statement: Not applicable.

Informed Consent Statement: Not applicable.

Data Availability Statement: The data used to support the findings of this study are available from the first author or the corresponding author upon request.

Conflicts of Interest: The authors declare no conflict of interest.

References

1. Fridleifsson, I.B. Geothermal energy for the benefit of the people. *Renew. Sustain. Energy Rev.* **2001**, *5*, 299–312. [CrossRef]
2. Mahbaz, S.B.; Dehghani-Sanij, A.R.; Dusseault, M.B.; Nathwani, J.S. Enhanced and integrated geothermal systems for sustainable development of Canada's northern communities. *Sustain. Energy Technol. Assess.* **2020**, *37*, 100565. [CrossRef]
3. Kinney, C.; Dehghani-Sanij, A.; Mahbaz, S.; Dusseault, M.B.; Nathwani, J.S.; Fraser, R.A. Geothermal Energy for Sustainable Food Production in Canada's Remote Northern Communities. *Energies* **2019**, *12*, 4058. [CrossRef]
4. Pettitt, R.A.; Becker, N.M. Mining Earth's Heat: Development of Hot Dry Rock Geothermal Reservoirs. *Geotherm. Energy* **1983**, 11.
5. Olasolo, P.; Juárez, M.C.; Morales, M.P.; D´Amico, S.; Liarte, I.A. Enhanced geothermal systems (EGS): A review. *Renew. Sustain. Energy Rev.* **2016**, *56*, 133–144. [CrossRef]
6. Kazemi, A.R.; Mahbaz, S.B.; Dehghani-Sanij, A.R.; Dusseault, M.B.; Fraser, R. Performance Evaluation of an Enhanced Geothermal System in the Western Canada Sedimentary Basin. *Renew. Sustain. Energy Rev.* **2019**, *113*, 109278. [CrossRef]
7. Kolditz, O. Modeling flow and heat-transfer in fractured rocks - conceptual-model of a 3-d deterministic fracture network. *Geothermics* **1995**, *24*, 451–470. [CrossRef]
8. Jiang, F.; Chen, J.; Huang, W.; Luo, L. A three-dimensional transient model for EGS subsurface thermo-hydraulic process. *Energy* **2014**, *72*, 300–310. [CrossRef]
9. Shaik, A.R.; Rahman, S.S.; Tran, N.H.; Tran, T. Numerical simulation of Fluid-Rock coupling heat transfer in naturally fractured geothermal system. *Appl. Therm. Eng.* **2011**, *31*, 1600–1606. [CrossRef]
10. Patton, F. Multiple modes of shear failure in rock. *Proceeding Congress Int. Soc.* **1966**, *1*, 509–513.
11. Mandelbrot, B.B.; Wheeler, J.A. The Fractal Geometry of Nature. *Am. J. Phys.* **1983**, *51*, 286–287. [CrossRef]
12. Barton, N. Review of a new shear-strength criterion for rock joints. *Eng. Geol.* **1973**, *7*, 287–332. [CrossRef]
13. Xie, H.; Pariseau, W.G. Fractal estimation of joint roughness coefficients. *Int. J. Rock Mech. Min. Sci. Geomech. Abstr.* **1995**, *32*, 266A. [CrossRef]
14. Ogino, F.; Yamamura, M.; Fukuda, T. Heat transfer from hot dry rock to waterflowingthrough a circular fracture. *Geothermics* **1999**, *28*, 21–44. [CrossRef]
15. Tsang, Y.W. The Effect of Tortuosity on Fluid Flow Through a Single Fracture. *Water Resour. Res.* **1984**, *20*, 1209–1215. [CrossRef]

16. Brown, S. Fluid-flow through rock joints - the effect of surface-roughness. *J. Geophys. Res. Solid Earth Planets* **1987**, *92*, 1337–1347. [CrossRef]

17. Zhao, J.; Tso, C.P. Heat-transfer by water-flow in rock fractures and the application to hot dry rock geothermal systems. *Int. J. Rock Mech. Min. Sci. Geomech. Abstr.* **1993**, *30*, 633–641. [CrossRef]

18. He, Y.; Bai, B.; Li, X. Comparative Investigation on the Heat Transfer Characteristics of Gaseous CO2 and Gaseous Water Flowing Through a Single Granite Fracture. *Int. J. Thermophys.* **2017**, *38*, 170. [CrossRef]

19. Neuville, A.; Toussaint, R.; Schmittbuhl, J. Hydrothermal coupling in a self-affine rough fracture. *Phys. Rev. E* **2010**, *82*, 036317. [CrossRef]

20. Huang, X.; Zhu, J.; Li, J.; Bai, B.; Zhang, G. Fluid friction and heat transfer through a single rough fracture in granitic rock under confining pressure. *Int. Commun. Heat Mass Transf.* **2016**, *75*, 78–85. [CrossRef]

21. Luo, J.; Zhu, Y.; Guo, Q.; Tan, L.; Zhuang, Y.; Liu, M.; Zhang, C.; Xiang, W.; Rohn, J. Experimental investigation of the hydraulic and heat-transfer properties of artificially fractured granite. *Sci. Rep.* **2017**, *7*, 39882. [CrossRef]

22. He, R.; Rong, G.; Tan, J.; Cheng, L. Numerical investigation of fracture morphology effect on heat transfer characteristics of water flow through a single fracture. *Geothermics* **2019**, *82*, 51–62. [CrossRef]

23. Shu, B.; Zhu, R.; Elsworth, D.; Dick, J.; Liu, S.; Tan, J.; Zhang, S. Effect of temperature and confining pressure on the evolution of hydraulic and heat transfer properties of geothermal fracture in granite. *Appl. Energy* **2020**, *272*, 115290. [CrossRef]

24. Zhang, X.; Wang, Z.; Sun, Y.; Zhu, C.; Xiong, F.; Tang, Q. Numerical Simulation on Heat Transfer Characteristics of Water Flowing through the Fracture of High-Temperature Rock. *Geofluids* **2020**, *2020*, 1–14. [CrossRef]

25. Andrade, J.S., Jr.; Henrique, E.A.A.; Almeida, M.P.; Costa, M.H.A.S. Heat transport through rough channels. *Physica. Sect. A* **2004**, *339*, 296–310. [CrossRef]

26. Zhang, L.; Jiang, P.; Wang, Z.; Xu, R. Convective heat transfer of supercritical CO2 in a rock fracture for enhanced geothermal systems. *Appl. Therm. Eng.* **2017**, *115*, 923–936. [CrossRef]

27. Fox, D.B.; Koch, D.L.; Tester, J.W. The effect of spatial aperture variations on the thermal performance of discretely fractured geothermal reservoirs. *Geotherm. Energy* **2015**, *3*, 21. [CrossRef]

28. Luo, S.; Zhao, Z.; Peng, H.; Pu, H. The role of fracture surface roughness in macroscopic fluid flow and heat transfer in fractured rocks. *Int. J. Rock Mech. Min. Sci.* **2016**, *87*, 29–38. [CrossRef]

29. Li, Z.-W.; Feng, X.-T.; Zhang, Y.-J.; Xu, T.-F. Feasibility study of developing a geothermal heating system in naturally fractured formations: Reservoir hydraulic properties determination and heat production forecast. *Geothermics* **2018**, *73*, 1–15. [CrossRef]

30. Elmouttie, M.K.; Poropat, G.V. A Method to Estimate In Situ Block Size Distribution. *Rock Mech. Rock Eng.* **2011**, *45*, 401–407. [CrossRef]

31. Leung, C.T.O.; Zimmerman, R.W. Estimating the Hydraulic Conductivity of Two-Dimensional Fracture Networks Using Network Geometric Properties. *Transp. Porous Media* **2012**, *93*, 777–797. [CrossRef]

32. Bruel, D. Heat extraction modeling from forced fluid-flow through stimulated fractured rock masses - application to the rosemanowes hot dry rock reservoir. *Geothermics* **1995**, *24*, 361–374. [CrossRef]

33. Chen, Y.; Ma, G.; Wang, H. Heat extraction mechanism in a geothermal reservoir with rough-walled fracture networks. *Int. J. Heat Mass Transf.* **2018**, *126*, 1083–1093. [CrossRef]

34. Li, J.; Sun, Z.; Zhang, Y.; Jiang, C.; Cherubini, C.; Scheuermann, A.; Torres, S.A.G.; Li, L. Investigations of heat extraction for water and CO2 flow based on the rough-walled discrete fracture network. *Energy* **2019**, *189*. [CrossRef]

35. Li, Z.-W.; Feng, X.-T.; Zhang, Y.-J.; Zhang, C.; Xu, T.-F.; Wang, Y.-S. Experimental research on the convection heat transfer characteristics of distilled water in manmade smooth and rough rock fractures. *Energy* **2017**, *133*, 206–218. [CrossRef]

36. Huang, Y.; Zhang, Y.; Yu, Z.; Ma, Y.; Zhang, C. Experimental investigation of seepage and heat transfer in rough fractures for enhanced geothermal systems. *Renew. Energy* **2019**, *135*, 846–855. [CrossRef]

37. He, Y.; Bai, B.; Cui, Y.; Lei, H.; Li, X. 3D Numerical Modeling of Water–Rock Coupling Heat Transfer Within a Single Fracture. *Int. J. Thermophys.* **2020**, *41*, 1–22. [CrossRef]

38. Shu, B.; Zhu, R.; Tan, J.; Zhang, S.; Liang, M. Evolution of permeability in a single granite fracture at high temperature. *Fuel* **2019**, *242*, 12–22. [CrossRef]

39. Bai, B.; He, Y.; Li, X. Numerical study on the heat transfer characteristics between supercritical carbon dioxide and granite fracture wall. *Geothermics* **2018**, *75*, 40–47. [CrossRef]

40. Fluent Inc. *FLUENT 6.3 User's Guide*; Fluent Inc.: Lebanon, NH, USA, 2007.

41. Qu, Z.-Q.; Zhang, W.; Guo, T.-K. Influence of different fracture morphology on heat mining performance of enhanced geothermal systems based on COMSOL. *Int. J. Hydrogen Energy* **2017**, *42*, 18263–18278. [CrossRef]

42. Ma, Y.; Zhang, Y.; Yu, Z.; Huang, Y.; Zhang, C. Heat transfer by water flowing through rough fractures and distribution of local heat transfer coefficient along the flow direction. *Int. J. Heat Mass Transf.* **2018**, *119*, 139–147. [CrossRef]

43. Chen, Y.; Zhao, Z. Heat transfer in a 3D rough rock fracture with heterogeneous apertures. *Int. J. Rock Mech. Min. Sci.* **2020**, *134*. [CrossRef]

44. Tan, J.; Rong, G.; He, R.; Yang, J.; Peng, J. Numerical investigation of heat transfer effect on flow behavior in a single fracture. *Arab. J. Geosci.* **2020**, *13*, 1–16. [CrossRef]

45. He, Y.; Bai, B.; Hu, S.; Li, X. Effects of surface roughness on the heat transfer characteristics of water flow through a single granite fracture. *Comput. Geotech.* **2016**, *80*, 312–321. [CrossRef]
46. Bai, B.; He, Y.; Hu, S.; Li, X. An Analytical Method for Determining the Convection Heat Transfer Coefficient Between Flowing Fluid and Rock Fracture Walls. *Rock Mech. Rock Eng.* **2017**, *50*, 1787–1799. [CrossRef]

Article

Well-Doublets: A First-Order Assessment of Geothermal SedHeat Systems

SeyedBijan Mahbaz [1,2], Ali Yaghoubi [1], Alireza Dehghani-Sanij [2,*], Erfan Sarvaramini [3], Yuri Leonenko [1,2,4] and Maurice B. Dusseault [1,2]

[1] Department of Earth and Environmental Sciences, University of Waterloo, Waterloo, ON N2L 3G1, Canada; smahbaz@uwaterloo.ca (S.B.M.); ali.yaghoubi@uwaterloo.ca (A.Y.); leonenko@uwaterloo.ca (Y.L.); mauriced@uwaterloo.ca (M.B.D.)

[2] Waterloo Institute for Sustainable Energy (WISE), University of Waterloo, Waterloo, ON N2L 3G1, Canada

[3] GLJ Ltd., Calgary, AB T2P 3C5, Canada; ESarvaramini@gljpc.com

[4] Department of Geography and Environmental Management, University of Waterloo, Waterloo, ON N2L 3G1, Canada

* Correspondence: a7dehgha@uwaterloo.ca; Tel.: +1-416-522-8809

Abstract: Renewable and sustainable energy sources can play an important role in meeting the world's energy needs and also in addressing environmental challenges such as global warming and climate change. Geothermal well-doublet systems can produce both electrical and thermal energy through extracting heat from hot-water aquifers. In this paper, we examine some potential challenges associated with the operation of well-doublet systems, including heat conductivity, chemical, and mechanical issues. In these systems, geomechanics issues such as thermal short-circuiting and induced seismicity arise from temperature and pressure change impacts on the stress state in stiff rocks and fluid flow in fractured rock masses. Coupled chemical processes also can cause fluid channeling or formation and tubular goods plugging (scaling) with precipitates. Mechanical and chemical disequilibrium conditions lead to increased production uncertainties; hence risk, and therefore coupled geo-risk assessments and optimization analyses are needed for comparative commercialization evaluations among different sites. The challenges related to heat transfer processes are also examined. These studies can help better understand the issues that may arise during the operation of geothermal well-doublet systems and improve their effectiveness, subsequently reducing associated costs and risks.

Keywords: geothermal; well-doublet system; sustainability; disequilibrium; thermomechanical effects; chemical coupling; climate change

1. Introduction

Energy is an essential and unavoidable need in today's world and has played a crucial role in human civilization [1–3]; demand is increasing, with the principal reasons being the world's growing population and the general desire for an improved life quality [4–7]. Fossil fuels comprise over 80% of primary energy sources [8,9], but effects arising from greenhouse gas (GHG) emissions and air pollution, leading to environmental degradation, global warming, and climate change, are of increasing concern [10–13]. Geothermal energy, a sustainable and green source, is now meeting some communities' thermal and electrical energy requirements [10,11,14]; it can be reliable in the long term, is environmentally friendly [7,15], and could help reduce fossil fuel consumption [8,9].

1.1. Geothermal Energy Characteristics

Geothermal energy can be categorized as volcanic, sedimentary, geo-pressured, hot dry rock (HDR) or enhanced (engineered) geothermal (EG), or shallow [7,16]. It should be noted that shallow geothermal energy can be defined in terms of shallow geothermal systems

69

based on ground-source heat pumps that are installed at depths less than 500 m [17]. Geothermal resources can also be divided into three groups based on reservoir fluid temperatures [18]: low, medium, and high enthalpy resources. Their common point is accessing natural underground heat sources, whether from dry steam reservoirs (electrical power) to the normal warmth of deeply buried rocks and their interstitial fluids (district heating). Although such energy is often classified as renewable because of the continuous heat flux in the Earth's crust, realistically, the heat renewal rate ($\approx$100–1000 years) is far slower than the design life-span of a commercial project (25–40 years) unless strong hot fluid recharge is occurring. The extraction system and energy rate must be compatible with project life needs [19], and in most cases, from an engineering project life-span definition, geothermal energy is not renewable. In other words, the life-span of any commercial geothermal project is strongly dependent on the geological characteristics of the resources and the appropriate sizing of the power/heat plant.

Once a spatially limited volume of the reservoir has been "heat mined," the heat recharge rate from crustal thermal conduction is too slow to sustain commercial use unless an external heat source is being used to "recharge" the reservoir heat content. However, heat is everywhere available at depth, so the project design basis should include continued access to previously unmined heat (i.e., drilling more wells on an ongoing basis or recharging the repository heat).

Economically, the amount of energy available and the rate of energy production are essential criteria for project performance. Although initial reservoir temperature (T_o) is the dominant variable, which defines the energy content, the amount of energy production is also related to the reservoir pressure—P (natural or maintained if fluid injection is being exploited). Overall, a higher temperature and pressure reservoir is better [8], but there are a variety of other variables such as reservoir volume, permeability, porosity, storativity, and natural recharge rate (if any) that are important to the commercially viable project duration. Site assessment factors include reservoir geometry (depth, thickness, and lateral extent), flow characteristics (permeability heterogeneity, fracture vs. porous media flow, channels, etc.), the potential for natural recharge, the tectonic state and stress field, and structural geology factors [20].

Whether a reservoir is open or closed to natural high-temperature fluid influx impacts life-span assessment: in a closed system with a constant production and no injection, reservoir pressure decreases continuously, requiring aggressive pumping or leading to a rapid loss of water production, although the rock mass may remain at high temperature. These systems may be considered for re-injection operations, as a closed sedimentary geothermal formation can be developed with a well-doublet (or multi-well) system. In contrast, an open system has a more stable pressure but may require flow rate management and assessment of the recharge rate and energy content (production temperature T_{in}) to assure commercial viability [19]. An open system with an "infinite" flow capacity can be exploited with single pumped production wells, but the geothermal fluids have to be disposed of in the subsurface into suitable (likely shallower) saline aquifers.

In the current paper, we use the increasingly common term "SedHeat" (sedimentary heat) for systems where warm and hot fluids are being exploited from sedimentary rocks of sufficient permeability and porosity at depth [21,22], in contrast to steam systems (wet or dry), or to geothermal heat found in low-permeability rock masses (granites, shales, tight volcanic or metamorphic rocks, etc. [23,24]).

1.2. The Geothermal Doublet

The well-doublet design (Figure 1) is the simplest approach to energy extraction in a closed or limited recharge SedHeat system, whether it is a deep liquid reservoir or a shallow ground-source heat pump system using an unconfined aquifer. From one well equipped with a lifting pump, the SedHeat aquifer supplies hot-water from which energy is extracted by a heat exchanger to be sent for power generation or direct heat use. Cooled geofluid re-injection takes place into another well placed at an optimum distance designed

to meet the project's desired power profile (power = electrical and heat energy rate) [25] and sustain flow. The maximum energy rate (work or power) available, ignoring all of the minor hydraulic losses (pumps, fitting, etc.) and irrecoverable heat losses, is

$$\dot{E} = \Delta T \cdot \dot{Q} \cdot c_p \tag{1}$$

where $\dot{E}$ is the energy rate (power) in J/s, $\Delta T = (T_{in} - T_{out})$ in K, $\dot{Q}$ is the flow rate in kg/s, and c_p is the fluid heat capacity in J/kg·K. T_{in} and T_{out} (units of K) refer to the inlet and exit temperatures in the energy (electricity + heat) extraction system, likely a heat exchanger. The fluid involved may be the natural fluids in the case of SedHeat development, or in the case of EG systems, it is likely to be an introduced fluid such as water or supercritical CO_2 [26].
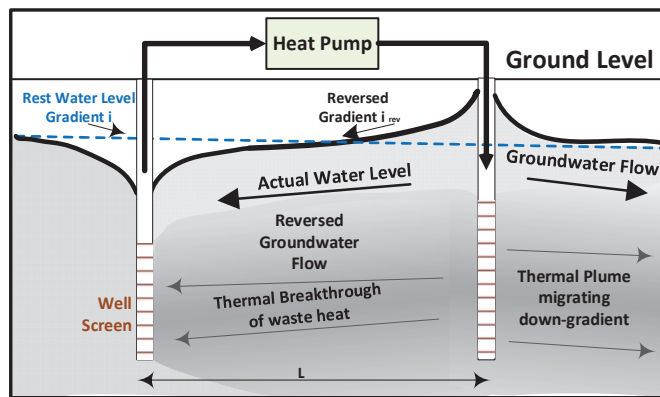
Figure 1. Schematic illustration of a typical shallow geothermal well-doublet system with a single primary loop, no heat exchanger, in an unconfined aquifer (modified from [27]).

Specifically, T_{in} is not the original reservoir T_o; it is the temperature at the surface going into the energy system (the heat exchanger between the primary loop and the secondary power/heat system loop). It will eventually change with time as cool injected fluids begin to impinge upon the production well. Nor is T_{out} equal to the ambient temperature; T_{out} will always be higher because of thermodynamic constraints. Unextracted heat in the primary loop fluid is returned to the reservoir through fluid re-injection; if there are low-grade waste heat sources to increase T_{out} through a downstream heat exchanger, the project life may be extended, and the low-grade heat exploited. The parameter $\dot{Q}$ is mainly a function of the aquifer's permeability, thickness, and layering, the amount of energy desired or achievable, the aquifer's thermal properties and heat recovery time [8], and several secondary factors. A reasonable value for c_p is 4180 J/kg·K for pure freshwater, somewhat different for geofluids of different salinities. For fluids such as supercritical CO_2, different specific heats, fluid densities, and viscosities must be used, and these may be quite sensitive to P and T, leading to additional non-linear effects in modeling heat extraction.

Using a recirculating well-doublet in a binary geothermal system means that remnant useable heat in the geofluid (e.g., 50–70 °C) is reinjected after electrical power generation, but if space heating is needed, additional heat can be stripped from the fluids, lowering re-injection T. Furthermore, coupling a deep doublet with a shallow ground-source heat pump system allows shallow seasonal heat storage and recovery (a thermal repository) and leads to higher efficiency and lower fossil-fuel use where there is a cooling deficiency in the summer [28], as in northern climates. Using a deep multi-well system allows injection/production strategies to be devised to maximize the system's value, while also exploiting the shallow heat repository in the winter when high heat demand exists. The

design of such a system depends on the estimated power/thermal energy profiles for the year, combined with a safety factor, and noting that design in Canada (for example) must be to meet November–March energy needs.

If natural or planned thermal recharge is rapid enough, considering the recovery time of the system and the injection/production strategy, a geothermal SedHeat system might approach being a renewable and sustainable energy source [25]. In other words, the deep system life-span can be extended by designing for slow energy extraction relative to the system volume, re-injection of unused heat, extracting value from sources of waste heat, and even using seasonal solar and excess wind power to recharge the thermal repository. It is possible to prolong the system's energy provision profile by keeping heat extraction at a sustainable level or by designing it initially so that the combined electrical power and heat outputs extend the long-term utility of the project. In addition, it may be possible for a SedHeat system to generate power and heat for 20–30 years, but in the later life stages when the T_{in} is degraded, and power generation is suffering, the original wells may be operated for heat production, but new sources developed for power generation. In this scenario, given that the capital investment has been recovered, the initial wellbore system can be economically continued for heat provision only. Geothermal energy developed in this way is inherently sustainable because of the huge masses of warm rock in the crust and within reasonable drilling depth. SedHeat is, of course, limited to sedimentary basins, but other technologies are being explored for low permeability rock masses such as crystalline rocks.

1.3. Disequilibrium Processes

Leaving aside initial geological conditions, the causes of disequilibrium that result in an inadequate or a drop in Ė are based on mechanical, geochemical, and heat conductivity conditions and issues, ranging from processes within the reservoir itself (flow, mineral precipitation, channelling, etc.) to the access and energy systems (wells, pumps, heat exchangers, surface tubing insulation, etc.).

1. Chemical condition:
    a. Well integrity
        i. Induced primary loop corrosion (e.g., acidic waters corroding steel), both internal and external to the well casing, potentially exacerbated by high temperatures and electrochemical corrosion
        ii. Primary loop internal mineral precipitation—scaling (increasing pipe friction losses)
    b. Reservoir condition
        i. Mineral and rock dissolution (e.g., dissolving of gypsum) or other alteration (e.g., induced clay mineral swelling from changing geochemistry).
        ii. Microbiologically induced pore blockage or corrosion through the generation of biofilms or weak organic acids that act on minerals (mainly carbonates)
        iii. Chemical changes and processes induced by flow, ΔT, and ΔP, leading to solubility gradients that trigger dissolution and precipitation
        iv. Flushing of pipe corrosion and precipitated mineral particles into the reservoir, generating blockage of flow paths
2. Mechanical condition:
    a. Rock mechanics issues: stress-strain (σ–ε) processes and their effects on porosity and permeability, particularly in systems dominated by fracture flow and susceptible to thermoelastic impacts
    b. The transition from laminar to turbulent flow regime near the well at high flow rates (short-term impacts on production and injection phases)
3. Heat conductivity and recovery condition:

   a.   Pumping rates with respect to produced fluid temperature changes and well field life-span
   b.   Alterations of efficiency associated with thermal viscosity changes
   c.   Interference with the natural thermal recharge system in the deep aquifer
   d.   Channeling of flow, fracture dilation through cooling leading to flow short-circuiting, and related thermoelastic effects that lead to reductions in the sub-surface heat exchange area

The long-term result of disequilibrium processes in the reservoir may be evidenced as pore throat blockage and fracture aperture reduction, leading to reservoir fluid conductivity changes, including permeability reduction, channeling of flow, and related processes. If these changes are properly understood and predicted, project planning becomes easier, allowing answers to questions related to the drilling of new wells, workover scheduling for impaired wells, adding more injection or production wells, developing a new productive horizon (deeper or shallower), changing the electricity/heat output ratio, and so on.

To optimize energy production, increase the project life-time, enhance the fiscal outcomes and minimize environmental impacts, many issues associated with heat extraction from a geothermal well-doublet system need to be considered; these issues are addressed in this study.

2. Chemical Condition

Questions arise as to whether deep geothermal systems can be preserved while retaining their production quality, achieving the desired $\dot{E}$ over the project life. We note that the best outcome is keeping $\dot{E}$ constant, but a project can also be designed on the basis of a gradually declining $\dot{E}$, as long as it can be realistically predicted. Answers depend on water-rock reactions and reservoir condition changes over the project life, as chemical reactions may cause flow-path changes (precipitation in flow paths) and potentially alter the heat transfer efficiency between rock and water. To predict changes in permeability or fracture conductivity, chemical effects need to be investigated for the project's expected life-span [29].

2.1. Well Integrity

Hot (>60 °C) geothermal fluids are often associated with dissolved carbon dioxide (CO_2) and hydrogen sulfide (H_2S), which makes the saline brine slightly acidic, providing an aggressive thermochemistry environment [30], leading to severe internal corrosion of steel goods (casing, pipes, heat exchangers, etc.) through the sulfide reaction pathway, shown in Figure 2. Note that well integrity discussions include physical damage (shear, cracking) as well as applied mitigation measures to control corrosion. Corrosion/scaling damage reduces the system efficiency by changing the heat production capacity (Q) and adding corrosion products to the circulation system, potentially reducing reservoir permeability. Well integrity will be affected, shortening productive life [29] and generating various effects leading to efficiency loss, increased maintenance costs, and surface damage [31]. At a cost, anti-corrosion materials can be added to the system, and the choice of material depends on ΔT, ΔP, and formation water chemistry.

Chemical reaction:

$CO_2 + H_2O \rightarrow H_2CO_3$

$2H_2CO_3 \rightarrow 2H^+ + 2HCO_3^-$

$Fe^{2+} + 2HCO_3^- + 2H^+ \rightarrow 2H^+ + Fe(HCO)_2 \text{ soluble}$

$H_2S + H_2O \rightarrow H^+ + HS^- + H_2O$

$Fe \rightarrow Fe^{2+} + 2e^-$

$Fe^{2+} + HS^- \rightarrow FeS + H^+$
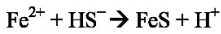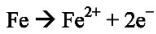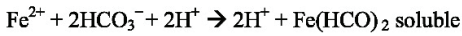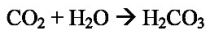
Corrosion induced and native

$2H^+ + 2e^- \rightarrow H_2$

for pH = 6

$H_2S + H_2O + CO_2 + Fe^{2+} \text{ (native)}$
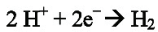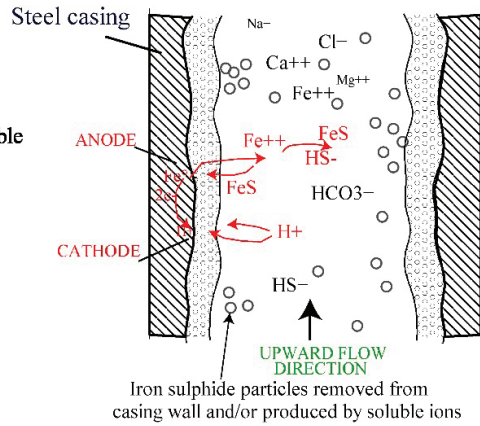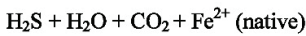
Figure 2. Schematic illustration of the process of iron dissolution and sulfide precipitation in a CO_2/H_2S aqueous system (modified from [29]).

External steel casing corrosion and cement degradation may occur in an accelerated manner if the formation temperature is increased (Figure 3). Existing outside-the-casing groundwater chemistry in the upper geological section will change from chloride-based to sulfate- or bicarbonate-based as the surface is approached in most sedimentary basins. Heating the cemented steel casing system sets up a large electrolytic cell where corrosion is accelerated by the temperature increase from rising hot fluids. External pitting leads to casing perforation and integrity loss.

Figure 3. External steel casing corrosion from acidic water attack [32].

In certain chemical conditions, specifically, the combined presence of archaebacteria, $CaSO_4 \cdot 2H_2O$, and a slow source of CH_4 in a stratum, acidic conditions (H_2S generated) are created and external steel corrosion accelerated by both the $+\Delta T$ and the increasing acidity. We note that the methane may even be traveling up the geothermal production well outside the casing [33].

2.2. Reservoir Condition

Mineral dissolution and precipitation, ΔT and ΔP, and steel goods corrosion are the main issues related to chemical disequilibrium in deep geothermal systems [34]. Geother-

mal fluids have diverse chemical components due to the diversity of geological settings (e.g., silica-rich, carbonate-rich, chloride brines, etc.). The recharging water source and associated dissolved gases also define the chemical characteristics of the geothermal fluid, and these may change with time because of the perturbation caused by production and injection. The precipitation of minerals or induced corrosion/scaling leads to small particles carried in suspension into the porous reservoir, altering the system's porosity and permeability. Bächler and Kohl [35] investigated such changes in a deep geothermal system using coupled Thermal-Hydraulic-Chemical (THC) modeling. The study found that the system's efficiency decreased more rapidly with more mineral dissolution at the start of the project, and it slowed down over a longer time. These results were attributed to the disequilibrium of the system at the start, then changes in the equilibrium condition over time [35]. For production and service life calculations, flow pathway impairment from particles and precipitates is an important disequilibrium effect.

Microbially induced (mediated) corrosion, MIC [36], and fouling affect geothermal energy projects (as well as other industrial activities); designing and implementing protection requires multiple knowledge perspectives—material science and metallurgy, electrochemistry, biochemistry, and microbiology [37]. Salas et al. [38] showed MIC's impact on the deterioration of geothermal power plant structures (e.g., vapor ducts and cooling tower supports), noting bacterial activity at temperatures as high as 140 °C. A MIC problem in the primary surface loop may migrate to the subsurface as corrosion products, and temperature changes impact the reservoir's chemical conditions and change the system's flow properties [39]. Tubular goods may experience general (e.g., steel thinning) or localized corrosion (e.g., pitting) [40]. Uniform corrosion [41], pitting, crevice, and contact (galvanic) corrosion [42–44], microbially mediated corrosion [45], and oxygen corrosion [38] are all common in geothermal systems.

Thermohydrochemical reservoir processes are impacted by stimulation efforts (e.g., hydraulic fracturing with gels, acid injection, etc.), and injection/production leads to ΔT and ΔP, triggering mineral precipitation. Even reservoir rock and fluid heat conductivities can be altered by ΔT and ΔP. Blöcher et al. [46] showed that significant changes occur in the porosity and permeability of a sandstone reservoir when the effective stress (σ) is increased, as shown in Figure 4.

Figure 4. Decrease in measured porosity and permeability of Flechtinger Sandstone geothermal reservoir because of increased effective stress (here called effective pressure) [46].
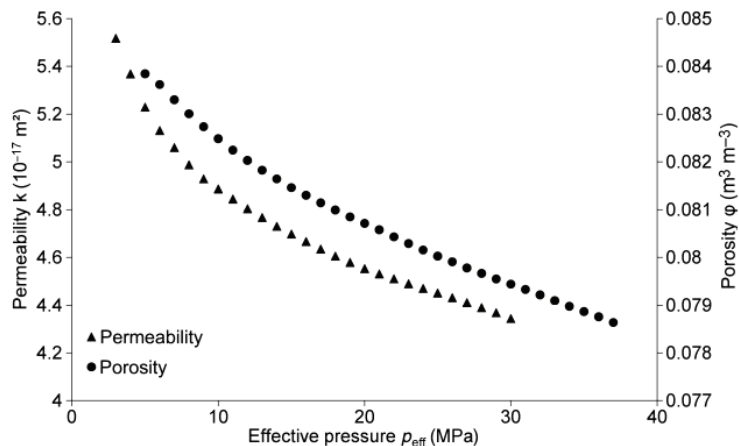
Remedial/preventive methods include cleaning, jetting, and waste removal in well workovers, and soft acidizing during stimulation to remove carbonate precipitates, with remediation processes guided by leak-off and injection step-rate testing and data from

other chemical and physical monitoring methods [47–49]. Note that soft acidizing of geothermal systems is taken to mean injecting the same acid volume as used in conventional oil and gas acid treatments but at a much lower rate [48,50]. Salimzadeh and Nick [51] developed a two-way chemical coupling method to include mineral dissolution in Thermal-Hydraulic-Mechanical (THM) coupling, generating a coupled Thermal-Hydraulic-Mechanical-Chemical (THMC) approach to explain noticeable changes in reservoir properties arising from chemical disequilibrium.

3. Geomechanical Conditions

Fluid injection into a geothermal well system can induce stress changes at a scale through hydromechanical, poroelastic, and thermoelastic mechanisms. In this section, we evaluated the geomechanics responses for cold water injection into a geothermal double-well system. Following geophysics symbology, we use "S" to mean total stress, which at a point is the sum of the effective stress σ and the pore fluid pressure, viz.: $S_v = \sigma_v + P_p$; $S_{Hmax} = \sigma_{Hmax} + P_p$; $S_{hmin} = \sigma_{hmin} + P_p$. Injecting cold water into hot rock perturbs the stress in two ways: through ΔP and temperature ΔT. As a preliminary example, assuming a uniform planar and linearly elastic stratum, the effective horizontal stress change ($\Delta\sigma_h - $ MPa) for a uniform reservoir wide temperature change ($\Delta T_r - $ K) is

$$\Delta\sigma_h \approx \frac{\Delta T \times E \times \alpha_T}{1 - \upsilon} \qquad (2)$$

where the elastic properties defining the volume change (ΔV) are Young's modulus ($E - $ GPa), Poisson's ratio (υ), and the coefficient of thermal expansion ($\alpha_T - $ K^{-1}); for a stiff rock $E \approx 60$ GPa, $\alpha_T \approx 10^{-5}$ K^{-1}, and $\upsilon \approx 0.2$, so that a ΔT of -30 K can lead to a large effective stress change, $\Delta\sigma_h \approx -22$ MPa in this example. In cases with steep temperature gradients from cooling (across boundaries of large permeability contrast, for example), stress changes can readily induce shear slip of pre-existing fractures or small faults and exceptionally trigger the shear yield or tensile rupture of intact rock. This is also impacted by pressure changes, and to evaluate shear yield, it is necessary to introduce a shear slip criterion.

The potential for fracture slip or shear yield of intact rock from combined ΔT and ΔP effects from the fluid injection can be evaluated using simplified (i.e., linearized) Mohr-Coulomb (MC) yield criteria [52]

$$\tau = C + \sigma_n \tan\varphi \qquad (3)$$

where, τ is the shear stress at yield (shear slip) along a plane, usually, a rock weakness plane in naturally fractured rock masses, and σ_n is the normal effective stress acting across the slip plane. C and φ are the cohesion and internal friction angle, respectively; that is, the shear strength parameters of the slip surface (e.g., fault or fracture surface). To apply the MC criterion, the in-situ effective stress tensor, the slip plane shear strength, and the slip plane orientation are needed. Determining the effective stress tensor (σ_{ij}) at the region of potential slip is a coupled THM problem.

Fluid injection changes stress through hydromechanical ($\Delta P - \Delta\sigma$), poroelastic ($\Delta P - \Delta S$), and thermoelastic ($\Delta T - \Delta\sigma$) volume changes that generate three-dimensional strains (ε_{ij}) and therefore stress changes (ΔS_{ij} and $\Delta\sigma_{ij}$). Of course, $\Delta\sigma_{ij}$, in turn, leads to more ΔV; hence, the term "coupled" is used: no process is independent of the others. The first mechanism accounts for the bulk compressibility effect ΔV, the second for the porous rock ΔV, and the third for the thermally induced ΔV. Quantification of ΔV requires coupling heat conduction and convection with fluid flow and stress-strain analysis. In general, in the low permeability host rock, higher pressures reduce the frictional strength (Equation (3)) of a slip plane by decreasing the effective normal stress ($\sigma_{ij} = S_{ij} - P\delta_{ij}$), facilitating yield. In a Mohr stress diagram (Figure 5a) using total stresses, a pressure increase shifts the

yield envelope (black line) into the Mohr circle (the stress state), and yield is said to have occurred when stresses lie outside the criterion limit.
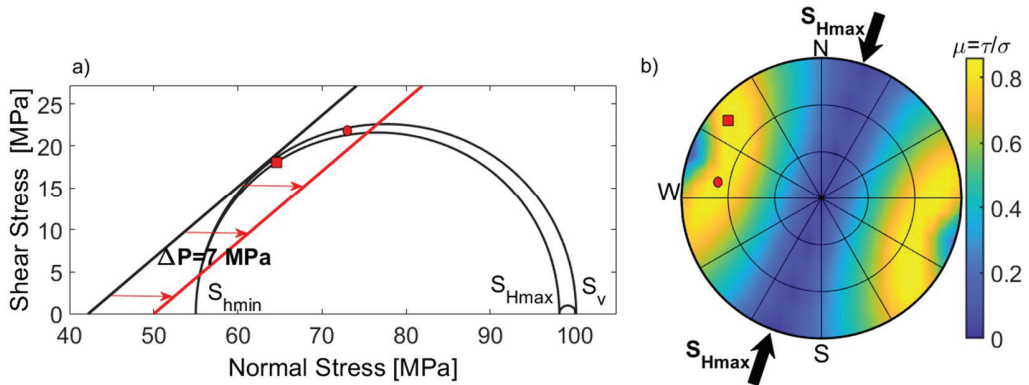
Figure 5. (**a**) 3D Mohr circles showing stress condition and slip tendency due to fluid injection in the deep geothermal reservoir Groß Schönebeck in the North German Basin. The red line is the Coulomb failure criterion when pore pressure has been elevated by 7 MPa, and (**b**) The lower hemisphere stereonet plot illustrates the slip-tendency (ratio of resolved shear to normal stress) and stress direction.

Because stiff, brittle earth materials store elastic strain energy but are strain-weakening, a sudden stress drop (weakening) accompanies shear slip, and a very small fraction of the released strain energy is evidenced as strain waves (seismic waves). Although the fluid-injection fracture-slip-induced deformation is not high, generally far less than a centimeter, $\Delta\sigma_{ij}$ may also trigger and reactivate nearby faults that are near critical stress conditions, causing felt seismicity and casing shear problems [53]. Injection-induced earthquakes are usually small with moment magnitude < 0. However, there are cases where large magnitude (>1) injection-induced seismicity has been recorded [54]. Two groups of field parameters can impact the magnitude and rate of injection-induced seismicity: controllable operational parameters that include fluid injection pressure, rate, temperature, and volume [54]. Uncontrollable subsurface parameters include the initial state of stress and pore pressure, size and density of pre-existing faults/fractures, fault/fracture orientation and shear strength, and other geomechanics parameters [55].

Figure 5 shows the effect of the pressure increase on the fault reactivation in the deep doublet geothermal Groß Schönebeck project in the North German Basin, where fluid-injection-induced seismicity is recorded [56]. The stress state at the injection depth of 4035 m is a normal faulting regime with S_v = 100 MPa, S_{Hmax} = 98 MPa, S_{hmin} = 55 MPa, and P_p = 43 MPa [56]. Faults striking in the S_{Hmax} direction with dip angles of 45–75° are critically stressed; increasing pore pressure by less than 7 MPa increases the risk of induced seismicity on two fault sets: the NW-SE set (rectangle), and the E-W set (Mohr circle). Shear slip of natural fractures in strong rocks is usually a dilatant process, so the rock mass permeability is enhanced in certain directions, which in turn will alter the fluid flow patterns, and probably increase the permeability anisotropy in a rock mass.

The second mechanism, poroelasticity, governs fluid pressure change effects on in-situ states of stress and rock mass deformation [52,57]. Geothermal SedHeat wells are drilled into porous, permeable reservoirs, and ΔP causes volume changes that lead to stress changes, altering porosity and permeability. Engelder and Fisher [58] demonstrated that stress/pore pressure changes in a normal faulting regime as follows

$$\frac{\Delta S_{hmin}}{\Delta P} = \alpha \frac{1 - 2\upsilon}{1 - \upsilon} \tag{4}$$

where α is Biot's poroelastic coefficient, for this relationship, it is assumed that vertical stress remains constant.

In this study, we evaluated the pore pressure stress coupling at different tectonic stress settings employing 3D geomechanics modeling. According to Anderson's classification scheme [52], the three states of stress are normal ($S_v > S_{Hmax} > S_{hmin}$), strike-slip ($S_{Hmax} > S_v > S_{hmin}$), and reverse faulting regimes ($S_{Hmax} > S_{hmin} > S_v$), where S values are the principal compressive stresses. One-way hydromechanical coupling is performed to evaluate the fluid injection effects on the stress tensor using the finite element platform Visage™ Geomechanics Simulator. We considered a hypothetical reservoir located at a depth of 2250 m where P_p is hydrostatic ($\approx$11 MPa/km), and S_v increases at a rate of $\approx$26 MPa/km. Simulation boundaries were sufficiently distant to have no effects on the deformations in the affected (reservoir) zone. This model was subjected to a $+\Delta P$ of 8 MPa.

Figure 6 shows the results for (a) normal faulting, (b) strike-slip, and (c) reverse faulting stress regimes, respectively. Pre- and post-injection stress tensors at the point of fluid injection are illustrated by 3D Mohr circles. In all cases, injecting fluid shifts the Mohr circles (stress magnitudes) leftward toward the yield criterion, indicating that the stress state is closer to the yield criterion. Note that in the case of the normal fault, incipient slip is apparent for the values chosen (P_p = 35 MPa). In the normal faulting regime, the effective maximum and minimum principal stress difference ($\sigma_v - \sigma_{hmin}$) decreases as P_p is increased, but not for the other two regimes; notably, in different states of stress, the local stress tensor components respond differently to fluid injection.
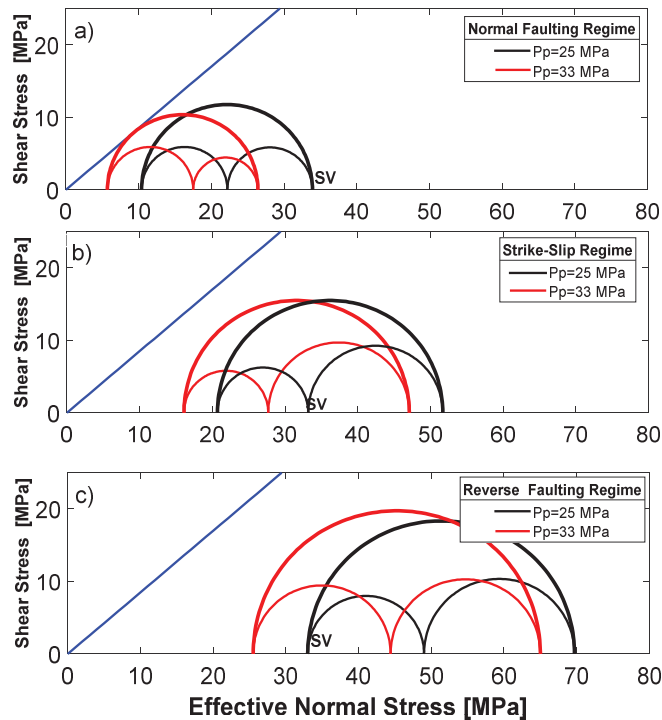
Figure 6. Mohr's Circle in three dimensions showing the effect of fluid injection (for pressure difference, ΔP = 8 MPa) at different states of stress: (**a**) normal faulting, (**b**) strike-slip, and (**c**) reverse faulting stress regimes.

The third ΔV mechanism, thermoelasticity, leads to slow rock shrinkage with cold water injection [52], inducing stress changes. The thermally induced stress magnitude ($\Delta\sigma_T$) effect was illustrated above (Equation (2)). We re-iterate that the stress redistribution process is driven by volume changes governed by ΔT and the host rock elastic properties [59]: $\Delta V = V \cdot \Delta T \cdot \alpha_T$, where the bulk rock thermal-expansion coefficient is α_T. As shown above, in stiff rocks (high E), $\Delta\sigma_T$ effects can be very large. Cooling occurs mostly convectively in permeable rocks, but in bounding low-permeability rocks, only conduction obtains. Therefore, strong local time-dependent differences in thermal expansion can take place, leading to shear stress concentrations at bounding interfaces (usually bedding), leading to shearing and induced seismicity. Figure 7 demonstrates how cool fluid injection changes the local state of stress around the cooled zone. Thermally-induced contraction decreases σ_{ij} in the cooled zone, and redistributes stresses around to maintain mechanical stress equilibrium. A similar (poroelastic) effect is expected to take place with ΔP, but the two processes, ΔT and ΔP, have widely different characteristic time scales. This implies that the rock deformation and stress changes are likely to be dominated by ΔP in the early time of a geothermal project, whereas ΔT effects become increasingly more important during the late time [60].
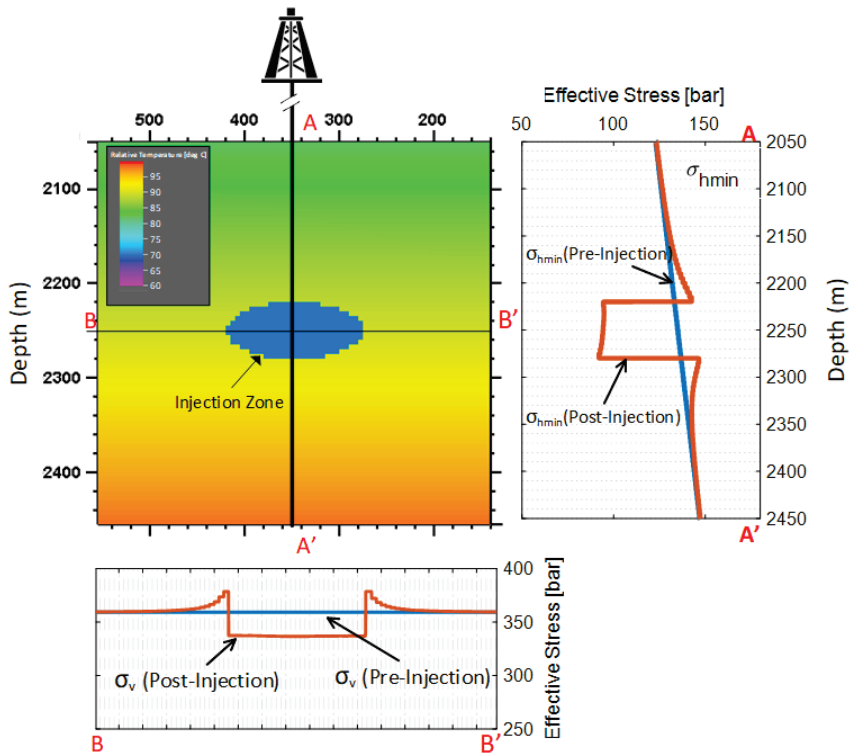
Figure 7. Induced thermal stress resulting from cold fluid injection into a geothermal reservoir. The color scale is the relative temperature range from 60 to 100 °C.

Hence, the zone being cooled relative to the rock mass loses compressive stress from thermoelastic shrinkage; this lost stress is transferred as increased stress to the surrounding, uncooled rock to maintain stress equilibrium (Figure 7). This stress redistribution generally increases local shear stresses, but the zone of maximum shear stress increase is distant from the injection well, near the region of the thermal front, which can be quite sharp because

the reservoir rock shrinks quickly (convectively), whereas the overburden shrinks very slowly (conductively).

In geothermal well systems, increasing the flow rate of the geothermal fluid can lead to the generation of a local turbulent flow regime, particularly around the injection well due to pumping the fluid flow with high pressure, affecting efficiency. In the short-term, the high flow rate of the injection fluid can lead to an increase in thermal energy production, although it has the inverse effect in the long-term. In addition, the turbulent flow near the injection well can cause more stress and, consequently, damage the well because of the induced stress created over time.

4. Heat-and Flow-Transport Challenges

4.1. System Thermal Issues

Eventually, loss of capacity to produce sufficient fluid rates at high enough temperatures to sustain commercial operation defines a geothermal reservoir's life-time [46]. The reservoir characteristics of porosity, permeability, initial temperature, and bulk heat capacity are performance indicators of a geothermal injection/production well system. These indicators dictate daily energy production and reservoir life-time. The recovery factor is the amount of producible energy compared to the total available energy, and it depends on the use of the heat at the surface (electrical power, power + heat, seasonal heat storage, etc.). Pure power production leads to a lower energy recovery factor. However, if the geothermal system is cooling, useful heat can likely be produced long after the period of electricity generation. Capital cost, operational cost, and the geothermal system performance over time define commercial viability [47]. The performance of a geothermal well system (commercially viable life-time and energy recovery) is related to both the natural physical parameters listed above and human-controlled factors. Transitioning a decaying geothermal system from power generation to sensible heat use makes great economic sense because the capital investment payback is dominated by the early years, when electricity is being generated. For long-term sustainability, this means there must be additional SedHeat systems added on episodically as the initial systems decay because of the slow drop of heat energy provision.

Human controlled parameters are [48]: (1) discharge rate from the reservoir, (2) injection rate and fluid input temperature, and (3) well spacing. Production, injection, and well spacing effects have been studied by Kazemi et al. [8] to show their importance on the life-time of a doublet geothermal system. Porosity, permeability, chemical components of pore fluid, initial temperature, reservoir minerals, and their chemical components and mechanical parameters, reservoir thickness, and the presence of shale layers and their thicknesses are the main natural subsurface physical parameters [48,49]. Thermal depletion happens by continuing injection of cooler water until the production well shows thermal breakthrough and decline in temperature, impacting the efficiency of the doublet geothermal system. Various means of extending life-span and project utility might include episodic electrical power production through integration of other energy sources (wind, solar, diesel, etc.), developing such a large well spacing that life-span is increased (but recovery efficiency may drop), and by thermal recharging from industrial waste heat sources or by use of excess solar and wind energy when available. Solar thermal collectors can be installed instead of photovoltaic systems, and these can feed the hot fluids into the system before the heat exchanger or afterward [61,62], depending on the time of year, the electrical power demand, and other factors. In all cases, the thermal capacity retention time of a project depends significantly on human-controlled parameters, given a set of physical system parameters [50].

Production-recovery cycles comprise an important process in any geothermal well system and need to be considered in any life-time assessment and economical assessment of such a system. A case study on a Riehen reservoir exploited by a doublet geothermal system showed that the recovery of the reservoir is closely related to the cyclic production-recovery plan [50], suggesting that shorter cycles allowed more thermal energy to be produced. If

there is some component of natural fluids recharge (a leaky reservoir), beneficially encouraging such recharge involved not only rate management but pressure management. Thermal breakthrough will occur sooner if production continues without letting the reservoir regain some heat through conduction from the surrounding rocks. The exploitation of the doublet aquifer is also affected by the pressure gradient in the aquifer, changing heat retention in the reservoir [63]. Table 1 summarizes some parameters for more effective heat production from a doublet geothermal system.

Table 1. Effective parameters for heat production from a doublet geothermal system.

Human Controlled Parameters	Natural Subsurface Physical Parameters
Doublet well spacing	Porosity of aquifer
Doublet distance	Permeability of aquifer
Flow rate	Conductivity of aquifer
Production recovery cycle	Specific heat capacity
Well types (horizontal/vertical)	Specific heat capacity of the brine
Re-injection water temperature	Density of brine
	Initial aquifer temperature
	Aquifer thickness

The main thermodynamic/commercial objective of a geothermal system must be economically viable heat recovery efficiency, defined as the ultimate recovered heat over the reserved heat in the aquifer [64–68], subject to commercial criteria. In order to achieve optimum efficiency from a geothermal system, the main goal should be to optimize heat recovery from the reservoir to service both the electrical grid needs and to provide useful heat for habitat and industrial needs. Most geothermal power plants are designed to provide electrical energy/heat to the surrounding area, which often is a local detached grid [69–72]. If geothermal electrical power can be used in a large grid to provide special services such as peak shaving or load displacement, the value of the energy provision increases.

4.2. Reservoir Geological Aspects

A first-order factor in the productivity of a geothermal SedHeat well array is the stratigraphy and flow properties of the reservoir. Figure 8 is a representation of a doublet in a typical SedHeat situation.

The target stratum is bounded by impermeable strata: U shale is the upper advective flow boundary, L shale is the lower advective flow boundary. Given typical permeability contrasts in geological media, it is usually assumed that the SedHeat fluid reservoir is bounded by impermeable strata, such that advective flow is confined to the more permeable intervals. In litharenite, SedHeat reservoirs (sand-silt-shale), the productive interval contains granular beds (sandstones) of differing permeability; the most common distribution is to find higher values in the lower beds, grading upward to lower permeability in the uppermost beds (also characteristic of transgressive sedimentary regimes).

Commonly, there are intraformational low-permeability strata, deposited under more quiescent flow conditions, called silts or shales; they are of much lower permeability than the low k sandstone, usually by more than two orders of magnitude. Furthermore, because of processes in the original depositional environment, these low-permeability strata may be continuous at the doublet spacing scale (shale C), or they may be laterally discontinuous (shale A and shale B). The complete disposition of the various strata between the doublet pair is difficult to specify, even with excellent seismic investigation; usually, stratigraphic details are known only from the geophysical logs available from the production and injection wells.

production   injection

A well doublet geological system

p p_o p

U shale

low k

shale A

med k   fluid reservoir   shale B

shale C

high k

L shale
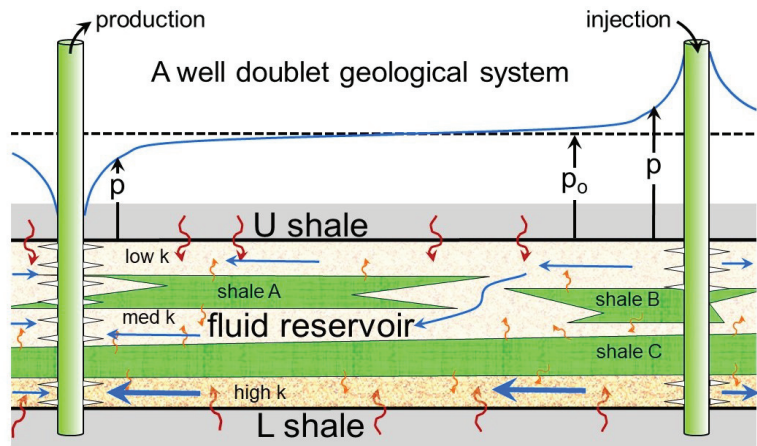
Figure 8. Geological disposition factors in doublet efficacy.

One may assume that in the stratigraphic disposition shown, the permeability of the lowermost sandstone is several times that of the central sandstone, which in turn is several times that of the upper sandstone (a permeability range for the sandstones might be from 1 D to 0.1 D). The silty shale interbeds (labeled "shale") have permeability values less than 0.001 D, so they may be considered functionally impermeable in the context of advective fluid flux. Thus, heat in these strata (water and mineral phases) can migrate to the sandstone only by conductive heat transport, and is thence taken to the production well advectively (blue arrows). Similarly, the heat in the bounding strata (U-, L-shale) can only flow conductively and be exploited when the advectively flowing fluid in the sandstone drops below the original temperature.

Another issue in a natural, unbounded reservoir is that flow is not constrained by lateral no-flow boundaries. Assuming an original pressure P_o and similar pressure build-up and draw-down cones around each well (blue line), part of the injected fluid will dissipate into the farfield to the right, driven by the positive ΔP, and at the production well, part of the warm fluids will come from the farfield to the left, driven by the pressure sink $-\Delta P$. The heterogeneity that is characteristic of all sedimentary rock geothermal reservoirs invariably decreases the energy recovery and the energy recovery rate. The most optimistic recovery scenario is the isotropic, constant permeability case, with the further assumption that the local permeability is not impaired by geochemical processes or fine-grained solids migration into the reservoir.

Finally, we point out that in geothermal reservoirs that are dominated by flow in natural fractures, there is an important short-circuiting mechanism associated with thermal effects: maximum fracture aperture increase occurs in the fracture with the most flow, reinforcing the flow rate [73]. It remains unclear if this process can be somewhat suppressed by flow management and by thermal recharge [74]. Assessing the commercial viability of a geothermal SedHeat reservoir that involves the injection of cold water is and will remain a challenging task. Currently, SedHeat projects in laterally extensive reservoirs that do not require re-injection of cold water seem commercially viable because the fluid entry temperature remains constant from continuous recharge. Injection/production projects based on well-doublets or variants require more careful evaluation.

5. Conclusions

Geothermal energy appears to be a green, generally available, potentially constant, and stable source of energy. If economically viable, it is a practical and sustainable solution for supplying energy needs (power or thermal) and can decrease environmental challenges and

threats (e.g., air pollution, global warming, climate change). Geothermal well systems can be used to generate both electrical and thermal energy. Despite the advantages listed here, these systems will evidence challenges over time, including heat conductivity, chemical, and mechanical issues, which will affect their operational efficiency, as well as costs. Based on the literature and studies conducted, the following results can be concluded:

- Chemical reactions can lead to flow-path alterations, as well as varying the heat exchange rate between rock and water, resulting in variations in the reservoir's porosity-permeability and heat capacity.
- Corrosion and scaling damage in the well systems decrease their operational efficiency and impact their life-span.
- Mineral dissolution and precipitation under ΔT and ΔP conditions play a substantial role in chemical disequilibrium in geothermal systems, particularly in deep ones.
- Factors having a significant impact on the life-span and heat recovery of a geothermal well system include energy discharge rate and strategy, injection rate, temperature and heat management, and well spacing.
- Optimization of heat recovery from the reservoir while sustaining a profitable commercial outcome is the most important issue in geothermal well systems.
- Fluid injection into a geothermal well system can induce stress changes at a scale that will increase the likelihood of fault/fracture reactivation and induced seismicity. Understanding the magnitude of these events and their recurrence in time is important.
- Channeling, short-circuiting, leaking, heterogeneity, and permeability impairment can all negatively affect project viability and must be carefully assessed during site assessment.

Knowing the issues discussed in this article will help designers/engineers to better design and implement geothermal SedHeat systems, based on the local geological characteristics of the resources and geographical and climate conditions, resulting in improving operations and enhancing efficiency of the systems as well as reducing their associated costs and risks.

Nomenclature

c_p	Heat capacity, J/kg·K
C	Cohesion of the rock, Pa
E	Young's modulus, Pa
$\dot{E}$	Energy rate or power, J/s
P	Pressure, Pa
P_p	Pore pressure, Pa
ΔP	Pressure difference, Pa
Q	Heat production capacity, J/K
$\dot{Q}$	Flow rate (of fluid), kg/s
S_v	Vertical stress, Pa

S_{Hmax}	Maximum horizontal stress, Pa
S_{hmin}	Minimum horizontal stress, Pa
ΔT	Temperature difference, K
T_o	Initial reservoir temperature, K
T_{in}	Fluid temperature entering the energy extraction system, K
T_{out}	Fluid temperature exiting the energy extraction system, K
V	Volume, m^3
α	Biot's poroelastic coefficient, -
α_T	Rock thermal-expansion coefficient, K^{-1}
υ	Poisson's ratio, -
σ	Effective stress, Pa
σ_n	Effective normal stress, Pa
φ	Friction angle of the slip plane or intact rock, °
τ	Shear stress, Pa

Abbreviations

EG	Enhanced (Engineered) Geothermal
GHG	Greenhouse Gas
HDR	Hot Dry Rock
MC	Mohr-Coulomb
MIC	Microbiologically Induced Corrosion
THC	Thermal-Hydraulic-Chemical
THM	Thermal-Hydraulic-Mechanical
THMC	Thermal-Hydraulic-Mechanical-Chemical

References

1. Bahadori, M.N.; Dehghani-Sanij, A.R. *Wind Towers: Architecture, Climate and Sustainability*; Sayigh, A., Ed.; Springer: Basel, Switzerland, 2014.
2. Dehghani-Sanij, A.R. *Cisterns: Sustainable Development, Architecture and Energy*; Sayigh, A., Ed.; River Publishers: Aalborg, Denmark, 2016.
3. Dehghani-Sanij, A.R.; Tharumalingam, E.; Dusseault, M.B.; Fraser, R. Study of energy storage systems and environmental challenges of batteries. *Renew. Sustain. Energy Rev.* **2019**, *104*, 192–208. [CrossRef]
4. Looney, B. *Energy Outlook*, 2020th ed.; BP p.l.c.: London, UK, 2020; p. 157.
5. Dusseault, M.B.; Mahbaz, S.B.; Fraser, R.A.; Dehghani-Sanij, A.R. Hybrid Energy Systems: Delivering Reliable Heat and Power in Remote Locations. In *Proceedings of the 46th Annual Yellowknife Geoscience Forum Abstracts*; Northwest Territories Geological Survey: Yellowknife, NT, Canada, 2018.
6. Kinney, C.; Dehghani-Sanij, A.R.; Mahbaz, S.B.; Dusseault, M.B.; Nathwani, J.S.; Fraser, R.A. Geothermal energy for sustainable food production in Canada's remote northern communities. *Energies* **2019**, *12*, 4058. [CrossRef]
7. Mahbaz, S.B.; Dehghani-Sanij, A.R.; Dusseault, M.B.; Nathwani, J.S. Enhanced and integrated geothermal systems for sustainable development of Canada's northern communities. *Sustain. Energy Technol. Assess.* **2020**, *37*, 100565. [CrossRef]
8. Kazemi, A.R.; Mahbaz, S.B.; Dehghani-Sanij, A.R.; Dusseault, M.B.; Fraser, R. Performance evaluation of an enhanced geothermal system (EGS) in the Western Canada Sedimentary Basin. *Renew. Sustain. Energy Rev.* **2019**, *113*, 109278. [CrossRef]
9. Dehghani-Sanij, A.R.; Bahadori, M.N. *Ice-Houses: Energy, Architecture, and Sustainability*; Elsevier, Imprint by Academic Press: Amsterdam, The Netherlands, 2021.
10. Soltani, M.; Kashkooli, F.M.; Dehghani-Sanij, A.R.; Kazemi, A.R.; Bordbar, N.; Farshchi, M.J.; Elmi, M.; Gharali, K.; Dusseault, M.B. A comprehensive study of geothermal heating and cooling systems. *Sustain. Cities Soc.* **2019**, *44*, 793–818. [CrossRef]
11. Soltani, M.; Kashkooli, F.M.; Dehghani-Sanij, A.R.; Nokhosteen, A.; Ahmadi-Joughi, A.; Gharali, K.; Mahbaz, S.B.; Dusseault, M.B. A comprehensive review of geothermal energy evolution and development. *Int. J. Green Energy* **2019**, *16*, 971–1009.
12. Guney, M.S.; Tepe, Y. Classification and assessment of energy storage systems. *Renew. Sustain. Energy Rev.* **2017**, *75*, 1187–1197. [CrossRef]
13. Dehghani-Sanij, A.R.; Mahbaz, S.B.; Dusseault, M.B. Feasibility study of enhanced geothermal Energy secondary application for agricultural production in Canadian Northern territories. In *Proceedings of the 46th Annual Yellowknife Geoscience Forum Abstracts*; Northwest Territories Geological Survey: Yellowknife, NT, Canada, 2018.
14. Bilgili, M.; Ozbek, A.; Sahin, B.; Kahraman, A. An overview of renewable electric power capacity and progress in new technologies in the world. *Renew. Sustain. Energy Rev.* **2015**, *49*, 323–334.
15. Rybach, L. Geothermal Sustainability. In Proceedings of the European Geothermal Congress, Unterhaching, Germany, 30 May–1 June 2007.
16. Grasby, S.E.; Allen, D.M.; Bell, S.; Chen, Z.; Ferguson, G.; Jessop, A.; Kelman, M.; Ko, M.; Majorowicz, J.; Moore, M.; et al. *Geothermal Energy Resource Potential of Canada*; Geological Survey of Canada: Ottawa, ON, Canada, 2011; p. 322.

17. Pérez, R.E. Shallow geothermal energy: Geological energy for the ecological transition and its inclusion in European and national energy policies. *Eur. Geol. Eur. Geol.* **2019**, *47*, 28–32.
18. Lee, K.C. Classification of geothermal resources by exergy. *Geothermics* **2001**, *30*, 431–442.
19. Axelsson, G. Production capacity of geothermal systems. In Proceedings of the Workshop for Decision Makers on the Direct Heating Use of Geothermal Resources in Asia, Tianjin, China, 11–18 May 2008.
20. Schiavone, R.; De Natale, G.; Borgia, A.; Troise, C.; Moretti, R.; Somma, R. Seismogenic potential of withdrawal-reinjection cycles: Numerical modelling and implication on induced seismicity. *Geothermics* **2020**, *85*, 101770. [CrossRef]
21. Holbrook, J.; Moore, J.N.; Elsworth, D.; Block, K.A.; Allis, R.; Einstein, H. An Opportunity of Geothermal Proportions in Sedimentary Basins. *Sediment. Rec.* **2014**, *12*, 4–9. [CrossRef]
22. Green, S.; McLennan, J.; Panja, P.; Kitz, K.; Allis, R.; Moore, J. Geothermal battery energy storage. *Renew. Energy* **2017**, *164*, 777–790. [CrossRef]
23. Carlino, S.; Somma, R.; Troiano, A.; Di Giuseppe, M.G.; Troise, C.; De Natale, G. The geothermal system of Ischia Island (southern Italy): Critical review and sustainability analysis of geothermal resource for electricity generation. *Renew. Energy* **2014**, *62*, 177–196. [CrossRef]
24. Carlino, S.; Troiano, A.; Di Giuseppe, M.G.; Tramelli, A.; Troise, C.; Somma, R.; De Natale, G. Exploitation of geothermal energy in active volcanic areas: A numerical modelling applied to high temperature Mofete geothermal field, at Campi Flegrei caldera (Southern Italy). *Renew. Energy* **2016**, *87*, 54–66. [CrossRef]
25. Satman, A. Sustainability of Geothermal Doublets. In Proceedings of the 36th Workshop on Geothermal Reservoir Engineering, SGP-TR-191, Stanford, CA, USA, 31 January–2 February 2011.
26. Esteves, A.F.; Santos, F.M.; Pires, J.C.M. Carbon dioxide as geothermal working fluid: An overview. *Renew. Sustain. Energy Rev.* **2019**, *114*, 109331. [CrossRef]
27. Banks, D. Thermogeological assessment of open loop well doublet schemes: An analytical approach. In *Proceedings of the 27th Annual Groundwater Conference*; International Association of Hydrogeologists (Irish Group): Tullamore, Ireland, 2007.
28. Banks, D. Hydrogeological assessment of open-loop well-doublet schemes: A review and synthesis of analytical approaches. *Hydrogeol. J.* **2009**, *17*, 1149–1155. [CrossRef]
29. Ungemach, P.; Antics, M.; Papachristou, M. Sustainable Geothermal Reservoir Management. In Proceedings of the World Geothermal Congress, Antalya, Turkey, 24–29 April 2005.
30. Ungemach, P. Chemical Treatment of Low Temperature Geofluids. In Proceedings of the International Course on District Heating Schemes, Cesme, Izmir, Turkey, 19–25 October 1997.
31. Lerm, S.; Westphal, A.; Miethling-Graff, R.; Alawi, M.; Seibt, A.; Wolfgramm, M.; Würdemann, H. Thermal effects on microbial composition and microbiologically induced corrosion and mineral precipitation affecting operation of a geothermal plant in a deep saline aquifer. *Extremophiles* **2013**, *17*, 311–327. [CrossRef]
32. Courtesy Terry, R. Carter from a published AAPG, American Association of Petroleum Geologists. In Proceedings of the GeoConvention 2014, Calgary, AB, Canada, 12–16 May 2014.
33. Dusseault, M.B.; Jackson, R.E. Seepage pathway assessment for natural gas to shallow groundwater during well stimulation, in production, and after abandonment. *Environ. Geosci.* **2014**, *21*, 107–126. [CrossRef]
34. Alt-Epping, P.; Diamond, L.W.; Häring, M.O.; Ladner, F.; Meier, D.B. Prediction of water–rock interaction and porosity evolution in a granitoid-hosted enhanced geothermal system, using constraints from the 5 km Basel-1 well. *Appl. Geochem.* **2013**, *38*, 121–133. [CrossRef]
35. Bächler, D.; Kohl, T. Coupled thermal–hydraulic–chemical modelling of enhanced geothermal systems. *Geophys. J. Int.* **2005**, *161*, 533–548. [CrossRef]
36. Gerchakov, S.M.; Little, B.J.; Wagner, P. Probing Microbiologically Induced Corrosion. *Corrosion* **1986**, *42*, 689–692. [CrossRef]
37. Liu, H.; Cheng, Y.F. Microbial corrosion of initial perforation on abandoned pipelines in wet soil containing sulfate-reducing bacteria. *Colloids Surf. B Biointerfaces* **2020**, *190*, 110899. [CrossRef] [PubMed]
38. Salas, V.B.; Wiener, S.M.; de la Peña, L.R.; Bedolla, N.M. Deterioration of materials in geothermal fields in Mexico. *Mater. Corros.* **2000**, *51*, 698–704. [CrossRef]
39. Iberl, P.; Alt, N.S.A.; Schluecker, E. Evaluation of corrosion of materials for application in geothermal systems in Central Europe. *Mater. Corros.* **2015**, *66*, 733–755. [CrossRef]
40. Letcher, T.; Sayigh, A. (Eds.) *Comprehensive Renewable Energy*; Elsevier: Oxford, UK, 2012.
41. DIN EN ISO. *15156-153 Grundbegriffe und Definitionen*; Beuth Verlag GmbH: Berlin, Germany, 1999.
42. Weißbach, W. *Werkstoffkunde*; Vieweg þ Teubner Verlag: Wiesbaden, Germany, 2012.
43. Gülich, J.F. *Kreiselpumpen*; Springer: Berlin/Heidelberg, Germany, 2010.
44. Merkblatt 821. *Edelstahl Rostfrei–Eigenschaften*; Informationsstelle Edelstahl Rostfrei: Düsseldorf, Germany, 2012.
45. Dinh, H.T.; Kuever, J.; Muszmann, M.; Hassel, A.W.; Stratmann, M.; Widdel, F. Iron corrosion by novel anaerobic microorganisms. *Nature* **2004**, *427*, 829–832. [CrossRef] [PubMed]
46. Blöcher, M.G.; Zimmermann, G.; Moeck, I.; Brandt, W.; Hassanzadegan, A.; Magri, F. 3D numerical modeling of hydrothermal processes during the lifetime of a deep geothermal reservoir. *Geofluids* **2010**, *10*, 406–421. [CrossRef]
47. Ungemach, P. Insight into Geothermal Reservoir Management. In *Textbook*; Rosca, M., Ed.; European Summer School on Geothermal Energy Applications: Oradea, Romania, 2001; pp. 43–76.

48. Ventre, A.V.; Ungemach, P. Soft Acidizing of Damaged Geothermal Injection Wells–Discussion of Results Achieved in the Paris Basin. In Proceedings of the 23rd Workshop on Geothermal Reservoir Engineering, Stanford, CA, USA, 26–28 January 1998; pp. 33–43.

49. Ungemach, P.; Ventre, A.V.; Nicolaon, S. Tracer Leak Off Tests as Means of Checking Well Integrity, Application to Paris Basin Geothermal Production Wells. In Proceedings of the 27th Workshop on Geothermal Reservoir Engineering, SGP-TR-71, Stanford, CA, USA, 28–30 January 2002.

50. Portier, S.; Vuataz, F.D.; Nami, P.; Sanjuan, B.; Gérard, A. Chemical stimulation techniques for geothermal wells: Experiments on the three-well EGS system at Soultz-sous-Forêts, France. *Geothermics* **2009**, *38*, 349–359. [CrossRef]

51. Salimzadeh, S.; Nick, H.M. A coupled model for reactive flow through deformable fractures in enhanced geothermal systems. *Geothermics* **2019**, *81*, 88–100. [CrossRef]

52. Jaeger, J.C.; Cook, N.G.; Zimmerman, R. *Fundamentals of Rock Mechanics*; John Wiley & Sons, Inc.: Hoboken, NJ, USA, 2009.

53. Dusseault, M.B.; Bruno, M.S.; Barrera, J. Casing shear: Causes, cases, cures. *Soc. Pet. Eng. Drill. Completion J.* **2001**, *16*, 98–107. [CrossRef]

54. McGarr, A. Maximum magnitude earthquakes induced by fluid injection. *J. Geophys. Res. Solid Earth* **2014**, *119*, 1008–1019. [CrossRef]

55. Yaghoubi, A.; Dusseault, M.B.; Mahbaz, S.B.; Leonenko, Y. Probabilistic Injection-Induced Fault Slip Assessment in Fox Creek Alberta. In Proceedings of the 54th US Rock Mechanics/Geomechanics Symposium, ARMA-2020-1880, Golden, CO, USA, 28 June–1 July 2020.

56. Blöcher, G.; Cacace, M.; Jacquey, A.B.; Zang, A.; Heidbach, O.; Hofmann, H.; Kluge, C.; Zimmermann, G. Evaluating micro-seismic events triggered by reservoir operations at the geothermal site of Groß Schönebeck (Germany) *Rock Mech. Rock Eng.* **2018**, *51*, 3265–3279. [CrossRef]

57. Hojka, K.; Dusseault, B.M.; Bogobowicz, A.D. Analytical solutions for transient thermoelastic stress fields around a borehole during fluid injection into permeable media. *J. Can. Pet. Technol.* **1993**, *32*. [CrossRef]

58. Engelder, T.; Fischer, M. Influence of poroelastic behavior on the magnitude of minimum horizontal stress, S_h in overpressure parts of sedimentary basins. *Geology* **1994**, *22*, 949–952.

59. Stephens, G.; Voight, B. Hydraulic fracturing theory for conditions of thermal stress. *Int. J. Rock Mech. Min. Sci. Geomech. Abstr.* **1982**, *19*, 279–284. [CrossRef]

60. Jalali, M.R.; Evans, K.F.; Valley, B.C.; Dusseault, M.B. Relative importance of THM effects during non-isothermal fluid injection in fractured media. In Proceedings of the 49th US Rock Mechanics/Geomechanics Symposium, San Francisco, CA, USA, 28 June–1 July 2015.

61. Greenhut, A.D. Modeling and Analysis of Hybrid Geothermal-Solar Thermal Energy Conversion Systems. Ph.D. Thesis, Massachusetts Institute of Technology, Cambridge, MA, USA, 2009.

62. Erdogan, A.; Colpan, C.O.; Cakici, D.M. Thermal design and analysis of a shell and tube heat exchanger integrating a geothermal based organic Rankine cycle and parabolic trough solar collectors. *Renew. Energy* **2017**, *109*, 372–391. [CrossRef]

63. Willems, C.J.L.; Nick, H.M.; Weltje, G.J.; Bruhn, D.F. An evaluation of interferences in heat production from low enthalpy geothermal doublets systems. *Energy* **2017**, *135*, 500–512. [CrossRef]

64. Babaei, M. Integrated carbon sequestration–geothermal heat recovery: Performance comparison between open and close systems. *Transp. Porous Media* **2019**, *126*, 249–273. [CrossRef]

65. Vik, H.S.; Salimzadeh, S.; Nick, H.M. Heat recovery from multiple-fracture enhanced geothermal systems: The effect of thermoelastic fracture interactions 500 m. *Renew. Energy* **2018**, *121*, 606–622.

66. Crooijmans, R.A.; Willems, C.J.L.; Nick, H.M.; Bruhn, D.F. The influence of facies heterogeneity on the doublet performance in low-enthalpy geothermal sedimentary reservoirs. *Geothermics* **2016**, *64*, 209–219. [CrossRef]

67. Williams, C.F. Updated methods for estimating Recovery Factors for geothermal resources. In Proceedings of the 32nd Workshop on Geothermal Reservoir Engineering, Stanford, CA, USA, 22–24 January 2007.

68. Salimzadeh, S.; Grandahl, M.; Medetbekova, M.; Nick, H.M. A novel radial jet drilling stimulation technique for enhancing heat recovery from fractured geothermal reservoirs. *Renew. Energy* **2019**, *139*, 395–409. [CrossRef]

69. Vasilyeva, M.; Babaei, M.; Chung, E.T.; Spiridonov, D. Multiscale modeling of heat and mass transfer in fractured media for enhanced geothermal systems applications. *Appl. Math. Model.* **2019**, *67*, 159–178. [CrossRef]

70. Lopez, S.; Hamm, V.; Le Brun, M.; Schaper, L.; Boissier, F.; Cotiche, C.; Giuglaris, E. 40 years of Dogger aquifer management in Ile-de-France, Paris Basin, France. *Geothermics* **2010**, *39*, 339–356. [CrossRef]

71. Nador, A.; Kujbus, A.; Toth, A.N. Geothermal energy use, country update for Hungary. In Proceedings of the European Geothermal Congress, Strasbourg, France, 19–24 September 2016.

72. Szanyi, J.; Kovács, B. Utilization of geothermal systems in South-East Hungary. *Geothermics* **2010**, *39*, 357–364. [CrossRef]

73. Gee, B.; Gracie, R. Comparison of fully-coupled and sequential solution methodologies for enhanced geothermal system. *Comput. Methods Appl. Mech. Eng.* **2021**, *670*, 113554. [CrossRef]

74. Iorio, M.; Carotenuto, A.; Corniello, A.; Di Fraia, S.; Massarotti, N.; Mauro, A.; Somma, R.; Vanoli, L. Low Enthalpy Geothermal Systems in Structural Controlled Areas: A Sustainability Analysis of Geothermal Resource for Heating Plant (The Mondragone Case in Southern Appennines, Italy). *Energies* **2020**, *13*, 1237. [CrossRef]

Article

Geothermal Assessment of Target Formations Using Recorded Temperature Measurements for the Alberta No. 1 Geothermal Project

Katherine K. Huang [1,*], Catherine J. Hickson [1], Darrell Cotterill [2] and Yannick Champollion [1]

[1] Alberta No. 1, Edmonton, AB T5J 3M1, Canada; c.hickson@albertano1.ca (C.J.H.); yannick.champollion@gmail.com (Y.C.)

[2] Parallax Resources, Parkland County, AB T7Y 0C4, Canada; parallaxres2014@gmail.com

[*] Correspondence: k.huang@albertano1.ca

Abstract: The Alberta No. 1 project is a planned power and heat (direct use) geothermal project located within the County of Grande Prairie and Municipal District of Greenview. For the project to successfully produce power and heat on a commercial scale, temperatures of 120 °C are desirable. The produced fluids must also be from highly permeable formations from depths of less than 4500 m. Bottomhole temperature measurements and wireline logs from Alberta's extensive oil and gas database were used to determine the depths to target formations and temperatures within these formations in the project area. The target formations include the dolomitized carbonate units of Devonian age from the Beaverhill Lake Group to the top of the Precambrian Basement. Permeable Devonian-aged sandstone units such as the Granite Wash Formation are also targets. Results suggest that elevation to the top of the Beaverhill Lake Group range from 3104 m to 4094 m and temperatures at the top of the formation range from 87 °C to 123 °C in the study area. Elevation to the top of the Precambrian Basement ranges from 3205 m to 4223 m and temperatures at the formation top range from 74 °C to 124 °C. Within the area where Alberta No. 1 plans to drill, temperatures close to and exceeding 120 °C are expected within the target formations.

Keywords: conventional geothermal; direct heat use; Western Canadian Sedimentary Basin; bottomhole temperatures; Alberta

1. Introduction

The No. 1 Geothermal Limited partnership (Alberta No. 1) geothermal power and direct heat use project has been awarded funding from Natural Resources Canada's (NR-Can) Emerging Renewable Power Program (ERPP). The program funding matches private sector dollars and stipulates that the geothermal project must produce 5 MWe net of power. To select the project location, Alberta No. 1 conducted a regional study to identify areas in the Alberta portion of the Western Canadian Sedimentary Basin (WCSB) where (1) temperatures are sufficiently high for power production, (2) there are formations at the target depths with known high fluid flows, and (3) there is adequate existing infrastructure that supports low-cost power grid connection as well as direct use applications [1]. Nine chosen areas were assessed for these three constraining factors; results concluded that the area that lies within the Municipal District of Greenview (MDGV) and County of Grande Prairie was most suitable for developing the Alberta No. 1 project (Figure 1).

The study area spans from the northwest corner of Township 73, Range 7, West of the 6th Meridian to the southeast corner of Township 65, Range 3, West of the 6th Meridian (Figure 2). The drilling area, where Alberta No. 1 plans to drill five production and injection wells, spans two ranges and three townships in the vicinity of the Norbord Oriented Strand Board (OSB) facility and a planned light industrial park near the Hamlet of Grovedale (Figure 2). The park and OSB facility are anticipated industrial heat offtakers from the direct use (heating and cooling) portion of the project.
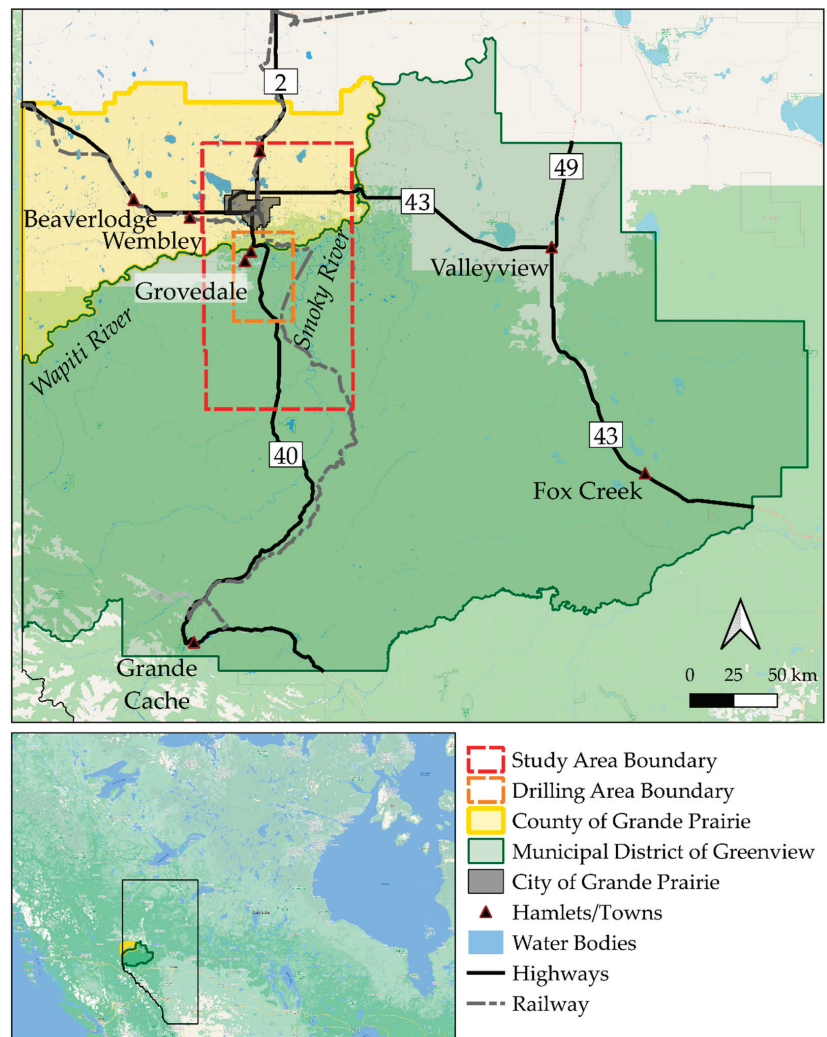
Figure 1. The study area lies within the Municipal District of Greenview (MDGV) and the County of Grande Prairie, and encompasses the City of Grande Prairie.

The study area is located within the western portion of the extensive WCSB. In a sedimentary basin such as the WCSB, formations generally decrease in porosity and increase in density (and therefore increase in thermally conductivity) with increasing depth. Permeability and fluid flow are also important parameters when selecting target formations. In the project area, the Precambrian Basement is overlain by thick, permeable carbonate units of Devonian age. Of particular importance are limestone units that have been hydrothermally altered to dolomite creating enhanced permeability [2]. The Alberta No. 1 project will preferentially target these dolomite units and interbedded sandstone units where they are near built infrastructure. Specifically, the target formations span from the top of the Beaverhill Lake Group to the base of the Granite Wash Formation, which overlies the Precambrian Basement (Figure 3).
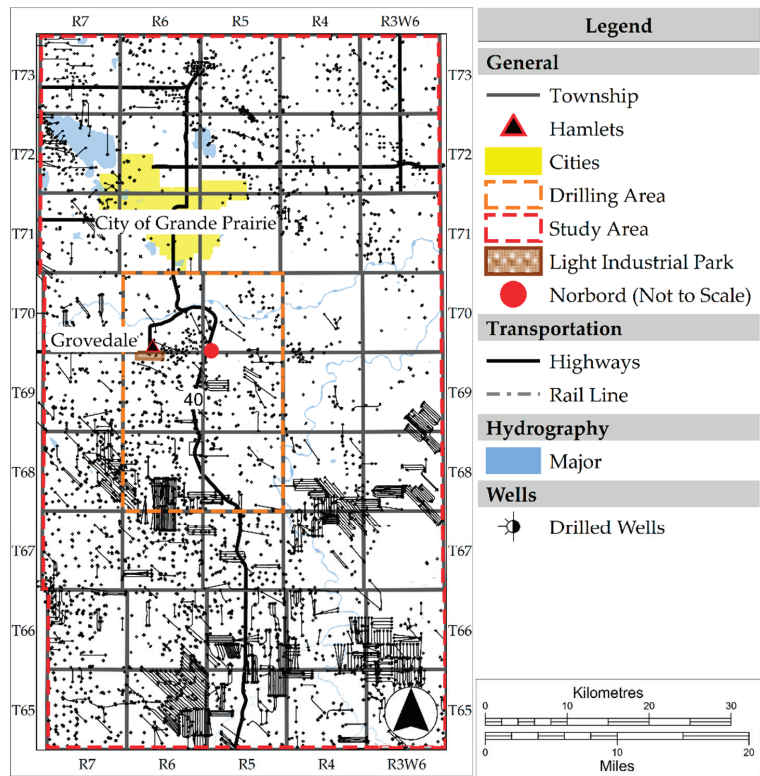
Figure 2. The wells previously drilled shown within the study area and the drilling area where Alberta No. 1 plans to drill production and injection wells. The areas encompass a planned light industrial park and the Norbord OSB facility.

To date, over 4000 wells have been drilled in the study area (Figure 2), providing an extensive database to understand the stratigraphy and formation properties of oil and gas targets. However, the data collected differ from the data that would typically be collected for geothermal exploration. The chief difficulty faced by geothermal developers when interpreting bottomhole temperature (BHT) measurements is that the temperatures taken for hydrocarbon development are a perfunctory data point at the end of completion of the well. The data are used for surface engineering designs, especially if the temperatures are high. Wells with BHT data have generally been measured with single, unequilibrated BHT measurements. In comparison, considerable care is taken to obtain accurate and equilibrated temperatures throughout the wellbore for geothermal exploration. This includes the process of allowing the bottom of the well to heat up to thermal equilibrium conditions following drilling. During and after this heat up period, continuous logs are run from top to the bottom. To account for such discrepancies, several correction methods have been created and used to predict equilibrated temperatures at depth from BHTs. Interpretation of geothermal resources from BHT data has been the subject of a considerable amount of research, for example, Harrison et al. (1983), Horner (1951), and Stutz et al. (2012) [4–6].
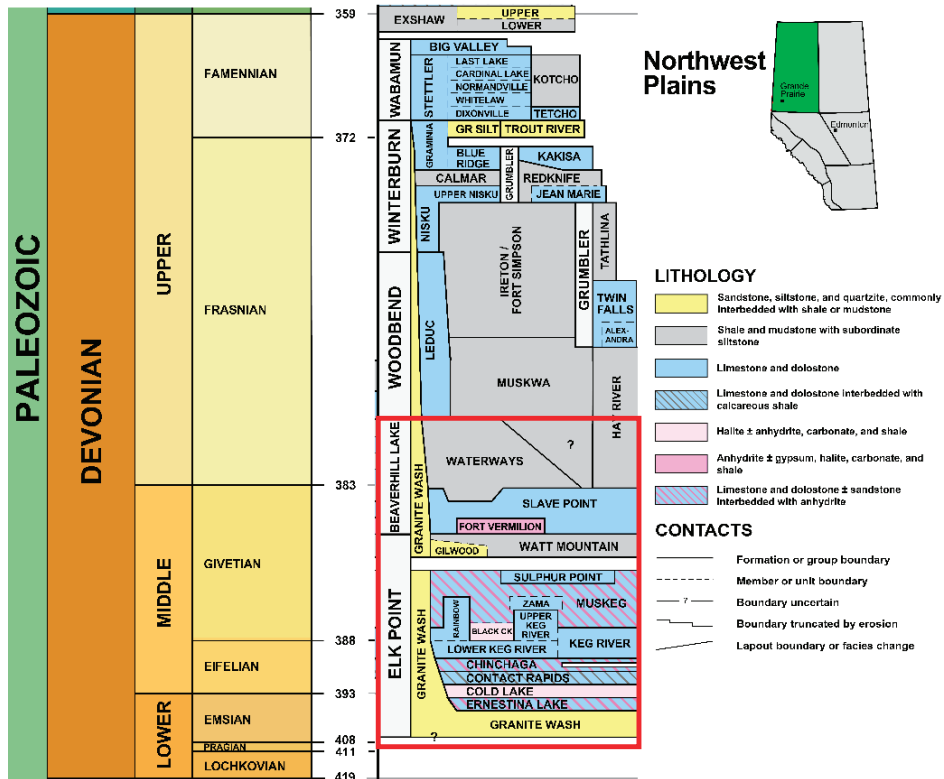
Figure 3. General stratigraphy of Devonian units in the Northwest Plains of Alberta. The Alberta No. 1 project area is not underlain by all the units depicted, but is targeting the formations from the Beaverhill Lake Group to the Granite Wash Formation, outlined in red [3].

Previous studies have analyzed oil and gas temperature data specifically within the WCSB to estimate geothermal resources [7–26]. Drill Stem Tests (DST), BHTs, and Annual Pool Pressure (APP) results all include significant errors that require the data to be filtered. BHT measurements generally provide lower temperatures than DST and APP measurements. These studies involve temperature corrections to adjust the recorded temperatures to try to represent the actual temperature at depth.

Several of these correction methods could not be used for this data set; the Horner correction requires input of elapsed time between cessation of circulation in the well bore and the temperature measurement. It is best when several temperature measurements have been made at regular time intervals. The data for this study do not include these measurements, so the Horner correction could not be applied. The thermal gradients of the study areas assessed by Huang et al. (2020) [27] (including the Alberta No. 1 study area) appear to be linear with depth, suggesting that the Harrison correction method, which uses a second-order polynomial fit, is not suitable for the data in this study. Huang et al. (2020) [27] suggest that the filtered, uncorrected BHT data in the WCSB may be more reliable than previously thought. Furthermore, many temperature correction methods increase the temperature from the measured BHT; if this estimation is overly optimistic, the temperature predictions can be detrimental to the project. An overestimation of temperature could falsely suggest that electricity production from the produced fluid is viable, but if the fluid is a few degrees lower, this may not be the case. For the purposes of the Alberta No. 1 geothermal project, a conservative, lower estimate of target formation temperatures is

required for understanding the reservoir, the well design, the expected flow rate, and the power plant design. Therefore, this study uses the raw, filtered BHT data to conservatively predict the lower limit of temperatures at depth. Fluid temperatures of at least 120 °C at depths of 4500 m or less are required to profitably operate the plant. As well, fluid temperature will dictate the required flow rate to produce 5 MWe net.

Our results suggest that elevation to the top of the Beaverhill Lake Group ranges from 3104 m to 4094 m and temperature at the top of the formation ranges from 87 °C to 123 °C in the study area. Elevation to the top of the Precambrian Basement ranges from 3205 m to 4223 m and temperature at the formation top ranges from 74 °C to 124 °C. Within the area where Alberta No. 1 plans to drill, our results calculate depths to the top of the Beaverhill Lake Group and Precambrian Basement to range from 3634 m to 3839 m and 3740 m to 3906 m, respectively. Temperatures range from 87 °C to 123 °C and 89 °C to 127 °C at the top of the Beaverhill Lake Group and Precambrian Basement, respectively.

2. Materials and Methods

All available well data, including BHT and True Vertical Depth (TVD) were exported from geoSCOUT from the study area. In total, there were 4261 data points.

2.1. BHT Data Filtering and Calculating Thermal Gradient

First, all points that did not include both BHT and TVD data were removed. The average thermal gradient (°C/km) from the surface for each data point was calculated using Equation (1):

$$\text{Thermal Gradient} = 1000 \times \frac{(\text{BHT} - \text{ST})}{\text{TVD}}, \tag{1}$$

where BHT is bottomhole temperature in °C, ST is surface temperature in °C (calculated from mean annual temperature), and TVD is true vertical depth in m. Mean annual temperature of Alberta from 1961 to 1990 was 0.6 °C [28]. The data were then plotted both by BHT vs. depth and thermal gradient vs. depth.

Next, the obvious outliers were removed, including wells with unusually high (>39 °C/km) or low (<20 °C/km) thermal gradients, because they were not consistent with the assumed conductive heat flow in the area and most of the data. The outliers of anomalously high temperatures at high depths were kept for future research, as it may be valuable to look at each data point to assess the legitimacy of the recording.

Other obvious outliers included wells where companies reported the same temperature for multiple wells with different depths. Also, temperature measurements for wells <1 km TVD have been shown to be biased, so these data points were removed [23]. From the work of others, individual outliers of high temperatures at greater depths could be Fahrenheit (F) recorded as Celsius (C), and outlier groups at shallow depth could be due to various factors such as incorrect reading or resetting of the maximum reading thermometers (which give anomalously high temperatures) and, occasionally, recording TVD and BHT as the same value [7]. These errors provide insight into the quality of the data and illustrate that great care must be taken to assess the validity of each measurement

After the filtering process, 1785 data points remained. BHT vs. depth data were plotted then fitted with a linear trendline to calculate the averaged uncorrected thermal gradient. The thermal gradient vs. depth data were also plotted and fitted with a linear trendline to assess the change in thermal gradient with depth.

The average thermal gradient of these wells was calculated to be 23.9 °C/km (Figure 4). The average thermal gradient change with depth was calculated to be −1.5 °C/km, suggesting that gradient does not change significantly with depth. This means that using the gradient to calculate temperature at depths may be straightforward, but caution should be taken when interpreting the results and extrapolating to depth due to uncertainty of the accuracy of the BHT data.
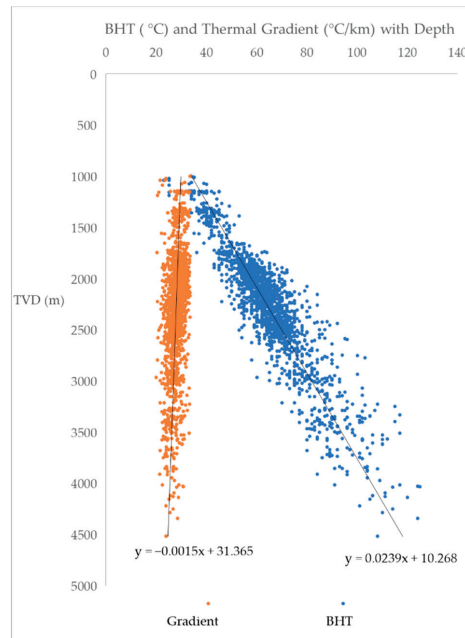
Figure 4. The calculated thermal gradient with depth of each well is shown as orange points. The BHT with depth of each well is shown as blue points.

2.2. Selecting Formation Tops

After the data were filtered, depths to target formations were analyzed. First, data points from horizontal wells, as well as re-entered well events, were removed. Additionally, six wells did not have wireline logs. In total, 1655 wells were assessed for formation tops. Depths to all formations between the Beaverhill Lake Group and the top of the Precambrian Basement were chosen by assessing wireline logs of each well that drilled to these formations and each TVD recorded. The wireline logs used were resistivity, gamma, neutron-density, and sonic if the former three logs were unavailable.

TVD data for all formation tops for each well were imported into Surfer. Next, grid files were created from TVD data for each formation and used to create contours with a simple Kriging method. Within the drilling area, only 2 wells penetrate to the Beaverhill Lake Formation and deeper. Therefore, the elevation contour maps were extrapolated to calculate the expected depth to Beaverhill Lake Group and the Precambrian Basement from the 16 wells that penetrate to the Wabamun Formation in the drilling area. This was done using the Point Sample calculator on Surfer.

2.3. Temperature and Elevation Maps

After formation tops were selected and depths to the Beaverhill Lake Group and the Precambrian Basement were extrapolated, we calculated the expected temperature at these formation tops using Equation (2):

$$\text{T}_{\text{Formation}} = \frac{\text{Thermal Gradient} \times \text{Formation Top TVD}}{1000}, \tag{2}$$

where $\text{T}_{\text{Formation}}$ is the temperature at the top of the formation at each well in °C, and Formation Top TVD is the depth to the top of the formation in m. For the study area, we used the TVDs from the well data. For the drilling area, we used the TVDs calculated from the elevation contour maps.

T_Formation data for each well were imported into Surfer. Next, grid files were created from the temperature data for both formations and used to create contours with a simple Kriging method.

3. Results

Within the study area, the depth to the top of the Beaverhill Lake Group ranges from 3104 m to 4094 m (Figure 5a) and temperature at the top ranges from 72 °C to 123 °C (Figure 5b). The depth to the top of the Precambrian Basement ranges from 3205 m to 4223 m (Figure 6a) and temperature at the top ranges from 74 °C to 124 °C (Figure 6b).
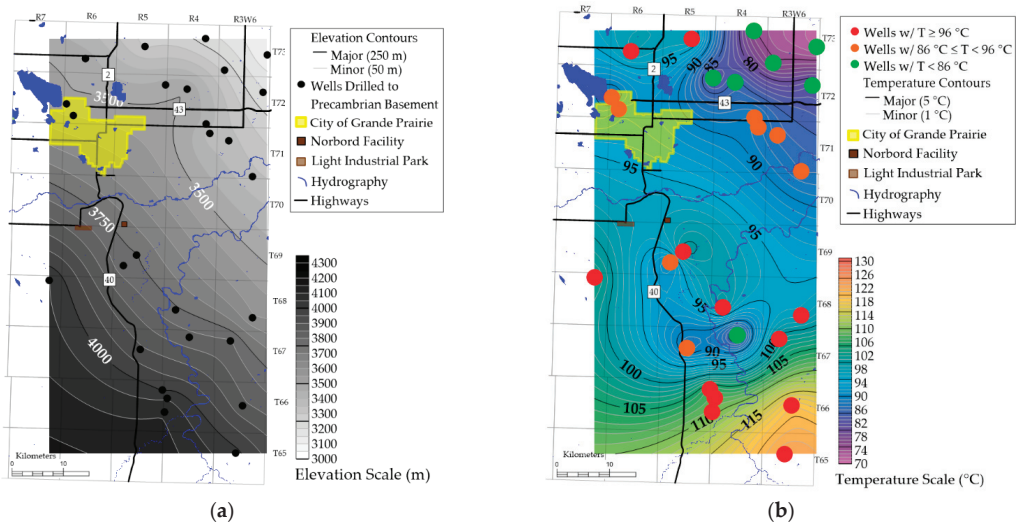
Figure 5. Contour maps of the study area for the Beaverhill Lake Group showing (**a**) depth to the top and (**b**) temperature at the top.
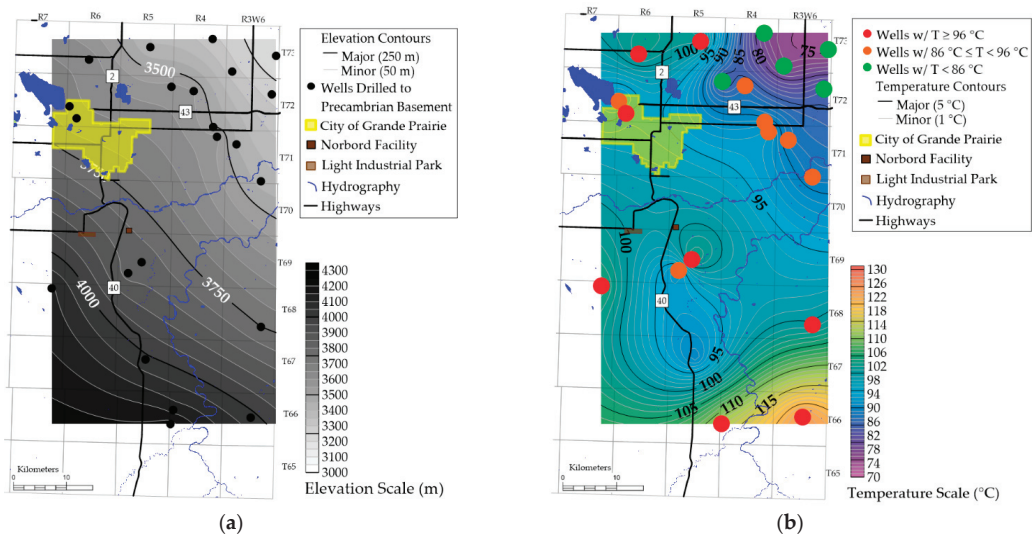
Figure 6. Contour maps of the study area for the Precambrian Basement showing (**a**) depth to the top and (**b**) temperature at the top.

Within the drilling area, the depth to the top of the Beaverhill Lake Group ranges from 3634 m to 3839 m (Figure 7a) and temperature at the top ranges from 87 °C to 123 °C (Figure 7b). The depth to the top of the Precambrian Basement ranges from 3740 m to 3906 m (Figure 8a) and temperature at the top ranges from 89 °C to 127 °C (Figure 8b).
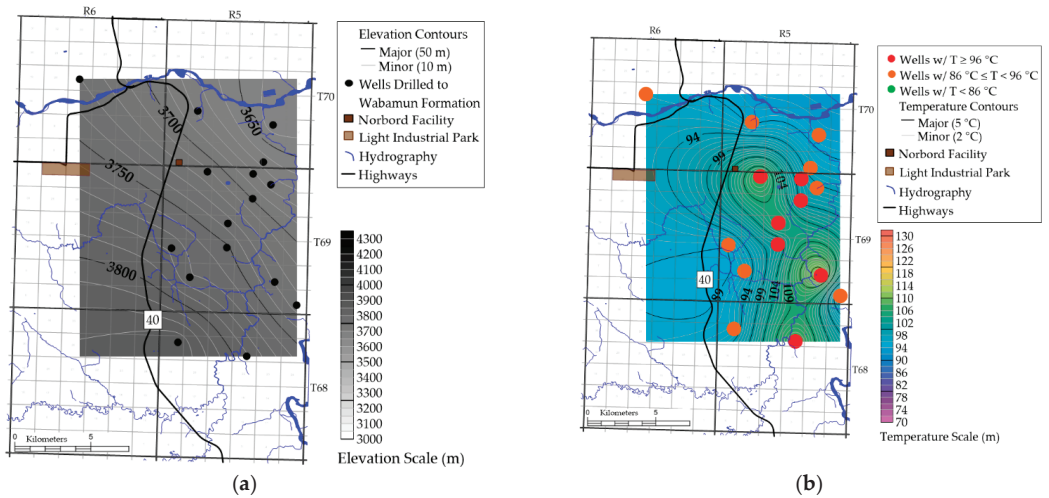
Figure 7. Contour maps of the drilling area for the Beaverhill Lake Group showing (**a**) depth to the top and (**b**) temperature at the top.
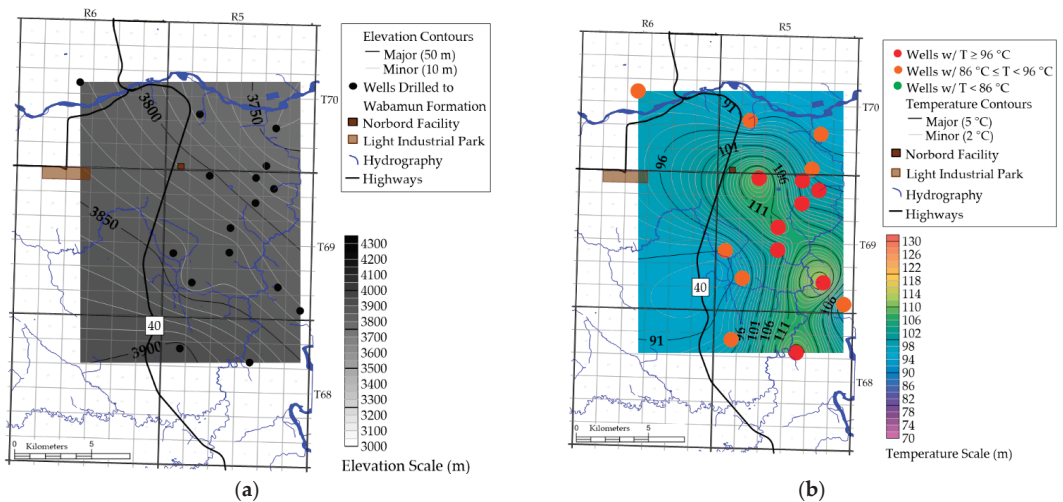
Figure 8. Contour maps of the drilling area for the Precambrian Basement showing (**a**) depth to the top and (**b**) temperature at the top.

On both a regional and local scale, the Beaverhill Lake Group and the Precambrian Basement both appear to be dipping to the southwest. From the limited data set, there are no apparent structural features that may indicate faulting through the formation tops.

Based on the temperature maps, there is a rough correlation between the southwest dipping stratigraphy and increasing temperature within the study area. This correlation,

however, is not present in the drilling area, which may be due to the scarce data set. There does appear to be a minor southeast- and south-trending temperature high which may be caused by a structural feature in this direction. However, this data set is too scarce to confidently determine the existence of this structure.

Because the temperature data is not corrected, great care must be taken when interpreting the results. The oil and gas data do not include fluid circulation time during drilling; therefore, it is unknown if BHTs represent equilibrium temperature. The actual formation temperatures will not be known until the first well is drilled and logged using proper equipment and methods. The temperatures from this study provide a conservative estimate for the purposes of exploration.

4. Conclusions

For a geothermal project to be economic in the area at this time, the estimated maximum depth of target formations must be less than 4500 m, and thermal fluids of at least 120 °C provide the best opportunity for commercial viability. The Devonian carbonate and sandstone formations between the Beaverhill Lake Group and the Precambrian basement are less than 4500 m depth in the study area. Within the drilling area, there are sections where temperatures have been calculated to almost reach or exceed 120 °C to the east and southeast of the Norbord OSB plant. Because we expect the BHT data to provide a lower-end temperature estimate, the actual formation temperatures may be higher. Based on these results, the Alberta No. 1 geothermal power and direct use heat project in this area fits the depth and temperature criteria to be successful. Other geological considerations that will be assessed include flow rate potential of these formations and areas of fluid convection such as faults and fractures, which can be delineated by seismic data.

Author Contributions: Conceptualization, C.H. and K.H.; Methodology, K.H., C.H., D.C. and Y.C.; Software, K.H. and D.C.; Validation, K.H., C.H., D.C. and Y.C.; Formal Analysis, K.H. and D.C.; Investigation, K.H. and D.C.; Resources, K.H. and D.C.; Data Curation, K.H. and D.C.; Writing—Original Draft Preparation, K.H.; Writing—Review & Editing, K.H. and C.H.; Visualization, K.H.; Supervision, C.H.; Project Administration, K.H. and C.H. All authors have read and agreed to the published version of the manuscript.

References

1. Hickson, C.J.; Huang, K.; Cotterill, D.; Gosnold, W.; Benoit, D. *Updated Resource Assessment*; Alberta No. 1 Internal Report; Edmonton, AB, Canada, 2020.
2. Davies, G.R.; Smith, L.B. Structurally controlled hydrothermal dolomite reservoir facies: An overview. *AAPG Bull.* **2006**, *90*, 1641–1690. [CrossRef]
3. Alberta Geological Survey. Available online: https://ags.aer.ca/publication/alberta-table-formations (accessed on 25 October 2020).
4. Harrison, W.E.; Luza, K.V.; Prater, M.L.; Chueng, P.K. *Geothermal Resource Assessment of Oklahoma*; Oklahoma Geological Survey, Special Publication 83-1; Oklahoma Geological Survey: Norman, OK, USA, 1983.
5. Horner, D.R. Pressure Build-up in Wells. In Proceedings of the 3rd World Petroleum Congress, The Hague, The Netherlands, 28 May–6 June 1951.

6. Stutz, G.; Williams, M.; Frone, Z.; Reber, T.; Blackwell, D.; Jordan, T.; Tester, J. A Well by Well Method for Estimating Surface Heat Flow for Regional Geothermal Resource Assessment. In Proceedings of the Thirty-Seventh Workshop on Geothermal Reservoir Engineering, Stanford, CA, USA, 30 January–1 February 2012.

7. Gray, D.A.; Majorowicz, J.; Unsworth, M. Investigation of the geothermal state of sedimentary basins using oil industry thermal data: Case study from Northern Alberta exhibiting the need to systematically remove biased data. *J. Geophys. Eng.* **2012**, *9*, 534–548. [CrossRef]

8. Grasby, S.E.; Allen, D.M.; Bell, S.; Chen, Z.; Ferguson, G.; Jessop, A.; Kelman, M.; Ko, M.; Majorowicz, J.; Moore, M.; et al. *Geothermal Energy Resource Potential of Canada*; Geological Survey of Canada, Open File 6914; Natural Resources Canada: Ottawa, ON, Canada, 2012. [CrossRef]

9. Anglin, F.M.; Beck, A.E. Regional heat flow pattern in Western Canada. *Can. J. Earth Sci.* **1965**, *2*, 176–182. [CrossRef]

10. Bachu, S.; Burwash, R.A. Geothermal regime in the Western Canadian Sedimentary Basin. In *Geological Atlas of the Western Canada Sedimentary Basin*; Mossop, G.D., Shetsen, I., Eds.; Canadian Society of Petroleum Geologists and Alberta Research Council: Calgary, AB, Canada, 1994.

11. Ardakani, E.P. Regional Geophysical Study of the Athabasca Region, Northeastern Alberta: Implications for Geothermal Development. Ph.D. Thesis, University of Alberta, Edmonton, AB, Canada, 2016.

12. Hackbarth, D.A. Groundwater temperatures in the Athabasca Oil Sands area, Alberta. *Can. J. Earth Sci.* **1978**, *15*, 1689–1700. [CrossRef]

13. Jones, F.W.; Lam, H.L.; Majorowicz, J.A. Temperature distributions at the Paleozoic and Precambrian surfaces and their implications for geothermal energy recovery in Alberta. *Can. J. Earth Sci.* **1985**, *22*, 1774–1780. [CrossRef]

14. Lam, H.L.; Jones, F.W. Geothermal gradients of Alberta in Western Canada. *Geothermics* **1984**, *13*, 181–192. [CrossRef]

15. Majorowicz, J.A. Regional heat flow pattern and lithospheric geotherms in northeastern British Columbia and adjacent Northwest Territories, Canada. *Bull. Can. Pet. Geol.* **2005**, *53*, 51–66. [CrossRef]

16. Majorowicz, J.; Gosnold, W.; Gray, A.; Safanda, J.; Klenner, R.; Unsworth, M. Implications of Post-Glacial Warming for Northern Alberta Heat Flow—Correcting for the Underestimate of the Geothermal Potential. In Proceedings of the GRC Transactions, Reno, NV, USA, 20 September–3 October 2012.

17. Majorowicz, J.; Grasby, S.E. Deep geothermal energy in Canadian sedimentary basins VS. Fossils based energy we try to replace—Exergy [KJ/KG] compared. *Renew. Energy* **2019**, *141*, 259–277. [CrossRef]

18. Majorowicz, J.; Nieuwenhuis, G.; Unsworth, M.; Phillips, J.; Verveda, R. High Temperatures Predicted in the Granitic Basement of Northwest Alberta—An Assessment of the EGS Energy Potential. In Proceedings of the Thirty-Ninth Workshop on Geothermal Reservoir Engineering, Stanford, CA, USA, 24–26 February 2014.

19. Majorowicz, J.; Unsworth, M.; Chacko, T.; Gray, A.; Heaman, L.; Potter, D.K.; Schmitt, D.; Babadagli, T. Geothermal energy as a source of heat for oil sands processing in Northern Alberta, Canada. In *Heavy-Oil and Oil-Sand Petroleum Systems in Alberta and Beyond*; Hein, F.J., Leckie, D., Larter, S., Suter, J., Eds.; American Association of Petroleum Geologists: Tulsa, OK, USA, 2013; pp. 1–22.

20. Majorowicz, J.A.; Jessop, A.M. Regional heat flow patterns in the Western Canadian Sedimentary Basin. *Tectonophysics* **1981**, *74*, 209–238. [CrossRef]

21. Majorowicz, J.A.; Garven, G.; Jessop, A.; Jessop, C. Present Heat Flow along a Profile Across the Western Canada Sedimentary Basin: The Extent of Hydrodynamic Influence. In *Geothermics in Basin Analysis*; Förster, A., Merriam, D.F., Eds.; Springer: Boston, MA, USA, 1999; pp. 61–79.

22. Nieuwenhuis, G.; Lengyel, T.; Majorowicz, J.; Grobe, M.; Rostron, B.; Unsworth, M.J.; Weides, S. Regional-Scale Geothermal Exploration Using Heterogeneous Industrial Temperature Data; a Case Study from the Western Canadian Sedimentary Basin. In Proceedings of the World Geothermal Congress, Melbourne, Australia, 19–24 April 2015.

23. Weides, S.; Majorowicz, J. Implications of Spatial Variability in Heat Flow for Geothermal Resource Evaluation in Large Foreland Basins: The Case of the Western Canada Sedimentary Basin. *Energies* **2014**, *7*, 2573–2594. [CrossRef]

24. Weides, S.; Moeck, I.; Majorowicz, J.; Grobe, M. The Cambrian Basal Sandstone Unit in central Alberta—An investigation of temperature distribution, petrography, and hydraulic and geomechanical properties of a deep saline aquifer. *Can. J. Earth Sci.* **2014**, *51*, 783–796. [CrossRef]

25. Weides, S.; Moeck, I.; Schmitt, D.; Majorowicz, J. Geothermal Assessment of Paleozoic Aquifers in the Central Alberta Basin, Canada. In Proceedings of the World Geothermal Congress, Melbourne, Australia, 19–24 April 2015.

26. Weides, S.N.; Moeck, I.S.; Schmitt, D.R.; Majorowicz, J.A.; Ardakani, E.P. Characterization of Geothermal Reservoir Units in Northwestern Alberta by 3D Structural Geological Modelling and Rock Property Mapping. In Proceedings of the Thirty-Eighth Workshop on Geothermal Reservoir Engineering, Stanford, CA, USA, 11–13 February 2013.

27. Huang, K.; Gosnold, W.; Hickson, C.; Benoit, D. Using Oil and Gas Data to Assess Geothermal Resources Within the Western Canadian Sedimentary Basin in Alberta. In Proceedings of the GRC Transactions, Virtual Conference, 19–23 October 2020.

28. Schneider, R.R. *Alberta's Natural Subregions under a Changing Climate: Past, Present and Future*; Report prepared for the Biodiversity Management and Climate Change Adaptation Project; AMBI: Edmonton, AB, Canada, 2013.

Dynamic and Static Investigation of Ground Heat Exchangers Equipped with Internal and External Fins

Atefeh Maleki Zanjani [1], Kobra Gharali [1,2,*], Armughan Al-Haq [2] and Jatin Nathwani [2,3,*]

[1] School of Mechanical Engineering, College of Engineering, University of Tehran, Tehran 11155-4563, Iran; atefeh.malekiz@ut.ac.ir

[2] Waterloo Institute for Sustainable Energy (WISE), University of Waterloo, Waterloo, ON N2L 3G1, Canada; armughan.al-haq@uwaterloo.ca

[3] Department of Management Sciences, Department of Civil and Environmental Engineering, University of Waterloo, Waterloo, ON N2L 3G1, Canada

* Correspondence: kgharali@ut.ac.ir or kgharali@uwaterloo.ca (K.G.); nathwani@uwaterloo.ca (J.N.)

Abstract: Using fins on the inner and outer surfaces of pipes is one method to improve the heat transfer rate of ground heat exchangers (GHEs), thereby reducing the borehole depth and construction and operation costs. Results of 3D numerical studies of simple and finned U-tubes with outer and inner fins are evaluated for GHEs under similar physical conditions. Dynamic and static simulations show the effects of longitudinal fins on the thermal performance of borehole heat exchangers (BHEs) and heat transfer rate between circulating fluid and soil around pipes, while the dynamic tests include short timescale and frequency response tests. The results indicate that the maximum fluid temperature change is about 2.9% in the external finned pipe and 11.3% in the internal finned pipe compared to the finless pipe. The effects of the inlet velocity on temperature profiles, the patterns of the velocity and temperature contours due to the borehole curvature and the response times of the systems under various frequencies are also investigated in detail.

---

1. Introduction

Ground source heat pump systems (GSHPs) offer the potential for significant energy savings, through low maintenance costs and contribute to reducing greenhouse gas emissions. GSHPs are used for heating/cooling residential and commercial buildings and for providing domestic hot water [1,2]. The use of GSHPs proved to be a technically feasible and economically viable solution as compared to other heating, ventilation, and air conditioning (HVAC) systems in cooling dominated environments such as the Arabian Peninsula where the air conditioning (A/C) systems account for 65% of the energy consumption strictly from fossil fuels [3]. The GSHPs are fully capable of meeting the cooling demands of buildings in hot climates, specifically, in the Middle East [4]. The most common type of ground heat exchangers is the vertical ground heat exchanger with the length of 100–150 m [5,6]. The empty space between pipe and borehole wall is usually filled with grout which helps to improve the heat transfer rate between circulating fluid inside pipes and ground [7]. Since the initial costs of vertical borehole heat exchangers (BHEs) are relatively high due to the limitations of drilling and manpower, efforts are being made to increase the heat transfer rate between fluid and soil around the pipes in various ways, and thus reducing the borehole depth [8].

Several methods have been proposed to calculate and reduce borehole resistance. In most thermal response test (TRT) analyses, the average of inlet and outlet temperatures of the fluid is used to calculate the fluid temperature along the ground heat exchanger (GHE). Some researchers have shown

that the average of inlet and outlet temperatures can cause significant errors in results and suggested alternative methods for estimating the average fluid temperature [9–15].

Grout materials are used to fill spaces between pipes and the soil around the borehole which can play a key role in the heat transfer rate between the fluid and undisturbed ground. Some researchers have worked on the effects of different grout materials on the thermal performance of the GSHP systems and found the best option for grout materials [16]. Borinaga et al. [17] used four different boreholes with the same geometric and geological characteristics but different grout materials to determine the appropriate thermal conductivity. They reported a proper type of grout for the thermal response test. Erol et al. [18] evaluated the performance of various grout materials and tested the effects of adding graphite on the thermal properties of grout material.

Various numerical and analytical models have been developed based on linear source or cylindrical source theory. Using these models, the influences of different geometric and thermal properties on the static and dynamic behavior of a BHE has been investigated. Eskilson [19] proposed a G-function to describe borehole performance. G-function curves based on borehole geometry were reported by calculating the soil temperature using the finite difference method. Beier [20] developed an analytical solution for calculating the vertical temperature profile of the fluid inside the pipe and the ground temperature distribution by using Laplace transforms.

There are several studies about GSHPs based on the Computational Fluid Dynamics (CFD) method. Pu et al. [21] investigated the effects of Reynolds number, pipe diameter, and U-tube shank spacing on the thermal performance of GHEs. The results showed that by increasing the Reynolds number and the pipe diameter in laminar flow, better performance can be achieved. Esen et al. [22] performed a numerical and experimental study to evaluate the temperature distribution in GHE using three U-tube BHEs with the same diameters and different depths. Li et al. [23] compared the thermal performance of U-tube heat exchangers with four different standard diameters. Zhu et al. [24] studied the thermal performance of a double U-tube GHE and the effects of parameters such as inlet velocity, temperature, and operating distance on the temperature distribution of the soil. Lee and Lam [25] performed computer simulations of borehole heat exchanger to determine ground and borehole the temperature along depth using a finite difference model.

Yang and Lee [26] performed a dynamic thermal analysis on a 4-ton residential GSHP and observed a design trade-off between cooling and heating modes. They obtained the optimal value of the evaporator area fraction in both cooling and heating modes.

Kharseh et al. [3] studied the energy savings by using GSHP systems in the residential buildings sector in cooling-dominated environments. It was found out that the energy savings by using GSHPs when compared to the conventional air source heat pump system are much higher. Similary, Beckers et al. [27] performed a techno-economic analysis on a hybrid ground-source heat pump systems for cooling-dominated applications. The results of their simulation showed that a ground-source heat pump-based system helped the owner to save up to 30% of lifetime electricity consumption as compared to an air-source heat pump-based system. In contrast, the air-source heat pump-based system can have up to 10% lower total cost of ownership due to the lower upfront capital cost. A study by Salem and Hashim [4] discussed that the commercial buildings in Dubai have fairly high occupancy, fluctuating demands, and extensively diverse cooling requirements within individual zones, which are difficult to meet effectively and efficiently with conventional HVAC systems. They concluded that there is potential for the efficient use of ground couple heat pumps (GCHPs) in Dubai commercial buildings leading to significant savings in energy usage and operating costs and substantial reduction in CO_2 and NOx emissions over a 20 year life cycle as opposed to other HVAC options.

The performance of fins for enhancing heat transfer of heat exchangers generally has been considered previuosly [28] and Bouhucina et al. [29] investigated the influence of internal fins on the dynamic and thermal performance of U-tube GHEs. Using fins increased heat transfer rate up to 7%. Saeidi et al. [30] performed a numerical simulation of GSHPs with a spiral pipe and investigated the

effects of a fin on the outer surface of the spiral pipes. The results showed that fins can improve thermal conductivity due to increased surface area.

Previous studies have been conducted to find a method to increase the thermal efficiency of GSHP systems. These methods were based on borehole configuration, thermal properties of the ground and grout materials, and generally finding suitable solutions to reduce the borehole depth. To the best of the authors' knowledge, the impacts of internal and external fins on the thermal performance of U-tube GHEs have not been compared yet which is the aim of the current study. Moreover, both dynamic and static behavior of simple and finned U-tube GHEs will be evaluated to obtain the best efficiency. For the dynamic tests, various conditions such as short timescale response and sinusoidal response tests will be investigated for the BHE equipped with fins. The velocity of the inlet flow with the resultant flow filed patterns and the frequency of the input temperature with its effects on the response time and amplitudes are other important parameters that are added to this investigation.

2. Case Study

The geometry of the simple U-tube ground heat exchanger consists of a U-tube, grout materials, and soil around the borehole, Figure 1. The grout materials and the surrounding soil are considered as two cylinders with different radii, the radius of the ground is approximately 16 times the radius of the borehole.
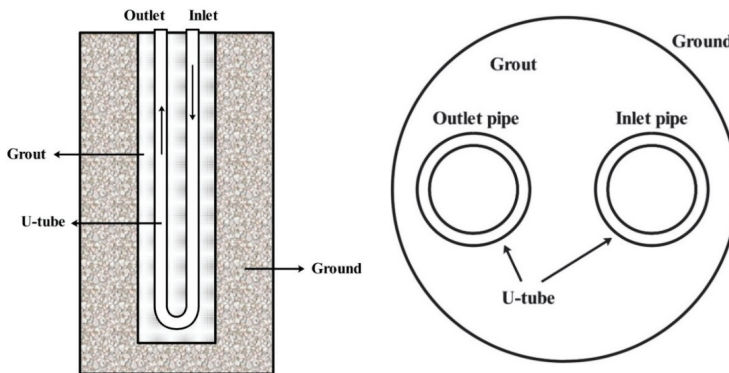
Figure 1. Schematic diagram of a single U-tube borehole heat exchanger.

The cross-sections of simple and finned U-tubes are illustrated in Figure 2. The details of the geometry of U-tube GHE are provided in Table 1. The borehole has a diameter of 128 mm and a depth of 25 m, which includes a vertical U-tube with a thickness of 2 mm. The ground around the borehole is a cylinder of 2 m in diameter with the same depth as the borehole. In finned pipes, six longitudinal fins with dimensions of 2×6 mm^2 (2 mm thickness and 6 mm length) are used in each leg of the U-tube. The fins are placed in a symmetrical arrangement relative to the horizontal axis.

Table 1. Geometric properties of U-tube ground heat exchanger (GHE).

Parameters	Value
Borehole diameter (mm)	128
Inner diameter of pipe (mm)	30
Outer diameter of pipe (mm)	34
Distance between centers of U-tube pipes (mm)	55
Borehole length (m)	25
Ground diameter (m)	2
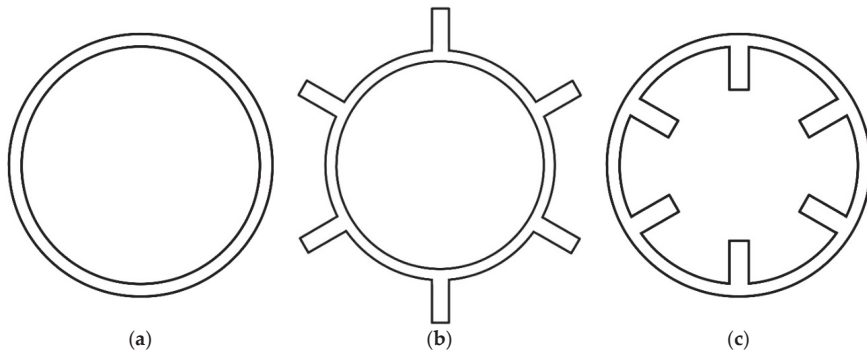
Figure 2. Cross-sections of smooth and finned U-tubes: (**a**) simple U-tube; (**b**) U-tube with outer fins; (**c**) U-tube with inner fins.

3. Numerical Setup

3.1. Mesh Generation

The mesh generation is performed based on both structured and unstructured grids. After defining the boundaries and edges of different parts of the geometry as lines or curves, a two-dimensional grid is created in Cartesian coordinates and then this 2D grid is extended in the direction of depth. The cells are equally or exponentially distributed in different parts of the geometry. For this purpose, a high number of cells are considered for places with steep temperature slope, for example, near the borehole and pipe walls. For the areas where the temperature slope is low, the size of the cells is increased. Figure 3 shows the computational mesh of the simple U-tube GHE. The upper and lower surfaces around the borehole are made up of 600 cells, which have bigger sizes in the middle part. The borehole is divided vertically into 70 layers with different distances. The curved area of the U-tube at the bottom of the pipe requires finer and different mesh from the other domains of the geometry due to the complexity of the geometry. Around the curved edges, using unstructured meshes is more practical.

Although the accuracy of the calculations increases with the number of cells, the higher computation time should also be considered. As a result, by examining the grid independency test, it is possible to obtain a suitable and optimal mesh with the necessary accuracy to achieve the final results and to avoid increasing computation time. Grid independency of simple and finned U-tube GHE has been investigated by varying the number of cells from coarse mesh to finer mesh. Table 2 shows the outlet fluid temperature in the simple U-tube GHE under the steady-state condition for different grid cells. A total cell number of 330×10^3 is used for smooth U-tube GHE since no temperature change is observed after increasing the number of cells. Grid independency for finned U-tube GHEs is presented in Table 3. Due to the small dimensions of the fins used on the inner and outer surfaces of the pipes, the numerical models require a finer grid size than a simple pipe. The number of cells specified in GHEs with external and internal fins is 500×10^3 and 420×10^3, respectively.

Table 2. Grid-independency test of smooth U-tube GHE.

	Mesh 1	Mesh 2	Mesh 3
Elements number ($\times 10^3$)	174	330	500
Fluid outlet temperature (°C)	24.86	24.85	24.85

Table 3. Grid-independency test of finned U-tube GHEs.

		Mesh 1	**Mesh 2**	**Mesh 3**
U-tube with external fins	Element number ($\times 10^3$)	300	500	600
	Fluid outlet temperature (°C)	24.64	24.71	24.72
U-tube with internal fins	Element number ($\times 10^3$)	300	420	600
	Fluid outlet temperature (°C)	24.64	24.67	24.67
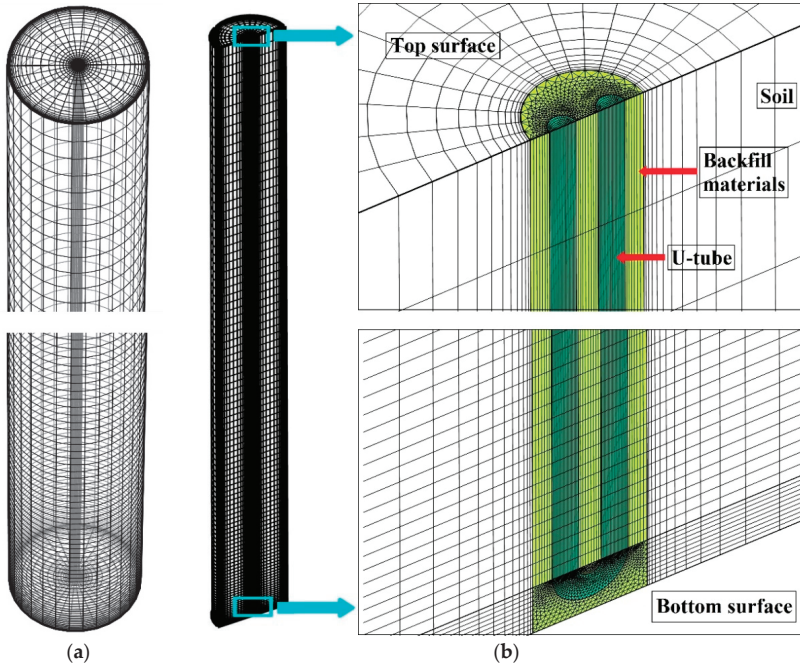
Figure 3. Three-dimensional mesh: (**a**) computational mesh around borehole; (**b**) half of computational domain.

3.2. Solver

The physical properties of circulating fluid, U-tube, backfill material, soil, and aluminum fins are demonstrated in Table 4. For pipes, high-density polyethylene (HDPE) material is considered. The selected grout material is a combination of silica sand and bentonite. Water is used as the fluid inside the pipes.

Table 4. Physical properties of materials.

Material	Density (kg/m^3)	Specific Heat Capacity (J/kg·K)	Thermal Conductivity (W/m·K)
Fluid	997	4148	0.6
U-tube	950	1500	0.44
Grout	1800	840	0.73
Soil	2200	2000	2.5
Aluminum fin	2700	904	237

The undisturbed ground temperature is defined as the initial temperature of the entire simulation domain, including fluid, U-tube, grout, and soil. This study is performed for the cooling mode of the system; therefore, the fluid is warmer than the surrounding soil. The constant temperature boundary condition is applied to the outer boundary of the simulation domain where there is no heat flux along this boundary and its temperature should not change until the end of the simulation.

According to the previous studies [29], since the fluid velocity is an important parameter in the heat transfer and the temperature change of the fluid along the borehole length, the same mass flow rate in pipes as a boundary condition is not a proper condition and the same inlet velocity is applied for the inlet condition of the pipes. The focus is on investigating the effects of the inner and outer fins on ground heat exchangers with the same physical dimensions and same inlet velocity; so, finding the more effective fin cannot be based on the same flow rate or the same hydraulic diameter. Comparing the simple and finned pipes with the same mass flow rate at the inlet of pipes showed that the axial velocity in the finned U-tube (inner surface) will be higher than the simple U-tube because of the hydraulic diameter reduction which changes the heat transfer rate significantly.

The incompressible Newtonian fluid is used inside the pipes. The soil is considered homogeneous and the physical properties of the fluid, pipe, grout material, and soil are assumed to be constant. The temperature of the ground's surface boundaries is constant and uniform, and any changes in the temperature of the ground over depth and time are ignored. The flow rate is constant along the pipe. A laminar flow is considered for all the simulations. The continuity and momentum equations are solved with the energy equation which is considered as [21,31]:

$$\frac{\partial}{\partial t}(\rho T) + \frac{\partial}{\partial x_j}(\rho T u_j) = \frac{\partial}{\partial x_j}\left(\frac{\mu}{Pr}\cdot\frac{\partial u_i}{\partial x_j}\right) \tag{1}$$

where u is velocity vector, ρ is fluid density, μ is dynamic viscosity, T is temperature vector and Pr represents the molecular Prandtl number. The heat conduction in grout and ground is illustrated in Equation (2),

$$\frac{\partial T}{\partial t} = \alpha \nabla^2 T \tag{2}$$

where α is the thermal diffusivity of grout and ground.

4. Validation

The experimental results of Beier et al. [32] have been used for validation. TRT analysis was performed to evaluate the thermal performance of an 18.3 m borehole including a U-shaped pipe. An aluminum cylindrical pipe with an inner diameter of 126 mm was considered as the borehole wall. The borehole was located in a large sandbox. The square cross-section box with sides of 1.8 m used as the ground around the well was filled with wet sand. The geometric and physical configurations of the borehole are listed in Table 5.

Table 5. Geometric and thermal properties for the experimental test of Beier et al. [32].

Parameters	Value
Borehole diameter (mm)	126
Inner diameter of pipe (mm)	27.33
Outer diameter of pipe (mm)	33.40
Distance between centers of U-tube pipes (mm)	53
Borehole length (m)	18.3
Pipe thermal conductivity (W/m·K)	0.39
Grout thermal conductivity (W/m·K)	0.73
Ground thermal conductivity (W/m·K)	2.82
Average volumetric flow rate (L/s)	0.197
Initial temperature of ground and grout (°C)	22

Figure 4 shows the comparison between the inlet/outlet flow temperatures from the current numerical simulation and the experimental data of Beier et al. [32]. The inlet temperature of both 2D and 3D models are the same as that of experimental results. The 3D outlet temperature is closer to the experimental results. The maximum temperature difference between the present 3D model and the experimental results is 1.2%, providing acceptable agreement.
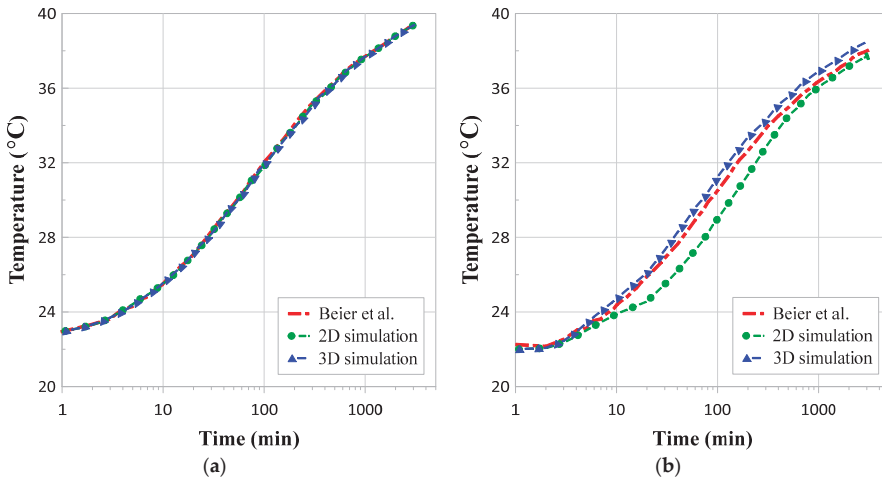
Figure 4. Temperature changes from 2D and 3D simulation results vs. temperature changes of experimental data of Beier et al. [32]: (**a**) inlet; (**b**) outlet temperature.

5. Results and Discussions

5.1. Long Timescale Response

Initially, the static behavior for the smooth and the finned U-shaped GHEs is investigated. All the results presented in this section are obtained from steady-state simulations [33]. The fluid inlet temperature has a value of 30 °C and far-field temperature is considered to be 15 °C. In addition, the initial temperature of the whole simulation domains is assumed to be equal to the soil temperature around the borehole. Different fluid velocities are considered as 0.02, 0.04, 0.06 m/s. The results are shown in Table 6. The selected velocities keep the laminar flow condition inside the pipes.

Using internal fins to the mentioned dimensions have reduced the cross-section area by about 1.11 times compared to the smooth pipe. Therefore, the mass flow rate in the pipe with internal fins has decreased compared to the other two models by the same ratio. A comparison of the outlet fluid temperatures between three pipes shows that the fluid temperature change of the pipe with the inner fins is greater than that of the pipe with the outer fins. According to the values listed in Table 6, the temperature change of the fluid in the pipe with external fins at velocities of 0.06, 0.04, and 0.02 m/s has increased up to 2.9%, 2.2%, and 0.5% compared to that of the simple pipe. These values are increased to 11.3%, 9% and 5% for the pipe with internal fins.

Table 6. Numerical results of simple and finned U-tube GHEs.

	Velocity (m/s)	**0.06**	**0.04**	**0.02**
	Flow rate (kg/s)	0.042	0.028	0.014
Simple U-tube	Reynolds number	2049	1366	683
	Outlet fluid temperature (°C)	25.20	23.73	20.88
	Borehole wall temperature (°C)	20.46	19.93	18.72

Table 6. *Cont.*

Velocity (m/s)		0.06	0.04	0.02
U-tube with outer fins	Flow rate (kg/s)	0.042	0.028	0.014
	Reynolds number	2049	1366	683
	Outlet fluid temperature (°C)	25.06	23.59	20.83
	Borehole wall temperature (°C)	20.67	20.08	18.78
U-tube with inner fins	Flow rate (kg/s)	0.038	0.025	0.013
	Reynolds number	1945	1297	648
	Outlet fluid temperature (°C)	24.66	23.13	20.42
	Borehole wall temperature (°C)	20.50	19.89	18.55

5.2. Short Timescale Response

Transient simulations of BHE show the dynamic behavior of the system in a short timescale [33]. Transient simulation results of simple and finned U-tube GHE are shown in Figure 5. The inlet velocity in three numerical models (simple, inner finned and outer finned U-tube) is 0.053 m/s. The inlet fluid temperature is 30 °C and the far field temperature (the soil temperature) is considered 15 °C, which has been used as the initial temperature of whole simulation domains (including the pipe, the fluid, grout materials and the soil). The outlet temperature of all three pipes reached a steady state after 330 min and no change was observed in the graphs after this time. The simulation is for the cooling mode of the system, and the inlet temperature of the fluid is higher than the temperature of the initial temperature and that of the soil around the borehole. The fluid temperature decreases as it passes through the pipe.
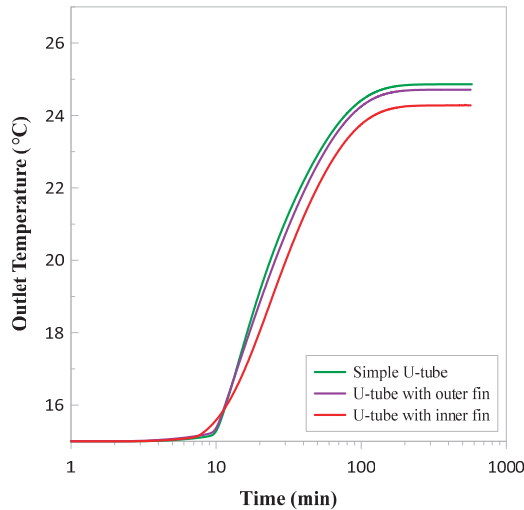
Figure 5. Outlet temperature of fluid in simple and finned U-tube GHE.

The outlet fluid temperature has reached 24.86 °C in a simple pipe, 24.71 °C in a pipe with external fins and 24.28 °C in a pipe with internal fins. The difference between the inlet and outlet temperatures of the fluid in the simple U-tube is 5.14 °C and in the finned U-tube on the outer and inner surfaces is 5.29 °C and 5.72 °C, respectively. The temperature reduction in the fluid in the outer and inner finned U-tube has increased, respectively, 2.9% and 11% compared to the simple pipe.

Frequency Response Test

BHEs are affected by temperature fluctuations at different ranges of time scales. Therefore, applying a periodic condition of the fluid inlet temperature instead of constant value is a useful way to

describe the thermal response of the borehole heat exchangers in short timescales [33]. To evaluate and compare the thermal responses of three numerical models, the inlet fluid temperature is applied as a sinusoidal function with the same amplitude and different frequencies. The inlet velocity for all three pipes is 0.053 m/s. The mass flow rates for the simple and external finned U-tube are 0.038 kg/s and for the U-tube with internal fins is 0.034 kg/s. The inlet fluid temperature is applied as follows [33]:

$$T_{in} = T_1 + a_{in}\,sin(2\pi f t) = T_1 + a_{in}\,sin\left(\frac{2\pi}{B}t\right) \tag{3}$$

where a_{in} is the inlet wave amplitude, T_1 is the mean of the wave, f is the frequency and B is the period. The outlet fluid temperature by variation of amplitude (a_{out}) and mean number (T_2) is defined as:

$$T_{out} = T_2 + a_{out}\,sin(2\pi f t + \varphi) = T_2 + a_{out}\,sin\left(\frac{2\pi}{B}t + \frac{2\pi}{\Delta B}\right) \tag{4}$$

where φ is the phase shift and ΔB is the time shift of outlet wave that shows delay in the system responses. The outlet temperature of the fluid obtained from the 3D simulation in response to the inlet temperature as a sine wave with 80 and 40 min periods (frequency of 1/4800 Hz and 1/2400 Hz) and the amplitude of 8 °C for three simple and finned U-tubes are shown by Figures 6 and 7. By increasing the wave frequency (1/2400 Hz), the output wave amplitude decreases due to the reduction in the system response time compared to the first mode (1/4800 Hz).
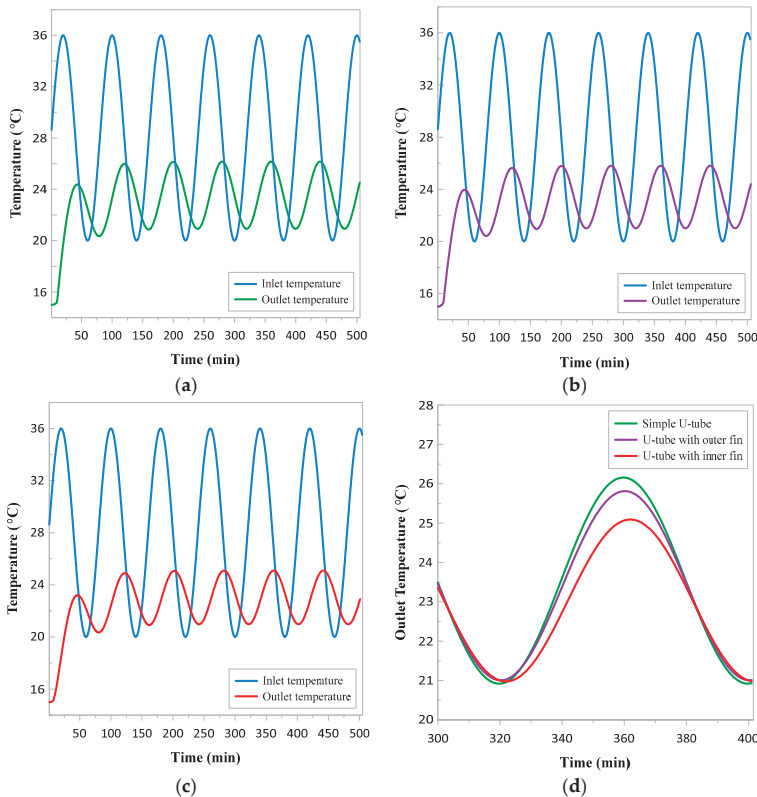
Figure 6. Fluid inlet and outlet temperatures with a frequency of 1/4800 Hz: (**a**) simple U-tube; (**b**) U-tube with outer fins; (**c**) U-tube with inner fins; (**d**) comparison of fluid outlet temperatures in three simple and finned U-tubes.
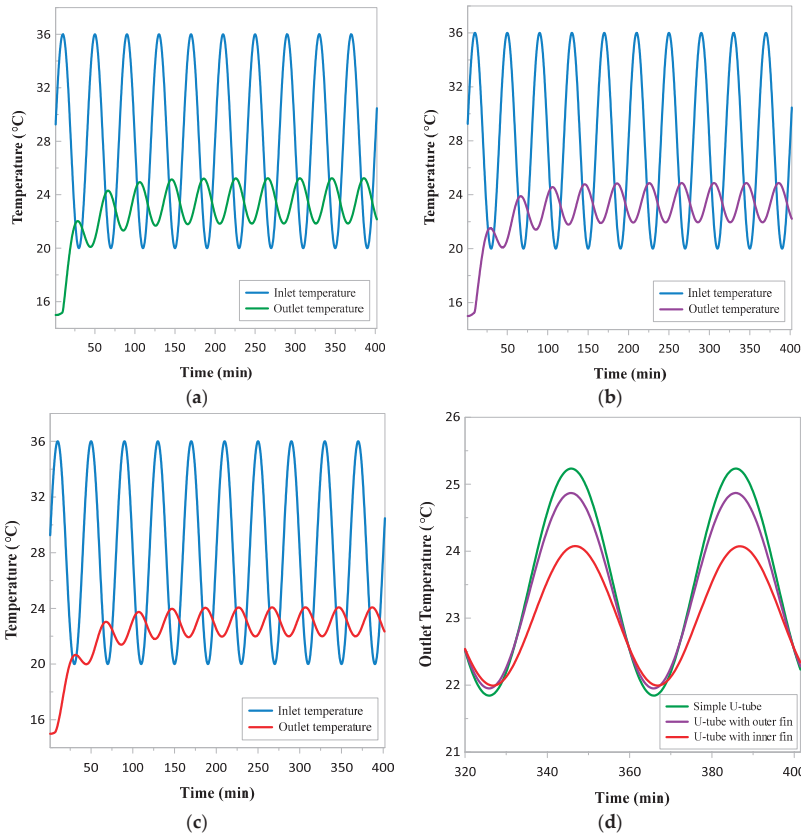
Figure 7. Fluid inlet and outlet temperatures with a frequency of 1/2400 Hz: (**a**) simple U-tube; (**b**) U-tube with outer fins; (**c**) U-tube with inner fins; (**d**) comparison of fluid outlet temperatures in three simple and finned U-tubes.

According to Table 7, the difference between the average value of the input and output waves, with a frequency of 1/4800 Hz, in the simple pipe is 4.46 °C, in the pipe with external fins is 4.59 °C and in the internally finned pipe is 4.97 °C. The use of external fins increases temperature reduction in the fluid by 2.9% compared to a simple U-tube and the internal fins increase temperature reduction in the fluid by 11%. By doubling the frequency, the average value of the output wave has not changed compared to the first frequency, but the wave amplitude has decreased by 35% in the simple pipe, 39% in the pipe with the outer fins and 49% in the inner finned pipe.

Table 7. Input and output wave characteristics with different frequencies.

		Amplitude of Wave	Mean of Wave
Inlet Temperature		**8**	**28**
Outlet temperature (°C) with a frequency of 1/4800	Simple U-tube	2.62	23.54
	U-tube with outer fins	2.40	23.41
	U-tube with inner fins	2.06	23.03
Outlet temperature (°C) with a frequency of 1/2400	Simple U-tube	1.69	23.54
	U-tube with outer fins	1.46	23.41
	U-tube with inner fins	1.04	23.03

It was expected that finned GHEs have faster thermal responses than the smooth one. A comparison of the phase shift between the inlet and outlet temperature of the fluid in the three U-tubes shows that the thermal response of the three numerical models is almost simultaneous. The time shift of the outlet temperature of the simple and the externally finned pipes is 1200 s and in the internally finned pipe is 1320 s in a frequency of 1/4800 Hz. The time shift values at the second frequency of 1/2400 Hz for simple and externally finned pipes is 900 s and in pipes with internal fins is 1020 s.

5.3. Fluid Velocity Effects with Sinusoidal Inlet Temperature

A comparison of the fluid outlet temperature at different velocities with the Reynolds of 1200, 1800, 2300 for simple and finned U-tubes is illustrated in Figure 8 and the outlet values are listed in Table 8. For all cases, the laminar flow condition is considered. The inlet temperature is considered the same as the previous section with a period of 80 min.

In Table 8, as the inlet velocity increases, the mean and amplitude values of the fluid outlet temperature increase for the cooling purpose; increasing the velocity reduces the difference between the inlet and outlet temperatures of the fluid (*dT*). By increasing the velocity, the heat transfer rate between the pipe and the surrounding soil increases, but the fluid temperature change decreases. At low velocities, the fluid remains longer in the pipe, which increases the temperature change of the fluid [34].

(a)
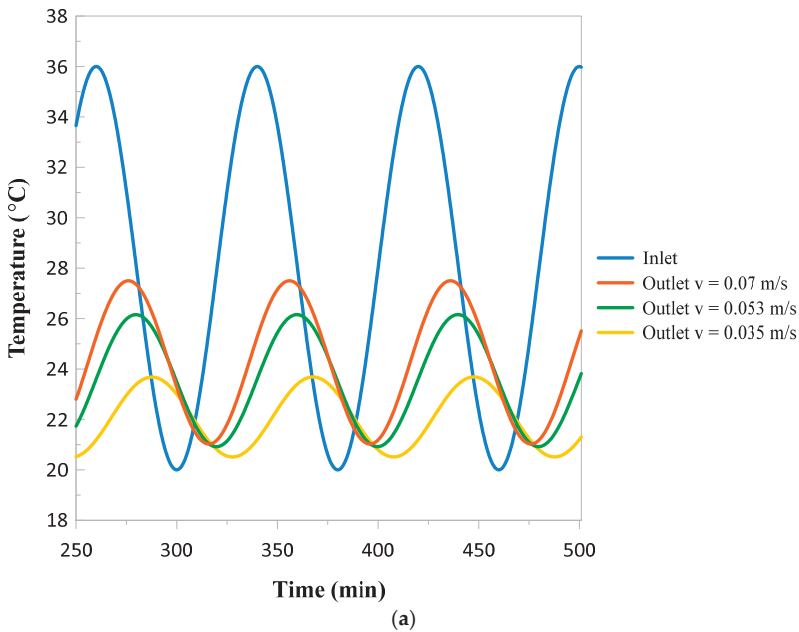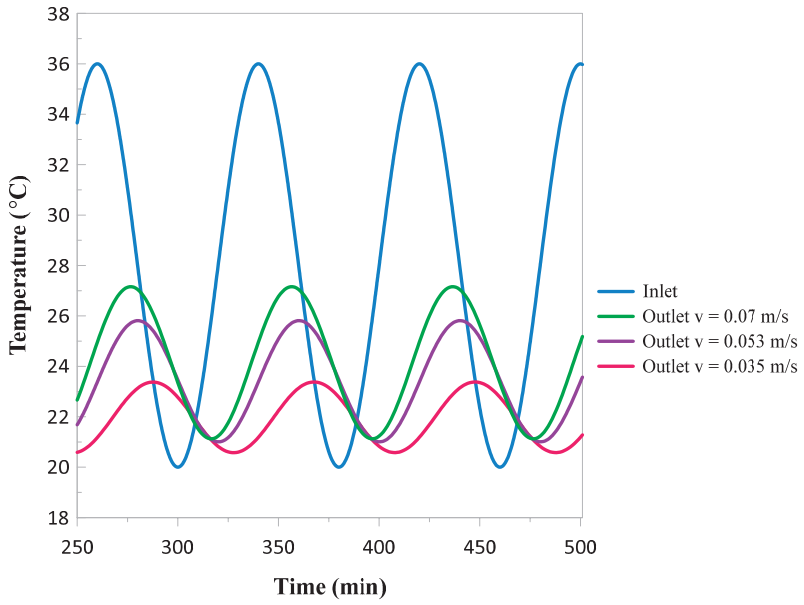
Figure 8. *Cont.*

(**b**)
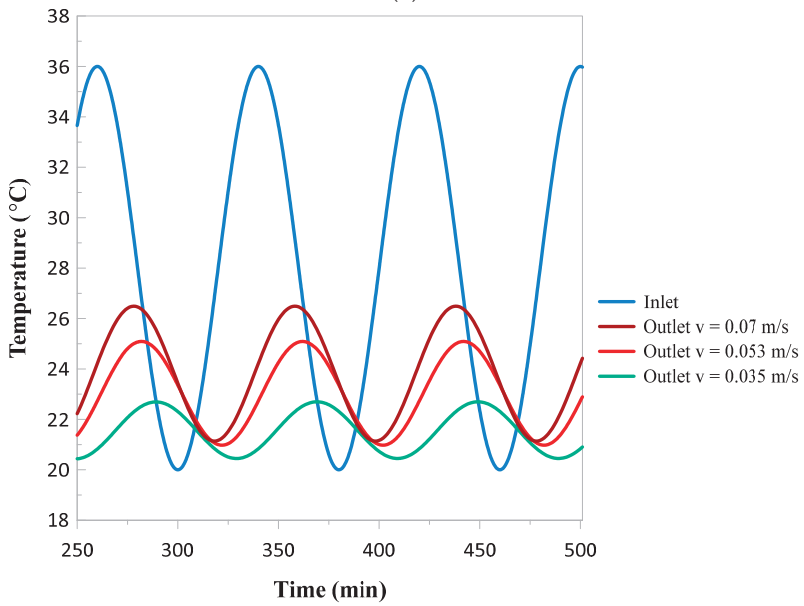
(**c**)

Figure 8. *Cont.*

Figure 8. Fluid temperature trends under different velocities: (**a**) simple U-tube; (**b**) U-tube with outer fins; (**c**) U-tube with inner fins; (**d**) comparison of simple and finned pipes.

Table 8. Output wave parameters with a frequency of 1/4800 Hz at different velocities.

	Velocity (m/s)	Amplitude of Wave (°C)	Mean of Wave (°C)	dT
Simple U-tube	0.035	1.59	22.10	26.7%
	0.053	2.62	23.54	19%
	0.070	3.24	24.26	15.4%
U-tube with outer fins	0.035	1.40	21.98	27.4%
	0.053	2.40	23.41	19.6%
	0.070	3.00	24.14	16%
U-tube with inner fins	0.035	1.12	21.57	29.8%
	0.053	2.06	23.03	21.5%
	0.070	2.68	23.81	17.6%

According to Figure 8, as the velocity of flow decreases, the phase shift of the fluid outlet temperature increases which means a delay in the thermal response of the BHE. Output temperature time shift for the simple U-tube for the first velocity (v = 0.07 m/s) is 960 s, for the second velocity (v = 0.053 m/s) is 1200 s and for the third velocity (v = 0.035 m/s) is 1680 s. These values for the externally finned pipe are 1020 s, 1200 s and 1680 s and for the internally finned pipe are 1080 s, 1320 s and 1740 s, respectively.

Figure 9 shows a comparison of borehole wall temperature for the simple and finned pipes at different velocities. According to the results obtained in the previous section, as the velocity of the fluid decreases, the difference between the inlet and outlet temperatures of the fluid increases and the average temperature of the fluid decreases in the cooling mode. As a result, by reducing the temperature difference between the fluid and the soil around the GHE, the heat transfer rate will be reduced.

Table 9 shows borehole temperature trends under different velocities. The fourth column shows the borehole wall temperature changes in three modes of pipes (dT_{bore}). The problem that should be considered in the comparison between simple and internally finned pipes, with the same fluid velocities, is the reduction in mass flow rate in the finned pipe due to the reduction in the cross-section. By comparing three numerical models, the increase in borehole wall temperature for the pipe with outer fins is more than two other pipes in applied velocities. This temperature change for the simple U-tube for the velocity of 0.035 m/s is more than that of the internally finned U-tube, but by increasing the fluid velocity, the bore wall temperature change for the finned pipe is more than the smooth one with the velocity of 0.07 m/s.
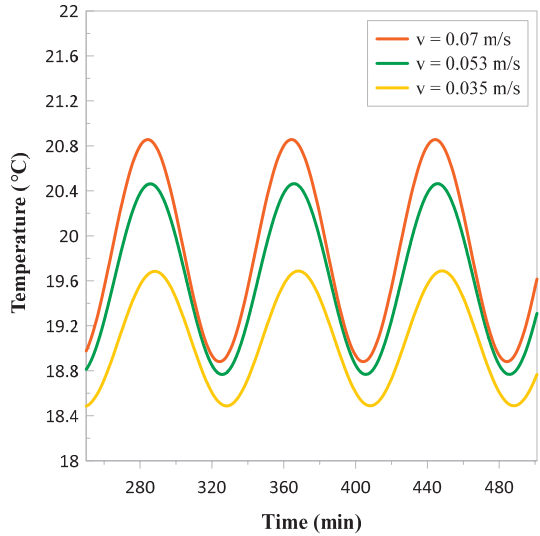
(a)
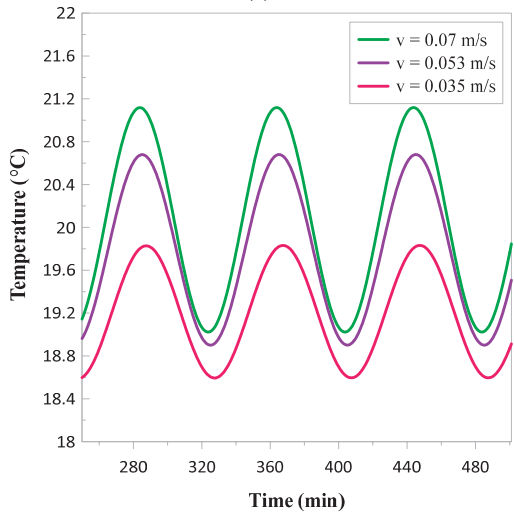
(b)

Figure 9. *Cont.*

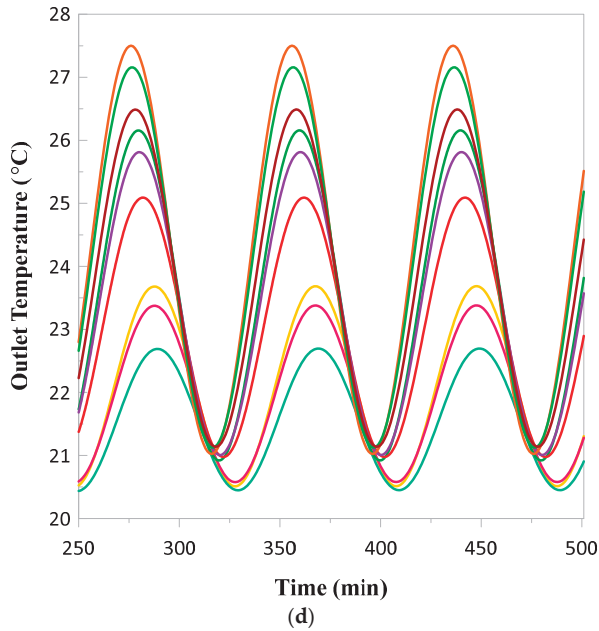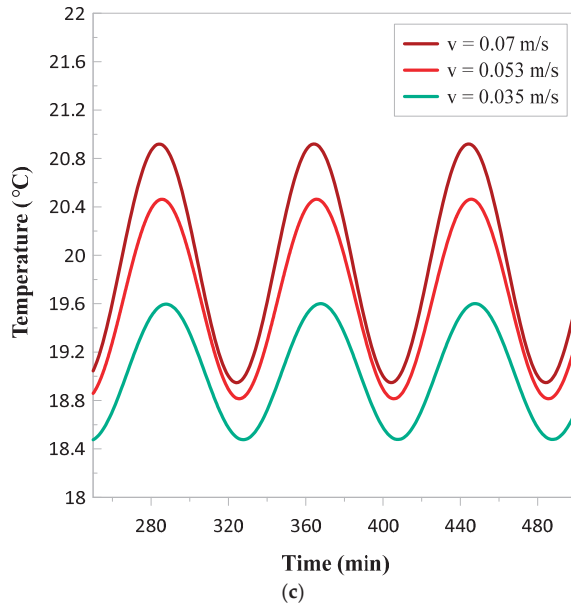**Figure 9.** Borehole wall temperature trends under different velocities: (**a**) simple U-tube; (**b**) U-tube with outer fins; (**c**) U-tube with inner fins.

Table 9. Borehole wall temperature with a frequency of 1/4800 Hz at different velocities.

	Velocity (*m/s*)	Amplitude of Wave (°C)	Mean of Wave (°C)	dT_{bore}
Simple U-tube	0.035	0.59	19.09	27%
	0.053	0.85	19.61	30.7%
	0.070	0.99	19.87	32%
U-tube with outer fins	0.035	0.62	19.21	28%
	0.053	0.89	19.80	32%
	0.070	1.04	20.07	34%
U-tube with inner fins	0.035	0.56	19.04	26%
	0.053	0.82	19.64	30.9%
	0.070	0.97	19.93	33%

5.4. Axial Velocity and Temperature Contours

The effects of longitudinal internal fins on the incompressible fluid flow inside U-tube GHE are investigated. The results are presented for different fluid velocities under steady-state conditions. Figure 10 shows axial velocity contours for two cases of a smooth U-tube and internally finned U-tube at different velocities. The two selected cross-sections of the pipe, in which the velocity contours are drawn, are located in the curvature of the inlet and outlet legs of the U-tube at a depth of 24.94 m under the ground surface.
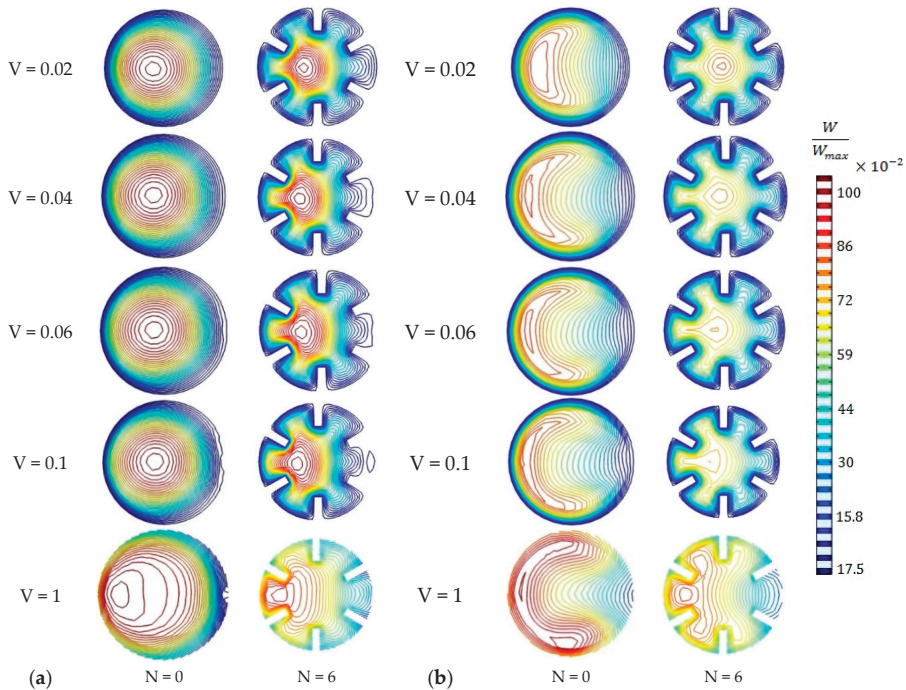
Figure 10. Axial velocity contours for smooth (**left**) and finned U-tube (**right**) at different velocities; (**a**) inlet pipe; (**b**) outlet pipe.

Initially, the fluid velocity is uniform at the inlet of the pipe. Then the fluid velocity is increased at the center of the pipe cross-section, while the velocity of the fluid attached to the wall of the pipe approaches zero because of the viscous effects [21]. The flow contours are symmetric until the flow passes the end of the straight pipe. Figure 10 shows that the symmetric patterns of the velocity contours both in simple and finned pipes are changed according to the curvature of the pipes similar to the previous studies of heat exchangers [28,35]. The velocity contours of the inlet pipe are less affected by the curvature of the pipe than those of the outlet pipe. As the fluid velocity increases, the flow field pattern becomes more complex and the high-velocity flow is pushed to one side of the pipe. The presence of internal fins attenuates the effects of secondary flow and makes the flow patterns close to the straight pipes.

Figure 11 shows the temperature contours at three different velocities with the same method and selected cross-sections of the pipe mentioned in velocity contours (Figure 10). θ^* is a dimensionless temperature parameter which is illustrated in Equation (5):

$$\theta^* = \frac{T - T_{min}}{T_{max} - T_{min}} \tag{5}$$

Similar to the velocity contours, with the increase in fluid velocity, because of strong secondary flow effects in curved pipes [28,35] the temperature field patterns become more complex.
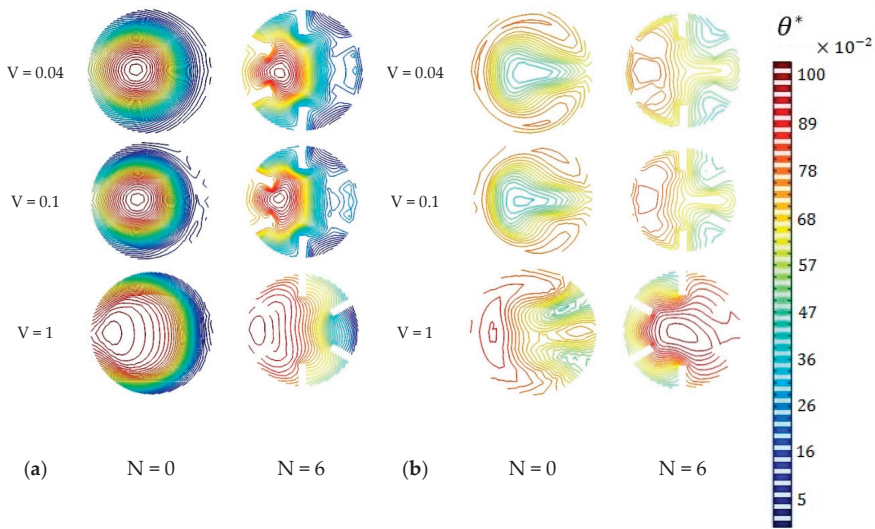
Figure 11. Temperature contours for smooth (**left**) and finned U-tube (**right**) at different velocities; (**a**) inlet pipe; (**b**) outlet pipe.

6. Conclusions

The influence of using fins in inner and outer surfaces of U-tube GHEs was investigated under the cooling mode. Internal fins increase the heat transfer rate more effectively. A GHE equipped with internal fins experiences enhanced fluid temperature changes along the borehole. For more details, under steady conditions (long timescale responses), when the fluid outlet temperature difference between a simple U-tube and a U-tube with external fins was 0.14 °C, the temperature difference between a simple U-tube and a U-tube with internal fins reached 0.6 °C, showing more than four times increase. Increasing the inlet fluid velocity can make the differences more noticeable; by changing the inlet fluid velocity in the range of 0.02–0.06 m/s, the fluid temperature change in the internally finned U-tube is increased by 5–11.3%, compared to the simple U-tube, while the fluid temperature change is just increased by 0.5–2.9% when the external fins are used. For the dynamic behavior, the priority of the inner fins is obvious too; for the short timescale response, with the inlet velocity of 0.053 m/s, the temperature change of the fluid in the outer and inner finned U-tube was increased up to 2.9% and 11% compared to the simple pipe. Short timescale responses by applying sinusoidal function boundary condition to the inlet fluid temperature show that the thermal responses of the smooth and finned GHEs are almost simultaneous by a considerable time shift. Simple and external finned pipes react up to two minutes faster than the pipe with internal fins. The fast, thermal response of the BHE helps to better fluid and ground temperature recovery which affects the performance of the ground source heat pump system.

Using fins has a positive effect on the fluid temperature changes inside the pipe and heat transfer rate between fluid and borehole wall. By using fins, in particular, internal fins, it is possible to increase the GSHP system's efficiency, decrease the length of the tubes and reduce the initial costs of the system.

Author Contributions: Investigation, A.M.Z.; methodology, A.M.Z.; project administration, K.G.; supervision, K.G. and J.N.; writing—review and editing, A.A.-H. All authors have read and agreed to the published version of the manuscript.

References

1. Zeng, H.; Diao, N.; Fang, Z. Heat transfer analysis of boreholes in vertical ground heat exchangers. *Int. J. Heat Mass Transf.* **2003**, *46*, 4467–4481. [CrossRef]
2. Soltani, M.; Kashkooli, F.M.; Dehghani-Sanij, A.; Kazemi, A.R.; Bordbar, N.; Farshchi, M.J.; Elmi, M.; Gharali, K.; Dusseault, M.B. A comprehensive study of geothermal heating and cooling systems. *Sustain. Cities Soc.* **2019**, *44*, 793–818. [CrossRef]
3. Kharseh, M.; Al-Khawaja, M.; Suleiman, M.T. Potential of ground source heat pump systems in cooling-dominated environments: Residential buildings. *Geothermics* **2015**, *57*, 104–110. [CrossRef]
4. Salem, A.; Hashim, H. Feasibility of Geothermal Cooling in Middle East. In *Latest Trends in Sustainable and Green Development, Proceedings of the 3rd International Conference on Urban Sustainability, Cultural Sustainability, Green Development, Green Structures and Clean Cars (USCUDAR'12), Barcelona, Spain, 17–19 October 2012*; Zahran, M., Ed.; WSEAS Press: Athens, Greece, 2012; pp. 105–112. ISBN 978-1-61804-132-6.
5. Biglarian, H.; Abbaspour, M.; Saidi, M.H. Evaluation of a transient borehole heat exchanger model in dynamic simulation of a ground source heat pump system. *Energy* **2018**, *147*, 81–93. [CrossRef]
6. Angelotti, A.; Alberti, L.; La Licata, I.; Antelmi, M. Energy performance and thermal impact of a Borehole Heat Exchanger in a sandy aquifer: Influence of the groundwater velocity. *Energy Convers. Manag.* **2014**, *77*, 700–708. [CrossRef]
7. Beier, R.A.; Acuña, J.; Mogensen, P.; Palm, B. Transient heat transfer in a coaxial borehole heat exchanger. *Geothermics* **2014**, *51*, 470–482. [CrossRef]
8. Keshavarzzadeh, A.H.; Zanjani, A.M.; Gharali, K.; Dusseault, M.B. Multi-objective evolutionary-based optimization of a ground source heat exchanger geometry using various optimization techniques. *Geothermics* **2020**, *86*, 101861. [CrossRef]
9. Hellström, G. Ground Heat Storage: Thermal Analyses of Duct Storage Systems. Ph.D. Thesis, University of Lund, Lund, Sweden, 1991.
10. Zhang, L.; Zhang, Q.; Huang, G.; Du, Y. A p(t)-linear average method to estimate the thermal parameters of the borehole heat exchangers for in situ thermal response test. *Appl. Energy* **2014**, *131*, 211–221. [CrossRef]
11. Zhang, L.; Zhang, Q.; Acuña, J.; Ma, X. Improved p(t)-linear Average Method for Ground Thermal Properties Estimation during in-situ Thermal Response Test. *Procedia Eng.* **2015**, *121*, 726–734. [CrossRef]
12. Beier, R.A.; Spitler, J.D. Weighted average of inlet and outlet temperatures in borehole heat exchangers. *Appl. Energy* **2016**, *174*, 118–129. [CrossRef]
13. Marcotte, D.; Pasquier, P. On the estimation of thermal resistance in borehole thermal conductivity test. *Renew. Energy* **2008**, *33*, 2407–2415. [CrossRef]
14. Beier, R.A.; Acuña, J.; Mogensen, P.; Palm, B. Vertical temperature profiles and borehole resistance in a U-tube borehole heat exchanger. *Geothermics* **2012**, *44*, 23–32. [CrossRef]
15. Sharqawy, M.H.; Mokheimer, E.M.; Badr, H.M. Effective pipe-to-borehole thermal resistance for vertical ground heat exchangers. *Geothermics* **2009**, *38*, 271–277. [CrossRef]
16. Sliwa, T.; Rosen, M. Efficiency analysis of borehole heat exchangers as grout varies via thermal response test simulations. *Geothermics* **2017**, *69*, 132–138. [CrossRef]
17. Borinaga-Treviño, R.; Pascual-Muñoz, P.; Castro-Fresno, D.; Blanco-Fernandez, E. Borehole thermal response and thermal resistance of four different grouting materials measured with a TRT. *Appl. Therm. Eng.* **2013**, *53*, 13–20. [CrossRef]
18. Erol, S.; François, B. Efficiency of various grouting materials for borehole heat exchangers. *Appl. Therm. Eng.* **2014**, *70*, 788–799. [CrossRef]
19. Eskilson, P. Thermal Analysis of Heat Extraction Boreholes. Ph.D. Thesis, University of Lund, Lund, Sweden, 1987.
20. Beier, R.A. Transient heat transfer in a U-tube borehole heat exchanger. *Appl. Therm. Eng.* **2014**, *62*, 256–266. [CrossRef]
21. Pu, L.; Qi, D.; Li, K.; Tan, H.; Li, Y. Simulation study on the thermal performance of vertical U-tube heat exchangers for ground source heat pump system. *Appl. Therm. Eng.* **2015**, *79*, 202–213. [CrossRef]
22. Esen, H.; Inalli, M.; Esen, Y. Temperature distributions in boreholes of a vertical ground-coupled heat pump system. *Renew. Energy* **2009**, *34*, 2672–2679. [CrossRef]

23. Li, Y.; An, Q.; Liu, L.; Zhao, J. Thermal Performance Investigation of Borehole Heat Exchanger with Different U-tube Diameter and Borehole Parameters. *Energy Procedia* **2014**, *61*, 2690–2694. [CrossRef]
24. Zhu, L.; Chen, S.; Yang, Y.; Sun, Y. Transient heat transfer performance of a vertical double U-tube borehole heat exchanger under different operation conditions. *Renew. Energy* **2019**, *131*, 494–505. [CrossRef]
25. Lee, C.K.; Lam, H.N. Computer simulation of borehole ground heat exchangers for geothermal heat pump systems. *Renew. Energy* **2008**, *33*, 1286–1296. [CrossRef]
26. Yang, S.; Lee, S. Dynamic thermal analysis of a residential ground-source heat pump. *Sustain. Energy Technol. Assess.* **2020**, *37*, 100608. [CrossRef]
27. Beckers, K.F.; Aguirre, G.A.; Tester, J.W. Hybrid ground-source heat pump systems for cooling-dominated applications: Experimental and numerical case-study of cooling for cellular tower shelters. *Energy Build.* **2018**, *177*, 341–350. [CrossRef]
28. Nobari, M.R.H.; Gharali, K.; Tajdari, M. A Numerical Study of Flow and Heat Transfer in Internally Finned Rotating Curved Pipes. *Numer. Heat Transfer Part A Appl.* **2009**, *56*, 76–95. [CrossRef]
29. Bouhacina, B.; Saim, R.; Oztop, H.F. Numerical investigation of a novel tube design for the geothermal borehole heat exchanger. *Appl. Therm. Eng.* **2015**, *79*, 153–162. [CrossRef]
30. Saeidi, R.; Noorollahi, Y.; Esfahanian, V. Numerical simulation of a novel spiral type ground heat exchanger for enhancing heat transfer performance of geothermal heat pump. *Energy Convers. Manag.* **2018**, *168*, 296–307. [CrossRef]
31. Patankar, S. *Numerical Heat Transfer and Fluid Flow*; Hemisphere Publishing: Washington, DC, USA; McGraw Hill: New York, NY, USA, 1980.
32. Beier, R.A.; Smith, M.D.; Spitler, J.D. Reference data sets for vertical borehole ground heat exchanger models and thermal response test analysis. *Geothermics* **2011**, *40*, 79–85. [CrossRef]
33. Rees, S.J.; He, M. A three-dimensional numerical model of borehole heat exchanger heat transfer and fluid flow. *Geothermics* **2013**, *46*, 1–13. [CrossRef]
34. Noorollahi, Y.; Saeidi, R.; Mohammadi, M.; Amiri, A.; Hosseinzadeh, M. The effects of ground heat exchanger parameters changes on geothermal heat pump performance—A review. *Appl. Therm. Eng.* **2018**, *129*, 1645–1658. [CrossRef]
35. Nobari, M.R.H.; Gharali, K. A numerical study of flow and heat transfer in internally finned rotating straight pipes and stationary curved pipes. *Int. J. Heat Mass Transf.* **2006**, *49*, 1185–1194. [CrossRef]

Article

Smart Heating and Cooling Heat Pump System by Standing Column Well and Cross-Mixing Balancing Well Heat Exchangers

Donggyu Kim [1], Myungkwan Lim [2], Byeongseok Yu [1] and Changhee Lee [1,*]

[1] Department of Mechanical and Shipbuilding Convergence Engineering, Pukyong National University, Busan 48547, Korea; dgkim@pknu.ac.kr (D.K.); youbs@pknu.ac.kr (B.Y.)

[2] Department of Architecture Engineering, Songwon University, Gwangju 61756, Korea; limmk79@naver.com

[*] Correspondence: leemech@pknu.ac.kr; Tel.: +82-51-629-7816

Abstract: Standing column well (SCW) geothermal heat exchanger permits a bleeding discharge of less than 20% in the event of a maximum load, which is an inappropriate method of using underground water. In this study, the existing operational method of two adjacent SCW geothermal heat exchangers, each with a single well, was modified. This technology aims to improve the coefficient of performance (COP) of the geothermal system by fundamentally preventing underground water discharge and maintaining a constant temperature of the underground heat exchanger. To curb the bleed water discharge, two balancing wells of cross-mixing methods were employed. The result of the cooling and heating operations with the existing SCW heat exchange system and the balancing well cross-combined heat exchange system showed that the measured COP increases by 23% and 12% during the cooling and heating operations, respectively. When operating with a balanced well cross-mixed heat exchange system, the initial temperature of the underground was constant with a small standard deviation of 0.08–0.12 °C.

Keywords: standing column well (SCW); thermal response test; effective thermal conductivity; bleeding rate; thermal conductivity; balancing well; coefficient of performance (COP)

1. Introduction

Technology using the underground environment in architecture has been applied in various forms from an energy-efficient perspective, such as in the composition of space and elements for responding to climate change. In particular, a ground source heat pump, which uses a constant layer of geothermal heat and water temperatures (100–200 m underground) inside the basement of buildings, is widely used as a heating and cooling system for buildings [1].

The soil constituting the underground environment is a porous body formed by three phases of water, pore, and soil particles. Meanwhile, the water constituting the soil is further divided into soil water and groundwater. Among them, groundwater fills the gap in the inner rock of the earth and has fluidity due to gravitational action. The pluggable stratum containing this groundwater is called the aquifer [2]. An open geothermal heat pump system using underground water from the aquifer is expected to perform better as a heat exchange medium than an enclosed system through a direct heat exchange with heat sources. However, its performance is considerably affected by the groundwater quality and quality conditions, such as groundwater heat. Problems such as a drop in groundwater levels, depletion of groundwater, and a drop in temperature occur due to groundwater intake and injection. Therefore, a technology that can fully preserve the underground quality while ensuring stable system performance should be developed. Research on the development

of optimal design methods for improving the performance of open geothermal systems or geological hydrological considerations of the ground, based on the use of systems, has been conducted in various fields. To develop an optimal design method for an open system, research on improving the existing geothermal system or analyzing the temperature profile and thermal behavior of the tube and soil according to system operation has been mainly conducted using numerical analysis models [3–6], and the underground water recovery and flow due to system introduction have been analyzed using numerical analysis models [7,8]. The effects of open geothermal heating and cooling system on the geochemical properties of groundwater and the repair and geology characteristics of aquifers, such as temperature and groundwater level, were actively determined [9,10]. Research has also been conducted on the proposed method of heat recovery or performance analysis by introducing an open geothermal system in certain areas where the geothermal energy potential is high, such as mines, and where large amounts of groundwater exist [11–19]. Clearly, research on the design method is actively conducted to improve the performance of open geothermal systems or on the mathematical considerations after the introduction of the system. However, few studies have developed design techniques that can maintain a long-term stable performance or continuous operation of the system.

Among the technologies using renewable energy sources, geothermal heat pump systems have better energy utilization efficiency than other heat source systems and provide stable heat sources throughout the year. In particular, the groundwater heat pump system, which utilizes groundwater in the aquifer, is expected to have a significantly higher performance than that of the enclosed geothermal heat pump system by performing direct heat exchange with groundwater. In addition, it can respond positively when a large-scale heating and cooling demand is required within a limited installation site, and economic feasibility can be ensured as the number of geothermal installations is lower than that of enclosed systems depending on the underground water and ground conditions. However, the open geothermal heat pump system is significantly affected by repair quality conditions, such as the size of the aquifer, groundwater quality, and the ground pitching factor. Hence, the operation of the system is restricted if the aquifer does not exist abundantly inside the soil or the groundwater quality and ground pitching factor conditions are unfavorable.

Therefore, the design and operational methods of the open geothermal heat pump system are being actively developed based on the ground repair geometrical conditions. In particular, Sciacovelli et al. [20] and Park et al. [21] conducted studies on open geothermal heat pump systems to review the conditions of water quality in soil according to the design factors. Russo and Civila [22] studied the optimal geothermal deployment plan for improving the performance of open geothermal systems. Kim et al. [23] conducted a study that improved the design method of open geothermal systems. Meanwhile, Bae et al. [24] conducted a study on the underground heat and groundwater movement in soil following the introduction of the system using simulation. Consequently, the underground water level rise of the infusion wells was confirmed if the ground pitching coefficient is unfavorable or if the water table is high. Another study [25] analyzed the effects of the groundwater level adjustment by simulating a multiple-static geothermal system connecting the inter-tube channels to prevent the occurrence of operation restriction due to the overflow of underground water in infusion wells due to the long-term operation of an open geothermal heat pump system. However, most of the studies performed thus far are based on numerical simulation and are still to be tested at the experimental stage.

Geothermal heat pump systems have been introduced and used in Korea since the early 2000s, and the supply and installation capacity has also increased every year. The geothermal heat pump system consists of a heat pump, which is responsible for the heating and cooling of buildings, and an underground heat exchanger, which absorbs heat from the ground and then releases it to the ground. Ground heat exchangers are used to maintain a constant ground temperature throughout the year, ensuring higher heat exchange efficiencies than those of air heat source heat exchangers. The table of compliance has not been established for standing column well (SCW)-type underground heat exchangers introduced in Korea; thus, there is an ambiguity in applying SCW-type underground heat exchangers to geothermal heat pump systems depending on regional characteristics (e.g., geology,

groundwater volume, number of aquifer layers, and level of development), installation methods, and shape of heat exchangers. Kim et. al. [26] established the shape of the heat exchanger through the standardization of products, including the shape and construction of an SCW underground heat exchanger, while establishing a measurement method for the underground thermal conductivity of SCW underground heat exchangers to develop a standard for the design of the heat exchanger.

The effects of circulation water temperature, borehole heat resistance, and underground heat conductivity on various design and operational variables of SCW underground heat exchangers were studied. Among them, the bleed is reported to have the largest effect on the heat transfer enhancement of SCW underground heat exchangers [27]. Bleeding is a method of operation in which underground water extracted from a geothermal well enters the heat pump, exchanges heat, and then releases some underground water to the surface during the process of injecting it back into the same well. Bleed rate is the ratio of the amount of groundwater extracted from the geothermal well and the amount of groundwater released to the surface. Bleeding can also induce underground water that exists near the geothermal well from the underground into the well. The heat exchange capacity of SCW underground heat exchangers can be increased through bleeding in areas where underground water is abundant, and guidelines on support for renewable energy facilities of the Korea Energy Corporation allow bleeding rates of up to 20% for SCW underground heat-burning machines [28]. However, a high rate of bleed application can drain the surrounding groundwater to which a geothermal heat pump system is applied and can also cause heat pump failure due to the groundwater level falling below the pump. Currently, various underground heat exchangers using thermal response tests have been studied in Korea and internationally [29–34], and the energy equilibrium using thermal response test data has also been studied [27,35]. From the results of an analysis in [36], the temperature change of the underground heat exchanger circulation water tends to decrease as the bleed rate increases, and the underground thermal conductivity increases from 0% to 179% at a bleed rate of 0% to 30%, respectively. Meanwhile, when groundwater is introduced from the underside of the underground heat exchanger, the underground heat exchanger circulation water is mixed with groundwater from the bottom after exchanging heat with the ground; thus, the temperature change of the underground heat exchanger circulation water tends to rise initially over time. However, as the bleed rate increases, the rise tends to decelerate and remain constant if the bleed rate exceeds approximately 10%.

In this study, geothermal cooling and heating systems, possessing superior energy utilization efficiency, are used owing to a stable supply of heat sources throughout the year, compared to other heat source systems. In particular, an open geothermal system that uses underground water in the aquifer has been selected for its better performance than an enclosed geothermal system because of its direct heat exchange with rocks. However, bleeding should be performed to improve the forced discharge of groundwater to prevent the geothermal circulating water temperature rise. Meanwhile, for this new technology, a water level difference was formed through refill to use the bleed-discharged water without being discarded, and the thermal performance characteristics were evaluated by applying the balancing well-type underground heat exchanger operation technology to prevent blockage of the underground heat exchanger through cross-operation. The system performance coefficient was compared and analyzed according to the application of an underground heat exchanger by cross-mixing the existing standing column well (SCW) and the balancing well method.

2. Experimental Methodology

Figure 1 shows a comparison test with the existing open underground heat exchanger and cooling and heating operation used to evaluate the energy efficiency and performance coefficient of the system suitable for on-site testing using the test method of the water-water geothermal source heat pump unit. An automatic cross-operating control system was used to maintain the optimal supply of heat sources for the existing SCW and for balancing well underground heat exchangers. The balancing well cross-mixed heat exchange geothermal heat pump system consisted of a geothermal source heat pump

and underground heat exchanger and includes the cross-operation controller among the mechanical piping and circulation pump and system control system.
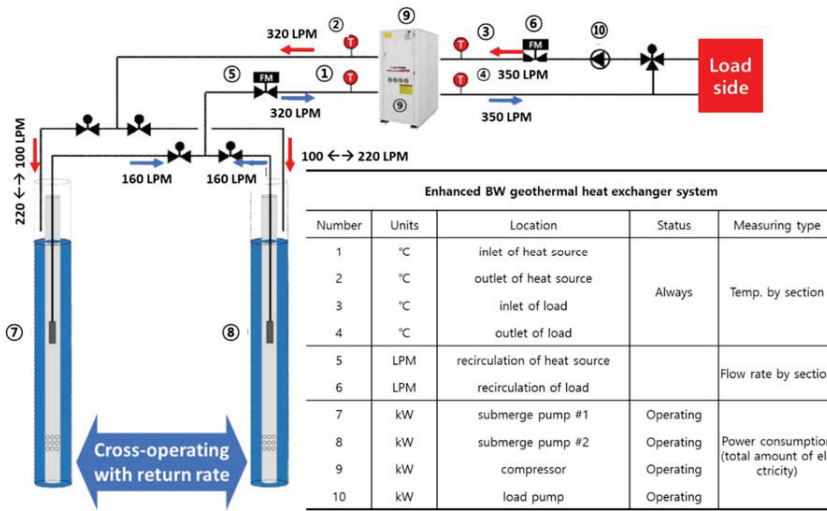
Figure 1. Schematic of the water-water geothermal heat pump system for operating standing column well (SCW) and balancing well geothermal heat exchanger system. LPM: liter per minute

The test targets were a geothermal source heat pump for 30RT-level cooling and heating and two underground heat exchangers with a typical SCW system installed with a diameter of 10 in (0.254 m) and depth of 300 m. The SCW underground heat exchanger had a natural water level of 4.7 m and a maximum quantity of 350 tons/day. The distance between the two wells was approximately 12 m.

To verify that the experimental measurements were reasonable, as shown in Figure 1, a justifiable means of validation was required. The simplest expression of the heat balance equation is

$$\dot{q}_{in} = \dot{m} \cdot C_p \cdot (T_{out} - T_{in}) \tag{1}$$

where $\dot{q}_{in}$ (W) represents the measured heat input to the water heater elements and pumps; $\dot{m}$ (liter per minute, LPM) is the flow rate; C_p denotes the specific heat of water; and T_{in} and T_{out} represent the temperatures measured with a thermostat.

After applying all the calibration equations to the measurement devices, the heat transfer rate predicted by the right-hand side of Equation (1) can be compared to the measured power input (left hand side of Equation (1)). The numbers summarised in Table 1 are the average values over the length of each test, and they were used to compare the instrumentation uncertainties and total heat input error.

Table 1. Heat balance check.

Location	Transducer Reading (W)	Average q (W)	Difference (W)	% of Average Power
A	2506.6	2657.8	101.2	3.88
B	3207.2	3302.5	93.3	2.82

The uncertainties in the temperature measurement were ±0.01 °C for the probes and ±0.04 °C for the signal conditioner of the digital displays with the analog signal. The total uncertainty for the temperature measurements are expressed in quadratic form, as shown in Equation (2):

$$\Delta T = \sqrt{(\pm 0.01)^2_{in} + (\pm 0.04)^2_{in}} + \sqrt{(\pm 0.01)^2_{out} + (\pm 0.04)^2_{out}} \approx \pm 0.0825\ °C \tag{2}$$

Considering that ΔT for each test is approximately 5 °C, the uncertainty due to the temperature measurement becomes:

$$Error = \frac{\pm 0.0825\ °C}{5\ °C} \times 100\% = \approx \pm 1.65\% \tag{3}$$

Using the highest error for the flowmeter taken from Table 2 of ±2.03%, the total uncertainty in the heat balance equation was computed as:

$$Total\ Error = \sqrt{(\pm 0.0165)^2 + (\pm 0.0203)^2} \approx 2.62\% \tag{4}$$

Table 2. Results from the flowmeter calibration.

Actual Flow (LPM)	Calibration Flow (LPM)	Error (%)
3.316	3.292	0.73
15.87	16.032	1.01
100.90	102.99	2.03
350.62	355.41	1.35

As shown in Figure 2, the balancing well cross-mixed heat exchanger system is characterized by different operation methods in the two SCW-type geothermal heat exchangers with 100% pumping from each geothermal heat exchanger, while the recovery quantity is different. In other words, the principle of generating a flow of groundwater in the underground aquifer was applied to generate a difference in the operation level of the two SCW geothermal heat exchangers. In this study, the experiment was conducted using the cross-operating condition supply and return of 80% and 120%, respectively, as depicted in Figure 2a. If the circulation water supplied simultaneously from both the ground heat exchangers is returned after the heat exchange, 120% of it is recovered to the ground heat exchanger (#1 zone), and 80% of the remaining circulation is recovered to the other ground heat exchanger (#2 zone) and the cross-operating mains, which are set to activate the aquifer by forming a difference in the groundwater level.

The system energy efficiency is calculated as the ratio of the resultant value of the production heat obtained by applying the liquid enthalpy test method of the heat source and load sides to the coefficient of performance (COP) of the system to compare it with the existing SCW geothermal system.

In the liquid enthalpy method, the temperature, flow rate, and electricity consumption of circulating water are recorded through the data logger at the entrance and exit of the heat exchanger on the heat source and the load side of the heat pump. The produced heat of the geothermal system is calculated using the following equations.

Where, total power consumption means the total consumption power used in the geothermal system. The COP of the actual geothermal system was calculated using Equations (5) and (6), and these results were configured to be calculated by the system [21,22].
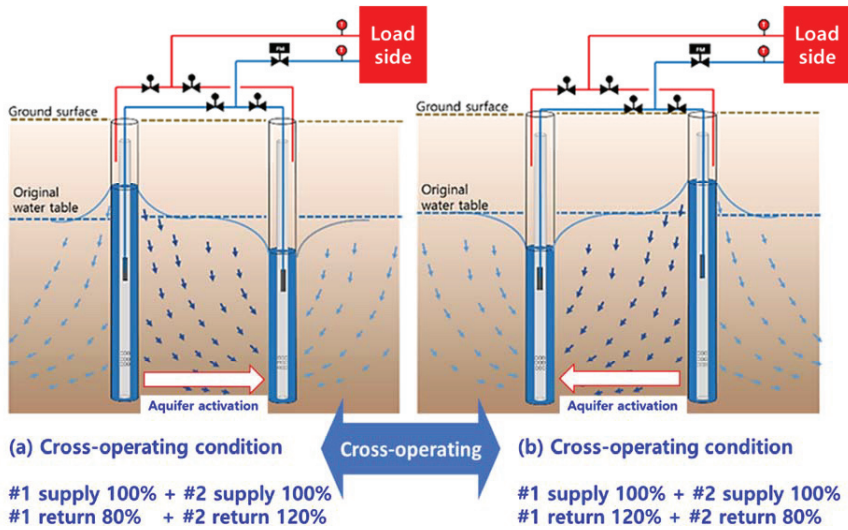
Figure 2. Cross operation of the balancing well geothermal heat exchanger system.

Cooling mode:

$$\varnothing_{\text{tco}} = w_f c_{pf}\left(t_{f4} - t_{f3}\right) - \varnothing_t \tag{5}$$

Heating mode:

$$\varnothing_{\text{tho}} = w_f c_{pf}\left(t_{f3} - t_{f4}\right) + \varnothing_t \tag{6}$$

where,

$\varnothing_{\text{tco}}$: Total cooling capacity of the heat pump (W)

$\varnothing_{\text{tho}}$: Total heating capacity of the heat pump (W)

t_{f3}: Heat pump inlet temperature (°C) of circulating water on the source side

t_{f4}: Heat pump outlet temperature (°C) of circulating water on the source side

c_{pf}: Specific heat of heat source circulation water (J/(kg·K))

w_f: Mass flow rate of circulating water on the heat source side (kg/s)

$\varnothing_t$: Total power Consumption (W)

3. Results and Investigations

3.1. Performance Evaluation under Cooling Operation

The experimental set-up stabilized after 30 min of test operation, and data were recorded once per day for five days, with each recording session lasting a continuous 6 h. Through this experiment, the initial underground temperature, temperatures at the entrance and exit of the geothermal circulation water, circulation flow rate, and the electricity used were recorded by the data logger. The results are presented in Figures 3 and 4. The COP was calculated by using the data recorded and by applying Equation (1). The measured values of the power and COP of the two systems are listed in Tables 3 and 4.
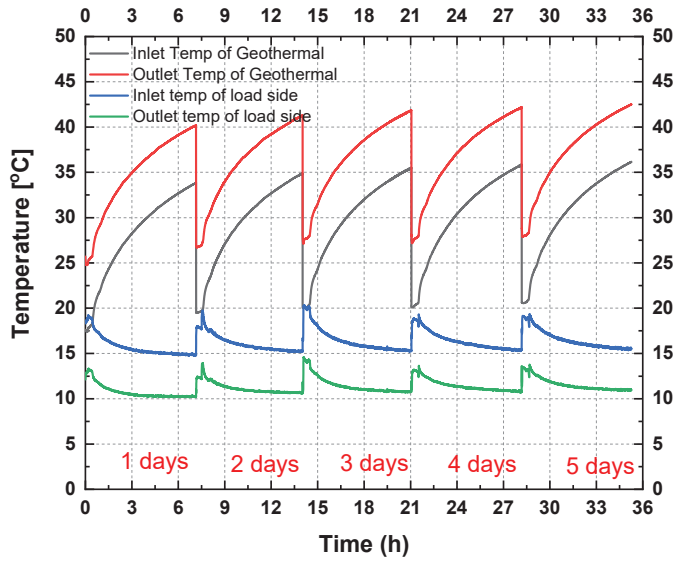
(**a**) Temperature variation of the SCW system
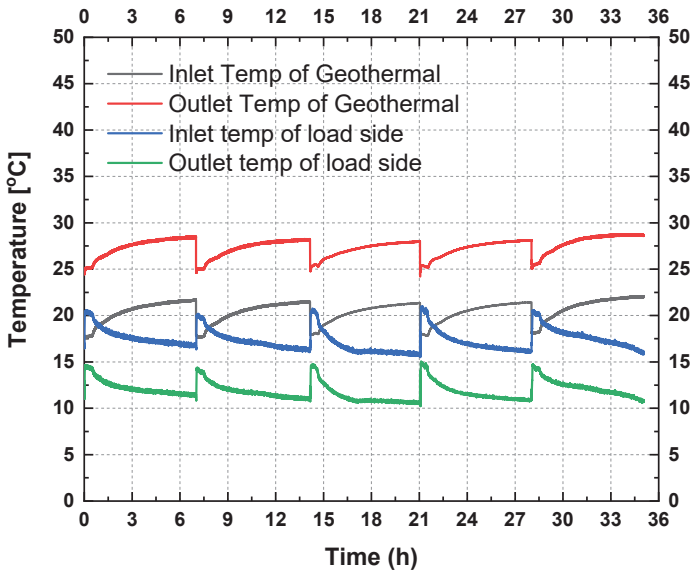
(**b**) Temperature variation of the balancing well (BW) and SCW system

Figure 3. Temperature variation characteristics of the SCW and BW cross-mixing ground heat exchanger system during cooling operation.
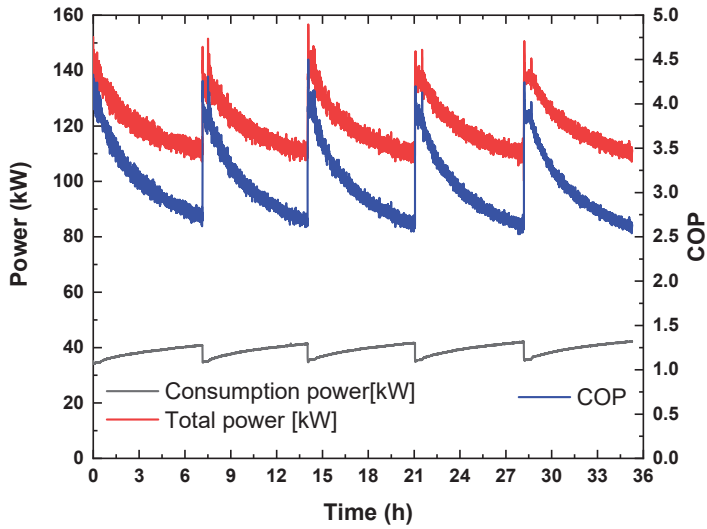
(**a**) Coefficient of performance (COP) characteristics of the SCW geothermal heat exchanger system
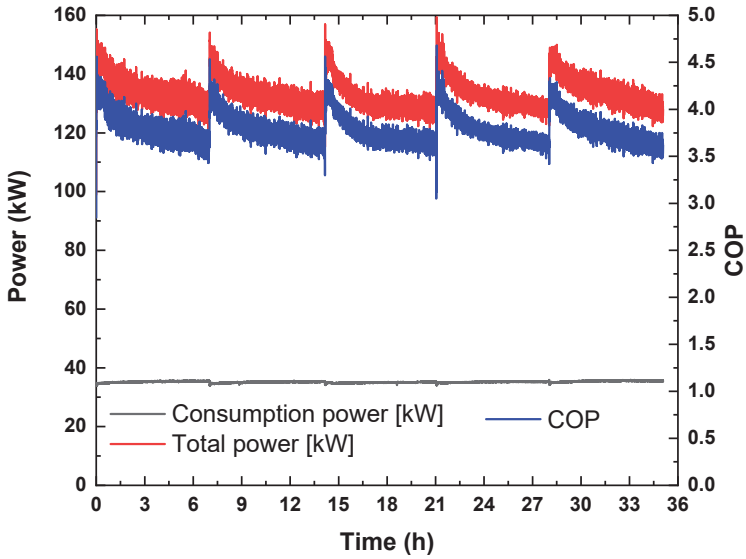
(**b**) Balancing well in SCW Geothermal heat exchanger system

Figure 4. COP characteristics of the SCW and BW cross-mixing ground heat exchanger system during cooling operation.

Table 3. Measured results of the SCW geothermal system cooling operation.

NO/Units	Initial Ground Water TEMP.	Temperature of Geothermal Side			Temperature of Load Side			Total Power	Consumption. Power	COP
		Inlet	Outlet	Flow Rate	Inlet	Outlet	Flow Rate			
	°C	°C	°C	LPM	°C	°C	LPM	kW	kW	(-)
1	17.72	28.37	35.08	305.69	15.60	10.63	346.39	120.11	38.35	3.13
2	19.94	29.90	36.62	304.75	15.60	11.10	346.68	119.10	39.03	3.05
3	19.98	30.45	37.14	306.05	16.28	11.35	346.58	119.06	39.29	3.03
4	20.09	30.61	37.31	306.03	16.34	11.43	347.47	119.22	39.52	3.02
5	20.54	31.01	37.71	304.36	16.46	11.53	348.26	119.83	39.74	3.02
Average	19.65	30.07	36.77	305.38	16.06	11.21	347.08	119.46	39.19	3.05

Table 4. Measured results of the BW SCW geothermal system cooling operation.

NO/Units	Initial Ground Water Temp.	Temperature of Geothermal Side			Temperature of Load Side			Total Power	Consumption Power	COP
		Inlet	Outlet	Flow Rate	Inlet	Outlet	Flow Rate			
	°C	°C	°C	LPM	°C	°C	LPM	kW	kW	(-)
1	17.75	20.61	27.56	317.81	17.61	12.14	349.69	133.55	35.26	3.79
2	17.63	20.44	27.33	318.14	17.22	11.79	349.47	132.58	35.13	3.77
3	17.91	20.44	27.21	318.76	16.49	11.13	349.14	130.54	35.00	3.73
4	17.64	20.46	27.32	318.73	17.05	11.63	349.64	132.37	35.18	3.76
5	17.84	20.48	27.33	318.90	16.99	11.58	349.63	132.06	35.19	3.75
Average	17.75	20.49	27.35	318.47	17.07	11.65	349.51	132.22	35.15	3.76

The plots of Figure 3a showed that the temperatures of the geothermal side shown in Figure 3a were significantly higher than those in Figure 3b when compared with the results of Figure 3b. The method of the conventional SCW ground heat exchangers shows that the temperature of the geothermal side of Figure 3a was significantly higher than that of Figure 3b. This phenomenon was caused by the accumulation of heat in the underground water due to the increase in heat load. However, Figure 3b demonstrates the characteristic that the cyclical water temperature of the geothermal heat remained constant without increasing. This phenomenon is assumed to be the result of the cross-mixing of the balancing well, which activates underground water in the aquifer to improve the heat transfer characteristics.

Figure 4 illustrates the results for the overall power and COP characteristics. To compare the performance of SCW and balancing well underground heat exchangers, the total power consumption, system power, and COP characteristics were compared and analyzed. The cross-mixed balancing well underground heat exchanger exhibited an improved heat transfer effect owing to underground water utilization in the ground and groundwater flow because of the difference in water level between the two wells. It is observed that an overall improvement of the COP of the balancing well SCW system was reported over that of the SCW system, as indicated by the plots of Figure 4a,b. As mentioned previously, the cross mixing of the balancing well resulted in an approximately 23% improvement of the COP.

3.2. Performance Evaluation under Heating Operation

The measurement of temperatures (plotted over time in Figures 5 and 6) was conducted under the same test conditions as those for the cooling operation mentioned in Section 3.1. Using the results obtained from the data logger of the system, the COP and power values are presented in Tables 5 and 6.
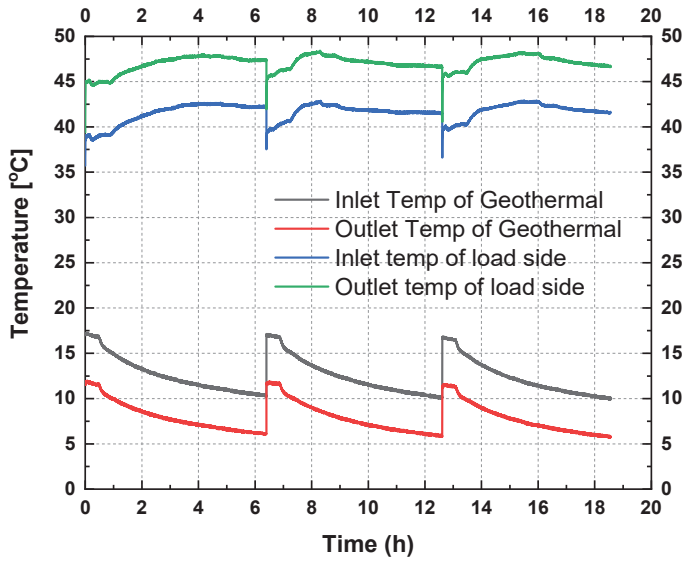
(**a**) Temperature variation of the SCW system
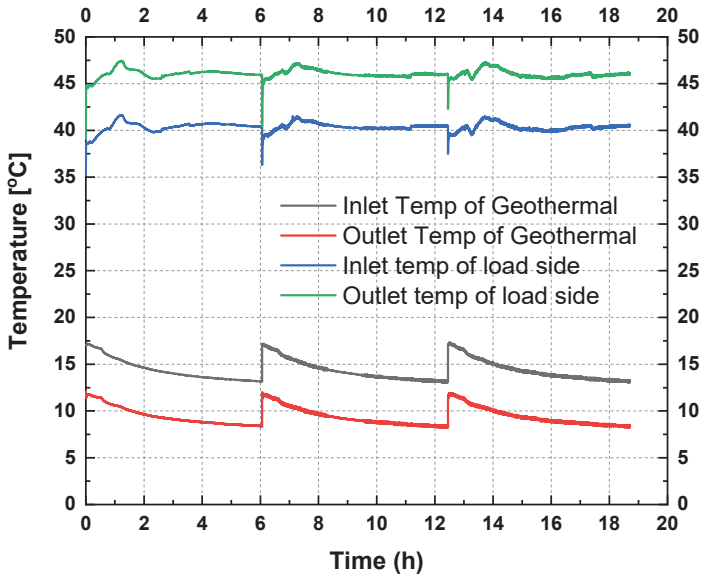
(**b**) Temperature variation of the BW SCW system

Figure 5. Temperature variation characteristics of the SCW and BW cross-mixing ground heat exchanger system during heating operation.
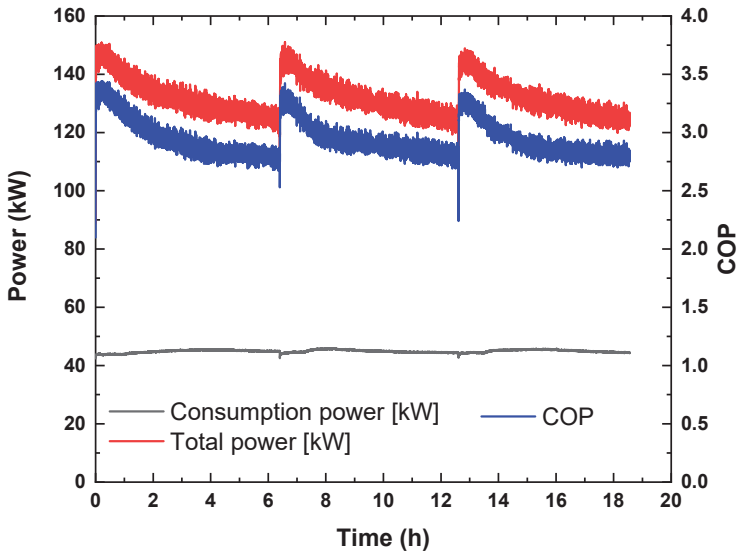
(**a**) COP characteristics of the SCW geothermal heat exchanger system
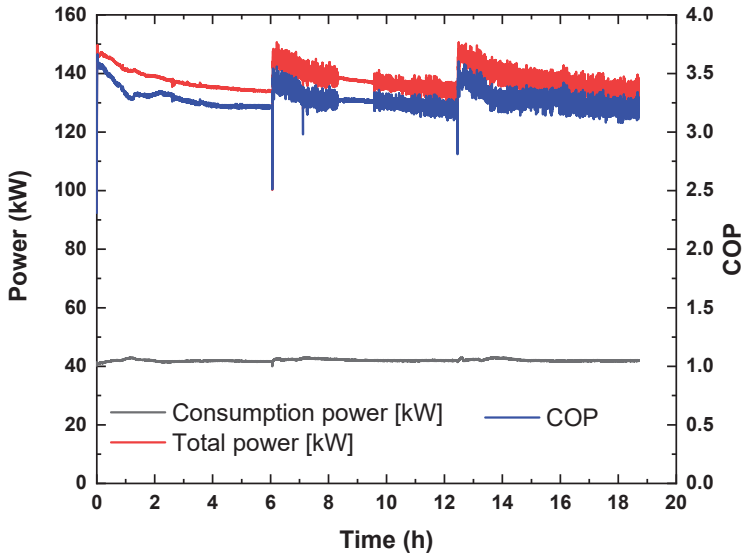
(**b**) COP characteristics of the BW SCW geothermal heat exchanger system

Figure 6. COP characteristics of the SCW and BW cross-mixing ground heat exchanger system during heating operation.

Table 5. Measured results of the SCW geothermal system during heating operation.

	Initial Ground Water Temp.	Temperature of Geothermal Side			Temperature of Load Side			Total Power	Consumption Power	COP
		Inlet	Outlet	Flow Rate	Inlet	Outlet	Flow Rate			
NO/Units	°C	°C	°C	LPM	°C	°C	LPM	kW	kW	(-)
1	16.99	12.30	7.77	324.62	41.64	47.03	349.12	131.26	44.89	2.92
2	16.15	12.40	7.87	324.31	41.85	47.25	349.12	131.65	45.01	2.92
3	15.84	12.12	7.62	324.55	41.99	47.37	349.29	131.01	45.01	2.92
Average	16.94	12.27	7.75	324.49	41.83	47.22	349.20	131.31	45.00	2.92

Table 6. Measured results of the BW SCW geothermal system during heating operation.

	Initial Ground Water Temp.	Temperature of Geothermal Side			Temperature of Load Side			Total Power	Consumption Power	COP
		Inlet	Outlet	Flow Rate	Inlet	Outlet	Flow Rate			
NO/Units	°C	°C	°C	LPM	°C	°C	LPM	kW	kW	(-)
1	16.98	14.28	9.36	319.20	40.53	46.19	348.31	137.48	41.91	3.28
2	16.85	14.26	9.33	318.75	40.47	46.14	348.60	137.95	41.91	3.27
3	16.85	14.29	9.36	319.32	40.36	46.03	348.32	137.80	41.91	3.27
Average	16.89	14.28	9.35	319.09	40.45	46.12	348.41	137.74	42.06	3.27

Figures 5 and 6 illustrate the temperature variation and COP characteristics during the heating operation using the SCW and balancing well underground heat exchangers. Compared with the results of Figure 5a, the variation in the temperature of Figure 5b was small, and the exit temperature on the geothermal side was higher than that of Figure 5a. As a result of comparative analysis of the inlet and outlet temperatures, the SCW underground heat exchanger exhibits higher characteristics than the cross-mixing balancing well underground heat exchanger as time passes during heating operation. Cross-mixing balancing well geothermal heat exchanger showed a characteristic of increasing heat transfer effect by groundwater flow in the ground due to the water level difference. However, the heat transfer characteristics of the SCW underground heat exchanger deteriorated due to heat accumulation in the ground. The COP is found to improve for the balancing well SCW system as compared to that of the SCW system, as shown in Figure 6.

3.3. Results of Performance Evaluation of the Two Types of Geothermal Systems

Table 7 presents the results of the variation of the initial underground temperature of the SCW and balancing well (BW) ground heat exchangers during the cooling and heating operations.

Table 7. Comparison of the initial groundwater temperature.

Initial Ground-Water Temperature	Cooling Operation		Heating Operation	
	SCW	BW SCW	SCW	BW SCW
1	17.72	17.75	16.99	16.98
2	19.94	17.63	16.15	16.85
3	19.98	17.91	15.84	16.85
4	20.09	17.63		
5	20.54	17.84		
Standard deviation	1.11	0.12	0.6	0.08

The circulation pump flow rate confirmed that the artificial function of the bleed discharge water was operated alternately according to the cross-operating cycle set to maintain the optimal heat supply state. Cooling and heating operations were conducted for 5 d and 3 d, respectively. During the

heating operation, it was confirmed that the balancing well heat exchange system maintained a constant initial underground temperature.

The energy efficiency of the system was calculated by the COP as the ratio of the heat produced from applying the liquid enthalpy test method of the heat source and load side to the power consumed by the heat pump and circulation pump. These values were compared with those of the geothermal systems of the existing SCW and balancing well cross-mixed methods.

Table 8 presents the test results obtained by operating the cooling and heating heat pump systems based on the concept demonstrated in Figure 2 for evaluating the performance of the cooling and heating heat pump systems by the alternative heat exchange of the balancing well. The overall COP of the heat pump system using the existing SCW heat exchange system was calculated to be lower in the balanced well heat exchange system; in particular, the efficiency of the cooling operation was improved by approximately 23%.

Table 8. Comparison of the performance factors of COP.

COP Performance Coefficient	Cooling Operation			Heating Operation		
	SCW	BW SCW	Remarks	SCW	BW SCW	Remarks
Minimum	2.58	3.45		2.08	2.21	
Maximum	3.96	4.29		3.44	3.66	
Average	3.05	3.76	23% ↑	2.92	3.27	12% ↑

3.4. Thermal Environment of the Ground-Water Temperature

Figure 7 shows the results of analyzing the thermal environment characteristics of the groundwater through the cross mixing of the SCW and balancing well methods. Figure 7a shows the characteristics of the circulating water intake temperature, circulation flow rate, bleed flow rate, input, and exit temperature difference, and injected heat caused by the change to the balancing well method from the SCW method after 24 h of operation. The SCW method initially showed the characteristics of a continuous increase in the temperature of the In/Out during operation. However, utilizing the SCW method instead of the balancing well method resulted in a decrease in temperature difference between the inlet and out temperatures of the circulating water. The possible reason is the activation of the underground aquifer by the water level difference of the well by the injected bleed flow and the activation of the flow of the underground aquifer. Consequently, the recovery of the temperature of the underground circulating water might increase. Figure 7b shows the results of the circulation water temperature, circulation flow rate, bleed flow rate, and injection heat, due to the utilization of the SCW method, instead of the balancing well operation, after 24 h of operation. When operating the balancing well method, the temperature difference between the inlet and exit temperatures of the circulating water was observed to be slightly higher than that shown in Figure 7a. However, when changing the operation from the balancing well method to the SCW method, the temperature of the In/Out increased rapidly. Through this technique, it is deemed that the heat accumulation phenomenon occurred because of the increase in the temperature of the circulating water in the ground. As shown in Table 5, when driving balancing well, the thermal efficiency increased more than that of the SCW, and the thermal environmental conditions of the groundwater were optimized, which could be a condition for long-term operation.
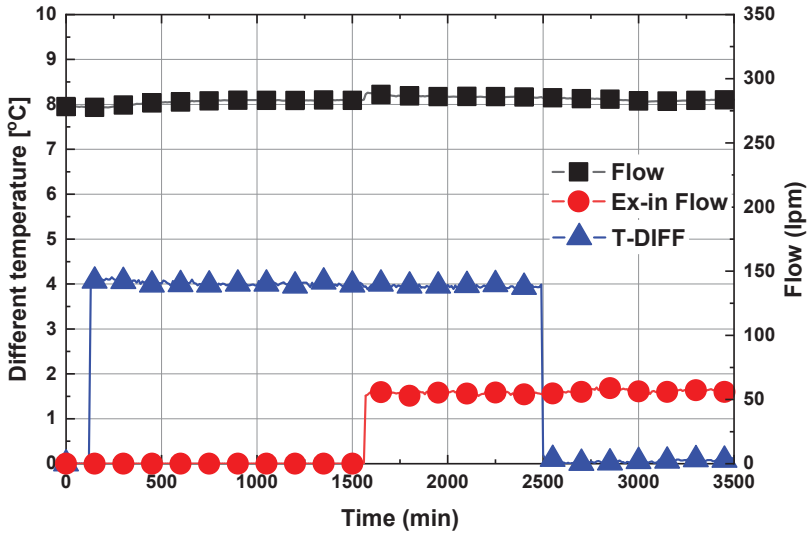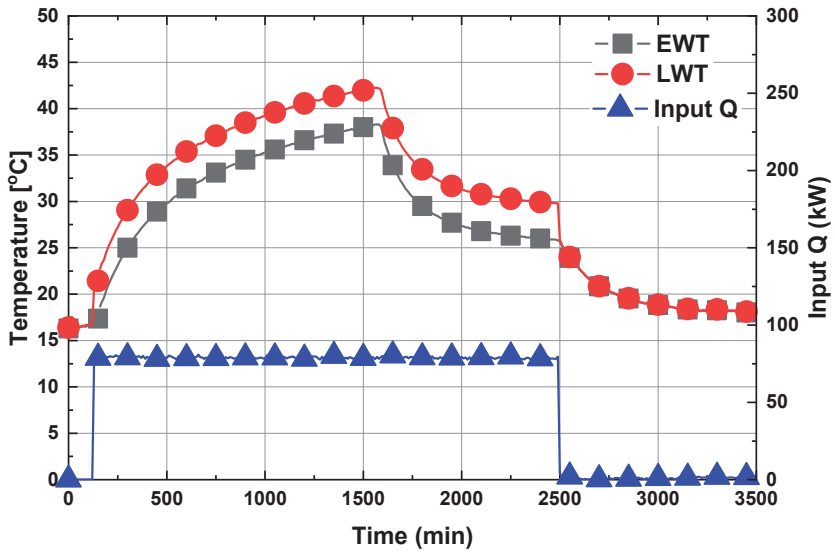
(**a**) SCW operation → balancing well operation

Figure 7. *Cont.*
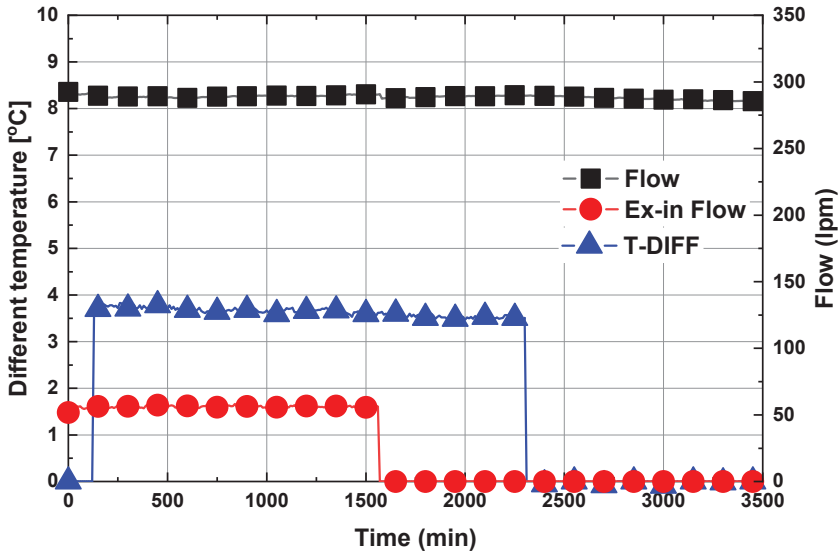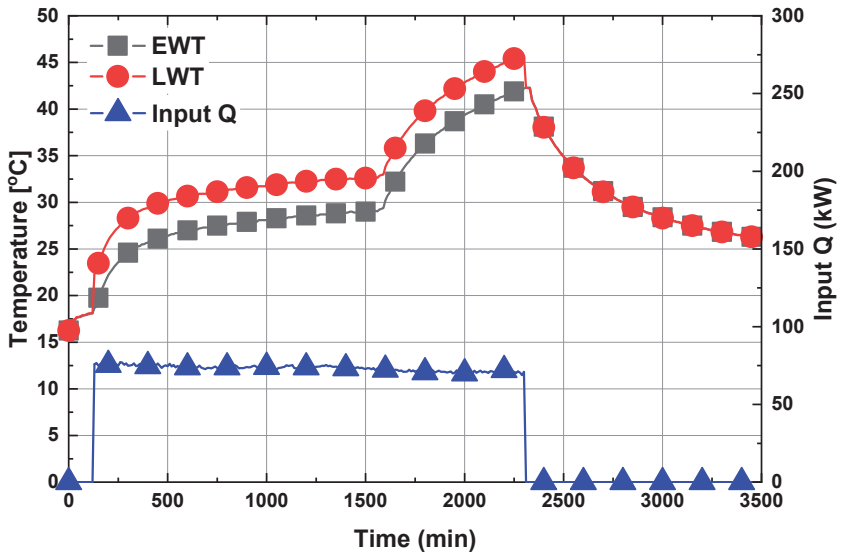
(**b**) Balancing well operation → SCW operation

Figure 7. Operating characteristics of the SCW and cross-mixing balancing well geothermal heat exchanger affecting the thermal environmental characteristics of the ground.

4. Conclusions

In this study, by installing calibrated thermometers, flow meters, and power spectrometer for a 30RT-level water-water geothermal heat pump installed at the site and by including two SCW underground heat exchangers, mechanical piping, circulation pumps, and cross-operation controllers, the following results were obtained:

1. The average COP values of the balanced well cross-heat exchange system were 3.76 and 3.27 during the cooling and heating operations, respectively. This signifies an improvement of the COP by 23% and 12% during the cooling and heating operations, respectively, compared to that of the existing SCW method of the heat exchange system.
2. The initial underground temperature was maintained constant with a small standard deviation of 0.08–0.12 °C for 3–5 d of continuous operation when using the balancing well cross-mixed heat exchange system, enabling a relatively stable supply of heat source.
3. A change in operational method from the ordinary SCW-type heat exchange system to the balanced well-intersected heat exchange system improved the COP of the cooling and heating system using geothermal heat and ensured a stable supply of geothermal energy by keeping the initial temperature constant. This could also eliminate the wasting of bleed water.

Conflicts of Interest: The authors declare no conflict of interest.

Nomenclature

q_{in}	Measured heat injection (w)
T_{in}	Inlet of temperature (°C)
T_{out}	Outlet of temperature (°C)
v	Flow rate (LPM)
$\varnothing_{tco}$	Total cooling capacity of the heat pump (W)
$\varnothing_{tho}$	Total heating capacity of the heat pump (W)
t_{f3}	Heat pump inlet temperature (°C) of circulating water on the source side
t_{f4}	Heat pump outlet temperature (°C) of circulating water on the source side
c_{pf}	Specific heat of heat source circulation water (J/(kg·K))
w_f	Mass flow rate of circulating water on the heat source side (kg/s)
$\varnothing_t$	Total power consumption (W)

References

1. Lund, J.; Sanner, G.; Rybach, L.; Curtis, R.; Hellström, G. Geothermal (ground-source) heat pumps: A world overview. *Geo-Heat Cent. Q. Bull.* **2004**, *53*, 1–10.
2. Lund, J.W. *Geothermal Heat Pumps—An Overview*; Geo-Heat Center Quarterly Bulletin, 22/1 (March); Geo-Heat Center, Oregon Institute of Technology: Klamath Falls, OR, USA, 2001; Available online: http://geoheat.oit.edu (accessed on 25 September 2020).
3. Lee, C. Thermal performance evaluation of a vertical closed-loop ground heat exchanger according to rock type in Korea. *Energy Build.* **2019**, *183*, 184–194. [CrossRef]
4. Tilley, B.S.; Baumann, T. On temperature attenuation in staged open-loop wells. *Renew. Energy* **2012**, *48*, 416–423. [CrossRef]
5. Woods, K.; Ortega, A. The thermal response of an infinite line of open loop wells for ground coupled heat pump systems. *Int. J. Heat Mass Transf.* **2011**, *54*, 5574–5587. [CrossRef]
6. Lee, C. Thermal performance of a standing column well geothermal heat exchanger system using re-injection of bleeding water. *Geothermics* **2019**, *82*, 73–80. [CrossRef]

7. Beretta, G.P.; Coppola, G.; Della Pona, L. Solute and heat transport in groundwater similarity: Model application of a high capacity open-loop heat pump. *Geothermics* **2014**, *51*, 63–70. [CrossRef]

8. You, J.; Lee, C. Comparative Analysis of Geothermal Energy in Korea Based on Closed Borehole and Single- and Two-Well Standing Column Well Geothermal Heat Exchange Systems. *Appl. Sci.* **2020**, *10*, 2467. [CrossRef]

9. Youngyun, P.; Jong-Koo, M.; Bum-Ju, J.; Yu-Chul, P.; Jin-Yong, L.; Jin-Gu, Y. Change of geothermal properties of groundwater by use of open loop geothermal cooling and heating system. *J. Geol. Soc. Korea* **2013**, *49*, 289–296.

10. Lee, C.; You, J.; Park, H.K. In-situ response test of various borehole depths and heat injection rates at standing column well geothermal heat exchanger systems. *Energy Build.* **2018**, *172*, 201–208. [CrossRef]

11. Hall, A.; Scott, J.A.; Shang, H. Geothermal energy recovery from underground mines. *Renew. Sustain. Energy Rev.* **2011**, *15*, 916–924. [CrossRef]

12. Athresh, A.; Al-Habaibeh, A.; Parker, K. Innovative Approach for Heating of Buildings Using Water from a Flooded Coal Mine Through an Open Loop Based Single Shaft GSHP System. *Energy Procedia* **2015**, *75*, 1221–1228. [CrossRef]

13. Szulc-Wrońska, A.; Tomaszewska, B. Low Enthalpy Geothermal Resources for Local Sustainable Development: A Case Study in Poland. *Energies* **2020**, *13*, 5010. [CrossRef]

14. Morrone, P.; Algieri, A. Integrated Geothermal Energy Systems for Small-Scale Combined Heat and Power Production: Energy and Economic Investigation. *Appl. Sci.* **2020**, *10*, 6639. [CrossRef]

15. Gatsios, T.; Cigna, F.; Tapete, D.; Sakkas, V.; Pavlou, K.; Parcharidis, I. Copernicus Sentinel-1 MT-InSAR, GNSS and Seismic Monitoring of Deformation Patterns and Trends at the Methana Volcano, Greece. *Appl. Sci.* **2020**, *10*, 6445. [CrossRef]

16. Parisi, M.L.; Douziech, M.; Tosti, L.; Pérez-López, P.; Mendecka, B.; Ulgiati, S.; Fiaschi, D.; Manfrida, G.; Blanc, I. Definition of LCA Guidelines in the Geothermal Sector to Enhance Result Comparability. *Energies* **2020**, *13*, 3534. [CrossRef]

17. Matuszewska, D.; Kuta, M.; Olczak, P. Techno-Economic Assessment of Mobilized Thermal Energy Storage System Using Geothermal Source in Polish Conditions. *Energies* **2020**, *13*, 3404. [CrossRef]

18. Čeryová, D.; Bullová, T.; Turčeková, N.; Adamickova, I.; Moravčíková, D.; Bielik, P. Assessment of the Renewable Energy Sector Performance Using Selected Indicators in European Union Countries. *Resources* **2020**, *9*, 102. [CrossRef]

19. Agemar, T.; Weber, J.; Moeck, I.S. Assessment and Public Reporting of Geothermal Resources in Germany: Review and Outlook. *Energies* **2018**, *11*, 332. [CrossRef]

20. Sciacovelli, A.; Guelpa, E.; Verda, V. Multi-scale modeling of the environmental impact and energy performance of open-loop groundwater heat pumps in urban areas. *Appl. Therm. Eng.* **2014**, *71*, 780–789. [CrossRef]

21. Park, Y.Y.; Mok, J.K.; Jang, B.J.; Park, Y.C.; Lee, J.Y. Influence of open and closed loop geothermal cooling and heating systems on hydrogeological properties. *J. Geol. Soc. Korea* **2013**, *49*, 649–659.

22. Russo, S.L.; Civita, M.V. Open-loop groundwater heat pumps development for large buildings: A case study. *Geothermics* **2009**, *38*, 335–345. [CrossRef]

23. Kim, W.; Lee, S.; Jeon, J.; Kim, M.; Kim, M.; Jeon, Y. Improved Design Method of Open Loop Geothermal System and its Applications. *New Renew. Energy* **2016**, *12*, 122–130. [CrossRef]

24. Bae, S.; Kim, H.; Kim, H.-W.; Nam, Y. Hydraulic feasibility study on the open-loop geothermal system using a pairing technology. *KIEAE J.* **2017**, *17*, 119–124. [CrossRef]

25. Bae, S.; Kim, H.; Kim, H.-W.; Nam, Y. Study on the Underground Thermal Environment around Wells for a Design Method of Open-Loop Geothermal System. *Trans. Korea Soc. Geotherm. Energy Eng.* **2017**, *13*, 14–20. [CrossRef]

26. Kim, M.J.; Choi, C.H.; Jeon, J.U. A study on the KS (Korea Standard) of SCW type ground heat exchanger - ground source heat pump system. *Korea Acad. Ind. Coop. Soc.* **2013**, *3*, 22–30.

27. Chang, K.-S.; Kim, M.J.; Kim, Y.-J. An Experimental Study on the Thermal Performance Evaluation of SCW Ground Heat Exchanger. *Int. J. Air-Cond. Refrig.* **2017**, *25*, 1750006. [CrossRef]

28. Ministry of Trade, Industry and Energy. *Standards of Support, Installation and Management for New and Renewable Energy System*; Announcement 2015-2632015; Ministry of Trade, Industry and Energy: Sejong, Korea, 2015.

29. Sanner, B.; Hellström, G.; Spitler, J.; Gehlin, S. More than 15 years of Mobile Thermal Response Test—A Summary of Experiences and Prospects. In Proceedings of the European Geothermal Congress, Pisa, Italy, 3–7 June 2013.

30. Beier, R.A.; Smith, M.D.; Spitler, J.D. Reference data sets for vertical borehole ground heat exchanger models and thermal response test analysis. *Geothermics* **2011**, *40*, 79–85. [CrossRef]

31. Chang, K.-S.; Kim, M.J. A Study on the Heat Transfer Characteristics of Various Construction of SCW Type Ground Heat Exchanger. *Korean J. Air-Cond. Refrig. Eng.* **2014**, *26*, 460–466. [CrossRef]

32. Gustafsson, A.-M.; Westerlund, L. Multi-injection rate thermal response test in groundwater filled borehole heat exchanger. *Renew. Energy* **2010**, *35*, 1061–1070. [CrossRef]

33. Raymond, J.; Therrien, R.; Gosselin, L. Borehole temperature evolution during thermal response tests. *Geothermics* **2011**, *40*, 69–78. [CrossRef]

34. Jang, C.-H.; Kim, M.J. Analysis and thermal response test for vertical ground heat exchanger with two U-loop configuration. *Int. J. Energy Res.* **2015**, *40*, 189–197. [CrossRef]

35. Incropera, F.P.; Dewitt, D.P. *Fundamentals of Heat and Mass Transfer*, 4th ed.; John Wiley and Sons: Hoboken, NJ, USA, 1996.

36. Chang, J.H.; Park, D.H.; Park, S.S.; Na, S.M. Evaluation of Application of Effective Hydraulic Conductivity in SCW Ground Heat Pump System. In Proceedings of the Korean Geo-Environmental Society, Fall Conference, Seoul, Korea, 2010; pp. 141–146.

Article

Evaluation and Optimization of the Annual Performance of a Novel Tri-Generation System Driven by Geothermal Brine in Off-Design Conditions

Mehri Akbari Kordlar *, Florian Heberle and Dieter Brüggemann

Chair of Engineering Thermodynamics and Transport Processes (LTTT), Center of Energy Technology (ZET), University of Bayreuth, 95440 Bayreuth, Germany; Florian.Heberle@uni-bayreuth.de (F.H.); Dieter.Brueggemann@uni-bayreuth.de (D.B.)

* Correspondence: lttt@uni-bayreuth.de or Mehri.Akbari-Kordlar@uni-bayreuth.de; Tel.: +49-921-55-7161

Abstract: The difference in heating or cooling to power ratio between required demands for district networks and the proposed tri-generation system is the most challenging issue of the system configuration and design. In this work, an adjustable, novel tri-generation system driven by geothermal resources is proposed to supply the thermal energies of a specific district network depending on ambient temperature in Germany. The tri-generation system is a combination of a modified absorption refrigeration cycle and a Kalina cycle using NH_3-H_2O mixture as a working fluid for the whole tri-generation system. A sensitive analysis of off-design conditions is carried out to study the effect of operational parameters on the system performances prior to optimizing its performance. The simulation show that the system is able to cover required heating and cooling demands. The optimization is applied considering the maximum exergy efficiency (scenario 1) and minimum total exergy destruction rate (scenario 2). The optimization results show that the maximum mean exergy efficiency in scenario 1 is achieved as 44.67% at the expense of 14.52% increase in the total exergy destruction rate in scenario 2. The minimum mean total exergy destruction rate in scenario 2 is calculated as 2980 kW at the expense of 8.32% decrease in the exergy efficiency in scenario 1.

Keywords: tri-generation; off-design analysis; ammonia-water solution; geothermal; flexible demand production; optimization

1. Introduction

Due to the non-fluctuating renewable and environmentally friendly nature of geothermal heat sources, it is inevitable to utilize these sources to reduce the consumption of fossil fuels and environmental pollution [1]. For applying geothermal sources to produce power, cooling and heating in different seasons, various multi-generation systems are investigated [2]. It has been observed that co-generation [3] and multi-generation systems [4,5] attract the interest not only of researchers but also of operators and energy suppliers because of their substantial energy conservation [6,7] and economic aspects [8]. Recently, some studies have been carried out to examine co-generation systems for producing power/cooling or power/heating using geothermal heat sources. In addition, some configurations of tri-generation systems have been presented to provide the demand of power, cooling and heating [9,10] with low-grade heat sources like geothermal heat sources. Coskun et al. [11] investigated a tri-generation system driven by geothermal heat source of 173 °C. The system was studied on two different main groups for hot and cold seasons. The exergy efficiency in winter with an ambient temperature of 10.1 °C was calculated as 52.8%. In summer with an ambient temperature of 22.3 °C the exergy efficiency of the system was 49.5%. In addition, in comparison to the single power generation system, the exergy efficiency was increased by 1.12 and 1.25 times for summer and winter

days, respectively. Zare [12] proposed and optimized two various designs of tri-generation systems utilizing geothermal heat source of 173 °C. The main difference in two introduced designs related to the power production system. An organic Rankine cycle was applied in one system while Kalina cycle was utilized in the other system. The author reported that the maximum exergy efficiency of tri-generation systems based on ORC and Kalina cycles were 46.51% and 50.36%, respectively. The multi-generation energy system driven by geothermal heat source of 185–215 °C to produce electricity, heating, cooling and hydrogen was introduced by Akrami et al. [13]. Their results revealed that energy and exergy efficiencies of the system were about 34.9% and 49.2%, respectively.

Based on the abovementioned studies and due to the increased attention paid to systems producing power, heating and cooling in recent years, the literature lacks any mention of the application of a one energy system using the same working fluid for tri-generation purposes. Mostly, in the previous proposed tri-generation systems, there are two different working fluids in each power and cooling section [11–13]. Generally, the organic Rankine cycle (ORC) in the power block utilizes natural hydrocarbons or fluorinated refrigerants as a working fluid. As well, the absorption refrigeration system with LiBr-water is used in the cooling block. It is important to note that using different working fluids can lead to significant higher investment costs for safety and environmental issues. Therefore, there is room for more work to investigate systems using one working fluid in tri-generation systems. In this context, an extension of the Kalina cycle by a cooling part also using ammonia-water as working fluid is a promising approach. The Kalina cycle is a proven technology for power generation based on low-temperature heat sources. The first geothermal application of the Kalina cycle in Europe was the Orkuveita Húsavíkur (Iceland) power plant [14]. This power plant began to operate in July 2000. The net electrical output of the plant is 1.7 MW [15]. The thermal efficiency of this power Kalina cycle was calculated to be between 12.3–17.1% depending on the cooling water temperature [16]. In Unterhaching (Germany) a combined heat and power system was realized at a geothermal temperature of 122 °C [17]. This Kalina cycle is designed for an electrical power of 3.35 MW. In addition, the thermal power of the district heating system is about 40 MW [18]. Another example for an existing geothermal application is the power plant in Bruchsal (Germany). This system started to operate in 2012 and is driven by a geothermal heat source of 122 °C. The electrical capacity of the power plant in Bruchsal is 550 kW [19].

In addition, existing studies of low-grade heat sources only pay small attention to tri-generation systems. On the other hand, previous analyses are based on constant ambient temperature with fixed values of power, cooling and heating generation without paying attention to heating and cooling periods as well as corresponding frequency demands. In this context, tri-generation systems are mostly studied under design conditions. However, it is obvious that changing the operating parameters due to the different geometry, characteristics and performance curves of the component, mainly heat exchangers and turbine, have been affected by the system performances corresponding off-design behavior [20,21]. Therefore, the off-design evaluation of the system is inevitable and should be considered in the system design in order to annual simulation.

The present works addresses all issues mentioned above by introducing a novel configuration of the tri-generation system driven by geothermal water. The system works only by one working fluid as ammonia-water solution. Due to the variable boiling temperature of an ammonia-water solution during the heat transfer process, the irreversibilities of heat exchangers decrease as well as the efficiency of the system increases [22,23]. In this context, the main objectives in this work are:

- to define heating and cooling demand in winter and summer conditions (different ambient temperatures) to evaluate the system performance using operational data of an existing geothermal district heating network in the German Molasse basin [24]. In particular, the geothermal source, mean ambient temperatures and heating/cooling demands are based on this case;
- to validate the power part (Kalina cycle) and to verify the cooling part in order to confirm the validity of the simulation model;
- to determine the main operational parameters to analyze the system;
- to develop and apply an off-design model of the tri-generation system;

- to apply the quasi-stationary simulation of a tri-generation system in different weather conditions to fulfill the heating and cooling demands;
- to obtain mean annual system performances;
- to optimize the system considering two criteria, maximum exergy efficiency and minimum total exergy destruction rate.

2. Methodology

2.1. Description of the System

The schematic diagram of the proposed tri-generation system is shown in Figure 1. The system is able to simultaneously generate heating, power and cooling for various purposes in different seasons. The system consists of three parts: the power section which produces electricity, the adaptable cooling part which is applied as absorption refrigeration in summer days and heat pump in winter days (by switching the evaporator) and the domestic heat exchanger (DHE) is used to supply heat demand. As shown in Figure 1, the geothermal hot water (state 21) is divided into two parts; one part provides the required heat input to satisfy the heat demand (state 24) via the DHE. The other part is coupled to the power section by the boiler (BOI) (state 22). The required heat for the generator (GEN) is supplied by stream 26 which is the combination of the two returning geothermal water streams coming from DHE (state 25) and BOI (state 23). The description of the tri-generation system is started with the ammonia-water solution in the power section. A saturated liquid ammonia-water solution (state 4) is pumped through pump 2 (PU2) (state 8) to the high pressure of the system. The stream is delivered to separator (SEP) after heating in the boiler via geothermal water (state 9). In the SEP, the liquid-vapor stream is separated to saturated liquid (state 10) and saturated vapor phases (state 11). The stream 12 is expanded via the turbine (TUR) and is mixed with the stream leaving the solution heat exchanger (SHE) via expansion valve 2 (EX2). This stream (stream 15) is led through CON_2 and then to absorber (ABS) (stream 17) through PU3. The ammonia-water solution at the outlet of the ABS (state 1) is forced to the medium pressure level (state 2) by PU1 and is led to SHE. This stream at the outlet of the SHE (stream 3) which is heated in the SHE via saturated liquid (state 11) from SEP. The stream 3 goes to GEN to heat with the geothermal water following to divide into two saturated liquid and vapor streams (stream 4 and 5). The vapor stream coming from the GEN (state 5) is cooled through rectifier (REC) and again the stream is divided into liquid and vapor phase to provide a strong ammonia solution (stream 7). The pure ammonia is saturated in the CON_1 (stream 18) and is led through the evaporator (EVA) via EX_1. In the EVA, the pure ammonia solution is heated by absorbing heat and can produce a cooling demand in the summer condition (stream 39–40). The stream coming from EVA (stream 20) leads to ABS and is mixed with stream 17 via PU3 and the proposed system is completed. The heat sink streams (streams 31–36) are used as coolant and the water- ethylene glycol streams 39 and 40 are utilized to cover the cooling demand. The water streams 29 and 30 are used to produce heating demand. Moreover, it is worthwhile to indicate that in the proposed system, two different evaporators are applied in summer and winter. In summer days, when the tri-generation mode is required, the evaporator for cooling is applied to the system. In winter days, when no cooling demand is required, the geothermal fluid coming from GEN (stream 27) is led through the evaporator for heating. In this regard, the useful productions in the tri-generation system are outlined as follows:

- heating via domestic heat exchanger
- power generation via turbine
- cooling via evaporator
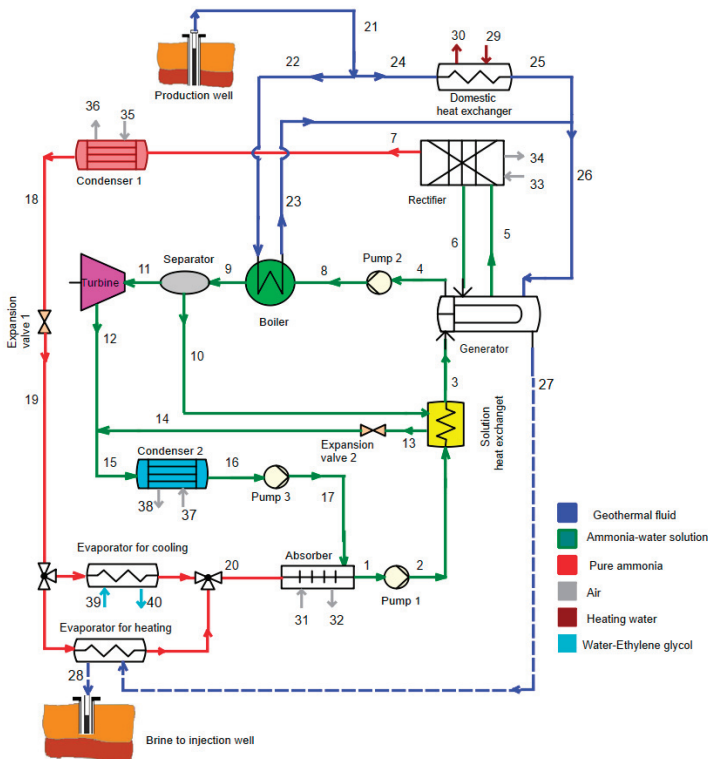
Figure 1. Schematic diagram of the proposed tri-generation system.

2.2. Assumption

For a process simulation and a detailed analysis of the proposed system, each component of the cogeneration cycle is considered as a control volume and a mathematical model is established by applying the conservation of mass and energy balances as well as the exergy principle. Simulation is carried out by the software Engineering Equation Solver (EES) [25]. The fluid properties of ammonia-water solution and water are estimated in EES by implementing correlations of Ibrahim [26] and Wagner [27], respectively. In addition, the thermodynamic and transport properties of water-ethylene glycol are applied in EES by adapting the correlations of Fujuita [28] and Lee [29].

Some assumptions are made to simplify the mathematical model [30]:

- Pressure and heat losses in the heat exchangers and pipelines are neglected.
- The isotropic efficiency for pumps is considered as constant.
- The changes of kinetic and potential energies are negligible.
- The state of leaving streams of absorber, condenser, generator and rectifier is saturated.
- In the cold season when heating demand is required, the extracted stream of geothermal fluid from the generator is used in the evaporator to supply the needed heat (stream 27–28) in the evaporator in the absorption heat pump cycle. In the summer days, the stream 27 goes to reinjection well and the cooling demand is produced in the evaporator for cooling.

The basic assumption and assumed boundary conditions for the simulation are summarized in Table 1.

Table 1. Input data and boundary conditions used for design the system and process the simulation.

Parameter	Symbol	Value
Dead state pressure (*bar*)	p_0	1
Dead state temperature (°C)	T_0	$T_0 + 5$
Geothermal hot water temperature (°C) [24]	$T_{in,geo}$	138
Geothermal hot water mass flow rate (kg/s) [24]	$\dot{m}_{geo}$	120
Ambinet temperature (°C) [24]	T_{amb}	−5.68
Heating demand (*MW*) [24]	$\dot{Q}_{heating}$	11.8
Evaporator temperature (°C) [24]	T_{eva}	5
Turbine inlet pressure (bar) [31]	TIP	20
Ammonia concentration in the boiler (%) [32]	ζ_B	50
Supply heating temperature (°C) [24]	T_{33}	90
Return heating temperature (°C) [24]	T_{32}	60
Turbine isentropic efficiency (%) [12]	$\eta_{is,tur}$	85
Pump isentropic efficiency (%) [22]	$\eta_{is,pump}$	75

2.3. Off-Design Model

The operating conditions of the system are influenced by the performance of the heat exchangers and turbine [33,34]. In this regard, the different steps of off-design calculation are indicated in Figure 2. As shown, the first step in off-design process calculation is related to obtain the heat transfer capacity (UA) of heat exchangers in the design mode which is outlined in Table 1. The heat transfer rate ($\dot{Q}$) in the heat exchangers is expressed as [35]:

$$\dot{Q} = UA\, \Delta T_{LMTD} \tag{1}$$

where U is the overall heat transfer coefficient, the area of the heat exchanger is A and ΔT_{LMTD} represents the logarithmic mean temperature difference between the hot and cold streams in the heat exchanger. In the next step, the off-design behavior of the heat exchangers is considered according to the method presented by Manente [34]. In off-design conditions, the variations in mass flow rates from the design conditions bring about a change in the UA. The heat exchange capacity is modified considering the actual mass flow rate:

$$\frac{(UA)_{off-design}}{(UA)_{design}} = \left(\frac{\dot{m}_{off-design}}{\dot{m}_{design}}\right)^m \tag{2}$$

The heat exchanger configuration determines the exponent m. The exponent m is set to 0.44 for the air-cooled condenser, 0.66 for the generator, solution heat exchanger and evaporators, 0.15 for the boiler [36]. After obtaining the off-design characteristics such as UA for the considered heat exchangers, calculation of the turbine isentropic efficiency is the next step. The isentropic efficiency of the turbine is considered as a function of enthalpy drop and volumetric flow rate at the outlet of the turbine. The off-design behavior of the isentropic efficiency of the turbine depends on two coefficients r_h and r_v according to [37]. The coefficients depend on the outlet volume flow rate and the enthalpy drop in the turbine:

$$r_T = \sqrt{\frac{h_{Turbine\ inlet} - h_{Turbine\ outlet}}{(h_{Turbine\ inlet} - h_{Turbine\ outlet})^{design}}} \tag{3}$$

$$r_h = ([(1.39r_T - 5.425) \times r_T + 6.274] \times r_T - 1.866) \times r_T + 0.619 \tag{4}$$

where h is the enthalpy and exponents design means the calculated value at design [37]:

$$r_{VT} = \frac{(\dot{V})}{(\dot{V})^{design}} \tag{5}$$

$$r_v = ([(-0.21 r_{VT} + 1.117) \times r_{VT} - 2.533] \times r_{VT} + 2,588) \times r_{VT} + 0.038 \tag{6}$$

where $\dot{V}$ shows the volumetric flow rate at the outlet of the turbine. Therefore, the isentropic efficiency of the turbine in off-design can be calculated as [32]:

$$\eta_{s,tur} = \eta_{tur} \times r_v \times r_h \tag{7}$$
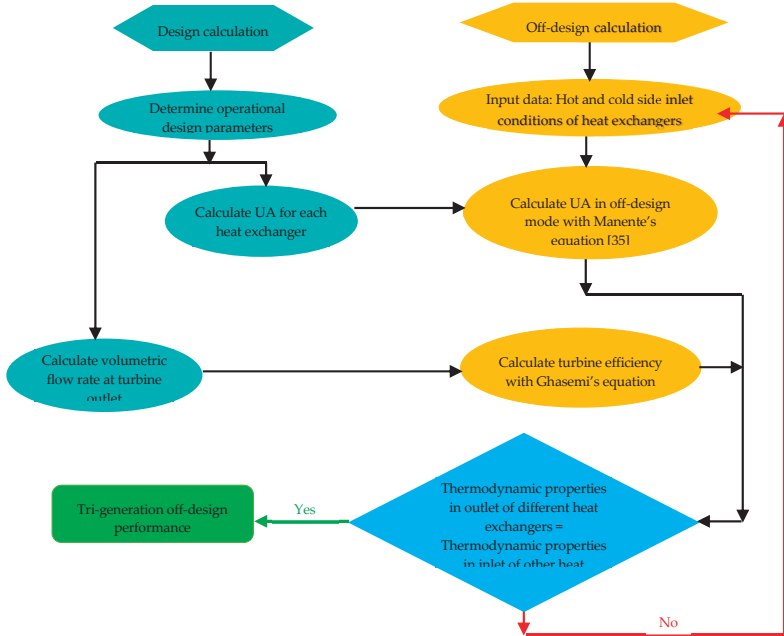
Figure 2. Off-design calculation procedure.

It is important to note that the off-design values of $\eta_{s,tur}$ and r_{VT} can take a value higher than the design mode values. In addition, the UA value and turbine isentropic efficiency, the thermodynamic properties of different states have been calculated. The whole off-design case is calculated in an iterative process which ends when the simulation shows convergence. The main criteria of convergence are related to the equality of the thermodynamic properties such as temperature, pressure and ammonia concentration in the outlet of different heat exchangers and the inlet of other heat exchangers. The convergence is obtained within 1%. The proposed system is designed under operational parameters under base case which is presented in Table 1. The design case results are calculated for the heating demand of 11.66 MW in the ambient temperature of −5.67 °C.

The heat exchange capacities (UA) and mass flow rates of all heat exchangers in the system for design case are shown in Table 2. In addition, in design conditions the volumetric flow rate at the turbine outlet is calculated to be 3.376 m^3/s.

Table 2. The calculated parameters of heat exchangers in design mode.

	$(UA)_{design}$ (kW/K)	$(\dot{m})_{design}$ (kg/s)
Domestic heat exchanger	313.2	92.64
Boiler	723.5	13.37
Generator	71.24	17.11
Solution heat exchanger	37.11	17.11
Absorber	343.9	263.8
Condenser 1	128.6	110.4
Condenser 2	514.4	1110
Dephlegmator	3.066	12.39
Evaporator for heating	24.18	1.74
Evaporator for cooling	1014	2.082

2.4. Heating and Cooling Demand Profiles

In order to analyze the proposed cycle, real heating data of an existing geothermal district heating network in the German Molasse Basin [24] and estimated cooling demand are applied. The VDI 4655 method [38] is applied to estimate the annual system performance. In this method, 10 typical days are analyzed. This procedure is distinguished from seasonal, i.e., summer (S), winter (W) and transition (T), and from the typical days, i.e., workdays (W) and Sundays (S). In this category, Saturdays are selected as the workday. Furthermore, fine (F) and cloudy (C) days are differentiated to reach acceptable results. However, in the summer days, no distinction between fine and cloudy days (X) is made. These 10 typical days categories are; WWF, WWC, WSF, WSC, TWC, TSC, TSF, TWF, SWX, SSX.

According to the test reference years (TRY), Germany is divided into various climate zones. As shown in Table 3, according to this climate zones in the mentioned category "VDI 4655", the number of typical days during the year changes. In this work, for the purpose of the annual simulation, the 10 typical days are simulated for TRY13 which is associated to the southern German Molasse Basin. The annual performances of the system are calculated by weighting these typical days considering their frequency.

Table 3. Test reference years according to VDI 4655 [38].

Climate Zone	Number of Typical Days (Frequency of the Different Typical Days)									
	WWF	**WWC**	**WSF**	**WSC**	**TWC**	**TSC**	**TSF**	**TWF**	**SWX**	**SSX**
. . .										
TRY12	23	57	2	16	91	18	8	27	104	19
TRY13	29	91	6	19	72	10	15	37	73	13
TRY14	22	115	5	25	81	15	11	42	42	7
. . .										

In order to conduct a quasi-stationary simulation, the heating and cooling demands for each typical day category are required. The profiles of corresponding heating demand for different typical days categories are developed depending on operational data of a real geothermal heat plant in the German Molasse Basin. The corresponding mean values of heating demands and the ambient temperatures for different typical days categories are illustrated in Table 4, respectively [18]. It is seen that the ambient temperature takes the lowest values in winter days and the highest values occur in the summer days. It is clear that the ambient temperature in cloudy days is basically lower than the fine days. For heating demand values which are listed in Table 4, it is observed that the heating demand has higher values in winter days in comparison to the summer and transition days. In addition, the heating demand in cloudy days, especially in the afternoon is considerably higher than the one in fine days. Furthermore, comparing the heat demand on Sundays and workdays shows that the heating demand is generally lower on Sundays and has a small variation.

Table 4. Corresponding mean values of heating, cooling and ambient temperature for different typical days categories.

	WWF	WWC	WSF	WSC	TWC	TSC	TSF	TWF	SWX	SSX
	n = 29	*n* = 91	*n* = 6	*n* = 19	*n* = 72	*n* = 10	*n* = 15	*n* = 37	*n* = 13	*n* = 73
$T_{ambient}$ (°C) [24]	−0.13	−5.68	2.27	1.1	7.37	4.81	13.81	15.42	15.67	17.24
$Q_{heating}$ (MW) [24]	11.68	11.66	11.8	10.79	6.3	6.15	4.79	5.69	2.99	2.9
$Q_{cooling}$ (MW)	-	-	-	-	-	-	1.78	1.9	2.43	2.48

The cooling demand is not available for specific real application; therefore, it is calculated with the following assumption. The cooling demand for an ambient temperature higher than 13 °C in four typical days according to some available real data in public buildings is assumed to be 0.33–0.85 times of the corresponding heating demand which is depending on the ambient temperature. It is noteworthy to note that this value is based on the ambient temperature in which with increasing of the ambient temperature, the corresponding value increases. Referring to Table 4, it is shown that the cooling demand takes higher values on workdays in comparison to Sundays. In addition, the cooling demand on all 4 typical days in the morning is lower than the one in the afternoon.

2.5. Exergetic Evaluation

In order to evaluate the cycle performance, the second law efficiency and exergy destruction rate are considered as main evaluation criteria. In general, in the absence of magnetic, electrical, nuclear and surface tension effects as well as ignoring the kinetic and potential exergies, the exergy rate consists of two physical and chemical exergy rates as [39]:

$$\dot{E} = \dot{E}_{ph} + \dot{E}_{ch} \tag{8}$$

Physical exergy can be obtained from [33]:

$$\dot{E}_{ph} = \dot{m}[(h - h_0) - T_0(s - s_0)] \tag{9}$$

and the chemical exergy for ammonia-water solution is expressed as [40]:

$$\dot{E}_{ch(NH_3/H_2O)} = \dot{m}\left[\left(\frac{X}{M_{NH_3}}\right)e^0_{ch,NH_3} + \left(\frac{1-X}{M_{H_2O}}\right)e^0_{ch,H_2O}\right] \tag{10}$$

The subscript 0 in Equation (3) indicates the dead state and T_0 shows its temperature. The standard chemical exergy for ammonia and water is set to 336.684 and 45 kJ/kmol [40].

For a detailed analysis, the exergy destruction rate is calculated. The exergy destruction rate is defined as the difference between the product exergy ($\dot{E}_P$), loss exergy ($\dot{E}_L$) and fuel exergy ($\dot{E}_F$) for each component of the proposed system [41]:

$$\dot{E}_{D,k} = \dot{E}_{F,k} - \dot{E}_{P,k} - \dot{E}_{L,k} \tag{11}$$

For parametric analysis, the energy and exergy efficiencies are calculated to be [42]:

$$\eta_{energy} = \frac{\dot{W}_{net} + \dot{Q}_{heating/cooling}}{\dot{Q}_{in}} \tag{12}$$

$$\eta_{exergy} = \frac{\dot{W}_{net} + \dot{E}_{heating/cooling}}{\dot{E}_{in}} \tag{13}$$

It is evident that the energy or thermal efficiency is the ratio of the net available products (net product power, heating and cooling rates) to the rate of thermal energy, which is absorbed from the geothermal heat source. In addition, the exergy efficiency is the ratio of the net available products exergy (net product power, heating and cooling exergies) to the rate of input exergy from the geothermal heat source. In Equations (12) and (13) $\dot{W}_{net}$ is the net output power of the system, $\dot{Q}_{cooling}$ is the cooling capacity in the summer condition, the heating capacity and the total heat input are $\dot{Q}_{heating}$ and $\dot{Q}_{in}$, respectively. $\dot{E}_{cooling}$ is the generated exergy rate for cooling purpose used in the summer days, the heating exergy and the total input exergy are $\dot{E}_{heating}$ and $\dot{E}_{in}$, respectively. These parameters are defined as:

$$\dot{W}_{net} = \dot{W}_{Tur} - \sum \dot{W}_P \tag{14}$$

$$\dot{Q}_{cooling} = \dot{m}_{39}(h_{39} - h_{40}) \tag{15}$$

$$\dot{Q}_{heating} = \dot{m}_{30}(h_{30} - h_{29}) \tag{16}$$

$$\dot{Q}_{in} = \begin{cases} \dot{m}_{21}(h_{21} - h_{28}) & \text{for winter condition} \\ \dot{m}_{21}(h_{21} - h_{27}) & \text{for summer condition} \end{cases} \tag{17}$$

$$\dot{E}_{cooling} = \dot{E}_{40} - \dot{E}_{39} \tag{18}$$

$$\dot{E}_{heating} = \dot{E}_{30} - \dot{E}_{29} \tag{19}$$

$$\dot{E}_{in} = \begin{cases} \dot{E}_{21} - \dot{E}_{28} & \text{for winter condition} \\ \dot{E}_{21} - \dot{E}_{27} & \text{for summer condition} \end{cases} \tag{20}$$

The total exergy destruction rate of the system is calculated to be:

on winter days:

$$\dot{E}_{D,tot} = \dot{E}_{in} - (\dot{W}_{net} + \dot{E}_{heating}) - (\dot{E}_{L,ABS} + \dot{E}_{L,CON1} + \dot{E}_{L,CON2} + \dot{E}_{L,REC}) \tag{21}$$

on summer days:

$$\dot{E}_{D,tot} = \dot{E}_{in} - (\dot{W}_{net} + \dot{E}_{heating} + \dot{E}_{cooling}) - (\dot{E}_{L,ABS} + \dot{E}_{L,CON1} + \dot{E}_{L,CON2} + \dot{E}_{L,REC}) \tag{22}$$

The corresponding parameters are:

$$\dot{E}_{L,ABS} = (\dot{E}_{17} + \dot{E}_{20} - \dot{E}_1) - (\dot{E}_{32} - \dot{E}_{31}) \tag{23}$$

$$\dot{E}_{L,CON1} = (\dot{E}_7 - \dot{E}_{18}) - (\dot{E}_{36} - \dot{E}_{35}) \tag{24}$$

$$\dot{E}_{L,CON2} = (\dot{E}_{15} - \dot{E}_{16}) - (\dot{E}_{38} - \dot{E}_{37}) \tag{25}$$

$$\dot{E}_{L,REC} = (\dot{E}_5 - \dot{E}_6 - \dot{E}_7) - (\dot{E}_{34} - \dot{E}_{33}) \tag{26}$$

3. Results and Discussion

The system is analyzed in off-design conditions by considering mass, energy and exergy balances as well as off-design model equations for each component as a control volume. In this regard, by adapting the geothermal mass flow division ratio ($r_{geo} = \dot{m}_{24}/\dot{m}_{21}$), the heating demand is totally covered by the geothermal resource. In addition, the sensitive analysis is applied to each typical day category displayed in Table 4 to find the operational parameters prior to optimization.

3.1. Validation and Verification

In Table 5, the real power plant parameters given in Ogriseck [16] are compared to the conducted simulations. The represented results display a good agreement between the present work and real data of the existing Kalina power plant with a deviation of less than 0.9%. The percentage of relative deviation between available data in the literature and obtained data from simulation in the present work is calculated as follows:

$$\text{Deviation }(\%) = \frac{\left|X_{reference\ data} - X_{simulation\ data}\right|}{X_{reference\ data}} \times 100 \qquad (27)$$

Table 5. Validation results of the power ammonia-water Kalina cycle operating conditions gained from present work (a) with reported data for the existing power plant in Húsavík [16] (b).

Point	Temperature (K)		Pressure (kPa)		Ammonia Concentration $(kg\frac{NH_3}{kg}solution)$	
	(a)	(b)	(a)	(b)	(a)	(b)
1	281.15	281.15	4.6	4.6	0.82	0.82
2	281.20	281.15	35.3	35.3	0.82	0.82
3	314.26	314.15	34.3	34.3	0.82	0.82
4	336.10	336.15	33.3	33.3	0.82	0.82
5	389.15	389.15	32.3	32.3	0.82	0.82
6	389.15	389.15	32.3	32.3	0.973	0.97
7	389.15	389.15	32.3	32.3	0.498	0.5
8	316.21	316.15	6.6	6.6	0.973	0.97
9	319.11	319.15	31.3	31.3	0.498	0.5
10	319.18	319.15	6.6	6.6	0.82	0.82
11	303.16	303.15	5.6	5.6	0.82	0.82

The cooling system (absorption refrigeration system) is verified using available data reported in literature [43]. In the absorption system, the verification results are obtained with some main design parameters such as absorber, condenser and generator temperatures and ammonia concentration. Figure 3 represents the data obtained in the present work and the data by Adewusi [43] for the absorption refrigeration ammonia-water cycle. The represented results display a good agreement between the present work and literature with a deviation of less than 1%.
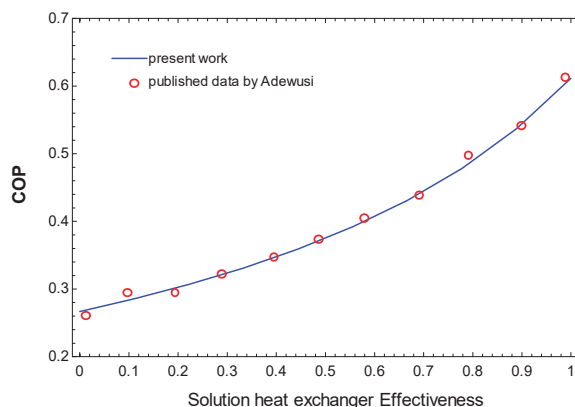

Figure 3. Verification results for absorption refrigeration cycle for the present work and with previously published data by [43].

3.2. Parametric Analysis

A parametric study is applied to investigate the influences of decision parameters such as the turbine inlet pressure (TIP), the generator temperature (T_{gen}), the temperature differences at the Absorber (δT_{ABS}) and condensers exit ($\delta T_{CON1} = T_{18} - T_{35}$, $\delta T_{CON2} = T_{16} - T_{37}$) on the system performance prior to optimization. It is noteworthy to mention that, in parametric analysis for off-design conditions only one parameter, among the ones outlined in Table 1, is changed and the other parameters are calculated in off-design conditions. The ammonia concentration in the power section is kept constant as $0.5 \, kg(NH_3)/kg(solution)$.

The variations of exergy efficiency as well as total exergy destruction rate with the turbine inlet pressure are shown in Figure 4a in off-design conditions. As shown, the exergy efficiency and $\dot{E}_{D,tot}$ take a local maximum and minimum values, respectively. The trends of these variations can be justified by representing the variation in power production, input exergy and loss exergy in some components with the TIP. Due to the reduction in reinjection geothermal temperature, the $\dot{E}_{in}$ is increased with an increase in TIP. In addition, changes in TIP has no effect on the produced heating capacity and the heating exergy of the system. On the other side, the power production is maximized locally at specific values of TIP. With an increase in TIP, the turbine mass flow rate decreases, however the turbine specific work has been optimized locally. As presented in the Figure 4b, the contrary effect of these parameters occurs in a way that leads to a local optimum for the produced net power output and the exergy efficiency. Furthermore, with an increase in TIP, the loss exergy rate in the ABS, REC, CON_1, CON_2 is increased. According to Equation (21), the total exergy destruction rate takes locally minimum values.
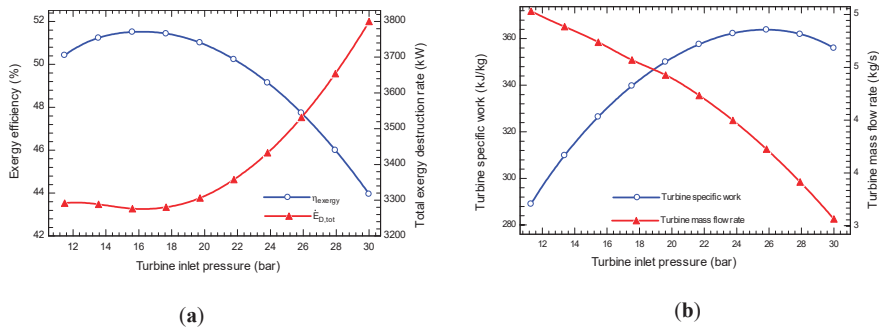
Figure 4. The effect of the TIP (**a**) on exergy efficiency and total exergy destruction rate (**b**) on the turbine specific work and mass flow rate.

The influence of the generator temperature on the exergy efficiency and total exergy destruction rate in off-design mode is presented in Figure 5a. It is seen that as the T_{gen} increases, the exergy efficiency is locally maximized as well as the $\dot{E}_{D,tot}$ is increased. With an increase in T_{gen}, the $\dot{E}_{in}$ and $\dot{W}_{net}$ are decreased as shown in Figure 5b. The reduction rate of these two parameters occur in such a way that leads to a local maximum value for the exergy efficiency. The loss exergy which occurs in ABS, REC, CON_1, CON_2, is decreased by increasing T_{gen}. In this regard, according to Equation (21) the total exergy destruction rate decreases with an increase in T_{gen}.
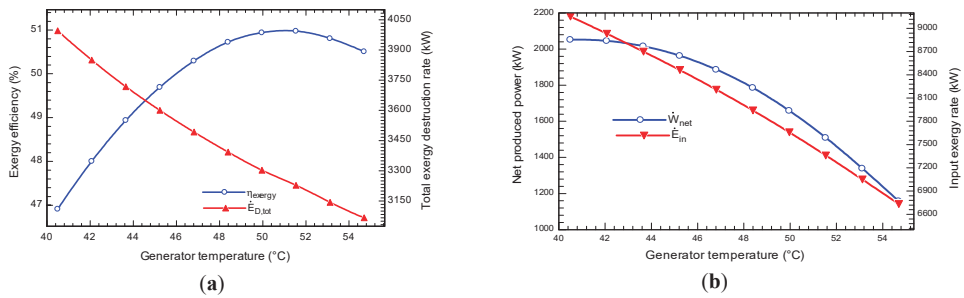
Figure 5. The influence of the T_{gen} (**a**) on exergy efficiency and total exergy destruction (**b**) on the net produced power and input exergy to the system.

The influence of the temperature differences at the exit of the condensers on exergy efficiency and total exergy destruction rate in off-design mode is depicted in Figure 6. It is seen that with an increase in δT_{CON1}, the η_{exergy} and $\dot{E}_{D,tot}$ are increased and decreased, respectively. In addition the η_{exergy} is decreased and $\dot{E}_{D,tot}$ increased as the δT_{CON2} changes. The net produced power is decreased with an increase in both δT_{CON1} and δT_{CON2}. However, the input exergy to the system is kept constant in changing δT_{CON2} and is decreased in variation δT_{CON1}.
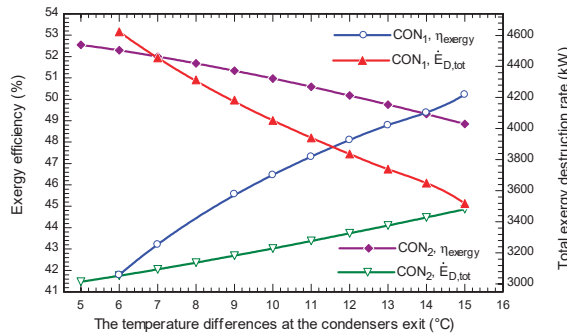
Figure 6. The variation of exergy efficiency and the total exergy destruction rate with the temperature differences at the condensers exit.

3.3. Discussion of Parametric Analysis

The general behavior of the system on the selected parameters may be summarized as follows:

- There is a local optimum value in the exergy efficiency at the specific value of TIP = 16.3 bar and T_{gen} = 51.5 °C in the typical day of WWC. In the other typical day categories, the exergy efficiency has local optimum at the different values of TIP and T_{gen} in comparison to typical day of WWC.
- The total exergy destruction rate in minimized locally at the specific values of TIP = 16.53 bar in the typical day of WWC. This value of TIP is changed in the other typical day categories in order to minimize locally the total exergy destruction rate.
- The general behavior of operational parameters for all typical days categories is almost the same of the typical day of WWC as shown in Figures 5–7.
- In the hot days; TSF, TWF, SWX and SSX, with an increase in the δT_{CON1} the exergy efficiency decreases which is in reverse for other category days.
- The values of δT_{CON1} and δT_{CON1} are limited by the ambient temperature and take different range in different typical day categories.

	$n=29$	$n=91$	$n=6$	$n=19$	$n=72$	$n=10$	$n=15$	$n=37$	$n=13$	$n=73$
	WWF	WWC	WSF	WSC	TWC	TSC	TSF	TWF	SWX	SSX
η_{exergy} (%)	49.29	53.21	52.17	51.23	44.56	43.55	38.27	41.16	36.16	34.76
η_{energy}(%)	53.12	49.64	49.36	47.15	33.28	29.79	33.13	23.32	19.27	19.08
$\dot{E}_D$ (kW)	3218	2937	3367	3312	4045	4037	2612	3386	3663	3538

Figure 7. The mean energy and exergy efficiencies as well as the mean total exergy destruction rate of each typical day under optimization condition based on maximum exergy efficiency.

3.4. The Optimized Quasi-Steady State Results For Different Typical Days
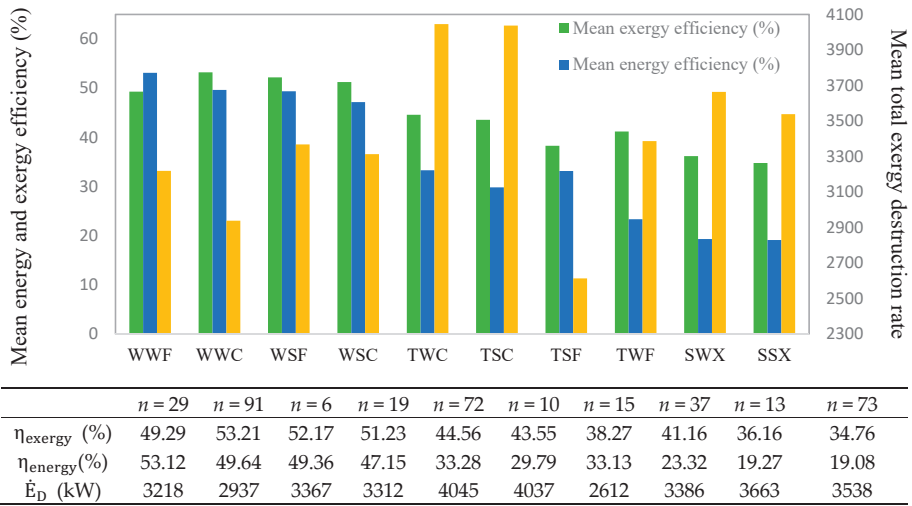
The quasi-steady state study under off-design conditions is calculated for the proposed system to examine the system performance. Then the system is optimized based on two main criteria, exergy efficiency and total exergy destruction rate. In the first scenario, the optimization is performed for the maximum exergy efficiency. The minimizing of the total exergy destruction rate is considered in the second scenario. According to the sensitive analysis, parameters such as: the turbine inlet pressure, the generator temperature, the temperature differences at the Absorber and condensers affect the system performance. The possible range of these parameters for optimization purpose is considered as follows:

$$\text{maximize } \eta_{exergy} \text{ and minimize } \dot{E}_{D,tot} \ (\text{TIP, } T_{gen}, \ \delta T_{CON1}, \ \delta T_{CON2}, \delta T_{ABS})$$

$$11 \le \text{TIP (bar)} \le 32$$

$$40 \le T_{gen}(°C) \le 67$$

$$5 \le \delta T_{CON1}(°C) \le 25$$

$$5 \le \delta T_{CON2}(°C) \le 15$$

$$5 \le \delta T_{ABS}(°C) \le 17$$

$$11 \le \text{TIP (bar)} \le 32$$

It is noteworthy to mention that in all annual calculations for 10 typical days, the ammonia concentration in the power section is kept constant as $0.5 \, \text{kg}(NH_3)/\text{kg}(\text{solution})$. The other operational parameters (pinch point temperature difference in the boiler, hot outlet-cold inlet temperature difference in the boiler, heat sink outlet temperature at the absorber, rectifier and condensers, reinjection geothermal hot water temperature) are calculated in off-design conditions for each 10 typical days category. The optimization results are presented in Figure 7 for maximum mean exergy efficiency and in Figure 8 for minimum mean total exergy destruction rate. In addition, the values of different operational parameters as well as the other parameters, which are obtained to optimize the system, are underlined in Table A1 for winter conditions and Table A2 for summer conditions in Appendix A.
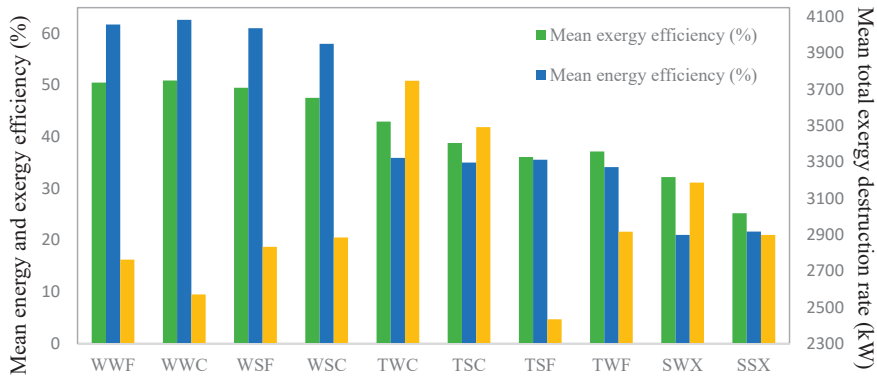
	n = 29	*n* = 91	*n* = 6	*n* = 19	*n* = 72	*n* = 10	*n* = 15	*n* = 37	*n* = 13	*n* = 73
η_{exergy} (%)	50.5	50.89	49.48	47.58	42.95	38.79	36.08	37.15	32.2	25.2
η_{energy}(%)	61.74	62.63	61.02	58	35.93	35.01	35.55	34.14	21.09	21.66
$\dot{E}_D$ (kW)	2762	2570	2832	2884	3747	3492	2433	2916	3186	2898

Figure 8. The mean energy and exergy efficiencies as well as the mean total exergy destruction rate of each typical day under optimization condition based on minimum total exergy destruction rate.

In order to maximize the exergy efficiency based on yearly calculation in the proposed system, the δT_{CON2} and δT_{ABS} take their highest values, the δT_{CON1} is considered its lowest value and the TIP and T_{gen} are selected as the variable parameters. In the first scenario, the mean annual exergy and energy efficiencies are calculated to be 44.67% and 35.47%, respectively due to the weighting according to the frequency of typical days. The mean total exergy destruction rate in the first scenario is calculated to be 3412.83 kW. As indicated in Figure 7, due to the high values of heating demand in winter days in comparison to the transition and summer days, the exergy efficiency in winter days is higher. In the weather category of WWC, the higher mean exergy efficiency (53.21%) happens. In addition, the mean exergy efficiency in summer days takes the lowest value because of the lower values of heating demand. The lowest decrease of the mean exergy efficiency takes place at SSX due to the lowest value of required heating demand. The cooling demand in summer days is higher; however, the cooling exergy takes lower values in comparison to heating exergy. Besides, in the first scenario the highest and lowest mean energy efficiency occurs in the WWF and SSX with values of 53.12% and 19.07%, respectively. The lower mean energy efficiency in hot days happens due to the lower values of heat input to the system. The higher reinjection geothermal temperature brings about reduction in heat input. In the typical day of WSF, in the first scenario the system is run under part load of 90% with net produced power of 1517 kW. However, in the typical day of TSF with the net produced power of 986.1 kW the system is run under part load of 58%.

In minimizing the total exergy destruction rate, the δT_{CON1}, δT_{ABS} and δT_{CON2} select their lowest values. The TIP and T_{gen} are considered as the variable parameters. In this regard, in the second scenario the annual mean exergy destruction rate is 2980.32 kW. In addition, the annual mean exergy and energy efficiencies in the second scenario are calculated to be 40.95% and 42.59%, respectively. It is observed that the highest mean exergy destruction rate occurs in the typical day TWC of 3747 kW. The lowest mean exergy achieves a value of 2433 kW in the typical day TSF. In the winter days, the total exergy destruction rate in the work days is lower than the one in the Sundays, however, in the transient and summer days this value in the workdays is higher than the one in the Sundays. In addition, a comparison between cloudy and fine days in the winter days shows that in the fine days the total exergy destruction rate takes higher value than the one in the cloudy days in the winter conditions. In the transient condition, this value in cloudy days in lower than the one in the fine days. In this

regard, the performances of tri-generation system have been changed with variation in the weather conditions. The system works under part load of 35.35% and 70.32% in the typical day of WWF and SWX, respectively.

Comparing two optimization cases, the reduction in the total exergy destruction rate in the second scenario is achieved at the expense of 8.32% decrease in the exergy efficiency. In addition, the higher mean exergy efficiency in the first scenario is obtained at the expense of 14.52% increase in the total exergy destruction rate. In this regard, the optimization results for minimizing the total exergy destruction rate bring about a better performance enhancement.

In detail discussion, the on-design exergy efficiency in [17] driven by geothermal heat source of 173 °C was 52.8% in winter days, however it was calculated to be 49.5% in summer days. However as seen in the Figures 7 and 8, the exergy efficiency in the winter days is varied between 38.79−53.21%. In the summer days, it varies between 25.2−36.16%. In addition, in the transient conditions, it is in the range of 36.08−41.16%. Furthermore, in Ref. [17] the ambient temperature was taken constant values of in summer and winter days 22.3 °C and 10.1 °C, respectively. However, in the present study it varies in different typical day categories according to an existing geothermal district heating network in the German Molasse basin, which makes the investigation more practical.

Referring to Tables A1 and A2 in the Appendix A, the turbine isotropic efficiency in the off- design mode in different typical day categories varies between 56−85%, however it took almost in the previous works constant value of 85%. It is important to mention that the turbine isotropic efficiency in the off-design calculation in the second scenario is almost 5−20% lower than the one in the first scenario. In addition, the pinch point difference temperature in the boiler in previous works always took a constant value of 10 °C. However, as shown in Tables A1 and A2, it varies between 14.22−25.47 °C for maximizing the exergy efficiency. It is obvious that the pinch point difference temperature in the boiler takes higher values in order to minimizing the total destruction rate in comparison to maximizing the exergy efficiency. On the other hand, the temperature difference of the heat sink streams (δT_{air}) in the previous studies almost was taken 10 °C. These values in the present work and referring to Tables A1 and A2, are calculating in the off-design conditions and vary in the range of 3.5−19.2 °C. It is shown that the heat sink temperature difference in the REC ($\delta T_{air,REC}$) is decreases with a reduction in the heating demand rate. Additionally, these values in the second scenario are higher than the ones in the first scenario. The heat sink temperature difference of the ABS ($\delta T_{air,ABS}$) and CON$_1$ ($\delta T_{air,CON1}$) in maximizing the exergy efficiency is almost higher than the one in minimizing the total destruction rate. However, the heat sink temperature difference in the CON$_2$ ($\delta T_{air,CON2}$) in the first scenario is lower than the one in the second one.

4. Conclusions

A novel tri-generation system using ammonia-water solution as working fluid driven by geothermal heat source is studied with the aim to fulfill corresponding heating and cooling demand in winter and summer conditions in Germany. The sensitive analyses are performed to study the influence of various optional parameters on the system performance. In addition, the result of parametric analysis for 10 different typical days is investigated in off-design modes.

The following main conclusions can be drawn according to the corresponding issues mentioned in the introduction:

- The required heating demand is covered by the geothermal mass flow division ratio in both winter and summer conditions. This value is decreased with a reduction in heating demand.
- There is a local optimum for the exergy efficiency and the total destruction rate at specific values of Turbine inlet pressure.
- With an increase in generator temperature, there is a local maximum in exergy efficiency, however, the total exergy destruction rate is decreased.
- Under optimization condition, the maximum annual exergy efficiency is obtained as 44.67% at the expense of 14.52% increase in the total exergy destruction rate in comparison to second scenario.

- The ooptimization results show the minimum mean total exergy destruction rate of the system is calculated as 2980 kW at the expense of 8.32% decrease in the exergy efficiency in the first scenario.
- Considering both exergy efficiency and total exergy destruction rate in off-design condition, the best enhancement through the optimization process is achieved on the typical day WWC with 53.21% of exergy efficiency and 2570 kW of total exergy destruction rate.
- Comparing the optimization results for maximum exergy efficiency and minimum total exergy destruction rate depicts a better performance improvement obtained in the second scenario.

In future studies, designing the heat exchangers will be applied to compare the off-design results. In addition, the annual economic analysis will be considered, as well.

Author Contributions: All authors contributed to this work by collaboration. M.A.K. is the main author of this manuscript. F.H. had the initial idea and assisted in the conceptual design of the study as well as in the writing of the manuscript. D.B. supervised the whole project. All authors have read and agreed to the published version of the manuscript.

Conflicts of Interest: The authors declare no conflict of interest.

Nomenclature

ABS	absorber	TIP	turbine inlet pressure
BOI	boiler	TUR	turbine
CON	condenser	$\dot{W}$	power (kW)
DEP	dephlepmator	X	ammonia concentration
DHE	domestic heat exchanger		
EVA	evaporator	**Subscripts and abbreviations**	
e_{ch}^0	standard chemical exergy	0	ambient
EX	expansion valve	CD	cooling demand
$\dot{E}$	exergy rate	ch	chemical
e	Specific exergy	D	destruction
GEN	generator	geo	Geothermal hot water
h	specific enthalpy	HD	heating demand
M	Molar weight	L	loss
$\dot{m}$	mass flow rate	p	product
P	pressure	ph	physical
Pu	pump	pp	pinch point
r_{geo}	Geothermal mass flow division ratio	**Greek symbols**	
s	specific entropy	η_{II}	Exergy efficiency
SHE	solution heat exchanger	η_{is}	isentropic efficiency
SEP	separator	ζ	Ammonia concentration
T	temperature	$Y_{D,k}^*$	ratio of exergy destruction for a certain component

Appl. Sci. **2020**, *10*, 6532

Appendix A

Table A1. Detailed parameters of the optimization calculation (a) maximum exergy efficiency (b) minimum exergy-destruction rate.

	WWF		WWC		WSF		WSC		TWC		TSC	
	(a)	(b)	(a)	(b)	(a)	(b)	(a)	(b)	(a)	(b)	(a)	(b)
$T_{ambient}$ (°C)	−0.13		−5.68		2.27		1.1		7.37		4.81	
$\dot{Q}_{heating}$ (MW)	11.8		11.66		11.8		10.79		6.3		6.15	
$\dot{Q}_{cooling}$ (MW)	-		-		-		-		-		-	
Decision operational variables												
TIP (bar)	16.4	15.7	17.5	17	17	17.5	18.4	20.3	20.5	21.9	19.5	22.5
T_{gen} (°C)	57.66	62.02	52.65	57.5	57.32	61.82	58	61.48	58.2	57.94	55	58.9
δT_{ABS} (°C)	15.8	9.8	11.2	5.5	12.6	6.4	14	5.6	15	8.6	6.897	5.2
δT_{CON1} (°C)	19.69	23.4	17.67	25.1	17	20.83	18.75	21.71	13.72	13.5	12.48	15.81
δT_{CON2} (°C)	5	5	5.2	5	5	5	5.2	5	5	5	5	5
Calculated parameters in the off-design conditions												
$\eta_{s,tur}$ (%)	84	68	85	70	84	64	85	64	85	81	84	76
δT_{PP} (°C)	17.99	34.5	19.16	35.3	16.85	33	17.67	29.6	13.28	16.66	15.86	22.32
T_{eva} (°C)	-	-	-	-	-	-	-	-	-	-	-	-
$\delta T_{air,ABS} = T_{32} - T_{31}$ (°C)	17.83	14.7	12.61	9.77	14.13	10.1	15.54	9.01	15.43	6.55	12	8.1
$\delta T_{air,CON1} = T_{36} - T_{35}$ (°C)	16.48	15.45	17.68	16.52	16.56	15.49	16.4	15.57	13.55	8.6	12.44	15.8
$\delta T_{air,CON2} = T_{40} - T_{39}$ (°C)	7.06	18.07	7.98	19.2	7.062	16.27	6.88	14.26	3.67	13.5	3.751	7.45
$\delta T_{air,REC} = T_{34} - T_{33}$ (°C)	10.81	14.5	11.81	16.34	9.485	12.47	9.37	11.59	5.14	5.3	5.426	5.7

Table A2. Detailed parameters of the optimization calculation (a) maximum exergy efficiency (b) minimum exergy destruction rate.

	TSF		TWF		SWX		SSX	
$T_{ambient}$ (°C)	13.81		15.42		15.67		17.24	
$\dot{Q}_{heating}$ (MW)	4.79		5.69		2.99		2.9	
$\dot{Q}_{cooling}$ (MW)	1.78		1.9		2.58		2.5	
	(a)	(b)	(a)	(b)	(a)	(b)	(a)	(b)
Decision operational variable								
TIP (bar)	20	21.7	19.5	25.2	20	26.06	20.2	29.6
T_{gen} (°C)	67.62	67.62	61.02	64.7	58.96	65	60.81	66.85
δT_{ABS} (°C)	12.11	7.81	12.71	7.69	11.61	11.51	12.01	7.55
δT_{CON1} (°C)	14.2	14.2	7.02	10.12	4.99	10.12	5	10.12
δT_{CON2} (°C)	5	5	5	5	5	5	5	5
Calculated parameters in the off-design conditions								
$\eta_{s,tur}$ (%)	71	60	079	66	80	71	79	56
δT_{PP} (°C)	25.47	26.01	14.65	15.14	14.22	12.46	14.84	11.78
T_{eva} (°C)	10.58	10.14	9.7	7.1	11.57	6.522	14.89	15.5
$\delta T_{air,ABS} = T_{32} - T_{31}$ (°C)	13.64	9.29	12.76	7.7	10.74	4.07	11.38	7.13
$\delta T_{air,CON1} = T_{36} - T_{35}$ (°C)	14.13	14.13	6.55	9.37	3.83	7.79	3.9	8.11
$\delta T_{air,CON2} = T_{40} - T_{39}$ (°C)	7.215	8.9	3.3	5.23	2.5	3.71	2.7	13.11
$\delta T_{air,REC} = T_{34} - T_{33}$ (°C)	4.311	4.5	3.1	3.22	2.45	2.43	2.4	2.42

References

1. Wanga, X.; Levya, E.K.; Pana, C.; Romeroa, C.E.; Banerjeeb, A.; Rubio-Mayac, C.; Pand, L. Working fluid selection for organic Rankine cycle power generation using hot produced supercritical CO_2 from a geothermal reservoir. *Appl. Therm. Eng.* **2019**, *149*, 1287–1304. [CrossRef]

2. Feng, P.H.; Zhao, B.C.; Wang, R.Z. Thermophysical heat storage for cooling, heating, and power generation: A review. *Appl. Therm. Eng.* **2020**, *166*, 114728. [CrossRef]

3. Cao, L.; Lou, J.; Wang, J.; Dai, Y. Exergy analysis and optimization of a combined cooling and power system driven by geothermal energy for ice-making and hydrogen production. *Energy Convers. Manag.* **2018**, *174*, 886–896. [CrossRef]

4. Seyfouri, Z.; Ameri, M.; Mehrabian, M.A. Exergo-economic analysis of a low-temperature geothermal-fed combined cooling and power system. *Appl. Therm. Eng.* **2018**, *145*, 528–540. [CrossRef]

5. Moharamian, A.; Soltani, S.; Rosen, M.A.; Mahmoudi, S.M.S.; Morosuk, T. Exergoeconomic analysis of natural gas fired and biomass post-fired combined cycle with hydrogen injection into the combustion chamber. *J. Clean. Prod.* **2018**, *180*, 450–465. [CrossRef]

6. Eller, T.; Heberle, F.; Brüggemann, D. Thermodynamic and economic analysis of geothermal combined heat and power based on a double-stage Organic Rankine Cycle. In Proceedings of the 5th International Seminar on ORC Power Systems, Athens, Greece, 9–11 September 2019.

7. Erdeweghe, S.V.; Bael, J.V.; Laenen, B.; D'haeseleer, W. Optimal combined heat-and-power plant for a low-temperature geothermal source. *Energy* **2018**, *150*, 396–409. [CrossRef]

8. AMosaffa, H.; Mokarram, N.H.; Farshi, L.G. Thermoeconomic analysis of a new combination of ammonia/water power generation cycle with GT-MHR cycle and LNG cryogenic exergy. *Appl. Therm. Eng.* **2017**, *124*, 1343–1353. [CrossRef]

9. Rostamzadeha, H.; Gargarib, S.G.; Naminb, A.S.; Ghaebib, H. A novel multigeneration system driven by a hybrid biogas-geothermal heat source, Part I: Thermodynamic modeling. *Energy Convers. Manag.* **2018**, *177*, 535–562. [CrossRef]

10. Zhang, Z.; Guo, Z.; Chen, Y.; Wua, J.; Hua, J.A. Power generation and heating performances of integrated system of ammonia–water Kalina–Rankine cycle. *Energy Convers. Manag.* **2015**, *92*, 517–522. [CrossRef]

11. Coskun, C.; Oktay, Z.; Dincer, I. Thermodynamic analyses and case studies of geothermal based multi-generation systems. *J. Clean. Prod.* **2012**, *32*, 71–80. [CrossRef]

12. Zare, V. A comparative thermodynamic analysis of two tri-generation systems utilizing low-grade geothermal energy. *Energy Convers. Manag.* **2016**, *118*, 264–274. [CrossRef]

13. Akrami, E.; Chitsaz, A.; Nami, H.; Mahmoudi, S.M.S. Energetic and exergoeconomic assessment of a multi-generation energy system based on indirect use of geothermal energy. *Energy* **2017**, *124*, 625–639. [CrossRef]

14. Mlcak, H.; Mirolli, M. Notes from the North: A Report on the Debut Year of the 2 MW Kalina Cycle Geothermal Power Plant in Húsavík, Iceland. In *Transactions-Geothermal Resources Council*; Geothermal Resources Council: Olympia, WI, USA, 2002; Available online: http://powerengineers.jobs/wp-content/uploads/2002/08/HusavikGRC2002.pdf (accessed on 26 March 2002).

15. Hjartarson, H.; Maack, R.; Jóhannesson, S.R. Húsavík Energy Multiple Use of Geothermal Energy. 2005. Available online: https://www.oh.is/static/files/Skyrslur_og_greinar/Enskar/OH_energy_multiple_use_grein_f_radstefnu.pdf (accessed on 30 January 2005).

16. Ogriseck, S. Integration of Kalina cycle in a combined heat and power plant, a case study. *Appl. Therm. Eng.* **2009**, *29*, 2843–2848. [CrossRef]

17. Dawo, F.; Wieland, C.; Spliethoff, H. Kalina power plant part load modeling: Comparison of different approaches to model part load behavior and validation on real operating data. *Energy* **2019**, *174*, 625–637. [CrossRef]

18. Knapek, E.; Kittl, G. Unterhaching Power Plant and Overall System. In Proceedings of the European Geothermal Congress, Unterhaching, Germany, 30 May–1 June 2007.

19. Mergner, H.; Schaber, K. Performance analysis of an evaporation process of plate heat exchangers installed in a Kalina power plant. *Energy* **2018**, *145*, 105–115. [CrossRef]

20. Schuster, S.; Markides, C.N.; Whitea, A.J. Design and off-design optimisation of an organic Rankine cycle (ORC) system with an integrated radial turbine model. *Appl. Therm. Eng.* **2020**, 115192. [CrossRef]

21. Ibarra, M.; Rovira, A.; Alarcón-Padillac, D. Performance of an Organic Rankine Cycle with two expanders at off-design operation. *Appl. Therm. Eng.* **2019**, *149*, 688–701. [CrossRef]

22. Eller, T.; Heberle, F.; Brüggemann, D. Techno-economic analysis of novel working fluid pairs for the Kalina cycle. *Energy Procedia* **2017**, *129*, 113–120. [CrossRef]

23. Heberle, F.; Eller, T.; Brüggemann, D. Thermoeconomic evaluation of one-and double-stage ORC for geothermal combined heat and power production. In Proceedings of the European Geothermal Congress, Strasbourg, France, 19–23 September 2016.

24. Eller, T.; Heberle, F.; Brüggemann, D. Transient Simulation of Geothermal Combined Heat and Power Generation for a Resilient Energetic and Economic Evaluation. *Energies* **2019**, *12*, 894. [CrossRef]

25. Klein, K.A.; Alvarado, F.L. *EES-Engineering Equation Solver*; Version 6.648 ND; F-Chart Software: Middleton, WI, USA, 2004.

26. Ibrahim, O.M.; Klein, S.A. Thermodynamic Properties of Ammonia-Water Mixtures. In *ASHRAE Transactions, Symposia*; ASHRAE Transactions: Atlanta, GA, USA, 1993; pp. 1495–1502.

27. Wagner, W.; Pruß, A. The IAPWS Formulation 1995 for the Thermodynamic Properties of Ordinary Water Substance for General and Scientific Use. *J. Phys. Chem. Ref. Data* **2002**, *31*. [CrossRef]

28. Fujuita, T.; Kikuchi, S. Vapor pressure of Aqueous Solutions of Ethylene Glycol. *Trans. Jpn. Soc. Refrig. Air Cond. Eng.* **2011**, *6*, 183–186.

29. Lee, D.J.; Huang, W.H. Enthalpy-entropy compensation in micellization of sodium dodecyl sulphate in water/methanol, water/ethylene glycol and water/glycerol binary mixtures. *Colloid Polym. Sci.* **1996**, *274*, 160–165. [CrossRef]

30. Kordlar, M.A.; Mahmoudi, S.M.S. Exergeoconomic analysis and optimization of a novel cogeneration system producing power and refrigeration. *Energy Convers. Manag.* **2017**, *134*, 208–220. [CrossRef]

31. McQuiston, F.C.; Spitler, D.P.J.; Jeffrey, D. *Heating, Ventilating and Azir Conditioning: Analysis and Design*, 6th ed.; Wilely: Hoboken, NJ, USA, 2004.

32. Zare, V.; Moalemian, A. Parabolic trough solar collectors integrated with a Kalina cycle for high temperature applications: Energy, exergy and economic analyses. *Energy Convers. Manag.* **2017**, *151*, 681–692. [CrossRef]

33. SeopKim, I.; Kim, T.S.; Lee, J.J. Off-design performance analysis of organic Rankine cycle using real operation data from a heat source plant. *Energy Convers. Manag.* **2017**, *133*, 284–291. [CrossRef]

34. Cao, Y.; Dai, Y. Comparative analysis on off-design performance of a gas turbine and ORC combined cycle under different operation approaches. *Energy Convers. Manag.* **2017**, *135*, 84–100. [CrossRef]

35. Manente, G.; Toffolo, A.; Lazzaretto, A.; Paci, M. An Organic Rankine Cycle off-design model for the search of the optimal control strategy. *Energy* **2013**, *58*, 97–106. [CrossRef]

36. Heberlea, F.; Hofera, M.; Brüggemanna, D.R. A Retrofit for Geothermal Organic Rankine Cycles based on Concentrated Solar Thermal Systems. *Energy Procedia* **2017**, *129*, 692–699. [CrossRef]

37. Ghasemi, H.; Sheu, E.; Tizzanini, A.; Paci, M.; Mitsos, A. Hybrid solar–geothermal power generation: Optimal retrofitting. *Appl. Energy* **2014**, *131*, 158–170. [CrossRef]

38. Energietechnik, G.; Ingenieure, V.D. *Referenzlastprofile von Ein-und Mehrfamilienhäusern für den Einsatz von KWK-Anlagen*; Beuth: Berlin, Germany, 2008. (In German)

39. Heberle, F.; Brüggemann, D. Exergy based fluid selection for a geothermal Organic Rankine Cycle for combined heat and power generation. *Appl. Therm. Eng.* **2010**, *30*, 1326–1332. [CrossRef]

40. Mahmoudi, S.M.S.; Kordlar, M.A. A new flexible geothermal based cogeneration system producing power and refrigeration. *Renewe Energy* **2018**, *123*, 499–512. [CrossRef]

41. Misraa, R.D.; Sahoob, P.K.; Guptab, A. Thermoeconomic evaluation and optimization of an aqua-ammonia vapour-absorption refrigeration system. *Int. J. Refrig.* **2009**, *29*, 47–59. [CrossRef]

42. Akbari, A.D.; Mahmoudi, S.M.S. Thermoeconomic performance and optimization of a novel cogeneration system using carbon dioxide as working fluid. *Energy Convers. Manag.* **2017**, *145*, 265–277. [CrossRef]

43. Adewusi, S.A.; Zubair, S.M. Second law based thermodynamic analysis of ammonia–water absorption systems. *Energy Convers. Manag.* **2004**, *45*, 2355–2369. [CrossRef]